FINAL REPORT: RPSEA PROJECT NO. 07121-DW1603D
RICE UNIVERSITY

Structural Health Monitoring System for Deepwater Risers with Vortex-induced Vibration: Nonlinear Modeling, Blind Identification Fatigue/Damage Estimation and Local Monitoring using Magnetic Flux Leakage

by

Chaojun Huang

A Thesis Submitted
in Partial Fulfillment of the
Requirements for the Degree
Doctor of Philosophy

Approved, Thesis Committee:

Satish Nagarajaiah, Chair
Professor of Civil and Environmental Engineering and Mechanical Engineering and Material Science

Jamie E. Padgett
Assistant Professor of Civil and Environmental Engineering

Andrew J. Dick
Assistant Professor of Mechanical Engineering and Material Science

Houston, Texas
June, 2012

ABSTRACT

Structural Health Monitoring System for Deepwater Risers with Vortex-induced Vibration: Nonlinear Modeling, Blind Identification Fatigue/Damage Estimation and Local Monitoring using Magnetic Flux Leakage

by

Chaojun Huang

This study focuses on developing structural health monitoring techniques to detect damage in deepwater risers subjected to vortex-induced vibration (VIV) and to inspect damage to the deepwater riser caused by corrosion based on magnetic flux leakage techniques (MFL).

Vibration-based damage detection needs both responses from the undamaged and damaged deepwater risers. Because no experimental data for damaged deepwater risers is available, a model to predict the VIV responses of deepwater risers with given conditions is needed, which is the forward problem. In this study, a new three dimensional (3D) analytical model is proposed considering coupled VIV (in-line and cross-flow) for top-tensioned riser (TTR) with wake oscillators. The model is verified by direct numerical simulations and experimental data.

The inverse problem is to detect damage using VIV responses from the analytical models with/without damage, where the change between dynamic properties obtained from riser responses represents damage. The inverse problem is performed in two steps: blind identification and damage detection. For blind identification, a wavelet modified second order blind identification (WMSOBI) method and a com-

plex WMSOBI (CWMSOBI) method are proposed to extract modal properties from output only responses for standing and traveling wave vibration, respectively. Numerical simulations and experiments validate the effectiveness of proposed methods. For damage detection, a novel weighted distribution force change (WDFC) index (for standing wave) and a phase angle change (PAC) index (for traveling wave) are proposed and proven numerically. Experiments confirm that WDFC can accurately locate damage and estimate damage severity. Furthermore, a new fatigue damage estimation method involving WMSOBI, S-N curve and Miner's rule is proposed and proven to be effective using field test data.

MFL based defect detection technique utilizes a non-contact measurement to detect changes in wall thickness with high resolution (as low as 0.2 mm thickness change, 5% of base 4 mm).

Acknowledgments

First of all, I would like to express sincere gratitude to Professor Satish Nagarajaiah. Prof. Nagarajaiah has always been a great mentor in all aspects of life and I thank him for the opportunity to study at Rice University, his direction and guidance through my Ph.D. research. Through the path to Ph.D., there are difficult moments with academic and non-academic issues, I even started to doubt my choice on pursuing the doctor's degree. With Prof. Nagarajaiah's patience, encouragement and support, I was able to go through those moments. I am indebted to him for his guidance that has helped me become a researcher. Also, I would like to thank other thesis committee members: Professor Jamie E. Padgett and Professor Andrew J. Dick.

I would like to specially thank Professor P. Frank Pai , University of Missouri-Columbia, for his support and help in the development of nonlinear finite element method and computer program. I would also like to thank Mr. Andrew Lynch, graduate student at Rice University, for his assistance and collaboration during the magnetic flux leakage inspection experiments.

I have always been enjoying working in a research group that has a sincere collaboration and bonds a relationship beyond colleagues. It has been a pleasure to work with Dr.Michael Contreras, Dharma Pasala, Srivishnu Vemuru, Chao Sun and others for their help and friendship. Also, support and help from other faculties, staff and graduate students at Rice University are greatly appreciated.

I would like also to thank Dr. Nadathur Varadarajan, Dr. Ertan Sonmez, Dr. Bilei Chen and Dr. Ziling Li. Although graduated, they took their time out from their professional lives to offer help, advices and suggestions on my research as well as future planning.

Last but most important, I would like to thank my father, Jingquan Huang and mother, Xingfeng Wang. They have been extremely supportive to let me study abroad as their only child. They have been through a lot during these years, especially my father. He was seriously ill in 2009 when I was away. I am indebted to them and words cannot carry the thankful feeling I want to depict. It is their support that make it possible to complete this dissertation.

This research is supported by Department of Energy and Research Partnership to Secure Energy for America (RPSEA), Project No. 07121-DW1603D. This support is gratefully acknowledged.

Contents

Illustrations

Tables

Chapter 1

Introduction, Overview and Literature Review

According to the US Energy Information Administration's 2011 estimate [1], the US energy consumption increased another 1% from 2009 to 2010. Of the energy consumption, more than 3/4 is still fossil energy. Oil remains the largest source at 37.8% of the total consumption, followed closely by natural gas at 25.1%. Under the pressure of increasing global energy demand, the oil industry is focusing its efforts on exploring oil and natural gas in deep sea. As offshore oil platforms move farther from the shore line, one critical issues emerge for oil extraction: the safety of the oil platform and its working environment, which means that there is a need for a reliable structural health monitoring system to detect damage in a timely manner.

1.1 Review of Riser Health Monitoring for Deepwater Platform

Risers are the most important component of offshore oil platforms. Risers are the conduits between the subsea wellhead and the drilling or production platform for development, production, gas lift or water injection purposes. They can be either rigid or flexible. Risers can further be classified as vertical top tensioned risers (TTR), steel cantenary risers, and flexible risers as shown in Fig. 1.1 [2]. This study concentrates on TTR for its widely applicable depth range.

From left to right in Fig. 1.1, the types of platforms are (1) Onshore platform,

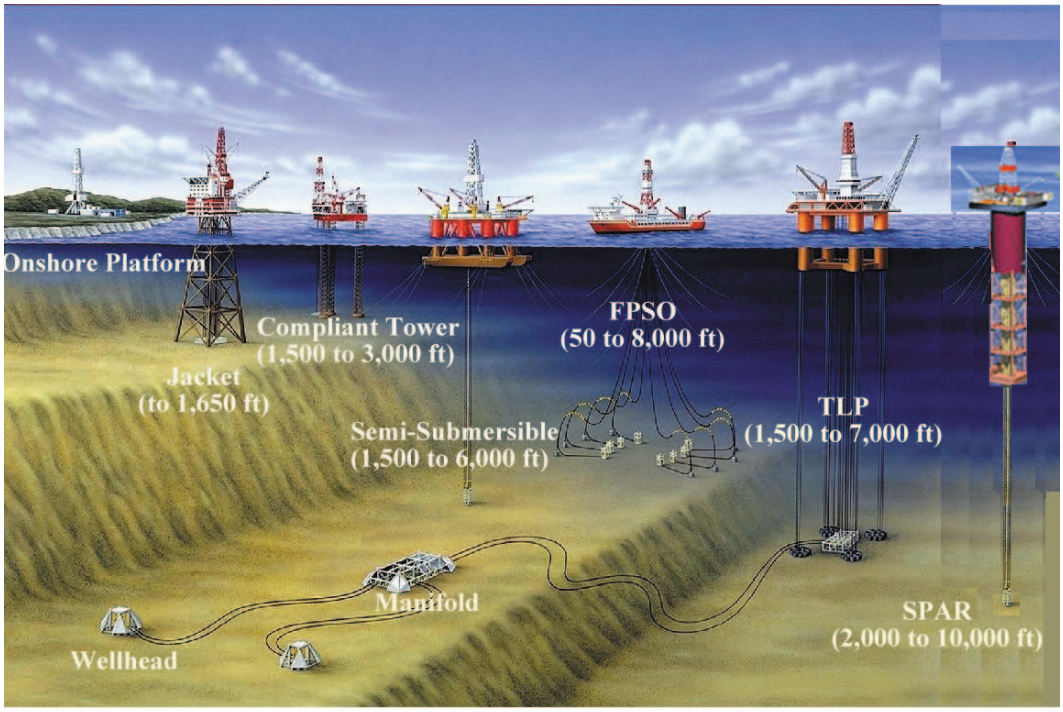

Figure 1.1 : Different Types of Platforms and Risers (modified from acrigs.com)

(2, 3) Fixed platforms, (4) Semi-submersible platform with top-tensioned riser, (5) Floating production, storage, and offloading (FPSO) facility with flexible risers, (6) Tensioned Leg Platform and (7) SPAR platform (Modified from [2]).

If everything on the deepwater platform functions smoothly, the crude oil and natural gas would find a safe route through risers to the global markets from the seabed wells. However, mistakes, no matter how small, can be costly, and especially the riser failure has serious consequences. Any failure incident in riser would not only be an economical and environmental disaster, but would have far reaching consequences affecting the entire community. During recent decades, there were quite a few incidents involving pipelines/riser. On May 6, 1990, the pipeline leakage of Eugene Island was caused by a 1-inch valve being snagged out by trawl net, which resulted in a 4,569

barrel oil spill [3]. On November 16, 1994, Hobbit Pipeline leak at Ship Shoal Block 281 was caused by bending failure of the pipe, which resulted in a 4,535 barrel oil spill [4]. On 23 June 2007, a pipeline leakage on Main Pass Area Block 288 was caused by four corrosion holes in one pipe section [5]. On April 20, 2010 the Deepwater Horizon, a semi-submersible mobile offshore drilling unit which was drilling an exploratory well in the Macondo Prospect, located in the Mississippi Canyon experienced a blowout. The resulting explosion engulfed the platform in flames. Multiple ships reached the site and attempted to douse the flames. After burning for more than a day, the drilling unit could not be saved. Deepwater Horizon sank on April 22, 2010 and the riser collapsed with the platform. 11 workers died in the explosion. An oil leak ensued from the drill site which leaked 4.9 million barrels of oil into the Gulf of Mexico, making it the largest oil spill recorded in U.S. history [6] (largest of its kind in the world history [7]).

To prevent this kind of disaster, real-time structural health monitoring systems for risers in offshore deepwater platforms are needed to quickly determine whether there is damage and to activate contingency plans or mechanisms to initiate damage protection measures or to prevent complete blowout.

1.1.1 Review of Riser Failure Mechanisms

Deepwater risers present a unique challenge due to harsh operating conditions. The operating depth at which deepwater risers are employed can currently reach up to 3000m. The analysis and measurement of deepwater riser response is complex due to vessel motions, vortex-induced vibrations, touchdown point variations and soil-structure interactions. Detecting damage and estimating the service life is very complex due to the additional degradation phenomenon (or process) such as corrosion [8].

To address damage detection and health monitoring of risers, a good understanding of different riser failure mechanisms is needed.

From offshore pipeline failure statistics for the past 4 decades, shown in Fig. 1.2 [9], it can be clearly seen that the main cause responsible for the riser failure is corrosion. The other major contributor for failure is natural hazard, such as hurricanes or tsunamis. So, a constant monitoring and timely inspection strategy becomes critical to detect the onset of damage early on and avert major disasters.

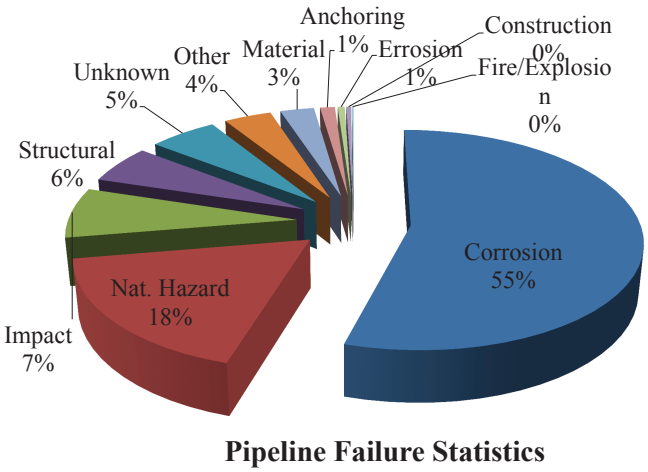

Figure 1.2 : General Pipeline Failure Statistics for Gulf of Mexico(DOE/MMS, 2002)

For deepwater risers, the fatigue damage caused by wave, vessel motion and vortex-induced vibration is another important cause of failure. Riser fatigue life is the governing criteria in riser design for ensuring a service life more than 25 years [10]. As a result, all the five major contributors to riser failure (corrosion, fatigue, natural hazards, impact and structure) should be detected in a timely manner by means of a monitoring and inspection system.

1.1.2 Review of Methods for Riser Damage Detection

Risers are thoroughly inspected for damages before installation. Any periodic inspection or damage detection of the riser has to be done on-site and the methods should not induce any damage to the riser. Various Non-destructive evaluation (NDE) methods have been introduced to the field of riser inspection [8]. Typically, we can classify them into the following types: Visual Inspection, Ultrasonic Technique (UT), Radiography, Electro-magnetic method, Vibration based NDE and other techniques. The effectiveness of these NDE methods for detecting damage in deep water risers has not been evaluated or demonstrated.

Traditionally, visual inspection and manual ultrasonic testing for damage assessment are the main approaches for inspection. However, visual inspection can only detect the external damage, cannot quantify damage and is too subjective. For deepwater risers, it is also impossible for the diver to get close to inspect the riser in ultra deep sea. For short-range UT [11], its applicability in deepwater risers is excluded by its requirement of clean and smooth surface of the pipe and couplant to ensure the attachment and transmissibility between sensor and pipe surface. Long-range UT [12] can only transmit around one wavelength of the guided wave into the riser, which results in neglecting the internal defects like corrosion if the wall of the riser is thicker than the wavelength. Safety issues and deepwater conditions keep radiography away from deepwater risers. Other new techniques like infrared thermography [13] and acoustic emission [14] technique are not applicable at deepwater scenarios.

All the electromagnetic testing methods currently in practice take advantage of the metallic characteristics of risers for damage detection: such as eddy-current testing [15], pulsed eddy current testing [16] , remote field eddy current [17, 18], magnetic flux leakage (MFL) [19]. Among them, MFL is one of the most commonly used and

the oldest in-line inspection methods to detect metal loss due to corrosion or gouging [11]. Damages like weld defects or inclusions can be detected by MFL as well. With its ability to work efficiently using a permanent magnet, MFL can be a possible solution as local inspection method for deepwater risers.

Vibration-based methods have been widely used in civil structures, space structures, planes and cars. The advantage of vibration-based monitoring methods lies in its inherent simplicity, i.e., damage detection is based on the measurement of vibration alone. Unlike earlier methods which impose certain requirements on the surface to be monitored (UT), or techniques where the detection depth is limited by their input guided wave wavelength, vibration based techniques suffer from no such limitations. Further, unlike local inspection methods (like MFL) the results of the vibration based monitoring help us understand the global behavior of the riser. Hence, vibration-based methods are a possible solution for deepwater riser monitoring systems.

Vandiver [20] proposed to use the natural frequency change as an indicator of damage from the vibration response of fixed offshore platforms-where riser motion is not as important as the motion of platform tower. Similarly, a modal distribution method is proposed by Sweetman et al. [21], which uses the significant change between the power spectrum from measured structural responses to indicate a change (such as damage) in primary system. This is also a frequency domain method based on output data, which is not applicable to deepwater risers with varying natural frequencies. Riveros et al. [22] suggested that a statistical pattern recognition method with a combined model with auto-regressive (AR) and auto-regressive with exogenous inputs (ARX) works better than modal distribution method. However, in deepwater situation, the inputs are unknown, which means the method is not suitable. In

addition, natural frequencies of the riser are time-varying due to the tension and touchdown points variation. Hence, there is a need for development of more reliable damage detection methods for deepwater risers that are based on vibration response.

1.2 Proposed SHM System for Deepwater Riser

As mentioned earlier, the safety of deepwater risers is essential for sustainable operation of offshore platforms. The structural health monitoring (SHM) system for deepwater risers is important to detect damage and perform repairs before failure occurs. Two main sources of damage are fatigue and corrosion. Failure of the riser would not only be an economical and environmental disaster, but also have far reaching consequences affecting communities. Since combining global and local monitoring can greatly increase the accuracy of damage detection and fatigue estimation, a structural health monitoring system is proposed with local inspection using robotic Magnetic Flux leakage (MFL) sensors, which is efficient and provides high resolution estimate of wall thickness changes due to corrosion or damage, while proposed vibration-based system identification can estimate global damage locations and fatigue life.

The flowchart for the proposed strategy is shown in Fig. 1.3. In Fig. 1.3, global monitoring refers to continuous monitoring of the dynamic properties of risers in real-time. Vibration measurement can be accelerations, displacement and strains etc. The measured data is then processed to obtain the dynamic properties. The damage indexes (or fatigue estimation) are then derived from the dynamic properties. The damages, which are defined as dynamic property changes between intact and damage systems, can be located; damage severity can be estimated based on the magnitude of damage indices as well. If damage occurs according to the global monitoring system, a warning signal with damage information is sent to the control center. Then a robotic

crawler carrying MFL sensors is sent to the predicted damage location to verify the warning and estimate its severity. Finally if both local and global monitoring indicate the occurrence of damage, the estimated service life and damage information is made available to the operators regarding the decision on repairing or replacement.

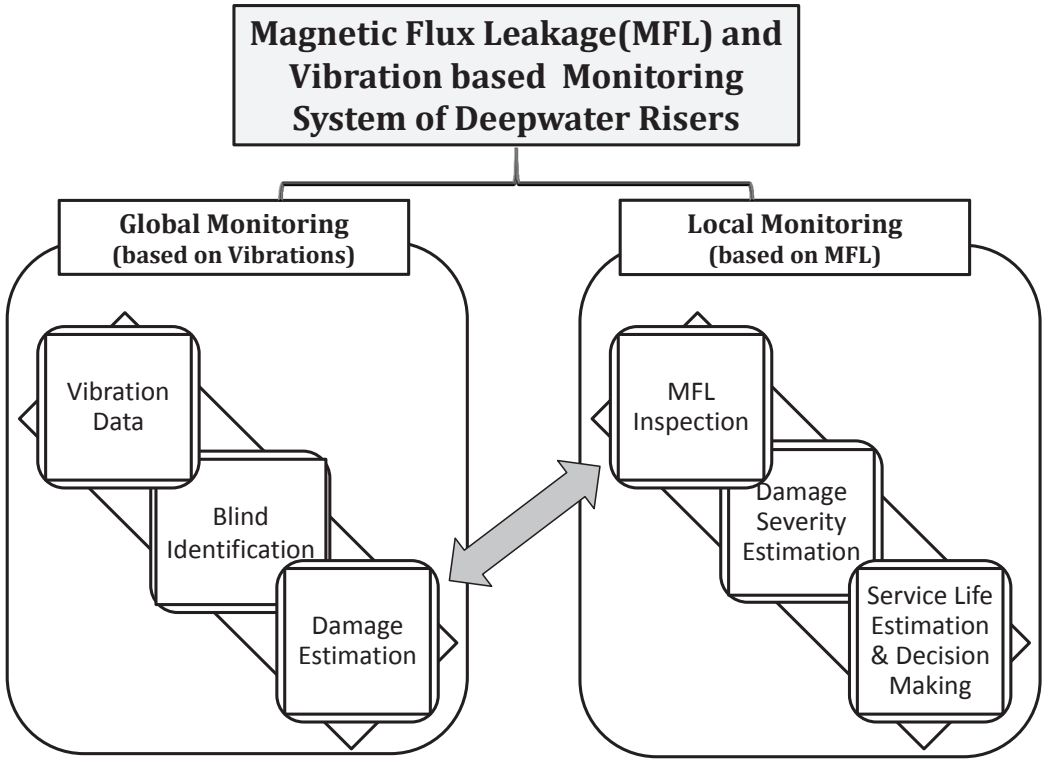

Figure 1.3 : Proposed Strategy for Deepwater SHM System

1.2.1 Global Monitoring - based on Measured Riser Vibrations

In this study, global monitoring is based on the vibration of deepwater risers. As shown in Fig 1.3, global monitoring is divided into three steps.

1. Measure the vibration response from the deepwater riser;

2. Perform modal estimation using blind identification method;

3. Estimate the damage or fatigue severity and location.

The response of risers is induced by vessel motions, wave and current etc., among which a special phenomenon,vortex-induce vibration (VIV), caused by current passing by the riser contains the most information about dynamic properties. When a bluff body is subjected to fluid flow with sufficiently large velocity, shedding vortices (a von Karman vortex street) will occur and exert oscillatory forces in both inline direction and the cross-flow direction. When one or more modes of bluff body are excited by the vortex shedding, steady state large amplitude vibrations occur; the phenomenon is called vortex-induced vibration (VIV). The modal estimation is based on VIV.

However, as the damages are defined as the changes of dynamic properties and their derivatives between undamaged and damaged system. There is no public field (measured) data available for both damaged and undamaged scenarios. Hence, there is a need for an analytical model to predict the responses with given conditions for output only real-time damage detection. Thus, the study of global monitoring is divided into two parts:

- Forward Problem: develop an analytical model to estimate the vibration responses of risers with given conditions

- Inverse Problem: based on the predicted vibration responses from analytical model with/without damage(s), estimate the damage location and severity continuously

1.2.2 Forward Problem - 3D Analytical Model

If field (experimental) data of vortex-induced vibration (VIV) for both undamaged and damaged risers were available, it would be much easier to develop and verify the damage detection algorithms. However, most of the scaled model experiments carried out for VIV study are for the undamaged case only. It is essential to have data for both damaged and undamaged cases in order to verify the damage detection algorithm. As a result, a reliable analytical model for TTR has to be developed.

The analytical model should predict the vortex-induced vibrations (VIV) caused in the TTR due to hydrodynamic forces acting on the TTR. According to Sarpkaya's review paper [23], direct numerical simulation (DNS) generates the hydrodynamic forces acting on the TTR by solving the time-dependent Navier-Stokes equations. DNS can provide good simulation results but consumes a tremendous amount of computing power, which makes it unrealistic for VIV prediction. An analytical model that directly models the hydrodynamic forces presents a more computationally efficient alternative to DNS. In this study, a new approach to model the VIV response of riser will be developed, and its accuracy will be evaluated using results from both DNS as well as experimental data.

1.2.3 Inverse Problem - Real-Time Damage Detection

The inverse problem is to detect damage using VIV responses from the analytical models with/without damage, where the change between dynamic properties obtained from riser responses represents damage in the riser. Solving the inverse problem involves:

- Development of modal identification and damage detection techniques for deep-

water risers subjected to vortex-induced vibration. Identification of frequency and mode shapes (dynamic properties) of deepwater risers from VIV responses using output only signal processing techniques such as wavelet and second order blind identification (SOBI) methods

- Development of a new damage index derived from dynamic properties to locate damage and to estimate the severity of damage. The difference in the new damage index between the undamaged and damaged cases is used to locate and quantify damage.

1.2.3.1 Step I - Output Only Dynamic Property Extraction

Output-only modal estimation methods need to be developed, since it is very difficult to measure the riser input excitation. The complexity of the currents and measurement of hydrodynamic forces applied on risers leads to riser damage detection to be an output only problem. A number of output-only modal identification methods such as frequency domain decomposition (FDD) [24], Ibrahim Time Domain (ITD) [25], eigensystem realization algorithms (ERA) [26] and empirical mode decomposition (EMD) [27], etc. have been developed for traditional structures.

However, for deepwater risers, these methods may not be suitable. The FDD method suffers from frequency domain problems such as leakage etc. ERA is the most widely used output-only modal estimation method, but its results are strongly influenced by the size of the Hankel matrix. Similar problem can be seen in ITD. EMD consumes excessive computing time even when the original signals are from linear time invariant systems. Secondly, when the riser is undergoing VIV motion, the spatial characteristics of vibration could be either a standing wave or a traveling wave. In field test, VIV of riser is more like a traveling wave. Traditional modal analysis

algorithms may not obtain the right modal information when the VIV is a traveling wave because the vibration shapes are different at different time step. Finally, most of the available data from the full-scale field tests have time synchronization problems which strongly influence the modal analysis results from traditional methods.

To address these problems, there are several possible alternatives to mode shapes: the maximum/minimum displacements along the riser depth, the standard deviation (STD) of the response time history and the root mean square (RMS) values of the steady state session. Due to the presence of noise or accidental large values, directly using max/min value is risky. For the in-line VIV, STD would be a good choice because of the equivalent static displacement. For the cross-flow VIV, RMS might be a good choice. These STD and RMS methods are applicable when only one of the modes is excited in VIV. However, there are cases in which several modes being exited at the single event in Gulf Stream 2006 field test [28]. In that case, RMS and STD method may not be suitable.

As a result, to overcome the above mentioned drawbacks, this study focuses on developing new modal identification techniques that are model independent and are based on blind source separation (BSS).

1.2.3.2 Step II - Method 1: Damage Index

There are a number of damage detection algorithms available for structures. Zak et al. [29] proposed changes in resonant frequencies of the primary structure as an indication of damage. West [30] used changes in natural frequencies and mode shapes to form a modal assurance criterion (MAC) as damage index. Pandey et al. [31] proposed the use of mode shape curvature change as a damage index. Zhang et al. [32] tested a structural damage index based on the change of elemental modal strain energy

combined by mode shapes and frequencies from undamaged and damaged structure. Bernal [33] presented and tested the change of flexibility matrix between damaged and undamaged case as a reliable damage index. The aforementioned algorithms have been proven to be effective in different applications.

However, as the deepwater riser has large aspect ratio (length-diameter-ratio), it vibrates like a cable rather than a beam. For simply supported beam with constant tension, the equation to calculate natural frequencies is given by Humar [34]:

$$\omega_n = \sqrt{\omega_{beam}^2 + \omega_{cable}^2} = \sqrt{\frac{n^4\pi^4}{L^4}\frac{EI}{m} + \frac{n^2\pi^2}{L^2}\frac{T}{m}} \tag{1.1}$$

where n is the mode number, ω_{beam} represents the natural frequency of the structure if no top tension is considered; ω_{cable} represents the natural frequency of the structure if there is no bending stiffness in the structure; EI is the bending stiffness and m is the mass per unit length, L is the total length and T is the constant tension.

According to equation 1.1, the natural frequencies of the deepwater riser is mainly determined by the top tension. As the riser moves, the top tension varies. As a result, the natural frequency of the riser is time-varying and it could not be utilized in the damage detection procedure. Hence damage detection techniques based on in the mode shape related changes are more suitable for deepwater risers.

Among all the mode shape based methods, modal assurance criterion (MAC) [30] is the first method proposed to identify the occurrence of damage, but MAC cannot predict the location of damage. MAC is calculated using the following equation.

$$\mathbf{MAC}_i = \frac{\left[\phi_i^T \Phi\right]^2}{\left(\phi_i^T \Phi\right)\left(\Phi_i^T \phi\right)} \tag{1.2}$$

where Φ_i is the i^{th} mode shape of undamaged structure, ϕ_i is the i^{th} mode shape of structure with unknown (damaged) status. To locate the damage, a few different modifications to MAC have been proposed. However, in VIV, only few modes are

excited. MAC based methods can't identify the presence of damage without enough modes. Hence, MAC is not suitable.

Another mode shape based methods proposed by Pandey et al. [31] is the curvature mode shape change. Curvature values are proportional to strain values.

$$\varepsilon = \frac{y}{\rho} = \kappa y \tag{1.3}$$

where ε is the strain, ρ is the radius of the curvature and κ is the curvature.

Strain gages occupy a higher proportion of riser measurement systems than other sensors implemented. In this case, directly utilizing curvature (strain) change as damage indicator, proposed by Pandey et al. [31], would be a good choice.

1.2.3.3 Step II - Method 2: Fatigue Estimation

When the vibration amplitude of the offshore structure becomes too large, it not only poses a risk to the safety of the workers on the rig and to the integrity of the structure, but also reduces the service life of the structure, which is evident from the classic material stress-number-of-cycles (S-N) curve shown in Fig. 1.4 [35].

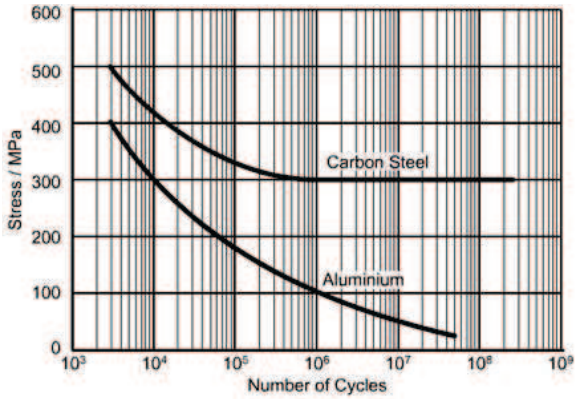

Figure 1.4 : Typical Material S-N Curve

There are quite a few methods that have been developed to estimate the fatigue damage or fatigue life: stress/strain cycle counting method (time domain as well as frequency domain), notch strain approach in the initiation phase, different fracture mechanics approach in propagation phase (crack growth rate models, various special phenomena related crack propagation as well as unstable crack propagation etc.) and fracture mechanics evaluation for strains larger than 0.5% [36]. Among all the methods, the most widely used method is stress-cycle counting methods combined with S-N curve and Miner's rule for randomly excited structures, such as risers under field current excitation.

According to Palmgren-Miners' rule [37], the accumulative fatigue damage of a member subjected to cyclic stress can be expressed as

$$\frac{n_1}{N_1} + \frac{n_2}{N_2} + \cdot + \frac{n_i}{N_i} = 1 \tag{1.4}$$

where n_i is number of cycles at the i^{th} stress level, and N_i is the number of cycles the structure could sustain at the i^{th} stress level. Thus, reducing the vibration amplitude will result in smaller stress level thereby extending the service life (load cycle number) of the offshore structure.

The equation 1.4 shows that two important factors determine the accumulative fatigue damage:

- The allowed fatigue life (number of cycles), N_I, respect to certain cyclic stress level, S_i, which can be found from the code [38] or Fig. 1.4;
- The counted cycle, n_i, from either time domain method or frequency method.

Currently, time-domain approach is the most commonly used. In the past, a mini-max time domain method was used to count the cycles as well as the stress level.

Since 2008, the rainflow cycle counting (RFC) method becomes the most popular method for fatigue estimation. The RFC method was originally presented by Matsuishi and Endo [39] in 1968. Downing and Socie [40] and Rychlik [41] provided simpler approaches to understand and realize the RFC method.

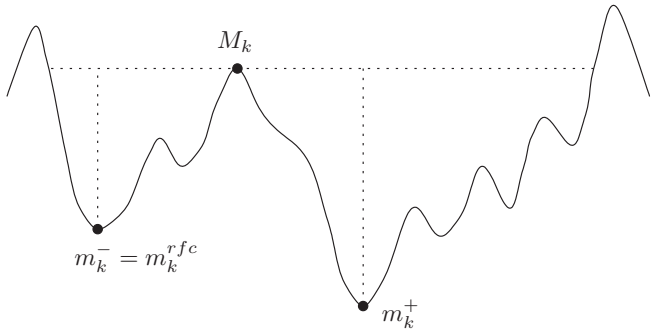

Figure 1.5 : Rainflow Cycle Definition by Rychlik

As shown in Fig. 1.5, from each local maximum M_k, within the values over the same level of M_k from both directions (the backward (left) and forward (right)), one should find as low downward peaks (the minima), m_k^- and m_k^+ , on each side as possible. The smaller deviation from the maximum M_k to each minimum is defined as the corresponding rainflow minimum m_k^{rfc} (m_k^- in the figure). In the figure the k^{th} rainflow cycle is defined as (m_k^{rfc}, M_k) [41].

In this thesis, a new approach of fatigue life estimation based on S-N curve [38] and Miner's rule will be discussed as one approach for global monitoring in the proposed SHM system.

1.2.4 Local Monitoring - based on Magnetic Flux Leakage

Local monitoring is performed using magnetic flux leakage (MFL) sensors. With MFL sensors and permanent magnets, a robotic crawler moves inside the riser pipe

to measure any change in the magnetic flux field. Based on the measured magnetic flux field strength, the thickness of the deepwater riser can be estimated. Any change in wall thickness will indicate a possible damage, most possibly a wall thickness reduction caused by corrosion. This non-contact, non-destructive technique has been widely used in pipeline inspection.

With the measurement of wall thickness reduction (remaining thickness as well as thickness reduction rate) using MFL sensors, the corrosion severity and corrosion rate can be estimated. Thus, the damage severity and remaining service life can be obtained. Combined with the fatigue life estimation by global vortex induced vibration monitoring, the proposed SHM system can provide useful information to operators to make appropriate decisions regarding repair or replacement of the riser.

To summarize, as shown in Fig. 1.3, MFL based local monitoring includes:

1. Measure the MFL with robotic crawler inside the deepwater riser;
2. Estimate the wall thickness and the damage severity;
3. Based on wall thickness reduction rate, estimate the remaining service life and provide suggestion on repair or replacement.

1.3 Thesis Organization

The dissertation focuses on studying the structural health monitoring system for deepwater risers. Chapter 1 introduces the motivation and background of structural health monitoring (SHM) system for deepwater platforms and their risers; reviews current SHM system, damage detection methods for offshore deepwater risers, proposes a SHM system combining local monitoring based on MFL and global monitoring based

on vibration; finally briefly introduces each step in the proposed SHM and overviews the organization of the thesis.

Chapter 2 proposes a 3D analytical model for deepwater risers considering coupled cross-flow and in-line vortex-induced vibration. Based on Lagragian strain under Lagragian coordinate, the derivation of equations of motion for deepwater risers with VIV is prosecuted. Comparison between numerical simulation carried out with finite difference method and experiments verifies the performance of the proposed model. Furthermore the proposed model are compared with the commercial software SHEAR7.

Chapter 3 introduces a finite element method (FEM) approach to replace the finite difference method (FDM) developed in chapter 2. Replacing Lagrangian strain with Jaunman strain with modified von Karman nonlinearity overcomes the limitation on large rotation, displacement for FDM model in Chapter 2. The FEM model is solved with Newmark-β method. Both numerical and field results are used to verify the proposed FEM method.

Chapter 4 studies the output only response analysis methods to extract the dynamic properties from the measured vibrations. Popular blind source separation methods are reviewed in this chapter. A wavelet modified second order blind identification (WMSOBI) method is proposed to solve the traditional second order blind identification time domain method in the time-frequency domain. Furthermore, a complex WMSOBI (CWMSOBI) method is introduced to take care of traveling wave properties. Numerical simulation and evaluation are carried out in this chapter.

Chapter 5 reviews the current damage detection algorithms for deepwater risers. A weighted distributed force change index is proposed to locate the damage locations based on the mode/strain shapes recognized from proposed CWMSOBI methods.

Furthermore, a phase angle change index is proposed for traveling wave dominant structures, such as deepwater risers. Numerical verifications are carried out.

Chapter 6 proposes a method to detect/locate the damage caused by fatigue in deepwater risers. A new fatigue damage and remaining service life estimation method is proposed and studied in this chapter.

Chapter 7 describes the experiments to verify the proposed blind identification method and damage detection method. Different excitations are applied on the horizontal pipe. Damages such as wall thickness reduction are machined into the intact pipe; the proposed damage detection methods are validated using the damaged pipe test.

Chapter 8 details the phenomenon of MFL and the corresponding experimental verification procedure. The experiments carried out by the author and his colleagues proves that MFL can provide reliable high resolution results of wall thickness of deepwater risers without strict contact requirements (non-contact technique).

Chapter 10 summarizes the conclusions and key contributions of this thesis. In addition, potential future works are outlined.

Chapter 2

Analytical Model using Finite Difference Method

As mentioned in the introduction chapter, a reliable analytical model for top-tensioned riser (TTR) has to be developed. The analytical model is required to predict the vortex-induced vibrations (VIV) caused in the TTR due to the hydrodynamic forces acting on it. This chapter will review the literature on analytical models and propose a new 3D analytical model with coupled VIV.

2.1 Review on Analytical Models for Riser VIV Study (Cross-flow Only)

VIV occurs when shedding vortices (a von Karman vortex street) exert oscillatory forces in both inline direction (X direction) and the cross-flow direction (Y direction). The cross-flow VIV of the riser is shown in Fig. 2.1. In addition to numerical methods such as direct numerical simulation (DNS) [42], several model types like force-decomposition models [23], single degree-of-freedom (SDOF) models [43] and wake-body coupled models have been proposed in the literature.

A force-decomposition model was introduced by Sarpkaya [23]. In this model, the lift force on an elastically mounted rigid cylinder is decomposed into an inertial force related to cylinder displacement and a damping force related to cylinder velocity. SDOF models were proposed by Basu and Vikery [43] in 1983. They used a single ordinary differential equation to describe the motion of the structure.

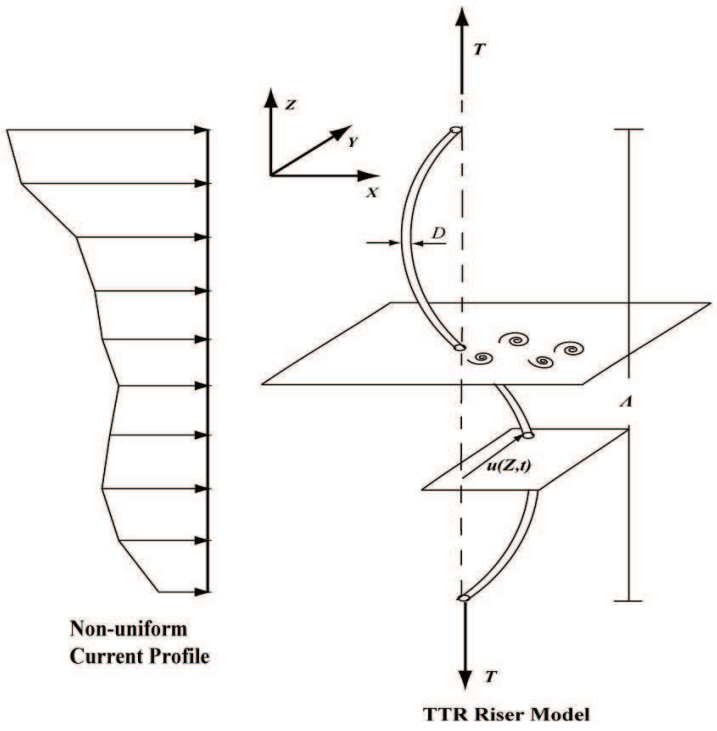

Figure 2.1 : Top-Tensioned Riser under Non-Uniform Flow

There are quite a few wake-body coupled models [23], among which wake-oscillator model is the most popular model. Bishop and Hanssan [44] suggest using a van der Pol type oscillator to describe the time-varying forces arising on a cylinder from shedding vortices. Classical van der Pol oscillator equation is shown in equation 2.1.

$$\ddot{q} - \varepsilon \left(1 - q^2\right) \dot{q} + q = 0 \tag{2.1}$$

where q is the variable for oscillator, which represents dynamic ratio of dynamic lift coefficients C_L and lift coefficient for fixed riser C_{L0}, $q = \dfrac{2C_L}{C_{L0}}$. Variable ε is the scalar indicating nonlinearity and damping.

Skop and Griffin [45], Griffin et al. [46], and Feng [47] developed different wake oscillator models. Facchinetti et al. [48] present a detailed review on wake oscillator

models, and conclude that coupled structure-fluid interaction force should be related to acceleration of the structure. Based on the conclusion by Facchinetti et al. [48], Violette et al. [49] developed a new wake-oscillator model, which is shown in Fig. 2.2.

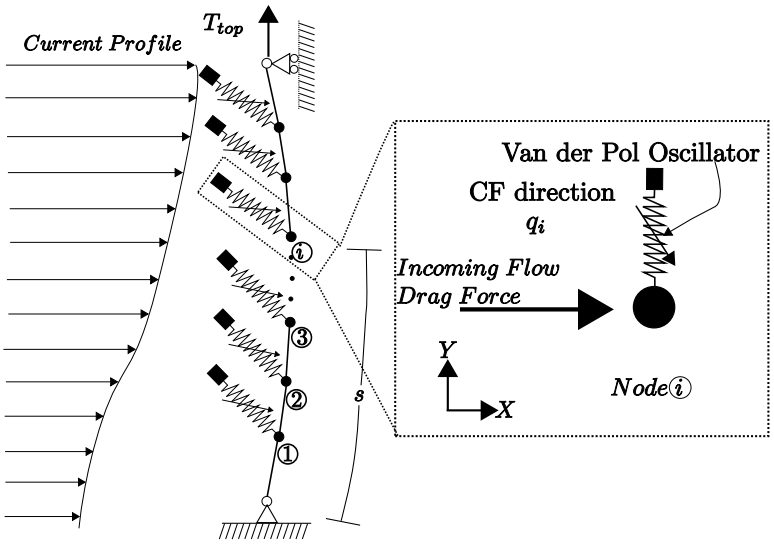

Figure 2.2 : Configuration of Wake Oscillator Model

The cross-flow equations of motion of a flexible riser (shown in Fig. 2.2) model coupled wake oscillators is solved by finite difference method (FDM). The fundamental components of FDM are the nodes in the figure, where masses and forces are lumped at each node. A wake-oscillator is attached to each node to simulate the hydrodynamic forces in cross-flow (CF) direction. Wake-oscillators are independent of each other and their motions are only determined by the current velocity and the motion of the corresponding node as shown in equation 2.2 [50].

$$\ddot{q} + \varepsilon\omega_z\left(q^2-1\right)\dot{q} + \omega_z^2 q = A_{CF}\ddot{v} \tag{2.2}$$

$$\ddot{v} + \frac{\gamma\omega_z}{\mu}\dot{v} - \left(\frac{T}{\left(m+m_a\right)\left(\Omega_{ref}D\right)^2}\right)\frac{\partial^2 v}{\partial z^2} + \left(\frac{EI}{\left(m+m_a\right)\Omega_{ref}^2 D^4}\right)\frac{\partial^4 v}{\partial z^4} = \omega_z^2\frac{qC_{L0}}{16\pi^2 S_t^2\mu}$$

where $v = y/D$ is the dimensionless cross-flow direction dynamic displacement, $z = Z/D$ is the dimensionless length and q is the van der Pol oscillator variable. $\omega_z = \Omega(z)/\Omega_{ref} = U(z)/U_{ref}$ is the relative vortex shedding frequency. $\Omega_{ref} = 2\pi S_t U_{ref}/D$ is the reference frequency for reference velocity, U_{ref}. S_t is the Strouhal number, D is the external diameter of riser. T is the top tension, $(m + m_a)$ is the mass of riser and added mass per unit length. μ is the mass ratio (between riser total mass $(m + m_a)$ and displaced fluid mass $(m_w = \rho D^2)$). γ, ε, C_{L0} and A_{CF} are the hydrodynamic interaction parameters determined by experimental data of fluctuating lift on a rigid cylinder driven in forced vibration; C_{L0} is the lift coefficient for rigid riser; EI is the bending rigidity.

2.2 Proposed Analytical Model for riser VIV study (Coupled VIV)

Field observations show that the motion of the deepwater riser combines the rigid body rotation caused by the floating platform drift, in-line (IL) mean drift (or called as equivalent static displacement in the proceeding sections) for steady incoming current drag force, cross-flow (CF) dynamic drift (vibration) and IL dynamic drift (vibration), shown in Fig. 2.3. The interactions between IL and CF drifts are not negligible because the large IL equivalent static displacement, which strongly influences the geometric nonlinearity. However, most of the established models consider only cross-flow (CF) direction VIV (part III in Fig. 2.3), such as SHEAR7 [51], the model developed by Violette et al. [49] and the model developed by Skop and Griffin [45]. Some models consider both in-line (IL) and cross-flow (CF) VIV (part III and IV in Fig. 2.3), but IL and CF vibrations are still considered to be totally independent

to each other and ignore the influence of in-line mean drift [52]. Hence, to correctly predict the VIV responses of deepwater riser, a analytical model with the coupling between IL and CF VIV is needed.

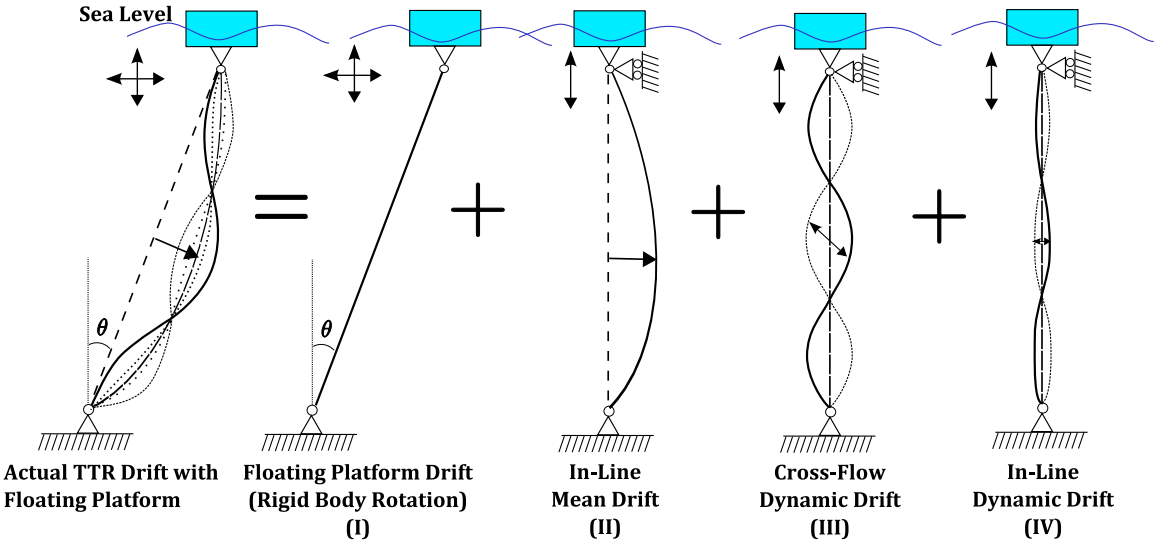

Figure 2.3 : Displacement Decomposition of Deepwater Riser with Platform Drift

In the proposed coupled analytical model, IL mean drift, CF nad IL dynamic drifts (Part II to Part IV in Fig. 2.3) are all included and simulated. The influences of the rigid body rotation caused by the platform drift (Part I in Fig. 2.3) are considered, but the actual riser drift simulation did not include the drift caused by rigid body rotation since it will not directly influence the dynamic behavior of the deepwater riser. Because the vortex shedding frequency is determined by the current speed perpendicular to the inclined riser, a different amplitude of incoming current speed ($U_{new} = U_{old} cos\,(\theta)$) is used due to the inclination caused rigid body rotation. In addition, the rigid body motion will change the top tension of the riser due to variation of buoyancy and riser axial direction. These changes of current speed amplitude and top tension are considered in the proposed model subjected to steady current.

Furthermore, in the proposed model, TTR is modeled as a straight slender vertical cylinder beam with pin-roller support at the ends, shown in Fig. 2.4. Independent van der Pol oscillators are used to simulate the hydrodynamic fluid structure interaction forces applied at each node. The IL and CF VIV are coupled by Green-Lagrangian strains.

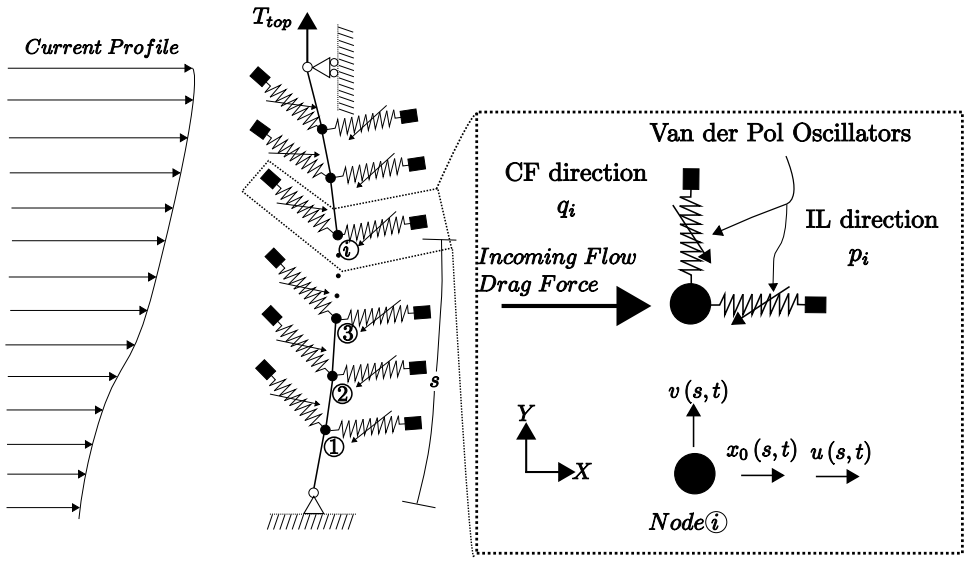

Figure 2.4 : 3D TTR Model with Coupled VIV

As shown in Fig. 2.4, IL equivalent static displacement, $x_{0,i}$, and IL dynamic displacement, u_i as well as the most important CF dynamic displacement, v_i, are taken into consideration for node i.

2.2.1 Lagrangian Coordinate and Green-Lagrangian Strain

A Lagrangian coordinate system is introduced to establish the total strain including the equivalent static strain. In Lagrangian coordinate system, s is the location along the curve of the structure. In Fig. 2.4, TTR will have in-line equivalent static displacement, $x_0(s)$ or $x_0(s,t)$ (for steady incoming flow profile and varying incoming

flow profile, respectively), and in-line dynamic displacement (due to vibration),$u\left(s,t\right)$, and cross-flow dynamic displacement, $v\left(s,t\right)$. The displacement in the Lagrangian coordinate system is:

$$x_i\left(s,t\right) = u_i\left(s,t\right) + x_{i0}\left(s,t\right) \tag{2.3}$$

where u_i is the dynamic displacement and x_{i0} is the static displacement, i represents X, Y, Z direction, respectively. s is the Lagrangian coordinate along the deformed shape of riser.

The (Green)-Lagrangian tensional strain is defined as

$$\epsilon = \frac{l_d^2 - l_i^2}{2l_i^2} = \frac{1}{2}\left(\frac{l_d^2}{l_i^2} - 1\right) \tag{2.4}$$

where l_d is the deformed length and l_i is the original length of deep water riser.

Substituting equation 2.3 into equation 2.4, one gets the total strain as

$$\begin{aligned} \epsilon &= \frac{1}{2}\left[\left(\frac{\partial x_i}{\partial s}\right)^2 - 1\right] = \frac{1}{2}\left[\left(\frac{\partial x_{i0}}{\partial s}\right)^2 - 1\right] + \frac{1}{2}\left[\left(\frac{\partial u_i}{\partial s}\right)^2 + 2\frac{\partial u_i}{\partial s}\frac{\partial x_{i0}}{\partial s}\right] \\ &= \epsilon_0 + \frac{1}{2}\left[\left(\frac{\partial u_i}{\partial s}\right)^2 + 2\frac{\partial u_i}{\partial s}\frac{\partial x_{i0}}{\partial s}\right] \end{aligned} \tag{2.5}$$

where ϵ_0 is the static strain component of the riser.

The strain energy is defined as

$$\Phi\left(\epsilon,\eta\right) = \frac{1}{2}EA\epsilon^2 + \frac{1}{2}EI\eta^2 \tag{2.6}$$

where EA is the axial stiffness of the riser, EI is the bending stiffness of the riser and η is the curvature of the riser, $\eta = \partial^2 u/\partial s^2 + \partial^2 x/\partial s^2$ for small slope, $\frac{\partial u}{\partial s} < 0.1$. Curvature η can be processed using the same procedure as strain ϵ.

Taylor expansion for equation 2.6 at initial time step (ϵ_0, η_0):

$$\begin{aligned}\Phi(\epsilon,\eta) &= \Phi(\epsilon_0,\eta_0) + \frac{\partial\Phi}{\partial\epsilon}|_{\epsilon_0}(\epsilon-\epsilon_0) + \frac{\partial\Phi}{\partial\epsilon}|_{\eta_0}(\eta-\eta_0) \\ &+ \frac{1}{2}\left\{\frac{\partial^2\Phi}{\partial\epsilon^2}|_{\epsilon_0}(\epsilon-\epsilon_0)^2 + 2\frac{\partial^2\Phi}{\partial\epsilon\partial\eta}|_{\epsilon_0,\eta_0}(\epsilon-\epsilon_0)(\eta-\eta_0) + \frac{\partial^2\Phi}{\partial\eta^2}|_{\eta_0}(\eta-\eta_0)^2\right\} \\ &+ O\{(\epsilon-\epsilon_0),(\eta-\eta_0)\}\end{aligned} \tag{2.7}$$

For vertical risers, one can treat ϵ_0 as constant and $\eta_0 = 0$, replacing $\epsilon_I = \epsilon - \epsilon_0$. In addition, as $\frac{\partial^2\Phi}{\partial\epsilon^2} = K_0 = EA$, $\frac{\partial^2\Phi}{\partial\eta^2} = EI$ and $\frac{\partial\Phi}{\partial\eta} = M_I = 0$ (for single cable, free cable static equilibrium) and omitting the higher order terms in the Taylor expansion, equation 2.7 can be simplified as

$$\begin{aligned}\Phi(\epsilon,\eta) &= \Phi(\epsilon_0,\eta_0) + \frac{\partial\Phi}{\partial\epsilon}|_0\epsilon_I + \frac{1}{2}\left\{\frac{\partial^2\Phi}{\partial\epsilon^2}|_0\epsilon_I^2 + \frac{\partial^2\Phi}{\partial\eta^2}|_0\eta^2\right\} \\ &= T\epsilon_I + \frac{1}{2}K_a^*\epsilon_I^2 + \frac{1}{2}K_f^*\eta^2\end{aligned} \tag{2.8}$$

where $T = \frac{\partial\Phi}{\partial\epsilon}|_0$, $K_a^* = \frac{\partial^2\Phi}{\partial\epsilon^2}|_0 = EA$ and $K_f^* = \frac{\partial^2\Phi}{\partial\eta^2}|_0 = EI$.

2.2.2 Extended Hamilton's Principle

Along with equations 2.3 to 2.8, the coupled equation of motion (EOM) of deepwater riser is derived from the extended Hamilton's principle [53],

$$\delta H = \int_{t_1}^{t_2}(\delta K_v - \delta\Pi_v + \delta W_v)\,dt = 0 \tag{2.9}$$

where K_v is the kinetic energy of whole riser, Π_v is the potential energy (which is integration of strain energy along the riser length), and W_v is the work done by non-conservative forces.

Considering the deepwater riser only (without hydrodynamic interactions), the energy terms in equation 2.9:

- Kinetic Energy:

  $K_v = \frac{1}{2}\int_{L_0} m_s \left(\dot{u}_{i,s} + \dot{x}_{i,s}\right)^2 ds$

- Potential Energy:

  $\Pi_v = \int_{L_0} \Phi\left(\epsilon_I, \eta\right) ds$

- Work done by non-conservative forces:

  $W_v = -\int_{L_0}\int_{t_1}^{t_2} c_s \left(\dot{u}_{i,s} + \dot{x}_{i,s}\right)^2 dsdt$

where $m_s = \rho A$ is the mass at Lagrangian coordinate s per unit length; $u_{i,s}$ is the dynamic displacement in direction i (including X,Y,Z) and at location s; $x_{i,s}$ is equivalent static displacement, which is constant for constant current profile and is time varying for varying current profile. c_s is the viscous damping coefficient at coordinate s. As the tension of riser $T << EA$, the vertical displacement is negligible. Hence, W_v represents the energy dissipated by damping.

Taking above energy terms with equation 2.8 into equation 2.9 results in

2.2.2.1 Kinetic Energy Term:

$$
\begin{aligned}
& \int_{t_1}^{t_2} \delta K_v dt \\
= & \int_{t_1}^{t_2} \left(\int_{L_0} m_s \left(\dot{u}_{i,s} + \dot{x}_{i,s} \right) \delta \left(\dot{u}_{i,s} + \dot{x}_{i,s} \right) ds \right) dt \qquad (2.10) \\
= & \int_{L_0} \left(\int_{t_1}^{t_2} m_s \left(\dot{u}_{i,s} + \dot{x}_{i,s} \right) \delta \left(\dot{u}_{i,s} + \dot{x}_{i,s} \right) dt \right) ds \\
= & \int_{L_0} \left(m_s \left(\dot{u}_{i,s} + \dot{x}_{i,s} \right) \delta \left(u_{i,s} + x_{i,s} \right) |_{t_1}^{t_2} - \int_{t_1}^{t_2} m_s \left(\ddot{u}_{i,s} + \ddot{x}_{i,s} \right) \delta \left(u_{i,s} + x_{i,s} \right) dt \right) ds \\
= & \int_{L_0} \left(- \int_{t_1}^{t_2} m_s \left(\ddot{u}_{i,s} + \ddot{x}_{i,s} \right) \left(\frac{\partial u_{i,s}}{\partial s} + \frac{\partial x_{i,s}}{\partial s} \right) \delta s dt \right) ds \\
= & - \int_{t_1}^{t_2} \left(\int_{L_0} m_s \left(\ddot{u}_{i,s} + \ddot{x}_{i,s} \right) \left(\frac{\partial u_{i,s}}{\partial s} + \frac{\partial x_{i,s}}{\partial s} \right) \delta s ds \right) dt \\
= & - \int_{t_1}^{t_2} \left(\int_{L_0} m \left(\ddot{u} + \ddot{x} \right) \left(\frac{\partial u}{\partial s} + \frac{\partial x}{\partial s} \right) \delta s ds \right) dt
\end{aligned}
$$

where $\delta u = \delta x = 0$ at time $t = t_1, t_2$. From here on, u is short for u_i; x is short for $x_{i,0}$. So are $\dot{u}$, $\ddot{u}$, $\dot{x}$, $\ddot{x}$, m and c for $\dot{u}_{i,s}$, $\ddot{u}_{i,s}$, $\dot{x}_{i,s}$, $\ddot{x}_{i,s}$, m_s and c_s, respectively;

2.2.2.2 Non-Conservative Work Term:

Similar derivation as kinetic energy term will result in:

$$
\delta W_v = - \int_{L_0} c \left(\dot{u} + \dot{x} \right) \left(\frac{\partial u}{\partial s} + \frac{\partial x}{\partial s} \right) \delta s ds \qquad (2.11)
$$

2.2.2.3 Potential Energy Term:

$$
\delta \Pi_v = \int_{L_0} \left(T \delta \epsilon_I + \frac{1}{2} EA \delta \left(\epsilon_I^2 \right) + \frac{1}{2} EI \delta \left(\eta^2 \right) \right) ds \qquad (2.12)
$$

where $\epsilon_I = \frac{1}{2} \left[\left(\frac{\partial u_i}{\partial s} \right)^2 + 2 \frac{\partial u_i}{\partial s} \frac{\partial x_{i0}}{\partial s} \right]$ in equation 2.5.

Taking the first term of $\delta\Pi_v$ on the right side of equation and integrating by parts,

$$\begin{aligned}
\int_{L_0} (T\delta\epsilon_I)\, ds &= \int_{L_0} \left(\frac{1}{2} T\delta \left[\left(\frac{\partial u}{\partial s} \right)^2 + 2\frac{\partial u}{\partial s}\frac{\partial x}{\partial s} \right] \right) ds \qquad (2.13)\\
&= \int_{L_0} \left(T \left[\frac{\partial u}{\partial s}\frac{\partial^2 u}{\partial s^2} + \frac{\partial u}{\partial s}\frac{\partial^2 x}{\partial s^2} \right] \delta s \right) ds \\
&= \int_{L_0} \left(T\frac{\partial u}{\partial s} \left[\frac{\partial^2 u}{\partial s^2} + \frac{\partial^2 x}{\partial s^2} \right] \delta s \right) ds \\
&= T\frac{\partial u}{\partial s} \left(\frac{\partial^2 u}{\partial s^2} + \frac{\partial^2 x}{\partial s^2} \right) \delta s|_0^{L_0} - \int_{L_0} \left(T\frac{\partial^2 u}{\partial s^2} \left[\frac{\partial u}{\partial s} + \frac{\partial x}{\partial s} \right] \delta s \right) ds \\
&= -\int_{L_0} \left(T\frac{\partial^2 u}{\partial s^2} \left[\frac{\partial u}{\partial s} + \frac{\partial x}{\partial s} \right] \delta s \right) ds
\end{aligned}$$

where $T\dfrac{\partial u}{\partial s} \left(\dfrac{\partial^2 u}{\partial s^2} + \dfrac{\partial^2 x}{\partial s^2} \right) \delta s = 0$ at both $s = L_0, 0$.

Taking the second term (EA) of $\delta\pi_v$ on the right side of equation and integrating by parts,

$$\begin{aligned}
&\int_{L_0} \left(\frac{1}{2} EA\delta \left(\epsilon_I^2 \right) \right) ds = \int_{L_0} (EA\epsilon_I \delta\epsilon_I)\, ds \qquad (2.14)\\
&= EA\epsilon_I^2 \delta s|_0^{L_0} - \int_{L_0} \left(EA\epsilon_I \frac{d}{ds} \left[\frac{1}{2} \left(\frac{\partial u}{\partial s} \right)^2 + \frac{\partial u}{\partial s}\frac{\partial x}{\partial s} \right] \delta s \right) ds \\
&= -\int_{L_0} \left(EA\epsilon_I \left[\frac{\partial^2 u}{\partial s^2}\frac{\partial u}{\partial s} + \frac{\partial u}{\partial s}\frac{\partial^2 x}{\partial s^2} + \frac{\partial^2 u}{\partial s^2}\frac{\partial x}{\partial s} \right] \delta s \right) ds \\
&= -\int_{L_0} \left(EA\epsilon_I \left[\frac{\partial^2 u}{\partial s^2}\frac{\partial u}{\partial s} + \frac{\partial u}{\partial s}\frac{\partial^2 x}{\partial s^2} + \frac{\partial^2 u}{\partial s^2}\frac{\partial x}{\partial s} + \frac{\partial^2 x}{\partial s^2}\frac{\partial x}{\partial s} - \frac{\partial^2 x}{\partial s^2}\frac{\partial x}{\partial s} \right] \delta s \right) ds \\
&= -\int_{L_0} \left(EA\epsilon_I \left\{ \left(\frac{\partial u}{\partial s} + \frac{\partial x}{\partial s} \right) \left(\frac{\partial^2 u}{\partial s^2} + \frac{\partial^2 x}{\partial s^2} \right) - \frac{\partial^2 x}{\partial s^2}\frac{\partial x}{\partial s} \right\} \delta s \right) ds
\end{aligned}$$

where higher order spatial derivatives like $\dfrac{\partial^2 x}{\partial s^2}\dfrac{\partial x}{\partial s}$ and $\dfrac{\partial^4 x}{\partial s^4}$ are much smaller than lower order derivatives, especially when the mean drift (equivalent static displacement, X) is constant. As a result, they can be omitted for constant equivalent static displacement, x. And the above equations becomes

$-\int_{L_0} \left(EA\epsilon_I \left\{ \left(\dfrac{\partial u}{\partial s} + \dfrac{\partial x}{\partial s} \right) \left(\dfrac{\partial^2 u}{\partial s^2} + \dfrac{\partial^2 x}{\partial s^2} \right) \right\} \delta s \right) ds.$

Taking the third term (EI) of $\delta\pi_v$ on the right side of equation and integrating by parts,

$$\begin{aligned}
\int_{L_0} & \left(\frac{1}{2}EI\delta\left(\eta^2\right)\right)ds = \int_{L_0}\left(EI\eta\delta\eta\right)ds \qquad (2.15)\\
= & \; EI\eta_I^2\delta s|_0^{L_0} - \int_{L_0}\left(EI\left[\frac{\partial^2 u}{\partial s^2}+\frac{\partial^2 x}{\partial s^2}\right]\frac{d}{ds}\left[\frac{\partial^2 u}{\partial s^2}+\frac{\partial^2 x}{\partial s^2}\right]\delta s\right)ds\\
= & \; -\int_{L_0}\left(EI\left[\frac{\partial^2 u}{\partial s^2}+\frac{\partial^2 x}{\partial s^2}\right]\left[\frac{\partial^3 u}{\partial s^3}+\frac{\partial^3 x}{\partial s^3}\right]\delta s\right)ds\\
= & \; -EI\left[\frac{\partial u}{\partial s}+\frac{\partial x}{\partial s}\right]\left[\frac{\partial^3 u}{\partial s^3}+\frac{\partial^3 x}{\partial s^3}\right]\delta s|_0^{L_0}\\
& + \int_{L_0}\left(EI\left[\left(\frac{\partial^4 u}{\partial s^4}\right)+\frac{\partial^4 x}{\partial s^4}\right]\left[\frac{\partial u}{\partial s}+\frac{\partial x}{\partial s}\right]\delta s\right)ds\\
= & \; \int_{L_0}\left(EI\left[\frac{\partial^4 u}{\partial s^4}+\frac{\partial^4 x}{\partial s^4}\right]\left[\frac{\partial u}{\partial s}+\frac{\partial x}{\partial s}\right]\delta s\right)ds
\end{aligned}$$

Substituting equations 2.10 - 2.15 into equation 2.9,

$$\begin{aligned}
\int_{t_1}^{t_2}\Big(\int_{L_0}\Big[-m\left(\ddot{u}+\ddot{x}\right)\left(\frac{\partial u}{\partial s}+\frac{\partial x}{\partial s}\right)\delta s \; & + \; T\frac{\partial^2 u}{\partial s^2}\left(\frac{\partial u}{\partial s}+\frac{\partial x}{\partial s}\right)\delta s + \qquad (2.16)\\
EA\epsilon_I\left(\frac{\partial^2 u}{\partial s^2}+\frac{\partial^2 x}{\partial s^2}\right)\left(\frac{\partial u}{\partial s}+\frac{\partial x}{\partial s}\right)\delta s \; & - \; EI\left(\frac{\partial^4 u}{\partial s^4}+\frac{\partial^4 x}{\partial s^4}\right)\left(\frac{\partial u}{\partial s}+\frac{\partial x}{\partial s}\right)\delta s\\
& - \; c\left(\dot{u}+\dot{x}\right)\left(\frac{\partial u}{\partial s}+\frac{\partial x}{\partial s}\right)\delta s\Big]ds\Big)dt = 0
\end{aligned}$$

For any variation $\left(\frac{\partial u}{\partial s}+\frac{\partial x}{\partial s}\right)\delta s$ and time period (t_1, t_2), the above extended Hamilton equation will stand. The only solution would be the equation inside the integration equal to zero in any situation; in addition, as mentioned before $\frac{\partial^4 x}{\partial s^4}$ can be omitted and considering constant current profile, $\dot{x} = \ddot{x} = 0$, which leads to

$$-m\left(\ddot{u}\right)+T\frac{\partial^2 u}{\partial s^2}+EA\epsilon_I\left(\frac{\partial^2 u}{\partial s^2}+\frac{\partial^2 x}{\partial s^2}\right)-EI\frac{\partial^4 u}{\partial s^4}-c\dot{u}=0 \qquad (2.17)$$

Removing the minus sign and substituting ϵ_I with equation 2.5 changes equation 2.17 into:

$$m\ddot{u}+c\dot{u}+EI\left(\frac{\partial^4 u}{\partial s^4}\right)-T\frac{\partial^2 u}{\partial s^2}-EA\epsilon_I\left(\frac{\partial^2 u}{\partial s^2}+\frac{\partial^2 x}{\partial s^2}\right)=0 \qquad (2.18)$$

In a similar way, the equations of motion (EOM) for the CF direction is obtained.

$$m\ddot{v} + c\dot{v} + EI\left(\frac{\partial^4 v}{\partial s^4}\right) - T\frac{\partial^2 v}{\partial s^2} - EA\epsilon_I\left(\frac{\partial^2 v}{\partial s^2}\right) = 0 \tag{2.19}$$

2.2.3 Equations of Motion for proposed model of deepwater riser

With assumption that the static displacement only occurs in in-line (X) direction, and replacing u in equation 2.18 with u, v representing IL and CF dynamic displacements and hydrodynamic fluid structure interaction forces F_1, F_2 in IL and CF directions, results in the equations of motion for the 3D analytical model with coupled VIV are obtained as follows:

$$\begin{aligned} m\ddot{u} + c\dot{u} &= \left[T\left(\frac{\partial^2 u}{\partial s^2}\right) + EA\epsilon_I\left(\frac{\partial^2 u}{\partial s^2} + \frac{\partial^2 x}{\partial s^2}\right) - EI\left(\frac{\partial^4 u}{\partial s^4}\right)\right] + F_1 \\ m\ddot{v} + c\dot{v} &= \left[T\left(\frac{\partial^2 v}{\partial s^2}\right) + EA\epsilon_I\left(\frac{\partial^2 v}{\partial s^2}\right) - EI\frac{\partial^4 v}{\partial s^4}\right] + F_2 \end{aligned} \tag{2.20}$$

where u, v is the dynamic displacements of X (in-line) and Y (cross-flow) direction; x is the static displacement in X direction; m is the mass per unit length of the riser; c is the structural damping term, F_1 and F_2 are the hydrodynamic force applied to the riser which can be generated by van der Pol oscillators. ϵ_I is the coupled interaction strain term and varies with time.:

$$\epsilon_I = \frac{1}{L}\int_0^L \left[\frac{\partial u}{\partial s}\frac{\partial x}{\partial s} + \frac{1}{2}\left(\frac{\partial u}{\partial s}\right)^2 + \frac{1}{2}\left(\frac{\partial v}{\partial s}\right)^2\right] \tag{2.21}$$

To further simplify the EOMs, the tension of the riser is linearly decreased as the depth increases (due to self weight, w). Hence, the EOMs are modified to

$$\begin{aligned} m\ddot{u} + c\dot{u} &= T_{top}u'' - wu' + EA\epsilon_I\left(u'' + x''\right) - EI\left(u''''\right) + F_1 \\ m\ddot{v} + c\dot{v} &= T_{top}v'' - wv' + EA\epsilon_I\left(v''\right) - EI\left(v''''\right) + F_2 \end{aligned} \tag{2.22}$$

where $\dot{}$ represents derivative with respect to time, t, and $'$ represents derivative with respect to Lagrangian coordinate, s (or vertical coordinate z in the proceeding sections). The weight per unit length of the riser is w. Usually, x'''' is very small and can be neglected.

2.2.4 Final EOMs with van der Pol Oscillators

2.2.4.1 Added Mass Term

As shown in equation 2.22, F_1 and F_2 represents the hydrodynamic fluid structure interaction (FSI) forces applied on each node of the deepwater riser. For in-line direction, the hydrodynamic FSI forces for flow crossing cylindrical structure can be estimated using Morrison's equation.

$$F_1 = \rho C_M \frac{\pi D^2}{4}\dot{U} + \frac{1}{2}\rho D C_D U|U| \tag{2.23}$$

in which ρ is the density of water; D = external riser diameter; F_1 = horizontal drag force per unit length; U = relative IL current velocity to the corresponding riser section. The empirical C_M and C_D are added mass coefficient and drag coefficient, respectively.

For constant current profile, the relative acceleration $\dot{U}$ is determined by the acceleration of corresponding section of the deepwater riser, $\ddot{u}$. Hence, the first term is usually moved to the left of EOM and treated as an added mass term (m_a). According to experiment done by Wendel in 1950 [54], the added mass coefficient for cylinder is chosen to be one. The second term is generally a dynamic term, where drag coefficient C_D is changing according to amplitude of relative velocity, U. The coefficient can be separated into two parts: equivalent static part, $C_{D,S}$, which literally is the mean value of C_D time history; dynamic part, $C_{D,D}$, which is the residual part of C_D after

removing the mean value. Hence, the equivalent static drag force (with $C_{D,S}$) need calibration for each experimental setup, while the dynamic drag force (with $C_{D,D}$) can be simulated using van der Pol oscillator.

2.2.4.2 Fluid Damping Term

In addition, the fluid will cause energy dissipation, which can be linearized as viscous damping. According to Blevins [55], the fluid-induced damping parameter, γ,

$$\gamma = \frac{C_{D,S}}{4\pi S_t} \tag{2.24}$$

where γ is a damping parameter determined by the oscillation amplitude of the riser, related to the mean drag coefficient at corresponding section. According to Blevins [55], the fluid damping term in the CF direction is obtained using the following equation.

$$D_{CF} = m_w \gamma \Omega_{z,CF} \tag{2.25}$$

where $m_w = \rho D^2$ and the vortex shedding frequency at location z in CF direction, $\Omega_{z,CF} = 2\pi \dfrac{S_t U_z}{D}$.

Conversely, based on observation, the fluid damping term in the IL direction is larger, $D_{IL} = m_w \gamma \Omega_{z,IL}$, where $\Omega_{z,IL} = 2\Omega_{z,CF}$.

2.2.4.3 Van der Pol Oscillator

Using wake oscillator to simulate the FSI forces in CF direction for the fluctuating lift coefficient was first proposed by Hartlen and Currie [56] in 1970, in which a viscous term $\varepsilon \Omega_z \left(\dot{q}^2 - 1\right) \dot{q}$ with Rayleigh equation was first proposed as well. Later an anlytical model using a combination of van der Pol oscillator and Rayleigh equations was also studied [57] considering energy balance. However, according to Facchinetti

et al. [48], a simple van der Pol oscillator is a better choice and the EOMs for the van der Pol oscillators in IL and CF directions are

$$\ddot{p} + \varepsilon\Omega_{z,IL}\left(p^2 - 1\right)\dot{p} + \Omega_{z,IL}^2 p = F_{IL}$$
$$\ddot{q} + \varepsilon\Omega_{z,CF}\left(q^2 - 1\right)\dot{q} + \Omega_{z,CF}^2 q = F_{CF} \tag{2.26}$$

where $\Omega_{z,CF} = 2\pi\dfrac{S_t U_z}{D}$ is the sectional vortex shedding frequency at section z in CF direction; and $\Omega_{z,IL} = 2\Omega_{z,CF}$ the sectional vortex shedding frequency at section z in IL direction. ε is the nonlinear coefficient to determine the level of nonlinearity. p, q is the FSI coefficient which corresponds to drag and lift coefficients, respectively. $F_{IL} = B_{IL}\ddot{u}/D$ and $F_{CF} = A_{CF}\ddot{v}/D$ is chosen to be corresponding to the acceleration of related section of riser based on energy balance [48].

Substituting the $F_1 = D_{IL}\dot{u} + S_1 p$ and $F_2 = D_{CF}\dot{v} + S_2 q$ with the above FSI terms into equation 2.22 results in

$$\begin{aligned}
\left(m + m_a\right)\ddot{u} + \left(c + D_{IL}\right)\dot{u} &= T_{top}u'' - wu' + EA\epsilon_I\left(u'' + x''\right) - EI\left(u''''\right) + S_1 p \\
\left(m + m_a\right)\ddot{v} + \left(c + D_{CF}\right)\dot{v} &= T_{top}v'' - wv' + EA\epsilon_I\left(v''\right) - EI\left(v''''\right) + S_2 q
\end{aligned} \tag{2.27}$$

where the van der Pol variable q is interpreted as the reduced vortex lift coefficient $q(t) = \dfrac{2C_L(t)}{C_{L_0}}$, and van der Pol variable p is interpreted as the reduced vortex drag coefficient $p(t) = \dfrac{2C_D(t)}{C_{D_0}}$. C_{L_0} and C_{D_0} are measured lift and drag coefficients for fixed rigid riser model tests, respectively.

The CF hydrodynamic FSI forces applied on the riser (without added mass term and damping term) equals $\dfrac{1}{2}\rho D U_z^2 C_L$ per unit length at location z. Considering $q(t) = \dfrac{2C_L(t)}{C_{L_0}}$ and $U_z = \dfrac{\Omega_{z,CF} D}{2\pi S_t}$,

$$S_2 = \frac{C_{L_0}}{2}\frac{m_w \Omega_{z,CF}^2}{8\pi^2 S_t^2} D \tag{2.28}$$

where $m_w = \rho D^2$. Similarly, $S_1 = \dfrac{C_{D_0}}{2}\dfrac{m_w \Omega_{z,IL}^2}{8\pi^2 S_t^2} D$

2.2.4.4 Final EOMs

Using the similar procedure for IL direction and considering dimensionless time $t = \tau\Omega_{ref}$ and amplitudes $u_1 = u/D$, $v_1 = v/D$, $z = Z/D$ and $x_1 = x/D$, the scaled time derivatives and spatial derivatives for CF dynamic displacements are

$$\begin{aligned}
v(t) &= v(\Omega_{ref}\tau) * D \\
\dot{v}(t) &= [v(\Omega_{ref}\dot{\tau})] * D = \Omega_{ref}\dot{v}(\Omega_{ref}\tau) * D \\
\ddot{v}(t) &= [v(\Omega_{ref}\ddot{\tau})] * D = \Omega_{ref}^2\ddot{v}(\Omega_{ref}\tau) * D \\
\frac{\partial^2 v(t)}{\partial Z^2} &= \frac{\partial^2 [v(\Omega_{ref}\tau) * D]}{D^2\partial z^2} = \frac{\partial^2 v(\Omega_{ref}\tau)}{D\partial z^2} \\
\frac{\partial^4 v(t)}{\partial Z^4} &= \frac{\partial^4 [v(\Omega_{ref}\tau) * D]}{D^4\partial z^4} = \frac{\partial^4 v(\Omega_{ref}\tau)}{D^3\partial z^4}
\end{aligned} \tag{2.29}$$

Similar procedure is performed for u, x, p and q.

By normalizing the terms in equation 2.20 with $(m + m_a)\Omega_{ref}^2 D$ and neglecting the structural damping, equation 2.27 becomes:

$$\ddot{p} + \varepsilon\omega_{z,IL}\left(p^2 - 1\right)\dot{p} + \omega_{z,IL}^2 p = B_{IL}\ddot{u} \tag{2.30}$$

$$\begin{aligned}
\ddot{u} + \frac{\gamma\omega_{z,IL}}{\mu}\dot{u} - \left(\frac{1}{(m + m_a)\Omega_{ref}^2 D^2}\right) \times \\
\left(T_{top}\frac{\partial^2 u}{\partial z^2} + EA\epsilon_I\left(\frac{\partial^2 u}{\partial z^2} + \frac{\partial^2 x}{\partial z^2}\right) - (w)\frac{D\partial u}{\partial z} - (EI)\frac{\partial^4 u}{D^2\partial z^4}\right) &= \frac{p\omega_{z,IL}^2 C_{D0}}{16\pi^2 S_t^2 \mu}
\end{aligned}$$

$$\ddot{q} + \varepsilon\omega_{z,CF}\left(q^2 - 1\right)\dot{q} + \omega_{z,CF}^2 q = A_{CF}\ddot{v} \tag{2.31}$$

$$\begin{aligned}
\ddot{v} + \frac{\gamma\omega_{z,CF}}{\mu}\dot{v} - \left(\frac{1}{(m + m_a)\Omega_{ref}^2 D^2}\right) \times \\
\left(T_{top}\frac{\partial^2 v}{\partial z^2} + EA\epsilon_I\left(\frac{\partial^2 v}{\partial z^2}\right) - (w)\frac{D\partial v}{\partial z} - (EI)\frac{\partial^4 v}{D^2\partial z^4}\right) &= \frac{q\omega_{z,CF}^2 C_{L0}}{16\pi^2 S_t^2 \mu} \\
\frac{1}{L}\int_0^L \left[\frac{\partial u}{\partial z}\frac{\partial x}{\partial z} + \frac{1}{2}\left(\frac{\partial u}{\partial z}\right)^2 + \frac{1}{2}\left(\frac{\partial v}{\partial z}\right)^2\right] &= \epsilon_I
\end{aligned}$$

where $\Omega_{ref} = 2\pi S_t U_{ref}/D$ is the reference frequency for a given frequency velocity, U_{ref}. Relative vortex shedding frequency in CF direction at depth z is represented

by $\omega_{z,CF} = \dfrac{\Omega_{z,CF}}{\Omega_{ref}} = \dfrac{U_z}{U_{ref}}$. Conversely, the vortex shedding frequencies in the IL direction is $\omega_{z,IL} = 2\omega_{z,CF}$ at depth z. Mass ratio $\mu = \dfrac{m + m_a}{m_w} = \dfrac{m + m_a}{\rho D^2}$. p, q is the van der Pol oscillator variables in the in-line (IL) and cross-flow (CF) direction, respectively. u, v is the IL and CF direction dimensionless displacement of riser. z represents the dimensionless vertical depth. $\dot{}$ means the derivative respect to time τ, and ∂ denotes the partial derivative respect to given vector, z in this case. μ is the mass ratio (riser total mass vs. displaced fluid mass). w is the self weight per unit length of the riser. S_t is the Strouhal number, D is the external diameter of the riser. T_{top} is the tension at the top of riser, m and m_a are the mass per unit length of riser and added mass. $\gamma, \varepsilon, A_{CF}$ and B_{IL} are determined by experimental data of fluctuating lifting and drag on a rigid cylinder driven in forced vibration. EI the bending rigidity, EA is the axial rigidity. C_{L0} and C_{D0} are fluctuating lift and drag coefficients from fixed cylinder experiments.

2.3 Parameter Setting and Calibration

According to equation 2.30 and 2.31, quite a few parameters for hydrodynamic FSI forces need experimental calibration or semi-empirical setting. The choice of those parameters will be detailed in this section.

2.3.1 Strouhal Number S_t

The Strouhal number, S_t is defined as $S_t = f_v D/U$, where f_v is taken as the natural vortex-shedding frequency of a fixed cylinder subjected to constant uniform current profile with velocity U; D is the diameter of the riser. Consequently, the vortex-shedding frequency (or Strouhal frequency) can be defined as $f_v = S_t U/D$.

The Stouhal number depends on the Reynolds number $Re = UD/v$, where v is the kinematic viscosity of the fluid. According to Blevins [55], the Strouhal number is around 0.2 when Re belongs to the sub-critical range $300 - 2 \times 10^5$. However, experimentally determined values may exhibit considerable variations. For example, the Delta Flume experiment carried out at Delft Hydraulics in 2003 [58] recorded a Strouhal number 0.176.

For simulation purposes in this study the value of Strouhal number is chosen to be 0.2 for $Re \in (300, 2 \times 10^5)$, in the event experimental verification is possible the value of Strouhal number determined experimentally should be considered in the proposed model.

2.3.2 Fixed Drag coefficient C_{D0} and Lift Coefficient C_{L0}

As described in Final EOMs 2.31, C_{L0} ad C_{D0} are the fluctuating lift and drag coefficients obtained from fixed cylinder experiments. Pantazopoulos [59] outlines the experimental results as shown in Fig. 2.5 as a function of Reynolds Number. The fixed drag coefficient value is estimated based on the study by Pantazopoulos [59] as 1.2. The closed mean value of fixed lift coefficient is estimated as 0.3 for sub-critical range based on the study by Pantazopoulos [59] and Blevins [55].

2.3.3 van der Pol damping ε and FSI coefficients A_{CF}, B_{IL}

The van der Pol damping parameter ε determines how many limited cycles occur before the oscillator reaches steady state. For $\varepsilon = 0$, there is no damping for the oscillator. The responses would be directly a sine-wave excitation interacting with the riser motion. When $\varepsilon > 0$, the system will get into a limit cycle to the steady state. Fig. 2.6 shows the famous characteristics of van der Pol oscillator: limited cycle

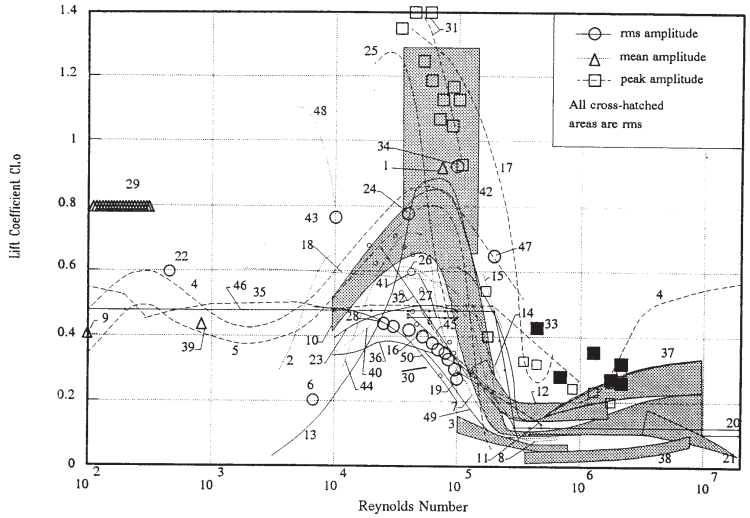

Figure 2.5 : Lift Coefficient v.s. Reynolds Number (Courtesy: Pantazopoulos 1994)

convergence and steady amplitude vibration after convergence. The phase plane plot confirms that the convergence can be achieved from both sides: small initial values and large values. Because these characteristics are quite similar to VIV phenomenon, van der Pol oscillator is a good choice wake oscillator model to predict VIV responses [44].

In addition, ε combined with the FSI coefficients A_{CF} will influence the lift amplification factor with respect to a fixed structure subjected vortex shedding, $K = \frac{q}{2}$. To ensure the response amplitude of q is smaller than the amplitude of natural limit cycle $q_0 = 2$, K has to be smaller than 1. Facchinetti et al. [48] proposed a least square interpolation to get the $A_{CF}/\varepsilon = 40$ to get the best increase/decrease trend. Furthermore, to match the experimental results from Blevins [55] and Stansby, the values $\varepsilon = 0.3$ and $A_{CF} = 12$ were chosen [48].

Similar approach can be adopted. Experiment studies [59] show that the amplitude of IL direction is much smaller than CF direction, usually one fifth to one half

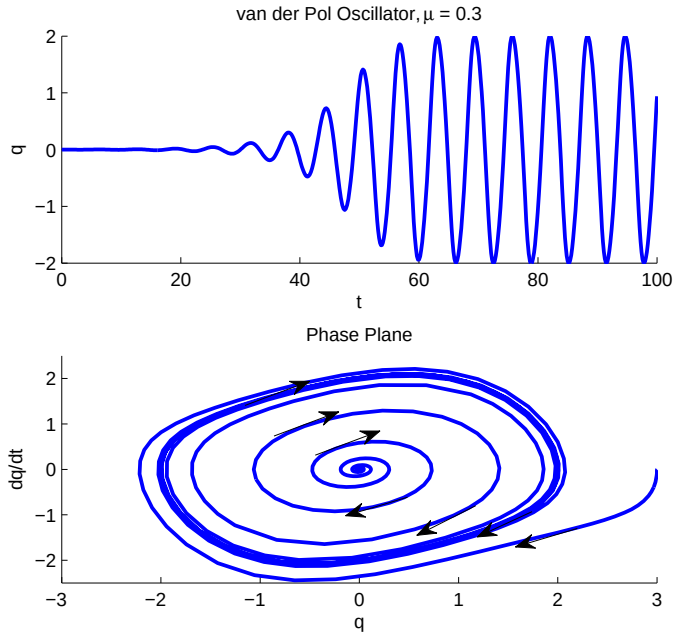

Figure 2.6 : Typical van der Pol Oscillator Time History and Phase Plane Plot.

of the CF direction. Generally, the value of B_{IL} is set to be around one when ε for IL van der Pol oscillator is 0.3 for one fifth ratio assumption. The value can be adjusted when the experimental calibration is available.

2.3.4 Added Mass Coefficient C_M and Mass Ratio μ

Added mass is a portion of fluid moving along with the riser at the frequency, either in phase or opposite (negative value). It is one of the well-known but least understood and most confusing phenomenon of fluid dynamics. It exists in all flow-bluff body interactions [23]. The phenomenon of added mass becomes observable only when the riser is excited and experiences sufficient accelerations. The magnitude of the added mass depends on various factors, such as the shape of the bluff body, the surface of the bluff body, types of the bluff body motion and properties of the fluid.

Various experiments have been carried out to study the behavior of added mass. The added mass coefficient C_M is defined as $C_M = \frac{m_a}{m_f}$, where m_a is the added mass per sectional length; $m_f = \rho\frac{\pi D^2}{4}$ is the displaced fluid mass per sectional length. In addition, the mass ratio μ is obtained using $\mu = \frac{(m + m_a)}{m_w}$, where m is the mass of riser per sectional length and $m_w = \rho D^2$.

According to a series of experiments carried out by Wendel in 1950s [54], the added mass is considered to be equal to the displaced fluid mass by the riser section in the sub-critical range, which means the added mass ratio equals to one. In most of the commercial software products like SHEAR7 [51], VIVA [60] and semi-empirical models for deepwater risers, the added mass is also chosen as one. However, it has to be noted that the value of μ varies spatially along the length of the riser. In the proposed model, the variation is not considered.

2.3.5 Mean Drag Coefficient $C_{D,S}$ and FSI Damping Parameter γ

The mean drag coefficient $C_{D,S}$ is defined as the equivalent static part of the drag coefficient C_D. According to the second term of Morison's equation 2.23, the equivalent static IL drag force will cause an equivalent static IL displacement of the riser. The actual mean drag coefficient can be obtained by matching the experimental IL equivalent static displacement and the analytical model IL static displacement under the mean drag force loading. Consequently, for FSI damping parameter, γ can be calculated using equation 2.25.

2.4 Model Verification

To finalize the development of 3D analytical model, hydrodynamic force related parameters need to be determined from the experiment. This section selects and calibrates those parameters for the 3D model, and then verifies the final model with numerical simulation results (from DNS [61]) and experimental data (Delta Flume (2003) [58]).

2.4.1 Numerical Verification-Uniform Current on Infinitely Long TTR

A schematic of an infinitely long slender TTR under uniform current excitation is shown in Fig. 2.7. The dynamic response was simulated using direct numerical simulation (DNS) method by Newman and Karniadakis [61]. The riser response is also simulated using the proposed model. The cross-flow VIV responses from the numerical methods, such as DNS, will be compared to responses from the proposed model. The details of the simulation is described next.

2.4.1.1 Parameters for Infinitely Long Riser

In the DNS simulation by Newman and Karniadakis [61], the added mass coefficient for cylinder, C_a is set to 1 according to Wendel's experiments in 1950 [54]. Same value for added mass is used in proposed model. As shown in Fig. 2.7, boundary conditions of the infinitely long riser are assumed to be spatially periodic, $u(0,t) = u(\Lambda,t)$. The wave length, Λ, of VIV caused by the uniform current speed is 8π.

In the proposed model, the vortex shedding frequency ω_z is treated as a constant through the height for uniform current profile. For a certain U_{ref} , the current speed, the relative vortex shedding frequency of $\omega_z = 1$ rad/s (0.159 Hz) is chosen. To

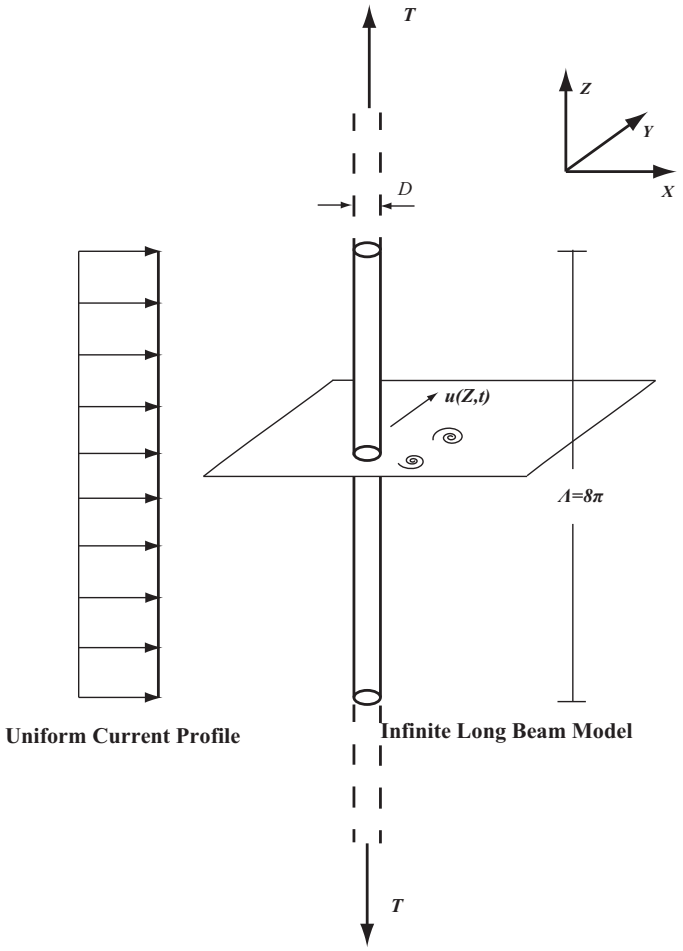

Figure 2.7 : Infinitely Long Beam subjected to Uniform Current

simplify equation 2.30 and 2.31, let $B = \dfrac{T_{top}}{(m+m_a)(\Omega_{ref}D)^2}$, $C = \dfrac{EI}{(m+m_a)\Omega_{ref}^2 D^4}$, $M = \dfrac{C_{L0}}{2}\dfrac{1}{8\pi^2 S_t^2 \mu}$ and $\gamma = \dfrac{C_{D,S}}{4\pi S_t}$. The detailed parameter is shown in Table 2.1.

Equation 2.30 and 2.31 are solved by an explicit approach of finite difference method, which is performed using a forward difference at time t_n and a second order and fourth order central difference for the spatial derivatives at that time t_n to get the dynamic responses from the proposed model [62].

For initial conditions, the fluid variable p, q are set to white noise with amplitude

Table 2.1 : Parameters for Simulation

Case	B	C	S_t	μ
I	16	0	0.16	1.785
ε	C_{L0}	$C_{D,S}$	$\Lambda(L)$	A_{CF}
0.3	1.2	0.3	8π	12

of order 10^{-3}. The displacement u, v and velocity of the riser are initialized to 0 (zero). The first time derivative of the fluid variable is also set to zero. For the spatial discretization, 250 sections are used for the simulation and a dimensionless time step of 0.01 is used. The integration is carried out for a dimensionless time t of 500.

2.4.1.2 Results Comparison between DNS and Proposed Model

The contour plot of the cross-flow displacement time history with respect to depth and dimensionless time using DNS is shown in Fig. 2.9, and the results from proposed model is shown in Fig. 2.8. Fig. 2.8 clearly shows that up to the first 40 seconds, the vibration amplitude gradually increases before reaching a standing wave vibration. After additional 60 seconds, the standing wave vibration changes to a traveling wave vibration at 100 seconds. The result from the proposed model in Fig. 2.8 matches the result from DNS (in Fig. 2.9) presented by Newman and Karniadakis [61] when $Re = 100$, which numerically validates the proposed model. (Notes: the time in Fig. 2.8 and Fig. 2.9 is dimensionless time.)

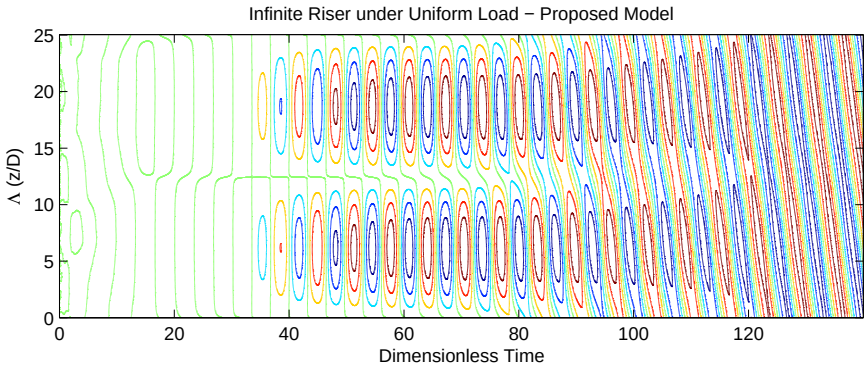

Figure 2.8 : Response Contour from The Proposed Model

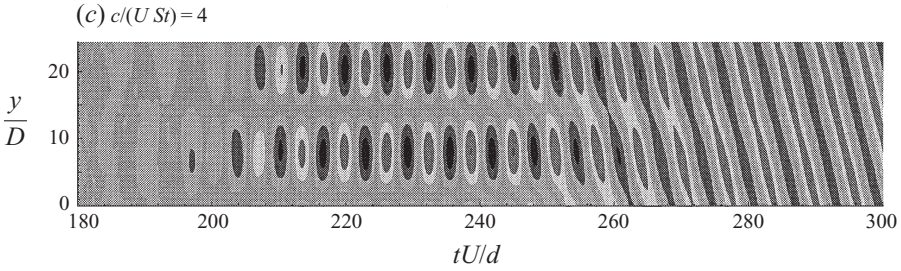

Figure 2.9 : Response Contour from DNS (Courtesy: Newman)

2.4.2 Experimental Verification - Delta Flume 2003

The experiments were carried out by Delta Flume of Delft Hydraulics in 2003 [58]. The proposed model is used to simulate the VIV responses of the test riser. And the results from the proposed model is compared with the results from experiments.

2.4.2.1 Delta Flume 2003 Experiments

The schematic setup of the Delta Flume 2003 experiment is shown in Fig. 2.10, in which a vertical model riser is subjected to a stepped current. The riser was 13.12 m long with 0.028 m diameter. Only lower 45% of the riser was subjected to uniform

current with velocity up to 1 m/s, while the upper portion of the riser is in still water [63].

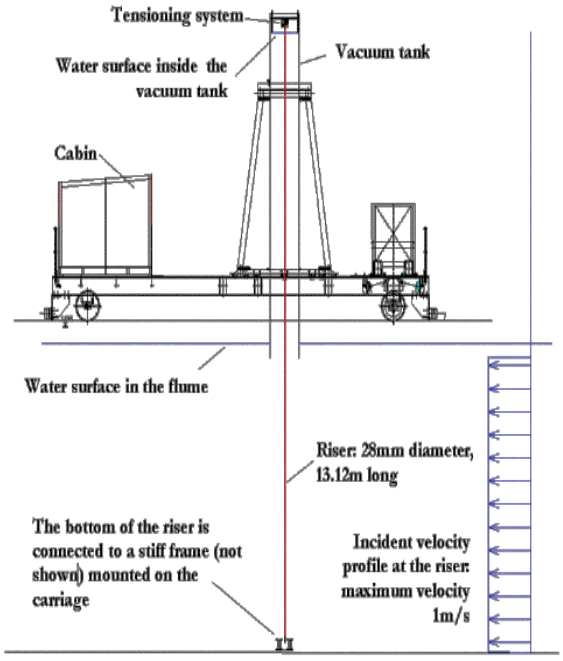

Figure 2.10 : Delta FLume Experimental Setup (Courtesy: Chaplin)

Table 2.2 : Parameters for Delta Flume 2003

Outside Diameter	Surface Condition	Length	Mass
0.028 m	Very smooth	13.12 m	1.47 kg/m
Mass in Water	Bending Stiffness	Damping Ratio	Axial Stiffness
1.85 kg/m	$EI = 29.9N \cdot m^2$	$\xi = 0.33\%$	$EA = 5.88 \times 10^6 N/m$

The in-line equivalent static displacement is shown in Fig. 2.11(b) for constant current. The maximum and minimum dynamic displacements of in-line VIV are

shown in Fig. 2.11(c). Parameters of the riser from the experiment (Delta Flume 2003), which are used in the numerical simulations, are shown in Table 2.2.

In the proposed model for Delta Flume(2003), the test riser is modeled as simply supported beam with 101 nodes with lumped mass and pin-roller supports at the ends. At each nodes, two independent van der Pol oscillators are connected in CF and IL direction. Most of the parameters are derived based on the actual properties in Table 2.2. Some of the parameters, such as the equivalent static drag coefficient, $C_{D,S}$, need calibration using experimental results. The dynamic responses are estimated using finite difference method to solve the equations 2.30 and 2.31.

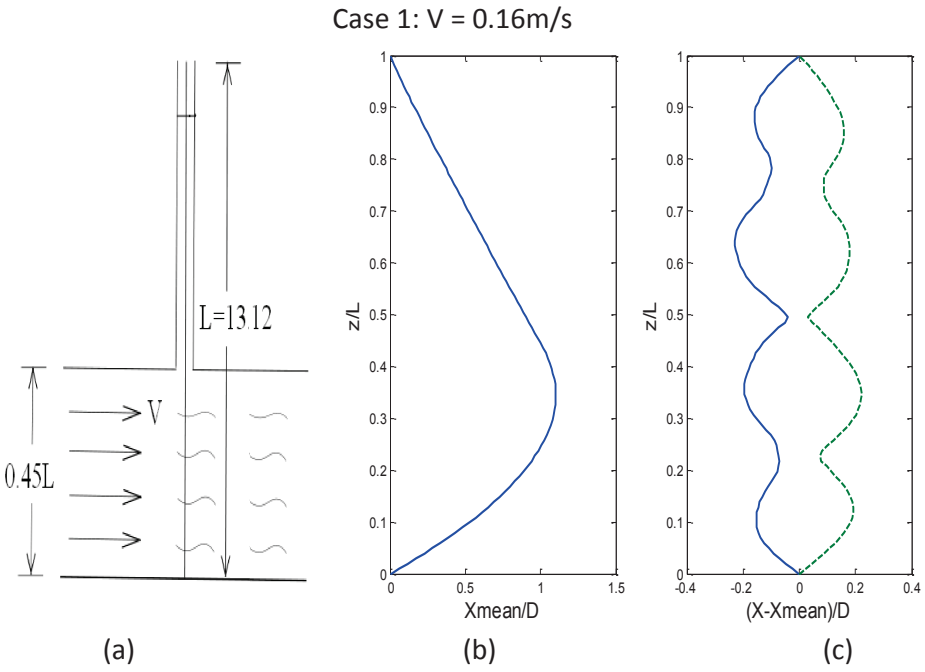

Figure 2.11 : Delta Flume Experimental Results - Case 1

2.4.2.2 Parameter Calibration

According to the parameter calibration section, the equivalent static drag coefficient $C_{D,S}$ can be estimated using the second term in equation 2.23. The parameters in Table 2.2 are used in the finite element method (FEM). The riser is modeled as simply supported beam (pin-roller supports at the ends) with top tension using 100 elements including geometric nonlinearity. The equivalent static drag force is modeled as uniformly distributed force applied on the riser as shown in Fig. 2.12(a). The static displacements of the riser model, x_0, are calculated based on the assumed $C_{D,S}$.

The equivalent static drag coefficient $C_{D,S}$ is calibrated by matching the equivalent IL displacements of the FEM model, x_0, with the corresponding measured equivalent static displacement (mean drift) results shown in Fig. 2.12. The equivalent static displacement is shown as solid line and the measured static displacement from the experiment is shown as dashed line in Fig. 2.12. The comparison between the computed and measured displacement shown in Fig. 2.12 is satisfactory.

According to the calibration results using case 1, $U = 0.16$ m/s, the calibrated IL equivalent static drag coefficient $C_{D,S} = 2.8$. The calibrated value will then be used in the numerical simulations of other experimental cases.

2.4.2.3 Verification with Experiments

Similar to the model for riser cross-flow VIV, the model for riser in-line VIV is also modeled by van der Pol oscillator coupled with a simply supported riser. The time history is generated by finite difference method. The primary difference between the in-line VIV and cross-flow VIV model are the amplitude and frequency of the van der Pol oscillators. According experimental observations, we set $B_{IL} = 0.2A_{CF}$ and $\omega_{IL} = 2\omega_{CF}$. Equivalent static drag coefficient $C_{D,S} = 2.8$ is used in the simulation.

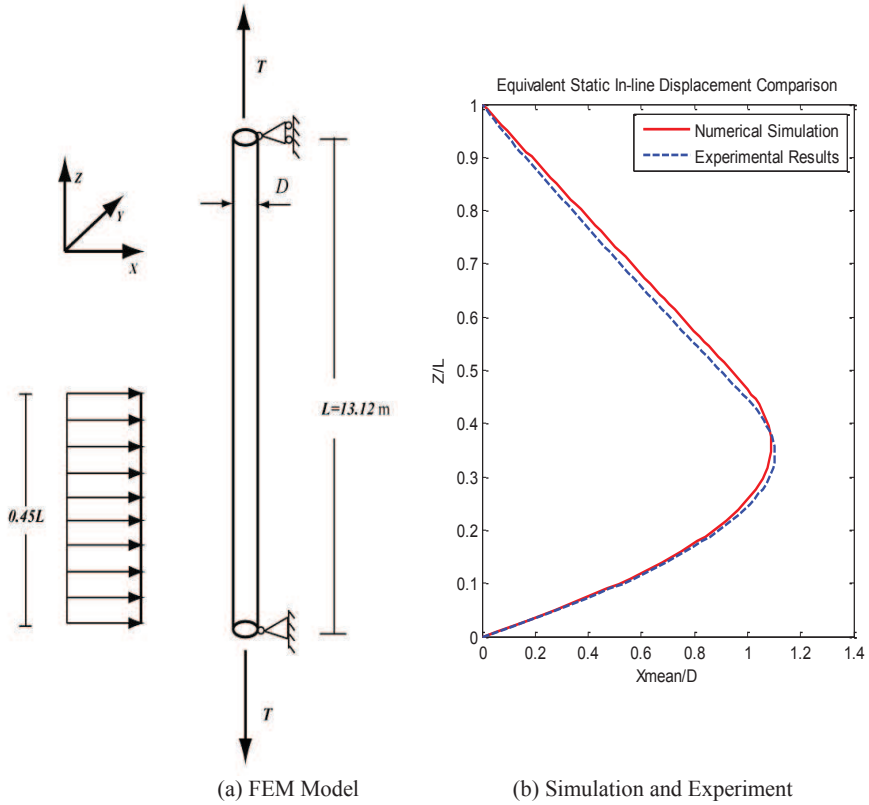

(a) FEM Model (b) Simulation and Experiment

Figure 2.12 : Inline Equivalent Static Drag Coefficient $C_{D,S}$ Calibration

Using equation 2.30 and 2.31, the coupled in-line and cross-flow VIV are simulated. All parameters (from experimental setup) are the same as the static displacement simulation in Table 2.2. Further test conditions are recorded in Table 2.3. To validate the calibrated parameters, Case 6 is chosen. The velocity of the stepped current is $U = 0.60$ m/s.

Fig. 2.13 shows the comparison of results from the proposed model and experiment. Static displacements from simulation and experiment, shown in Fig. 2.13(a) perfectly match with each other.

The peak response of in-line VIV at each point along the height is shown in Fig. 2.13(b), wherein the peak value at a point represents the maximum value of

Table 2.3 : Test Conditions for Delta Flue 2003

Case Number	Current Velocity	Top Tension
1	0.16 m/s	457 N
3	0.31 m/s	457 N
6	0.60 m/s	670 N
9	0.95 m/s	1002 N

the in-line VIV displacement time history. The comparison between the simulated and the measured peak response at each point shown in Fig. 2.13(b) for in-line VIV response is satisfactory for the spatial shape; however, the amplitudes differ.

Fig. 2.13(c) shows peak response of cross-flow VIV at each point along the height. The comparison for cross-flow VIV responses are satisfactory for both spatial shape and amplitude.

In general, the comparison proves that the proposed model is a satisfactory, especially for the inline static displacement and cross-flow dynamic displacement (VIV).

2.5 Comparison with SHEAR7

To further study the proposed model, performance comparisons between proposed model and commercial software products such as SHEAR7 are carried out using Delta Flume results.

2.5.1 Dynamic Response Estimation

SHEAR7 uses mode superposition method to estimated the response of riser subjected to current excitation [51]. The general steps for SHEAR7 are:

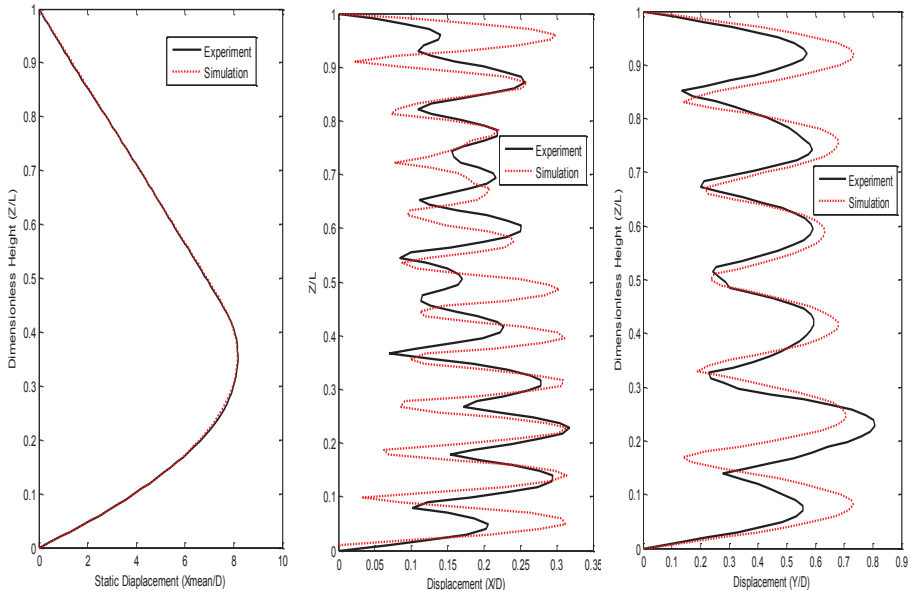

(a) In-line Static (b) In-line VIV (c) Cross-flow VIV

Figure 2.13 : Comparison between Experimental and Simulated Results - Case 6

- Calculating the dynamic properties (frequency, mode shapes and modal damping etc.) of the test structure;
- Using reduced velocity, $V_R = \dfrac{U}{f_e D}$, estimate the occurrence of lock-in (power-in region). For mode with frequency f_e, the power-in region occurs when $V_R \in [4, 8]$ for the corresponding mode [51];
- In each time step (iteratively) calculating the lift and damping coefficients based on given curve (shown in Fig. 2.14) and amplitude;
- Estimating the response and fatigue life of the structure using excited mode shapes.

In the proposed model, the response is obtained using finite difference method to solve the wake oscillator model. No pre-calculation is needed for structural dynamic properties or which modes are excited and where will the power-in region be. Only parameters like Strouhal number S_t and some other hydrodynamic coefficients should be determined by experiments or experience. These parameters are also used in SHEAR7. The power-in region and modes being excited are determined based on the interaction between the vortex and structure.

2.5.2 Lift Coefficient

In the popular riser design software SHEAR7 [51] and some other similar softwares, the lift and drag coefficients, C_D and C_L, are determined by a preset curve as shown in Fig. 2.14. where the lift coefficient curve in SHEAR7 is obtained by fitting two

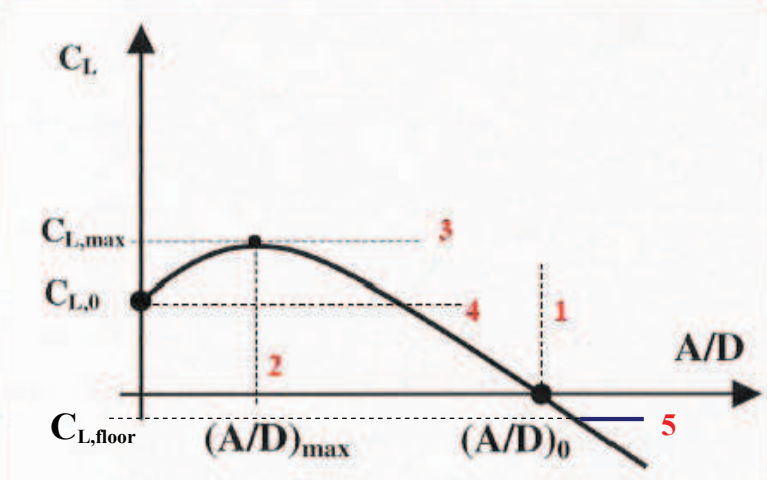

Figure 2.14 : Lift Coefficient (C_L) v.s. Dimensionless Amplitude($\frac{A}{D}$) Courtesy: Vandiver et al.

parabolas curve through three points with four user-defined values.

On the other hand, the lift coefficient is not directly obtained from preset curve

in the proposed model. The lift coefficient is obtained using van der Pol oscillator, $\ddot{q} + \varepsilon\omega_z (q^2 - 1)\dot{q} + \omega_z^2 q = A_{CF}\ddot{v}$, which considers both the motion (acceleration, $\ddot{v}$) of the corresponding riser section and the differential functions of lift coefficient.

In summary, in SHEAR7 the lift coefficient only depends on displacement of riser; its frequency is equal to that of the structure. In the proposed model, the lift coefficient is determined by both the motion of riser and the fluid; it is determined by the interaction of the structure and vortex.

2.5.3 Standing Wave v.s. Traveling Wave

SHEAR7 uses the mode superposition method, the response is generally standing wave. However, lots of field and experimental tests [58] [48] show that the response is mostly a traveling wave. Only uniform current profile and some pure linearly sheared currently profile will lead to standing wave response.

The proposed model has the capability to produce both traveling and standing waves. The response arising is based on the input current profile. A travelling wave is generated in response to an input sheared or non-uniform current profile. Such a response is more realistic.

2.5.4 Capability for Damage Detection Study

Since SHEAR7 is based on mode superposition method and cannot generate traveling wave responses, its simulated response time history cannot be treated as actual responses. The key application for SHEAR7 is fatigue estimation and response amplitude estimation, which only requires consideration of amplitude and frequency. Hence, SHEAR7 is unsuitable for damage detection.

On the contrary, the proposed oscillator model with FDM is suitable for damage

detection application. The stiffness parameters of the model can be changed to estimate the damage occurring. Instances of damages like reduction of wall thickness due to corrosion can be directly simulated using the FDM model proposed here.

2.5.5 Experimental Comparison with Other Software Products

According to the sources from Delta Flume [58], the predicted RMS values of VIV responses of the test riser are calculated for VIVANA [60], OrcaFlex [64] and SHEAR7 [51]. The VIVANA program is a semi-empirical frequency domain program based on 2D finite element model (only cross-flow dynamic estimation and inline static displacement). The program was developed to predict cross-flow VIV response by MARINTEK and NTNU. Orcina vortex tracking model is based on strip theory and implemented in OrcaFlex (version 2007) software by Orcina Ltd. SHEAR7 (version 2007) is based on modal superposition and power-in region assumption.

The RMS values of CF VIV dimensionless displacement of experiments and various software predictions for case 6 with step uniform current velocity are shown in Fig. 2.15. The results from SHEAR7 is clearly wrong as it assumes that the vibration mode shape is single pure sine wave. This assumption leads to zero values at those sine crossings in the RMS plot. In addition, the result from Orcina vortex tracking model shows mode 7 with 7 peak values, while all the other shows mode 6 with 6 peaks. This indicates the vortex shedding frequency estimation in Orcina vortex tracking model is wrong.

To further compare the other results, the RMS values from different methods are plotted together in Fig. 2.16. Though results from VIVANA and proposed analytical model both show six peaks and reasonable amplitudes, the dashed line (proposed model) shows a closer amplitude and peak locations to experimental results than

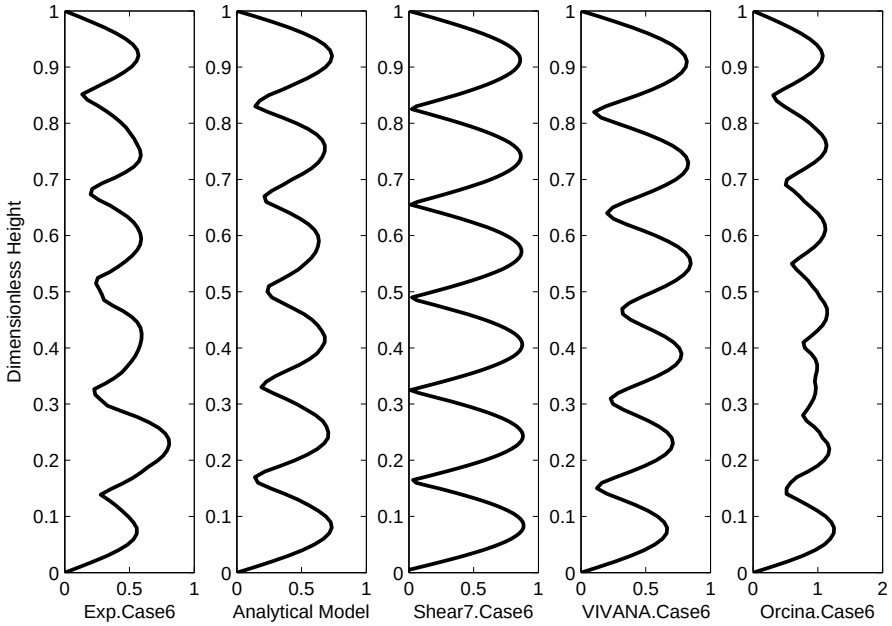

Figure 2.15 : RMS Comparison among Experiment and Estimation from Various Software Products - Case 6

dash-dot line (VIVANA).

Comparison between static inline displacements shown in Fig. 2.17 clearly indicates that proposed model has a much better displacement estimation than all the other methods. The dashed line (proposed model) exactly matches with the experimental value while the other two differ.

The comparison between the proposed model and other commercial software products further proves the effectiveness of proposed 3D analytical model. The limitation of SHEAR7 on traveling wave estimation is clearly evident. The proposed model has the potential to be better for VIV response prediction of deepwater risers, especially TTR.

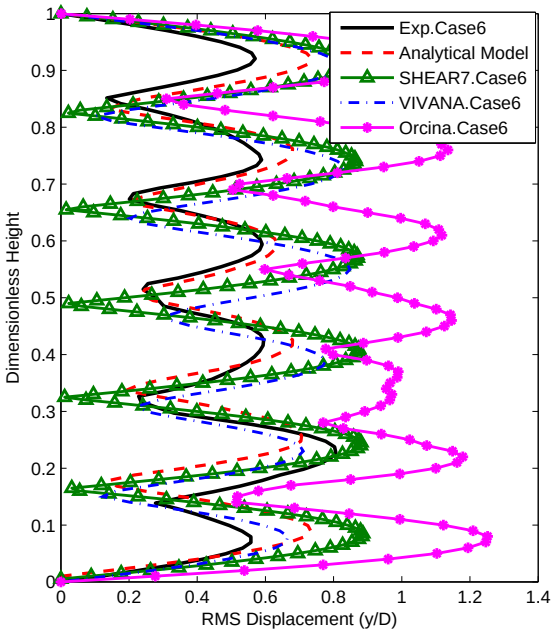

Figure 2.16 : CF RMS Displacements Comparison all together - Case 6

2.6 Summary

This chapter reviewed a few previous studies on numerical models for deepwater riser VIV simulations, and proposed a new 3D analytical riser model with coupled VIV. Finally the proposed model was verified with both numerical simulation and experimental results. In summary,

- A 3D analytical model of deepwater riser with coupled VIV is proposed in this chapter. Lagrangian coordinates and Green-Lagrangian strains are used in the model. Van der Pol oscilltors are used to simulate the hydrodynamic fluid structure interaction force coefficients. Based on extended Hamilton's equation, detailed derivation procedures of equations of motion for the proposed model are provided using variation method.

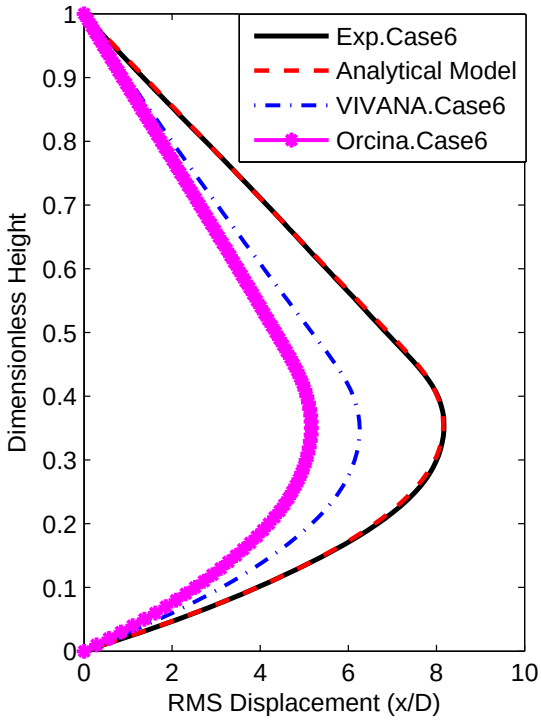

Figure 2.17 : IL Static Displacements Comparison all together - Case 6

- Finite difference method is used to solve the equations of motion for the proposed model and estimate the responses of the deepwater riser subjected to current excitation. Further detailed comparisons between popular commercial software, SHEAR7 and the proposed model show that the proposed model is a better solution to estimate the response history of deepwater risers.

- In addition, all the important parameters in the proposed model are well described and documented.

- Furthermore, the comparison between the proposed analytical model and SHEAR7, VIVANA and OrcaFLex proves that the proposed model is better for VIV re-

sponse prediction than the others.

- Finally, both numerical simulation (using direction numerical simulation to estimate the riser response by directly solving Navier-Stroke equation) and experimental results (Delta Flume 2003) verified the effectiveness of the proposed model.

However, as dimensionless time and amplitude (references) are used in the finite difference approach, the results are not directly reflecting the actual behavior before scaling back to actual dimension. This issue will be resolved in the next chapter by using finite element methods rather than finite difference method for the proposed model.

Chapter 3

Analytical Model using Finite Element Method

In the previous chapter, the 3D analytical model with coupled VIV using FDM method is proposed and verified. In the simulations using Finite Difference Method (FDM), the fundamental component is the individual node with lumped mass. The geometric nonlinearity is realized by the spatial derivatives such as curvature (the second order derivative of displacement respect to vertical length) and distributed force (the fourth order derivative of displacement respect to vertical length). There is neither global stiffness matrix nor global excitation forces in the simulation. The key assumption is the fluid at each vertical depth is laminar and will not interact with the adjacent layers.

On the other hand, in the simulations using Finite Element Method (FEM), the fundamental component is the individual element. The geometric nonlinearity is considered by using element type with nonlinear capability. In this way, the global stiffness matrix can be obtained with geometric nonlinear portion for each time step. The wake oscillators should be considered at each element level. However, it is simpler to apply those oscillators at each node level with consideration of the Fluid-Structure Interactions (FSI) combining contribution from upper element and the lower element. In this way, the global FSI vector can be constructed.

The main reason for replacing FDM model, with FEM model, is the Green-Lagrange strain. According to the previous definition, $\varepsilon = \frac{l_i^2 - l_d^2}{2l_i^2}$, Green-Lagrange strain is an energy strain, while the actual measured strain or engineering strain

is geometric strain, $\varepsilon = \frac{l_i - l_d}{l_i}$. As a result, to estimate the measured strain using Green-Lagrange strain from simulation is not always appropriate. Furthermore, as mentioned in [65], Green-Lagrange strains are only suitable for small strain problems ($\varepsilon \leqslant 0.04$).

To address the problems with Green-Lagrange strains, Jaumann strains are introduced into this chapter. Jaumann strains are defined by the co-rotational coordinate system and keep three perpendicular directions (remain cartesian coordinates). The benefits of this definition are consideration of shear stress conditions along with rigid body motions [65].

$$\begin{aligned} [\mathbf{B}] &\equiv [\mathbf{U}] - [\mathbf{I}] \\ [\mathbf{B}] &= \frac{1}{2}\left([\mathbf{e}] + \left[\mathbf{e}^{\mathbf{T}}\right]\right) \\ [\mathbf{e}] &\equiv \left[\frac{\partial u_n}{\partial z_m}\right] \\ [B_{mn}] &= \frac{1}{2}\left(\frac{\partial u_m}{\partial z_n} + \frac{\partial u_n}{\partial z_m}\right) \end{aligned} \tag{3.1}$$

where $[\mathbf{U}]$ represents the strains along the deformed coordinated system or so called as right stretch tensor; $[\mathbf{I}]$ takes care of the rigid body motions. Since $[\mathbf{e}]$ is a symmetric tensor, $[B_{mn}] = \dfrac{\partial u_n}{\partial z_m}$. When there is no rigid body motion, then $[\mathbf{I}] = 0$, Jaumann strains are equal to engineering strain as shown in the last two equations of equation 3.1.

In summary, Jaumann strains are with respect to relative displacements and rotated coordinates [65]. However, since the riser undergoes large motions , the Jaumann strain is more appropriate for the FEM formulation developed in this chapter. As a result, a FEM model with Jaumann strains is needed for this study.

The proposed FEM model contains two important parts: the nonlinear FEM model for the riser and the van der Oscillators for the FSI forces. The nonlinear FEM

model for the geometric nonlinear riser is adapted and executed using Geometrically Exact Structural Analysis (GESA) algorithm [65], developed and provided by Pai [65]. With the help from Pai [66], the model is expanded to account for FSI foces by introducing van der Pol oscillators.

This chapter describes the proposed FEM model and the numerical simulation method. First, the transformation from time-scaled wake oscillators to actual time wake oscillators is described; Second, the actual FSI force terms are obtained from previous scaled model. Third, the choice of element type for FEM analysis is detailed. Finally, the numerical and experimental verifications of the proposed model are presented.

3.1 FSI Estimation using van der Pol Oscillator - {F}

To transform the FDM model to FEM model, the critical part is to remove the scaling effects from both the van der Pol wake oscillators and the related FSI terms. This section starts with the van der Pol oscillators and wraps up with FSI force terms, [**F**],. The equations of motion (EOM) for the FDM model are shown as following:

$$\begin{aligned} \ddot{p} + \varepsilon\omega_{z,IL}\left(p^2-1\right)\dot{p} + \omega_{z,IL}^2 p &= B_{IL}\ddot{u} \qquad (3.2)\\ \ddot{u} + \frac{\gamma\omega_{z,IL}}{\mu}\dot{u} - \left(\frac{1}{\left(m+m_a\right)\Omega_{ref}^2 D^2}\right) &\times \\ \left(T_{top}\frac{\partial^2 u}{\partial z^2} + EA\epsilon_I\left(\frac{\partial^2 u}{\partial z^2}+\frac{\partial^2 x}{\partial z^2}\right) - (w)\frac{D\partial u}{\partial z} - (EI)\frac{\partial^4 u}{D^2\partial z^4}\right) &= \frac{p\omega_{z,IL}^2 C_{D0}}{16\pi^2 S_t^2\mu} \end{aligned}$$

$$\begin{aligned} \ddot{q} + \varepsilon\omega_{z,CF}\left(q^2-1\right)\dot{q} + \omega_{z,CF}^2 q &= A_{CF}\ddot{v} \qquad (3.3)\\ \ddot{v} + \frac{\gamma\omega_{z,CF}}{\mu}\dot{v} - \left(\frac{1}{\left(m+m_a\right)\Omega_{ref}^2 D^2}\right) &\times \\ \left(T_{top}\frac{\partial^2 v}{\partial z^2} + EA\epsilon_I\left(\frac{\partial^2 v}{\partial z^2}\right) - (w)\frac{D\partial v}{\partial z} - (EI)\frac{\partial^4 v}{D^2\partial z^4}\right) &= \frac{q\omega_{z,CF}^2 C_{L0}}{16\pi^2 S_t^2\mu} \end{aligned}$$

where $\Omega_{ref} = 2\pi S_t U_{ref}/D$ is the reference frequency for a given reference velocity, U_{ref}. p, q are the van der Pol oscillator variables for the in-line (IL) and cross-flow (CF) directions, respectively. u, v are the IL and CF direction dimensionless displacements of riser, respectively. z represents the dimensionless vertical depth. $\dot{}$ means the derivative respect to time τ, and ∂ denotes the partial derivative respect to given vector z in this case. μ is the mass ratio (riser total mass vs. displaced fluid mass). w is the self weight per unit length of the riser. S_t is the Strouhal number, D is the external diameter of the riser. T_{top} is the tension at the top of riser, m and m_a are the mass per unit length of riser and added mass. γ, ε, A and B are determined based on experimental data of fluctuating lifting and drag on a rigid cylinder driven in forced vibration. EI the bending rigidity. EA is the axial stiffness. C_{L0} and C_{D0} are fluctuating lift and drag coefficients from fixed cylinder experiments. The frequencies of the wake oscillator are related by $\omega_{z,IL} = 2\omega_{z,CF}$ along the depth of the riser.

3.1.1 van der Pol Oscillator

For top-tensioned riser (TTR), the self weight does not play an important role when comparing the simulations with and without self weight term. In addition, when only considering the cross-flow direction VIV, the equation 3.3 reduces to the following equation:

$$\begin{aligned} \ddot{q} + \varepsilon\omega_{z,CF}\left(q^2 - 1\right)\dot{q} + \omega_{z,CF}^2 q &= A\ddot{v} \\ \ddot{v} + \frac{\gamma\omega_{z,CF}}{\mu}\dot{v} - \frac{1}{(m+m_a)\,\Omega_{ref}^2}\left(\frac{T + EA\epsilon_I}{D^2}\frac{\partial^2 v}{\partial z^2} - \frac{EI}{D^4}\frac{\partial^4 v}{\partial z^4}\right) &= \frac{q\omega_{z,CF}^2 C_{L0}}{16\pi^2 S_t^2 \mu} \end{aligned} \tag{3.4}$$

In finite difference method (FDM), the proposed van der Pol wake oscillator model uses a normalized frequency, $\omega_{z,CF} = \Omega_{z,CF}/\Omega_{ref}$, which results in a scaled time, τ. The scaled time τ in the FDM model is

$$\tau = \frac{t}{\Omega_{ref}},\ or\ t = \Omega_{ref}\tau \tag{3.5}$$

where t is the actual time in the model using finite element method (FEM).

Taking a uniform current loading as an example, the normalized frequency, $\omega_{z,CF}$, is one in the CF direction all along the depth, while in the IL direction $\omega_{z,IL} = 2$ all along the depth. Based on equation 3.5, the van der Pol variables can be changed to actual time t:

$$\begin{aligned} q(t) &= q(\Omega_{ref}\tau) \\ \dot{q}(t) &= [q(\dot{\Omega_{ref}\tau})] = \Omega_{ref}\dot{q}(\Omega_{ref}\tau) \\ \ddot{q}(t) &= [q(\ddot{\Omega_{ref}\tau})] = \Omega_{ref}^2\ddot{q}(\Omega_{ref}\tau) \end{aligned} \tag{3.6}$$

The van der Pol oscillator equation in equation 3.4 can also be written as

$$\ddot{q}(\Omega_{ref}\tau) + \varepsilon\omega_{z,CF}\left(q(\Omega_{ref}\tau)^2 - 1\right)\dot{q}(\Omega_{ref}\tau) + \omega_{z,CF}^2 q(\Omega_{ref}\tau) = A\ddot{v}(\Omega_{ref}\tau) \tag{3.7}$$

Replacing the above $q(\Omega_{ref}\tau)$ with $q(t)$ from equation 3.7 results in

$$\frac{1}{\Omega_{ref}^2}\ddot{q}(t) + \varepsilon\omega_{z,CF}\left(q^2(t) - 1\right)\frac{1}{\Omega_{ref}}\dot{q}(t) + \omega_{z,CF}^2 q(t) = \frac{A}{\Omega_{ref}^2}\frac{\ddot{v}(t)}{D} \tag{3.8}$$

where $v(\tau)$ follows the same process as equation 3.6.

Equation 3.8 will provide a oscillation with frequency at Ω_{ref}. The simplified equation becomes

$$\ddot{q}(t) + \varepsilon\Omega_{z,CF}\left(q^2(t) - 1\right)\dot{q}(t) + \Omega_{z,CF}^2 q(t) = A\frac{\ddot{v}(t)}{D} \tag{3.9}$$

where $\Omega_{z,CF}$ (or previously referred to as $\omega_{z,CF}\Omega_{ref}$) represents the vortex shedding frequency at the given depth, z.

In a similar manner, the van der Pol oscillator in the IL direction can be simplified to

$$\ddot{p}\left(t\right)+\varepsilon\Omega_{z,IL}\left(p^{2}\left(t\right)-1\right)\dot{p}\left(t\right)+\Omega_{z,IL}^{2}p\left(t\right)=B\frac{\ddot{u}\left(t\right)}{D} \tag{3.10}$$

The van der Pol oscillator variable will converge to a sine wave type excitation as shown in Figure 3.1 when there is no interaction force between the fluid and structure. The dominant or the only excitation frequency is around 8.38 Hz for given current speed. When there are fluid-structure interactions (FSI), the actual van der Pol oscillator variable time history can be obtained using ordinary differential equation (ODE) solver or Newmark-β method.

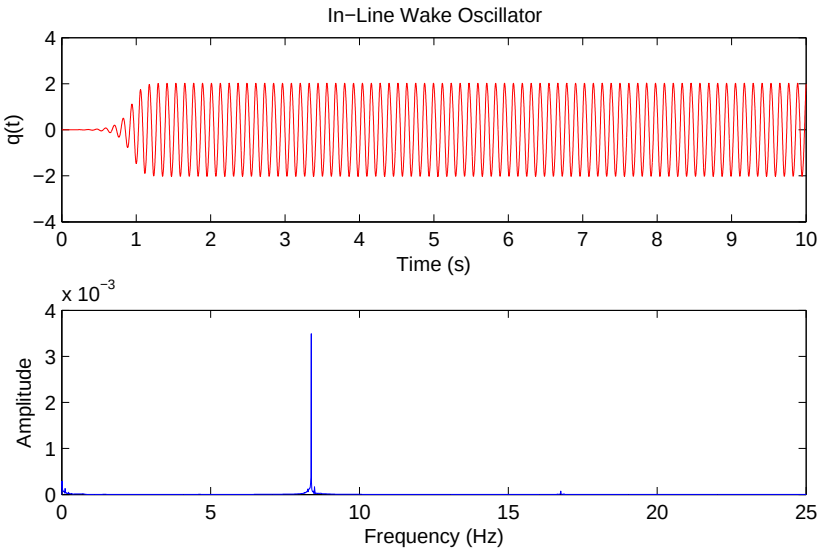

Figure 3.1 : In-Line Oscillator Vibration

3.1.2 Fluid-Structure Interactions (FSI)

Similar to van der Pol oscillator, the actual motion, $v(t) = v(\Omega_{ref}\tau)/D$ and $z = Z/D$. To transfer from scaled time/dimension to actual time/dimension,

$$\begin{aligned} v(t) &= v(\Omega_{ref}\tau) * D \\ \dot{v}(t) &= [v(\Omega_{ref}\dot{\tau})] * D = \Omega_{ref}\dot{v}(\Omega_{ref}\tau) * D \\ \ddot{v}(t) &= [v(\Omega_{ref}\ddot{\tau})] * D = \Omega_{ref}^2\ddot{v}(\Omega_{ref}\tau) * D \\ \frac{\partial^2 v(t)}{\partial z^2} &= \frac{\partial^2 [v(\Omega_{ref}\tau) * D]}{D^2\partial z^2} = \frac{\partial^2 v(\Omega_{ref}\tau)}{D^2\partial z^2} * D \\ \frac{\partial^4 v(t)}{\partial z^4} &= \frac{\partial^4 [v(\Omega_{ref}\tau) * D]}{D^4\partial z^4} = \frac{\partial^4 v(\Omega_{ref}\tau)}{D^4\partial z^4} * D \end{aligned} \tag{3.11}$$

Substituting equation 3.11 into equation 3.4, the original function can be simplified to

$$\begin{aligned} \frac{\ddot{v}(t)}{D\Omega_{ref}^2} + \frac{\gamma\omega_{z,CF}}{\mu D\Omega_{ref}}\dot{v}(t) - \left(\frac{T + EA\epsilon_I}{(m+m_a)\Omega_{ref}^2}\right)\frac{\partial^2 v(t)}{D\partial z^2} &+ \\ \left(\frac{EI}{(m+m_a)\Omega_{ref}^2}\right)\frac{\partial^4 v(t)}{D\partial z^4} &= \omega_{z,CF}^2\frac{C_{L0}}{2}\frac{1}{8\pi^2 S_t^2\mu}q(t) \end{aligned} \tag{3.12}$$

Multiplying $(m+m_a)\Omega_{ref}^2 D$ in both sides of equation 3.12, the equation becomes

$$\begin{aligned} (m+m_a)\ddot{v}(t) + (m+m_a)\frac{\gamma\Omega_{z,CF}}{\mu}\dot{v}(t) &- (T + EA\epsilon_I)\frac{\partial^2 v(t)}{\partial z^2} + \\ (EI)\frac{\partial^4 v(t)}{\partial z^4} &= \frac{C_{L0}(m+m_a)D}{16\pi^2 S_t^2\mu}\Omega_{z,CF}^2 q(t) \end{aligned} \tag{3.13}$$

where $\Omega_{z,CF} = \omega_{z,CF}\Omega_{ref} = 2\pi\dfrac{S_t U_z}{D}$.

In addition, the mass ratio $\mu = (m+m_a)/m_w$, where $m_w = \rho D^2$. Generally in simulation, added mass m_a is set to be equal to the displaced fluid mass, $m_f = \dfrac{\rho\pi D^2}{4}$.

$$\begin{aligned} (m+m_a)\ddot{v}(t) + m_w\gamma\Omega_{z,CF}\dot{v}(t) - (T + EA\epsilon_I)\frac{\partial^2 v(t)}{\partial z^2} &+ \\ (EI)\frac{\partial^4 v(t)}{\partial z^4} &= \frac{C_{L0}m_w D}{16\pi^2 S_t^2}\Omega_{z,CF}^2 q(t) \end{aligned} \tag{3.14}$$

Comparing to the general equations of motion (EOMs), $[\mathbf{M}]\ddot{\mathbf{x}} + [\mathbf{C}]\dot{\mathbf{x}} + [\mathbf{K}]\mathbf{x} = \{\mathbf{F}\}$, the corresponding parts are shown as

$$\begin{aligned} (m + m_a) &\rightarrow [\mathbf{M}] \\ -(T + EA\epsilon_I)\frac{\partial^2 v(t)}{\partial z^2} + (EI)\frac{\partial^4 v(t)}{\partial z^4} &\rightarrow [\mathbf{K}] \\ \frac{C_{L0} m_w D}{16\pi^2 S_t^2}\Omega_{z,CF}^2 q(t) - m_w \gamma \Omega_{z,CF}\dot{v}(t) &= \{\mathbf{F_{CF}}\} \end{aligned} \tag{3.15}$$

where $m_w \gamma \Omega_{z,CF}\dot{v}(t)$ is a damping force introduced by fluid-structure interaction (FSI). The $\Omega_{z,CF}$ term indicates that the FSI damping term should be considered as a part of FSI force term, $\{\mathbf{F}\}$. The $\{\mathbf{F}\}$ vector from the above equation represents the hydrodynamic FSI forces applied at each nodes of the proposed riser FEM model in the CF direction.

The global structural mass matrix, $[\mathbf{M}]$, stiffness matrix, $[\mathbf{K}]$, and damping matrices $[\mathbf{C}]$ term in the general EOM for the proposed FEM model will be constructed from elemental system matrices, which will be described in the next section.

Similarly, considering the dimension scaling factor, the FSI term for van der Pol oscillator becomes

$$\frac{A\ddot{v}(t)}{D} = \{\mathbf{F_{vdp,CF}}\} \tag{3.16}$$

As a result, the FSI terms for riser model in the CF direction will be the force term, $\{\mathbf{F_{CF}}\}$ as shown in equation 3.15. And the FSI term for van der pol oscillator in CF direction is shown in equation 3.16.

In a similar manner, the EOM for riser in the IL direction can be derived

$$\begin{aligned} (m + m_a)\ddot{u}(t) + m_w \gamma \omega_{z,IL}\dot{u}(t) - (T)\frac{\partial^2 u(t)}{\partial z^2} &- \\ (EA\epsilon_I)\left(\frac{\partial^2 u(t)}{\partial z^2} + \frac{\partial^2 x(t)}{\partial z^2}\right) + (EI)\frac{\partial^4 u(t)}{\partial z^4} &= \frac{C_{D0} m_w D}{16\pi^2 S_t^2}\omega_{z,IL}^2 p(t) \end{aligned} \tag{3.17}$$

Hence, the FSI force term applied on the riser in the IL direction is

$$\frac{C_{D0} m_w D}{16\pi^2 S_t^2} \Omega_{z,IL}^2 p(t) - m_w \gamma \Omega_{z,IL} \dot{u}(t) = \{\mathbf{F_{IL}}\} \tag{3.18}$$

where $\Omega_{z,IL} = 2\Omega_{z,CF}$.

The FSI term for van der Pol oscillator in the IL direction is

$$\frac{B\ddot{u}(t)}{D} = \{\mathbf{F_{vdp,IL}}\} \tag{3.19}$$

3.2 Finite Element Model - [M], [C] and $[\mathbf{K}]_\mathbf{t}$

In the FEM model, there are two main non-linearities influencing the dynamic properties of the TTR. One is geometric non-linearity, which is the secondary effect of tension when there are lateral displacements, also known as P-Δ effect. In the FDM model, this geometric non-linearity is taken care of by the top-tension term. In the FEM model, this non-linearity should be considered in the element type. The other non-linearity is the added mass. In reality, the added mass varies a lot for different current profiles. The ranges of added mass ratio can vary from 0 to 2 or even higher. According to Wendel's experiments in 1950s [54], the variation of added mass is not considered in the FEM model. The added mass is considered to be equal to the displaced fluid mass. In another words, the added mass ratio is set to one. In addition, since the stress of the riser section is usually much smaller than the yield stress, the material nonlinearity is not considered.

3.2.1 Non-linear Beam Element

As deepwater TTRs usually have very large aspect ratio (length v.s. diameter), TTRs can be approximately modeled as cables with tension if the purpose of the modeling is to estimate the responses subjected to current excitation. However, the goal of the

analytical model in this study is not only to predict the responses of the risers, but also to estimate the bending damage, thus, bending stiffness should be considered in the model. As shown in Figure 3.2, TTR is simulated as simply supported beam with top tension. Different beam element types [65] with previously mentioned geometric non-linearity are considered.

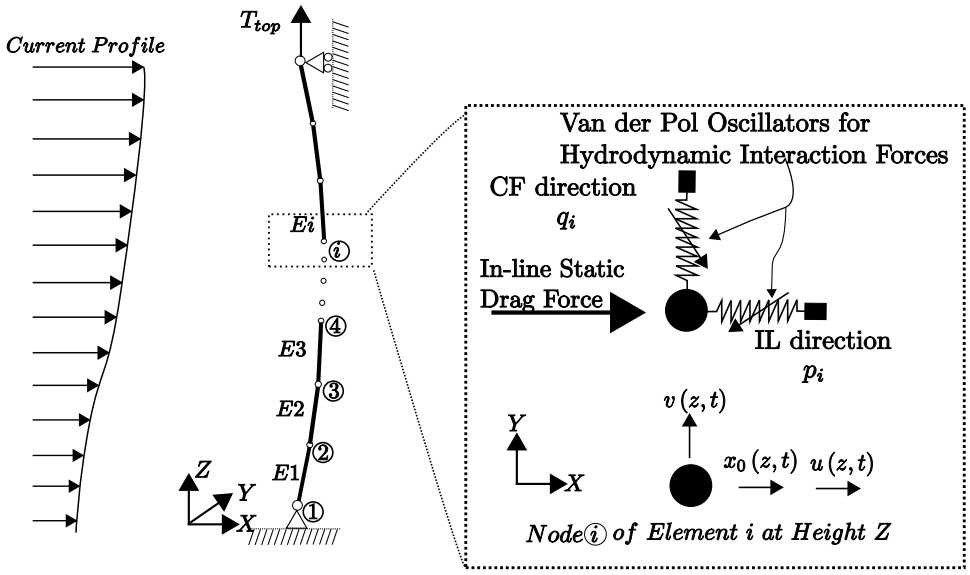

Figure 3.2 : Top-Tensioned Riser Model

3.2.2 Degrees of Freedom of Beam Element

The FEM model takes coupled VIV into consideration by using 3D beam element. Figure 3.3 shows the typical 3D beam element type used in this study. In the beam element, two end nodes are considered. For each node, there are six degrees of freedom (DOF): axial displacement, δ; in-line and cross-flow transverse displacements, u, v, respectively; torsional angle, ϕ; bending angles, κ and η.

As shown in figure 3.3, Euler-Bernoulli beam is used without consideration of

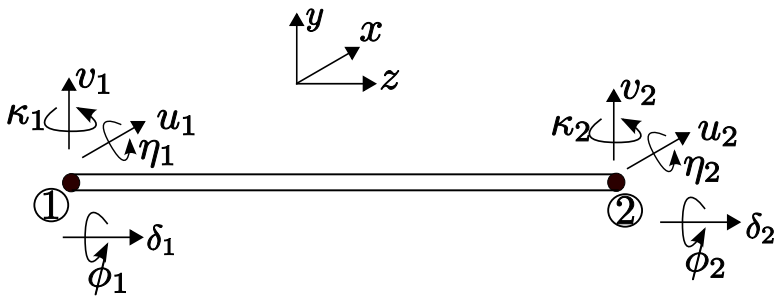

Figure 3.3 : 3D Beam Model with 6DOF at Each Node

shear deformations (warpings). The cross sections can be assumed to be plane and perpendicular to the z axis. Since TTR has a very long aspect ratio and top tension is much larger than transverse current loading, transverse shear deformations are so small that they can be neglected. As a result, Euler-Bernoulli beam element with six DOFs are used in the element.

3.2.3 Geometric Nonlinearity - Modified von Kármán nonlinearity

The popular usage of Lagrangian formulation for geometrically nonlinear structures is because the system will easily get the natural undeformed state when the structure is unloaded. As equilibrium equations require the balance of internal stresses, stresses should be defined respect to the deformed system. For nonlinear structures, the definition of strains and stresses should be objective, work-conjugate, geometric, and perpendicular in order to use them in the constitutional equations. Objective strains and stresses remove the rigid body motion (displacement/rotation). A common solution is using an incremental/iterative procedure with tangent stiffness matrix. This part will be further discussed later in the numerical simulation part [65].

As mentioned in the beginning of this chapter, Green-Lagrange strains are used in

FDM model to take care of the geometric nonlinearity as well as the coupling between in-line (IL) and cross-flow (CF) vibration. However, Green-Lagrange strains in the pervious FDM model has limitations when strains are large or there are large rigid body motions. One solution is to use FEM with Jaumann strain and von Kármán nonlinearity to account for geometric nonlinearity. The von Kármán nonlinearity is

$$\begin{aligned} B_{11} &= e + z\rho_2 - y\rho_3, \quad 2B_{12} = -z\rho_1, \quad 2B_{13} = y\rho_1 \\ e &= u' + \frac{1}{2}v'^2 + \frac{1}{2}w'^2, \quad \rho_1 = \phi', \quad \rho_2 = -w'', \quad \rho_3 = v'' \end{aligned} \tag{3.20}$$

where B_{mn} are Jaumann strains used for FEM model. Axial strain e is same as the definition of ε_I in FDM model as equation 2.21. So does ρ_1, ρ_2 and ρ_3. In the similar way, the von Kármán nonlinearity takes care of the geometric nonlinearity, but does not account for large strains. To address this problem, Pai and Nayfeh [67] modified the von Kármán nonlinearity to account for large strain effects.

$$\begin{aligned} B_{11} &= e + z\rho_2 - y\rho_3, \quad 2B_{12} = -z\rho_1, \quad 2B_{13} = y\rho_1 \\ e &= u' + \frac{1}{2}v'^2 + \frac{1}{2}w'^2, \quad \rho_1 = \phi', \quad \rho_2 = -w''\left(1 - w'^2\right), \quad \rho_3 = v''\left(1 - v'^2\right) \end{aligned} \tag{3.21}$$

where, the large strains are considered by the differences of ρ_2, ρ_3 between the classical von Kármán nonlinearity and modified von Kármán nonlinearity. Rigid body motions are removed by Jaumann Strain.

In summary, without consideration of warping, a 3D beam element using Jaumann strain with modified von Kármán nonlinearity is used in the FEM model to account for geometric nonlinearity.

3.2.4 Nonlinear Simulation Method for TTR VIV Response Estimation

Numerical evaluation of the dynamic responses of systems requires time-marching schemes (explicit or implicit) to solve the equations of motion (EOMs) either directly or indirectly. Directly integration methods directly integrate the EOMs with physical coordinates or degrees of freedom (DOFs), while within indirect methods the most commonly used one is the mode superposition method. The mode superposition method converts the physical DOFs into modal coordinates. As a result, for linear system with proportional damping (Rayleigh damping), the EOMs can be decoupled. Hence, the numerical evaluation of dynamic responses of linear systems can be easily solved using mode superposition methods without too much computation if there are only few modes being excited with proportional damping.

However, for nonlinear systems, the global stiffness matrix is displacement dependent. Hence, there is no such constant linear mode shape vector set to decouple the EOMs. To address this problem, both explicit and implicit directly integration methods can be used.

Explicit methods, such as Runge-Kutta mehtods and the central difference method, are extrapolation methods as the acceleration of next time step $t + \Delta t$ is not used. Thus they easily lose stability. The explicit method is efficient because there is no need to compute and invert the tangent system dynamic matrices at every time step [65]. But the so-called Courant stability criterion [68] depicts the largest time step allowed for stable integration equals the minimum time for an elastic wave to pass the the smallest meshed element size. Hence, in some cases, explicit methods require very small time steps which the total computing time is also very large.

Implicit methods, such as the Newmark-β method, Wilson-θ and generalized-α method, are interpolation methods as the acceleration of next time step $t + \Delta t$ is

used. Thus they can be unconditionally stable if appropriate parameters are selected. Furthermore, the time step of implicit methods are controlled by the the accuracy consideration, thus large time steps can be used with low accuracy requirement [65]. However, the computing cost for a time step of implicit methods is often ten to a thousand times for that of explicit methods as the matrix factorization, large computer storage and many operation are needed to get the transient system dynamic matrices. Hence, an appropriate time step size is very important and depends on the mesh size of FEM. Among all the implicit methods, the Newmark-β method is the most popular one considering the unconditional stability and time efficiency, which is used for TTR dynamic response prediction and detailed in this section [65, 67].

3.2.5 Newmark-β method

The equations of motion for a nonlinear system at time step t is as follows:

$$[\mathbf{M}]\,\ddot{\mathbf{u}}_\mathbf{t} + [\mathbf{C}]\,\dot{\mathbf{u}}_\mathbf{t} + [\mathbf{K}]_\mathbf{t}\,\mathbf{u}_\mathbf{t} = \mathbf{F}_\mathbf{t} \tag{3.22}$$

where $[\mathbf{M}], [\mathbf{C}], [\mathbf{K}]_\mathbf{t}$ and $\mathbf{F}_t$ are displacement dependent. $\mathbf{u}_t$ is the displacement vector at time t.

Expanding the time step t to the next step $t + \Delta t$, the displacement, velocity, acceleration and force vectors can be described as

$$\begin{aligned}
\mathbf{u}_{\mathbf{t}+\boldsymbol{\Delta}\mathbf{t}} &= \mathbf{u}_\mathbf{t} + \boldsymbol{\Delta}\mathbf{u}_\mathbf{t} \\
\dot{\mathbf{u}}_{\mathbf{t}+\boldsymbol{\Delta}\mathbf{t}} &= \dot{\mathbf{u}}_\mathbf{t} + \boldsymbol{\Delta}\dot{\mathbf{u}}_\mathbf{t} \\
\ddot{\mathbf{u}}_{\mathbf{t}+\boldsymbol{\Delta}\mathbf{t}} &= \ddot{\mathbf{u}}_\mathbf{t} + \boldsymbol{\Delta}\ddot{\mathbf{u}}_\mathbf{t} \\
\mathbf{F}_{\mathbf{t}+\boldsymbol{\Delta}\mathbf{t}} &= \mathbf{F}_\mathbf{t} + \boldsymbol{\Delta}\mathbf{F}_\mathbf{t}
\end{aligned} \tag{3.23}$$

Substituting equation 3.23 into equation 3.22 leads to:

$$[\mathbf{M}]\,\boldsymbol{\Delta}\ddot{\mathbf{u}}_\mathbf{t} + [\mathbf{C}]\,\boldsymbol{\Delta}\dot{\mathbf{u}}_\mathbf{t} + [\mathbf{K}]_\mathbf{t}\,\boldsymbol{\Delta}\mathbf{u}_\mathbf{t} = \boldsymbol{\Delta}\mathbf{F}_\mathbf{t} \tag{3.24}$$

where $[\mathbf{M}], [\mathbf{C}]$ and $[\mathbf{K}]_{\mathbf{t}}$ are mass, damping and tangent stiffness matrices at time t. In addition, force increment at time t equals

$$\boldsymbol{\Delta}\mathbf{F}_{\mathbf{t}} = \mathbf{F}_{\mathbf{t}+\boldsymbol{\Delta}\mathbf{t}} - [\mathbf{M}]\,\ddot{\mathbf{u}}_{\mathbf{t}} - [\mathbf{C}]\,\dot{\mathbf{u}}_{\mathbf{t}} - [\mathbf{K}]_{\mathbf{t}}\,\mathbf{u}_{\mathbf{t}} \tag{3.25}$$

Usually, if the riser mass is not changing during the simulation, mass matrix is a constant matrix. In the TTR dynamic response predictions, added masses are considered to be constant so that the mass matrix is constant. As the hydrodynamic damping force is considered as a loading, the damping matrix is considered to be constant. Thus, only the global stiffness is considered to be displacement dependent, and loading vector depends on displacement and external loading time history.

According to Newton's law, $\dot{u}_{t+\Delta t} = \dot{u}_t + \ddot{u}_t \Delta t$ if the acceleration $\ddot{u}_t$ is a constant during time period $[t, t+\Delta t]$. However, the acceleration is varying. To solve the problem, an interpolation scheme is used in Newmark-β method as shown in the following equation:

$$\begin{aligned} \dot{\mathbf{u}}_{\mathbf{t}+\boldsymbol{\Delta}\mathbf{t}} &= \dot{\mathbf{u}}_{\mathbf{t}} + \left[(1-\alpha)\,\ddot{\mathbf{u}}_t + \alpha\ddot{\mathbf{u}}_{t+\Delta t}\right]\Delta t \\ \mathbf{u}_{\mathbf{t}+\boldsymbol{\Delta}\mathbf{t}} &= \mathbf{u}_{\mathbf{t}} + \dot{\mathbf{u}}_{\mathbf{t}}\boldsymbol{\Delta}\mathbf{t} + \left[\left(\frac{1}{2}-\beta\right)\ddot{\mathbf{u}}_t + \beta\ddot{\mathbf{u}}_{t+\Delta t}\right]\Delta t^2 \end{aligned} \tag{3.26}$$

where α and β are constants selected in Newmark-β method to ensure its accuracy and stability.

After series of derivation, the incremental displacement $\Delta\mathbf{u}_t$ can be obtained as

$$\left[\bar{\mathbf{K}}\right]_{\mathbf{t}}\boldsymbol{\Delta}\mathbf{u}_{\mathbf{t}} = \Delta\bar{\mathbf{F}}_{\mathbf{t}} \tag{3.27}$$

where

$$\begin{aligned} \left[\bar{\mathbf{K}}\right]_{\mathbf{t}} &= [\mathbf{K}]_{\mathbf{t}} + \frac{1}{\beta\Delta t^2}[\mathbf{M}] + \frac{\alpha}{\beta\Delta t}[\mathbf{C}] \\ \boldsymbol{\Delta}\bar{\mathbf{F}}_{\mathbf{t}} &= \left(\mathbf{F}_{\mathbf{t}+\boldsymbol{\Delta}\mathbf{t}} - [\mathbf{M}]\,\ddot{\mathbf{u}}_{\mathbf{t}} - [\mathbf{C}]\,\dot{\mathbf{u}}_{\mathbf{t}} - [\mathbf{K}]_{\mathbf{t}}\,\mathbf{u}_{\mathbf{t}}\right) \\ &+ [\mathbf{M}]\left(\frac{1}{2\beta}\ddot{\mathbf{u}}_{\mathbf{t}} + \frac{1}{\beta\Delta t}\dot{\mathbf{u}}_{\mathbf{t}}\right) + [\mathbf{C}]\left[\left(\frac{\alpha}{2\beta}-1\right)\ddot{\mathbf{u}}_{\mathbf{t}}\Delta t + \frac{\alpha}{\beta}\dot{\mathbf{u}}_{\mathbf{t}}\right] \end{aligned} \tag{3.28}$$

Subsequently, the the incremental velocity and acceleration, $\Delta\dot{\mathbf{u}}_t$ and $\Delta\ddot{\mathbf{u}}_t$ can be obtained by

$$\begin{aligned} \boldsymbol{\Delta}\ddot{\mathbf{u}}_t &= -\frac{1}{2\beta}\ddot{\mathbf{u}}_t - \frac{1}{\beta\Delta t}\dot{\mathbf{u}}_t + \frac{1}{\beta\Delta t^2}\Delta\mathbf{u}_t \\ \boldsymbol{\Delta}\dot{\mathbf{u}}_t &= \left(1 - \frac{\alpha}{2\beta}\right)\ddot{\mathbf{u}}_t - \frac{\alpha}{\beta}\dot{\mathbf{u}}_t + \frac{\alpha}{\beta\Delta t}\Delta\mathbf{u}_t \end{aligned} \tag{3.29}$$

3.2.5.1 Newton-Raphson's Iteration

According to equation 3.23 and 3.29, the dynamic responses at time step $t + \Delta t$ can be obtained. However, as the actual motions between time step t and $t + \Delta t$ are not necessarily linear, Newmark-β method is based on the interpolation which is essentially a linear assumption. Single iteration may introduce too large simulation error. Thus, Newton-Raphson's iterations are needed to retain the accuracy.

$$\begin{aligned} \mathbf{u_{t+\Delta t}} &\Leftarrow \mathbf{u^{j}_{t+\Delta t}} = \mathbf{u^{j-1}_{t+\Delta t}} + \delta\mathbf{u}^j_t \\ \dot{\mathbf{u}}_{\mathbf{t+\Delta t}} &\Leftarrow \dot{\mathbf{u}}^j_{\mathbf{t+\Delta t}} = \dot{\mathbf{u}}^{j-1}_{\mathbf{t+\Delta t}} + \delta\dot{\mathbf{u}}^j_t \\ \ddot{\mathbf{u}}_{\mathbf{t+\Delta t}} &\Leftarrow \ddot{\mathbf{u}}^j_{\mathbf{t+\Delta t}} = \ddot{\mathbf{u}}^{j-1}_{\mathbf{t+\Delta t}} + \delta\ddot{\mathbf{u}}^j_t \end{aligned} \tag{3.30}$$

As shown in Fig. 3.4, initial incremental displacement Δu^0_t is obtained using equation 3.27 and 3.28. Then the iterative incremental displacement δu^j_t is obtained using equation 3.27 and 3.28 after updating $\left[\bar{\mathbf{K}}\right]_t$ and $\Delta\bar{\mathbf{F}}_{\mathbf{t}}$ at each iteration.

The iteration stops when the maximum allowable iterations are reached or satisfies the convergence criterion [65]:

$$\frac{\left\|\delta\mathbf{u}^{\mathbf{j}}_{\mathbf{t}}\right\|_2}{\left\|\boldsymbol{\Delta}\mathbf{u}^{\mathbf{j}}_{\mathbf{t+\Delta t}}\right\|_2} \leq \epsilon \tag{3.31}$$

where the tolerance $\epsilon << 1$. In this study, $\epsilon = 1 \times 10^{-5}$ is selected.

For linear system, Newmark-β is unconditionally stable if $\alpha \geq \frac{1}{2}$ and $\beta \geq \frac{1}{4}\left(\alpha + \frac{1}{2}\right)^2$. By choosing $\alpha = \dfrac{1}{2}$ and $\beta = \dfrac{1}{4}$, Newmark-β method becomes the average-acceleration

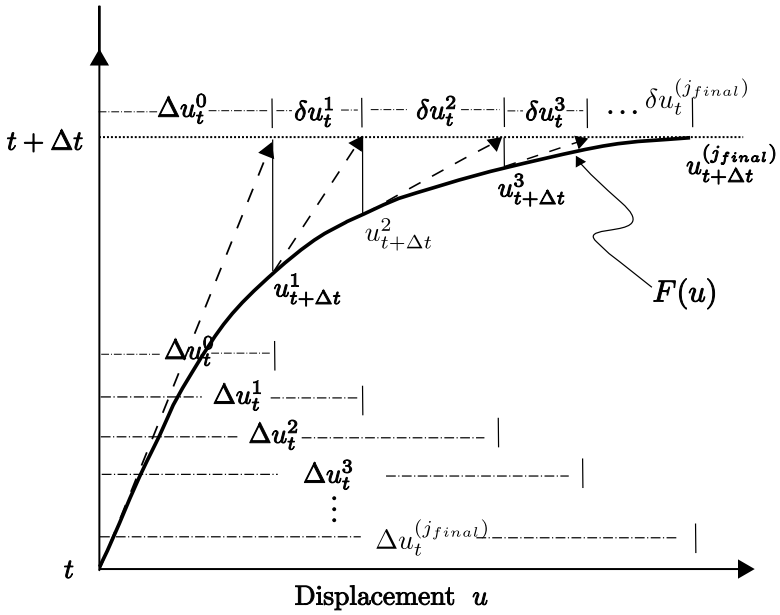

Figure 3.4 : Schematic of Newton-Raphson Iteration

method. The only limitation for nonlinear analysis using the constant-acceleration method is the time step size are determined by the accuracy. When $\alpha = \frac{1}{2}$ and $\beta = \frac{1}{6}$ are chosen. The Newmark-β method becomes the linear-acceleration method. The simulation is conditionally stable when the time step is less than the half of the minimum period. In this study, the average-acceleration is chosen to ensure unconditionally stable solution.

3.2.6 The Strategy for Numerical Simulations

As shown in Fig. 3.5, numerical simulations are started with initial settings including the material properties, geometric properties and current profile. Then with initial conditions, all the system matrices $[\mathbf{M}], [\mathbf{C}], [\mathbf{K}]_\mathbf{t}$ and final global incremental stiffness matrix $\left[\bar{\mathbf{K}}\right]_\mathbf{t}$ are obtained using the following steps.

The key response integrations are carried out with two Newmark-β integration

parts. The first part is to integrate the van der Pol oscillator equations with the previous step (t_i) motions of corresponding TTR segments (elements) as initial conditions, and obtain van der Pol status update of the FSI interaction forces applied on the corresponding TTR segments (elements) at current(t_{i+1}) time step. The Newton-Raphson iteration for this step is omitted to increase computing efficiency. As long as the current profile doesn't change, the omittance will not affect the final results because van der Pol wake oscillators ($q(t)$) will converge to a sine-wave like signal as in Fig. 3.1. This part also serves as the starting step for the second part in which the convergence criterion is satisfied by the Newton-Raphson iterations.

The second part includes Newmark-β integration as well as Newton-Raphson iteration. The detailed steps are

1. Start with the global incremental FSI forces estimation $\Delta\bar{\mathbf{F}}_{\mathbf{t}}$ using equation 3.27, based on the global FSI forces estimated using van der Pol oscillator in the first part;

2. Estimate the initial incremental displacements, velocities and accelerations at current time step (t_i), $\boldsymbol{\Delta}\mathbf{u}_{\mathbf{i}}^{(\mathbf{j=1})}, \boldsymbol{\Delta}\dot{\mathbf{u}}_{\mathbf{i}}^{(\mathbf{j=1})}, \boldsymbol{\Delta}\ddot{\mathbf{u}}_{\mathbf{i}}^{(\mathbf{j=1})}$ using equation 3.29;

3. Re-evaluate the global incremental stiffness matrix, $\left[\bar{\mathbf{K}}\right]^{(\mathbf{j})}$, as well as global incremental FSI force vector, $\boldsymbol{\Delta}\bar{\mathbf{F}}_{\mathbf{i}}^{(\mathbf{j})}$ using equation 3.28. Obtain incremental motion vector $\delta\mathbf{u}_{\mathbf{i}}^{(\mathbf{j+1})}$ in Newton-Raphson iteration using $\boldsymbol{\Delta}\bar{\mathbf{F}}_{\mathbf{i}}^{(\mathbf{j})} = \left[\bar{\mathbf{K}}\right]^{(\mathbf{j})}\delta\mathbf{u}_{\mathbf{i}}^{(\mathbf{j+1})}$;

4. With $\delta\mathbf{u}_{\mathbf{i}}^{(\mathbf{j+1})}$ and $\boldsymbol{\Delta}\mathbf{u}_{\mathbf{i}}^{(\mathbf{j})}$, check whether $\dfrac{\left\|\delta\mathbf{u}_{\mathbf{i}}^{(\mathbf{j+1})}\right\|_2}{\left\|\boldsymbol{\Delta}\mathbf{u}_{\mathbf{i}}^{(\mathbf{j})}\right\|_2} \leq \epsilon$ is satisfied or if iteration number j is greater than the maximum allowed iteration cycles, it_{max}:

   (a) If the answer is **YES** for either question, then the Newton-Raphson iteration is stopped. The final motion vectors at time step t_{i+1} are determined

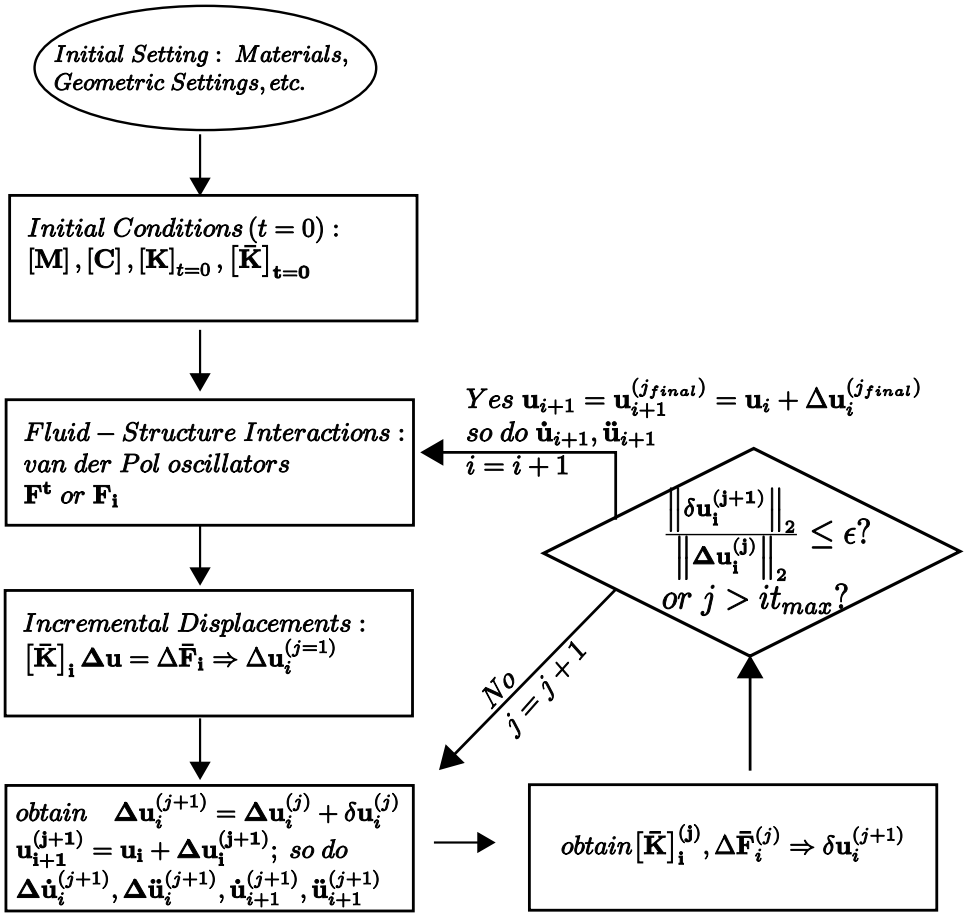

Figure 3.5 : Flowchart for Numerical Simulation

by $\mathbf{u_{i+1}} = \mathbf{u_{i+1}^{(j_{final})}} = \mathbf{u_i} + \mathbf{\Delta u_i^{(j_{final})}}$; update $\mathbf{\dot{u}_{i+1}}$ and $\mathbf{\ddot{u}_{i+1}}$ using equation 3.30. Global time step increases by one, $i = i + 1$. Go to step 1.

(b) If the answer is **NO** for both questions, then the Newton-Raphson iteration continues. Incremental displacement vector for next Newton-Raphson iteration is obtained by $\mathbf{\Delta u_i^{(j+1)}} = \mathbf{\Delta u_i^{(j)}} + \delta \mathbf{u_i^{(j+1)}}$ and global displacement vector $\mathbf{u_{i+1}^{(j+1)}} = \mathbf{u_i} + \mathbf{\Delta u_i^{(j+1)}}$. Then update $\mathbf{\Delta \dot{u}_{i+1}^{(j+1)}}$, $\mathbf{\Delta \ddot{u}_{i+1}^{(j+1)}}$, $\mathbf{\dot{u}_{i+1}^{(j+1)}}$ and $\mathbf{\ddot{u}_{i+1}^{(j+1)}}$ using equation 3.29. Newton-Raphson iteration number increase by one, $j = j + 1$. Go to step 3 and re-do evaluation and tolerance check, until either criterion is

satisfied.

5. End the simulation when the final time step is done.

3.3 Model Verifications of the Proposed FEM Model

Before using the predicted dynamic responses for later study on structural health monitoring, verifications of the model are carried out. Numerical simulations are carried out using the above described FEM model and solution method. Both DNS based numerical and experimental results are used to verify the proposed FEM model.

3.3.1 Numerical Verification - Direct Numerical Simulation (DNS)

A DNS simulation of vortex-induced vibration (VIV) for TTR with a very large aspect ratio ($\Lambda = \frac{L}{D} = 2028$) was performed by Lucor et al. [69]. In the model, TTR is modeled as simply supported beam. A linearly sheared current profile with 70% velocity variation of maximum current velocity was used as incoming current profile. The corresponding Reynolds number for maximum current velocity was $Re = 1000$. Strouhal number is set to be 0.2. Mass ratio (total mass density of TTR v.s. displaced fluid mass) was 2.785. Parameter B_d corresponding to bending stiffness (EI) was 91,809, while parameter T_s corresponding to top tension was 556.96. The root mean square (RMS) values of the displacements from DNS is shown in figure 3.7(a). Detailed parameters are shown in Table 3.1.

3.3.1.1 Parameters Adapted from DNS Model to FEM model

According to equations of motion for FDM model in the previous chapter, $B_d = \frac{EI}{(m+m_a)\,\Omega_{ref}^2 D^4}$, and $T_s = \frac{T_{top}}{(m+m_a)\,(\Omega_{ref} D)^2}$. Assuming the diameter of riser,

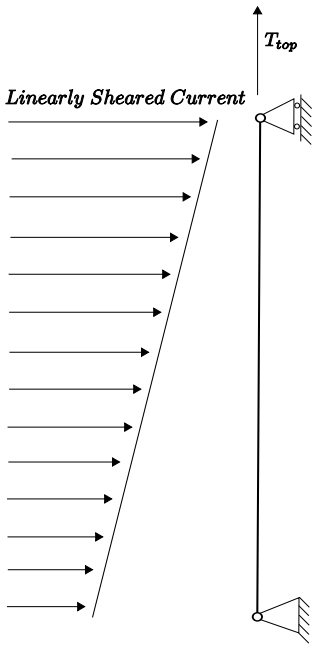

Figure 3.6 : Pin-Roller Riser with Top Tension and Sheared Current Loading

Table 3.1 : Parameters of DNS Simulation

S_t	0.2	T_s	556.96
Λ	2028	Re	1000
μ	2.785	$\Delta U/U_{Max}$	0.7
B_d	91,809	Δt (s)	0.001

$D = 0.1m$, then the parameters such as top tension, current velocity, bending stiffness etc. can be derived. The hydrodynamic parameters are selected to be the same as previous chapter. All the parameters used in the proposed FEM model are shown in Table 3.2.

Table 3.2 : Parameters used in FEM Model

S_t	0.2	$T(N)$	4.8768×10^3	E (Pa)	9.21×10^9
D(m)	0.1	L (m)	202.8	I (m^4)	8.73×10^{-7}
$Area(m^2)$	$7.9 \times 10^{-}3$	U_{max}(m/s)	0.5	U_{min}(m/s)	0.15
C_{L0}	0.2	C_{D0}	0.2	ε	0.3
A	12	B	0.5	Δt(s)	0.002

3.3.1.2 Results Comparison

The RMS values for cross-flow VIV of FEM simulation are shown in Fig. 3.7(b). In the plot, x-axis denotes the relative amplitude (displacement v.s. diameter of riser); y-axis (z) denotes the relative height of riser (height v.s. diameter). The general RMS shapes from FEM simulations match with the results from DNS simulation, especially at the both ends. The amplitude and trends prove that at the both end the vibrations are closer to standing wave, while in the middle of TTR, the vibrations are closer to traveling wave. In summary, the FEM simulation provides satisfactory results.

3.3.2 Experimental Verification - Gulf Stream Field Test

To further evaluate the performance of the proposed FEM model, a comparison with field data from Gulf Stream 2006 test was carried out.

3.3.2.1 Parameters and Setup of Gulf Stream 2006 Test

Gulf Stream 2 (2006) scale riser model field test was carried out by Vandiver et al. [28] in offshore Miami. It was a 500-foot long riser model with 1.49 inches outer diameter

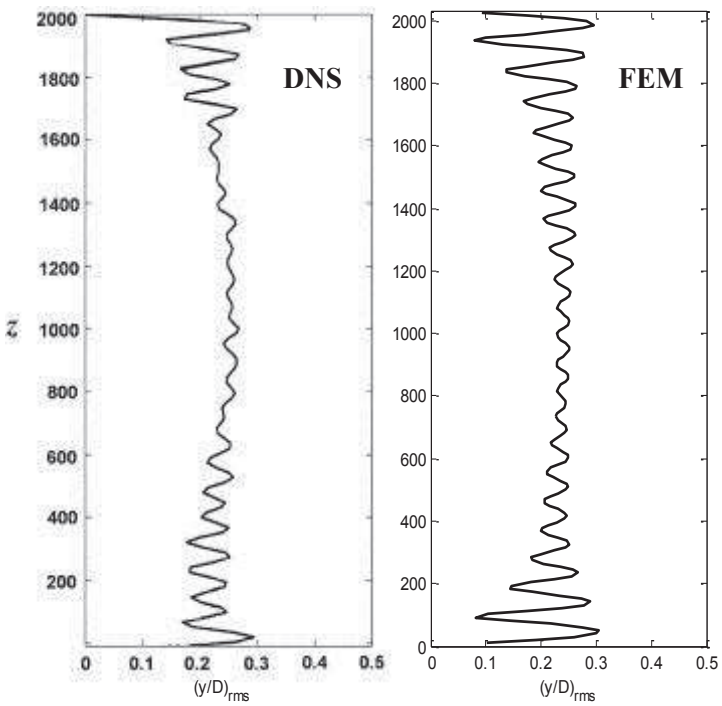

Figure 3.7 : Cross-Flow RMS Responses Comparison (DNS v.s. FEM)

and 0.09-inch wall thickness. The upper end was connected to a towing ship and at the lower end a 725 lb train wheel was hung to mimic a top-tensioned riser (TTR) as shown Fig. 3.8. There were eight fiber optical sensors in each 90-degree direction. Each fiber optical sensor had 35 brag gratings which measured the strains. As a result, there were 70 strain measuring locations for each direction (two in IL and two in CF). The corresponding parameters for the test pipe are included in Table 3.3.

3.3.2.2 Experimental Data Correction and Analysis

Quite a few tests with different current profiles and different riser surface conditions were carried out, and vibration response (strain) time histories were recorded. Among all the recorded events, "EVENT20061020174124" is a typical example of

Table 3.3 : Parameters of Gulf Stream Test Pipe

Inner Diameter	0.0249 m	Outer Diameter	0.0363 m
EI	613 Nm^2	Modulus of Elasticity, E	$9.21 \times 10^9 N/m^2$
EA	3.32×10^6 N	L	152.4 m
T_{top}	3225 N	Material	Fiber reinforced epoxy
Weight in Air	7.46 N/m	Weight in Water	1.924 N/m

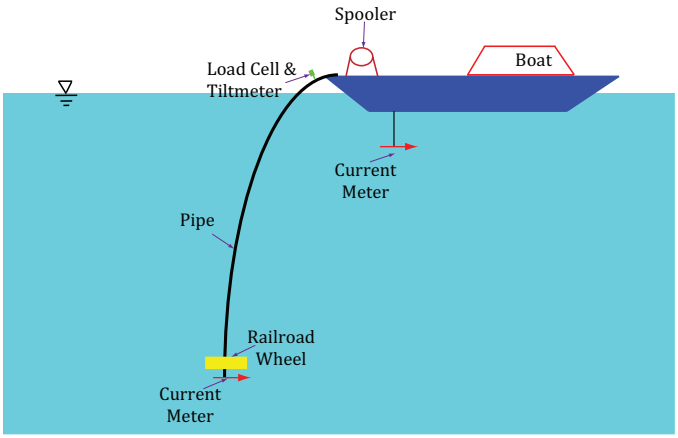

Figure 3.8 : Gulf Stream 2006 Test Setup

bare riser under sheared current excitation. The sheared current profile is shown as figure 3.9(a). The RMS values of measured strains of CF and IL directions are shown in figure 3.9(b). Q2 and Q4 are in CF direction, while Q1 and Q3 are in IL direction.

Generally, when VIV occurs, the cross-flow (CF) RMS amplitude is much larger-one to four times larger than the RMS amplitude of in-line (IL) direction. In the CF direction, the dominant frequency component is called as 1X frequency (or base frequency) [51] , and a third harmonic frequency component (also called as 3X where

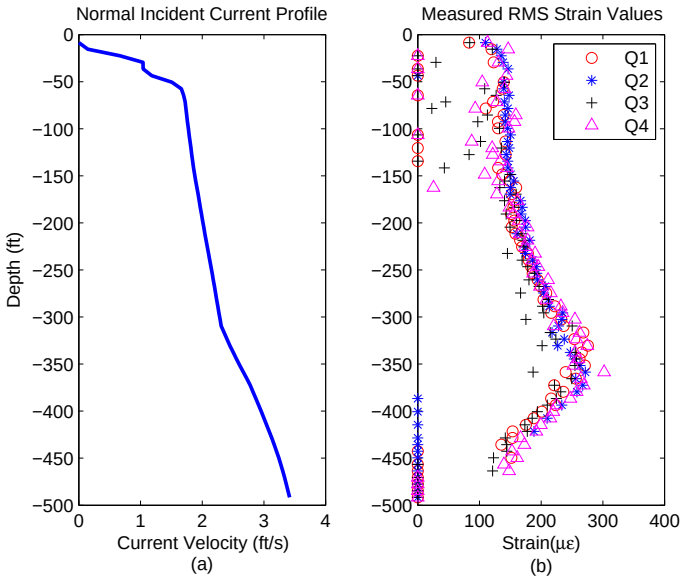

Figure 3.9 : Current Profile for Event 1020

the frequency is three times of the base frequency) caused by nonlinear vibration is also in CF direction, but with smaller amplitude. Conversely, 2X and 4X frequency components are the main parts of IL VIV. Unfortunately, during the manufacturing, the fibers were twisted 180 degrees all the way along the model riser [28]. Due to this manufacture error, the measured signals mixed cross-flow and in-line strains together, resulting in close amplitudes between IL and CF vibration and mixed frequency components in one direction, shown in upper plots of Fig. 3.11. To resolve this issue, a data rotation is needed.

The objective of the data rotation is to ensure that vibration in CF direction has the largest base vibration frequency, which is also called as 1X frequency [51] component. In the mean time, vibration in the IL direction will have no 1X frequency component. The data rotation is performed in following steps:

1. Treat the IL (Q1) and CF (Q2) direction strain measurements at each depth and

each time step as a two component vector, $S = [\epsilon_{IL}\ \epsilon_{CF}]^T$; Fourier transform to the each vector component time history to the frequency domain; Get the sum of frequency energy around the 1X frequency for Q2, as E_{Q2}

2. Rotate the vector by a certain angle, θ; The rotation is performed by multiplying the vector (S) with a transforming matrix, $T = \begin{bmatrix} \cos\theta & \sin\theta \\ -\sin\theta & \cos\theta \end{bmatrix}$ [70, 71];

3. Re-do the frequency analysis to the rotated vector and get the new sum of frequency amplitudes around the 1X frequency for Q2, as E_{temp};

4. If $E_{temp} > E_{Q2}$, then $E_{Q2} = E_{temp}$, $\alpha = \theta$;

5. Repeat step (2) to (4) by iterating rotation angle θ from 0 ot π; Final α is the proper rotation angle for vector at the corresponding depth

For "EVENT20061020174124", the final rotation angles for each depth are plotted in Fig. 3.10. The circles represent the calculated rotation angles for each depth. The linear fitted line in the center range confirms the 180-degree fiber twist.

The further rotation effect is shown in Fig. 3.11 for sensor measurements at depth 315 ft. Comparing the frequency spectra of IL (Q1) direction before and after rotation, the 1X frequency component is gone and amplitudes of 2X and 4X components are increased. Similarly the amplitude of 1X and 3X frequency components in the CF (Q2) direction are increased. However, the higher frequency component, 2X (twice the frequency value of 1X frequency) remains in the CF direction.

The unchanged higher frequency components lead to the similar amplitude of RMS values in IL and CF direction, shown in Fig. 3.12. The vector shapes of the RMS plots remain the same before and after the rotation. Thus, a further separation in the frequency domain is needed to separate the 1X frequency [51] component in CF

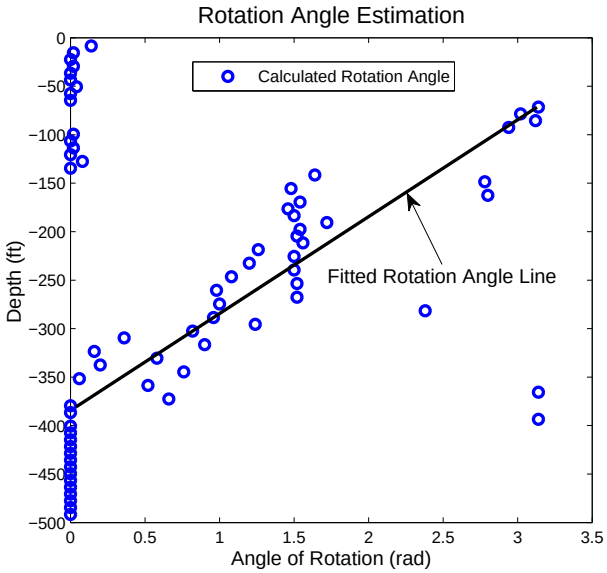

Figure 3.10 : Rotation Angle Estimation

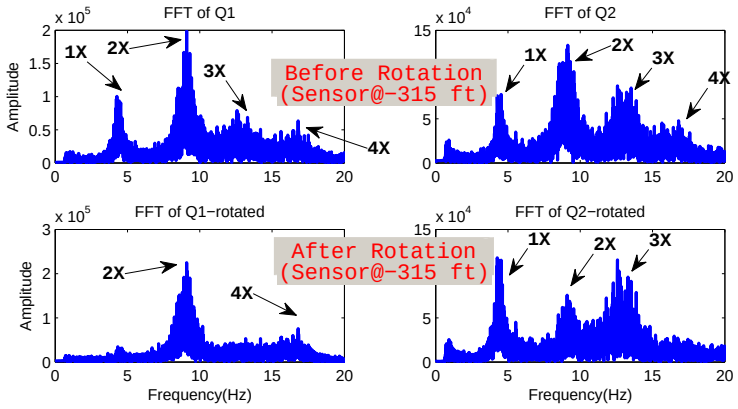

Figure 3.11 : Frequency Comparison before and after Rotation - 315 ft

direction and 2X frequency component in IL direction. The simulated results from proposed FEM model will be verified by the 1X component as well as 2X component in frequency domain. Similarly, the RMS values of rotated measured strains are compared with curvature from simulated results.

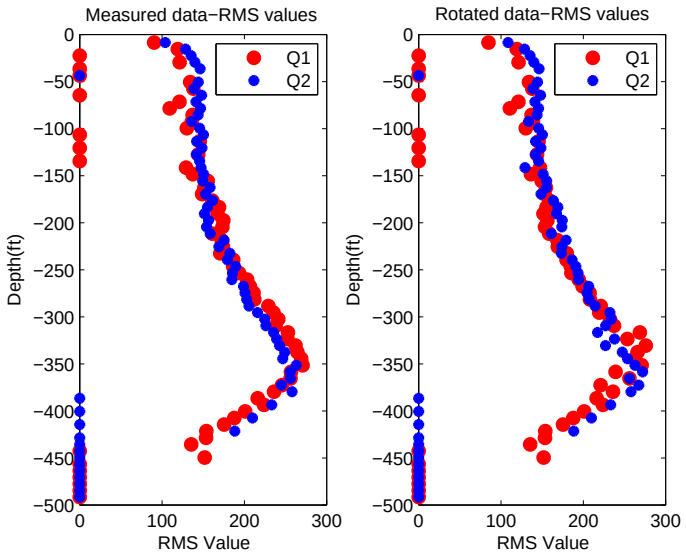

Figure 3.12 : RMS Comparison before and after Rotation

3.3.2.3 Comparison between Experimental and Predicted Results

The 1X CF responses from field test was obtained by filtering out the higher frequency components. RMS values of 1X strain values are shown in figure 3.13, labeled as "EXP-1X" using "*" symbol. The simulated results are labeled as "FEM" with solid line. The strain shape from simulation matches with the measured 1X strain shape, which proves the effectiveness of proposed model. In addition, the similar noisy peaks in the frequency spectra at depth -420 ft of TTR from both FEM and EXP-1X further verify the proposed FEM model.

On the other direction, as shown in figure 3.14, the 2X IL responses from field test has almost the same amplitude as the amplitude of 1X CF responses. This unusual phenomenon causes the mis-match between the 2X IL peak locations and simulated IL peak locations. The main possible reason is the twisted fiber optical sensor. Another reason may be the high Poisson's ratio for glass fiber epoxy material, which can be

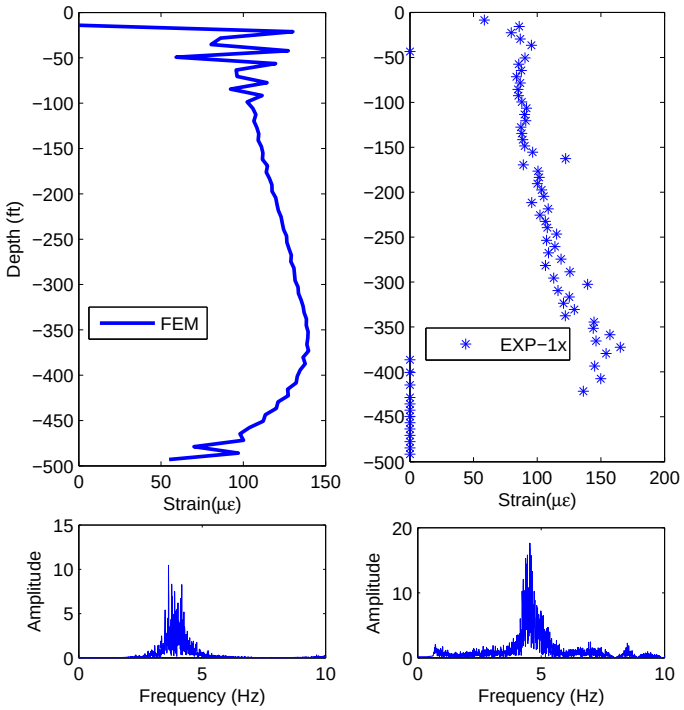

Figure 3.13 : Comparison between EXP-1X v.s. FEM (CF)

as high as 0.32. In the frequency domain, similarly to the CF direction, the noisy frequency spectrum at depth -420ft of TTR from simulated results shows a similar trend as the 2X IL responses at the same depth.

Figure 3.13 and 3.14 prove that the proposed FEM is consistent with field test data in the CF and IL direction. Though there are minor differences in the IL direction, the proposed FEM model is satisfactory.

3.4 Summary

To account for the drawbacks of finite difference method (FDM) using Green-Lagrange strains, this chapter presented a new analytical finite element method (FEM) model

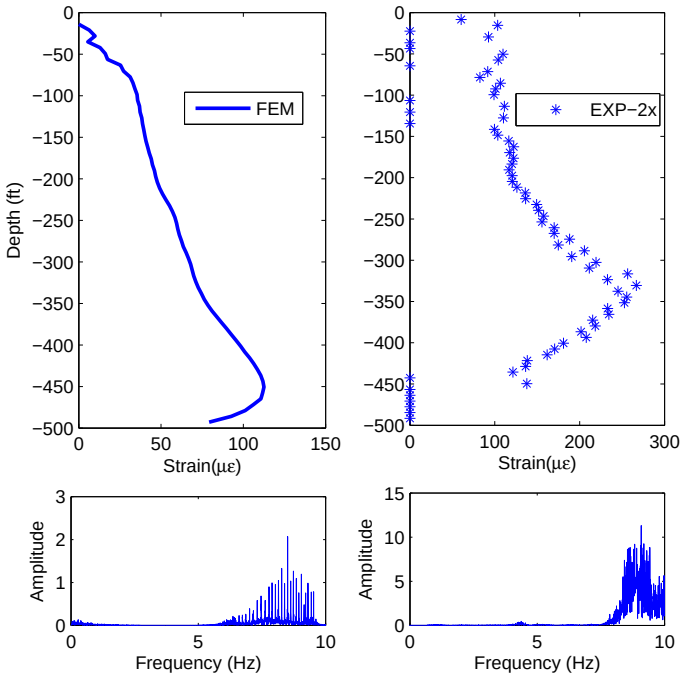

Figure 3.14 : Comparison between EXP-2X v.s. FEM (IL)

for TTR using Jaumann strains with modified von Kármán nonlinearity.

1. The time and dimensional scalings were eliminated using the methods mentioned to get the actual fluid structure interactions on both van der Pol wake oscillators and TTR segments.

2. Detailed FEM nonlinear Euler-Bernoulli beam element was studied.

3. The average acceleration method (Newmark-β) with Newton-Raphson iteration method and the programming strategy were detailed.

4. Both numerical and experimental verification proved the effectiveness of the proposed FEM model in predicting the riser VIV responses.

To summarize, the dynamic response prediction using the proposed FEM model is a satisfactory method. Further damage detection can use the predicted responses from the damaged TTR model.

Chapter 4

Blind Identification - Output Only Analysis

Previous two chapters provide details about two different approaches to solve the proposed 3D analytical model for deepwater risers, which essentially solve the forward problem. The forward problem aims to estimate the riser responses from given current profile, riser status (configuration and damage information). Next step will be the inverse problem, with the aim to estimate or estimate damages from the measured (or simulated) response of the riser, which is the key object for SHM systems. The inverse problem contains two parts: one is to identify the current dynamic properties of the riser from the measured response; the other is to estimate the riser health/damage status by comparing the current dynamic properties with that of the healthy condition. This chapter presents the identification algorithms.

It is very difficult to measure excitations (actual hydrodynamic fluid structure interaction (FSI) forces) of deepwater risers. As a result, the structural health monitoring system for deepwater risers needs to focus on output only identification techniques.

This output only identification is also needed in large scale on shore structures, such as long span bridges, where the excitation measuring is difficult. Researchers have developed innovative sensor technologies, such as fiber optical sensors [72] and wireless sensor network [73, 74]. Researchers have developed output only identification and damage estimation algorithms for long span bridges, such as Frequency Domain Decomposition Algorithm (FDD) [24], Eigensystem Realization Algorithm

(ERA) [26]. This chapter focuses on finding more reliable real-time system identification methods to estimate damages more accurately. The searching leads this study to an inter-disciplinary field, blind source separation.

4.1 Review of Blind Identification

Blind Source Separation (BSS) is a statistical signal processing technique, which attempts to recover the individual unknown but statistically independent source components from mixed signals (measurements). The mixing process is shown as equation 4.1, where vector $\mathbf{x}$ represents the mixed signals, matrix $\mathbf{A}$ is the linear mixing matrix and vector $\mathbf{s}$ represents the independent source components.

$$\mathbf{x} = \mathbf{A}\mathbf{s} \tag{4.1}$$

The original problem for BSS can be referred to as the 'cocktail-party problem' defined by Cherry in the 1953 [75] about the analogy of human ears in differentiating what another person is speaking when quite a few people are speaking at the same time. BSS as a solution to the original problem was first proposed by French researchers in the early 1980s as a signal processing method [76]. But it only started to attract more attentions in the mid-90s. Since then, the applications of BSS have been reported in quite a few areas such as acoustics (cross-talk removal, hearing aids,airport surveillance etc.), biomedical image processing (EEGs and MEGs) [77], digital communications (multichannel equalization, multiuser separation etc.) [78], financial applications (stock predication and risk managements etc.) [79], geophysics [80], image processing and statistics [81]. This chapter explores the potential application of BSS in bridge SHM and provide theoretical and experimental verifications.

4.1.1 Independent Component Analysis

The most widely used technique to perform BSS is independent component analysis (ICA). Cardoso [82] was the first to extensively study ICA in 1889. However, it was Comon's formal definition of ICA that greatly promoted its development [83]. According to Comon, ICA is to search for a linear transformation that minimizes the statistical dependence between its non-gaussian components (sources). Later, Hyvarine further explored the theory and applications of FastICA [84]. He proposed to use one of the simplest definitions of the measure of non-gaussianity, kurtosis, which is the fourth order cumulant of an independent source signal, s, shown in equation 4.2. For a gaussian random variable, the kurtosis should be zero.

$$kurt(s) = E\left(s^4\right) - 3\left(E\left(s^2\right)\right)^2 \tag{4.2}$$

The main purpose of BSS is to differentiate independent sources, represented by s. According to equation 4.1, finding the mixing matrix A or the de-mixing matrix (inverse of the mixing matrix), W, will result in the original sources by multiplying the transpose of W on the left side of mixed signal x, as shown in equation 4.3.

$$\mathbf{s} = \mathbf{W^T x} \tag{4.3}$$

ICA can be executed by maximizing the absolute value of kurtosis of $\mathbf{W^T x}$ to get the instantaneous de-mixing matrix $\mathbf{W}$. However, due to the assumption of non-gaussian sources and higher statistical independency requirements, there are a few drawbacks for the application of ICA to Civil engineering. Higher statistical independency usually requires better measured signal, which is expensive. Furthermore, damping is the key factor influencing the identification results. ICA was first used as an output only system identification method by Poncelet et. al in 2007 [85]. Though

the paper showed promising results in half the random vibration experiments, it didn't mention that lightly damped system was a critical requirement to have good identification results. Kershcen et al. [86] proved that FastICA can only generate good results in light damped system (below 1% damping ratio).

4.1.2 Second Order Blind Identification

To address the limitations of ICA, a lower order statistical independency method without light damping limitation is needed for output only system identification in bridge SHM. Within the BSS methods, there are principle component analysis (PCA) and second order blind identification (SOBI) algorithms which are based on the second order statistical independency. However, several factors constrain PCA's applicability. First, the measured data contains measured and process noises; second, the modal damping is nonzero (usually not light damping); third, the mode shapes are not directly orthogonal to each other (but mass orthogonal); fourth is that PCA cannot differentiate the corresponding eigenvectors for repeated eigenvalues [87]. All those factors lead to the result that SOBI is the suitable method to identify the sources from measured signals from bridge SHM system.

For a noisy model like bridge structures, there is a need to add an additional noise term ,δ, on the right side of the equation 4.1. This modification is shown in equation 4.4.

$$\mathbf{x} = \mathbf{A}\mathbf{s} + \delta \tag{4.4}$$

ICA or PCA are always based on a model with independent sources and identically distributed variables. As a result, the sample order does not influence the identified results. On the other hand, SOBI takes the advantage of the temporally structure of the sources to enhance their separation [86]. Therefore, SOBI is an important

algorithm for sources with different spectral contents, such as signals in structural dynamics. SOBI is entirely based on the second order statistics as the input signals are pre-processed as time-lagged covariance matrix functions [87]. The noise is assumed to be stationary and temporally white noise, which is independent from the source signal. As result, $E\left(\mathbf{As}\cdot\delta^{*}\right)=0$. The covariance matrices can be calculated as the following equation:

$$\mathbf{R_x}\left(\tau\right)=E\left\{x\left(t\right)x\left(t+\tau\right)^{*}\right\}=E\left\{\mathbf{As}\left(\mathbf{As}\right)^{*}\right\}+E\left(\delta\delta^{*}\right)=E\left\{\mathbf{As}\left(\mathbf{As}\right)^{*}\right\}+\boldsymbol{\delta^{2}} \quad (4.5)$$

where superscript * represents the conjugate transpose, τ denotes a time shift and signal x denotes the centralized signal by removing the mean values for each channel.

SOBI utilizes a joint approximate diagonalization (JAD) [86] method to obtain a joint diagonalizer, Ψ, which is an orthogonal matrix. Ψ is obtained by minimizing the off diagonal terms of $\Psi^{T}R_{x}\left(\tau\right)\Psi$ for several $R_{x}\left(\tau\right)$. Then the joint diagonalizer ,Ψ, combined with whitening matrix, $\mathbf{W_m}$, are used to derive the de-mixing, $\mathbf{W}$, and mixing matrix, $\mathbf{A}$, as shown in the following equation.

$$\begin{aligned}\mathbf{W}&=\boldsymbol{\Psi}^{\mathbf{T}}\mathbf{W_m}\\ \mathbf{A}&=\mathbf{W_m^{-1}}\boldsymbol{\Psi}\\ \mathbf{W_m^{-1}}&=\mathbf{ED}^{\frac{1}{2}}\end{aligned} \quad (4.6)$$

where the whitening matrix is derived from the eigenvalue decomposition of $E\left(\mathbf{xx^{T}}\right)$ $=R_{x}\left(0\right)=\mathbf{EDE^{T}}$. In which, $\mathbf{E}$ is the orthogonal matrix of eigenvectors and $\mathbf{D}$ is the diagonal matrix of eigenvalues according to Poncelet et al. [85].

As shown in Figure 4.1, the procedure of SOBI can be divided into pre-processing, JAD analysis and modal analysis. Pre-Processing includes centering and whitening to ensure the unit variance. JAD is to find the de-mixing and mixing matrix for

given measured data. Finally modal analysis contains separation of the independent sources and identification of frequencies and damping ratio for each mode shape.

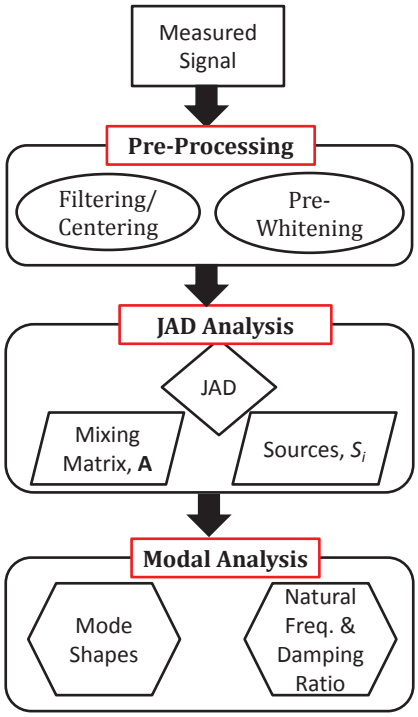

Figure 4.1 : Flowchart of SOBI

SOBI works well in simulation studies as all the modes can be excited numerically. However, for a large scale civil structure like long-span bridges, the higher modes of vibration are not easily excited. In addition, spatially un-correlated noise strongly influences the identified results. The measurement noise need separate treatment before introducing covariance function. Last but not the least, traditional SOBI can only identify as many sources as the number of sensors. It cannot guaranty as good estimation results when there are more sources than sensor numbers. To address these shortcomings, wavelet transform is introduced to SOBI to expand its capability in this study.

4.2 Wavelet Modified Second Order Blind Identification (WM-SOBI)

To obtain time and frequency properties of the propagating wave signals, time-frequency analysis has to be performed. There are many signal processing tools for time-frequency analysis. Short time Fourier transform (STFT) is one of the most popular techniques that map a signal into both time and frequency domains simultaneously. It provides information about the variation of frequencies as a function of time (spectrogram). However, the precision of the time-frequency information is limited by the size of the window. To overcome the limitations, wavelets have been used for modal identifications by Nagarajaiah and Basu [88]. Similar study has been carried out using stationary wavelet transform by Harza and Narasimhan [89]. But they did not fully study the further potential of wavelet transform in solving under-determinate problem. In this chapter, a different strategy with continuous wavelet transform (CWT) and the full potential of wavelet modified SOBI are studied.

4.2.1 Wavelet Coefficients and Sources

Wavelet transform has a variable-sized window which overcomes the shortcoming of STFT. The CWT is defined as

$$W(a,\tau) = \frac{1}{\sqrt{a}} \int_{-\infty}^{+\infty} x(t)\, \psi\left(\frac{t-\tau}{a}\right) dt \tag{4.7}$$

where $W(a,\tau)$ are the wavelet coefficients, a is the scale, $\psi(t)$ is the mother wavelet function, $x(t)$ is the origin signal, τ is the current time step. From the scalogram of the wavelet coefficients, we can easily find the scale range of interest by their amplitudes in the wavelet (time-frequency) domain.

For a chosen scale, j, the orthogonal continuous wavelet decomposition of mea-

sured signals can be discretized in terms of its decomposition coefficients as in the following equation:

$$x_i^j(t) = \sum_k g_{ki}^j \psi_k^j(t) \quad i = 1, 2, \cdots, N \tag{4.8}$$

where $\psi(t)$ is the chosen wavelet, and g_{ki}^j are the wavelet coefficients for scale j, sensor index i and the time shift index k. Similarly, the sources can also be processed using the same procedure, which results in the following equation:

$$s_i^j(t) = \sum_k f_{ki}^j \psi_k^j(t) \quad i = 1, 2, \cdots, N \tag{4.9}$$

where $s_i^j(t)$ is the ith source signal for scale j, and f_{ki}^j are the wavelet coefficients for scale j, source index i and the time shift index k. Inserting equation 4.8 and equation 4.9 into equation 4.1 and combining the orthogonality conditions for wavelets results in the equation:

$$g^m = \mathbf{A} f^m \tag{4.10}$$

where m is a selected scale for wavelet transform; $\mathbf{A} \in R^{N \times N}$ is the instantaneous mixing matrix for N sensors with assumption of N sources.

Equation 4.10 proves that transforming the time domain signal into time-frequency domain does not change the mixing matrix. The mixing matrix can be estimated using the wavelet coefficients instead of the originally measured noisy signals. This replacement can greatly increase the signal to noise ratio (SNR) as the widest application for wavelet is de-noising. Therefore, the first shortcoming for SOBI can be alleviated.

In addition, a certain scale of wavelet coefficients may only contain a few sources if not all of them. By choosing different scales for wavelet transformation, the identified sources can be different. This strategy can solve the dilemma of more sources than sensors as well as identify poorly excited modes.

4.2.2 Strategy for Wavelet Modification of SOBI

The wavelet modified SOBI can be divided into four steps instead of three steps. Details are as follows (see Figure 4.2).

- **Pre-Processing**: Including centering, de-trending or filtering to remove the offset and slope in the measured signals;

- **Wavelet modification**: Apply CWT to pre-processed signal, $Z(t)$ results in the wavelet coefficients, g_{ki}^{j}, in the time-frequency domain. Taking a certain scale of wavelet coefficients which contains important information about sources as the input signal for JAD. Usually, the dominant wavelet coefficients is the first choice. And then either iteration to the second dominant wavelet coefficients or manually choosing based on which higher mode (scale) need to be identified. Then whitening using eigenvalue decomposition of $R_{g^m}(0)$ to get the pre-whitened signal, $Y(t)$. It is the same procedure as SOBI.

- **JAD Analysis**: Apply Joint approximate diagonalization technique to the covariance matrices from the whitened wavelet coefficients, $Y(t)$, to get the joint diagonalizer,$\Psi(t)$. Then derive the de-mixing, $\mathbf{W}$, and mixing matrix, $\mathbf{A}$.

- **Modal Analysis**: Based on the de-mixing matrix, separate the measured signal to get the independent sources. If it is free vibration data, directly apply fast fourier transform (FFT) and exponential decay method to get the damped natural frequency $\omega_d = \omega_n\sqrt{1-\xi^2}$ and damping ratio, ξ. If it is ambient excited response, approximate free vibration sources are obtained by de-mixing the cross-correlation functions of measured signal.

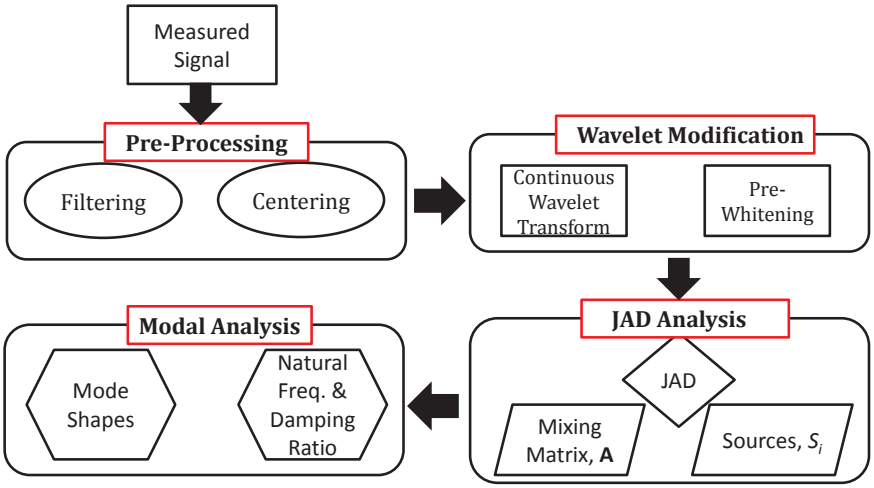

Figure 4.2 : Flowchart for Wavelet Modified SOBI.

4.2.3 Numerical Study for Wavelet Modified SOBI

To study and verify the proposed wavelet modified SOBI methods, numerical study is needed.

4.2.3.1 Numerical Model and Simulated Responses

A simply-supported bridge model is developed as shown in Figure **??**. Only vertical vibration is considered in the simulations. The stiffness of each span is $k_i = 1000N/m, i = 1, 2,...,9$, respectively. The model has nine equally lumped masses, $m_i = 10kg$. Damping is simplified as mass proportional damping, $\mathbf{C} = \alpha\mathbf{M}$, where $\alpha = 0.8$, which leads to damping starting at 12.78% for the first mode.

The bridge system is subjected to freely vibration due to initial displacement. Simulation is performed for 100 sec with 0.01 sec time step. To demonstrate the advantage of wavelet modified SOBI and the shortcoming of SOBI, only four nodal vibrations are measured, which are numbered as A1,A2, A3 and A4 in Figure 4.3.

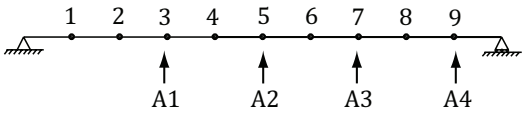

Figure 4.3 : A simply-supported bridge model

$$\mathbf{M}\ddot{\mathbf{X}} + \mathbf{C}\dot{\mathbf{X}} + \mathbf{K}\mathbf{X} = 0 \tag{4.11}$$

$$\mathbf{C} = \alpha\mathbf{M} \quad \alpha = 0.8$$

Figure 4.4(a) shows the free vibration response of the third node and Fig. 4.4(b) shows the frequency spectrum of third node vibration. Similarly, Fig. 4.4(c) and (d) show the vibration time history and frequency spectrum of the fifth node vibration, respectively. In Fig. 4.4(b) and (d), there are 9 different peaks that represent 9 possible natural modes. Next modal analysis comparing the results from eigensystem realization algorithm (ERA), SOBI and wavelet modified SOBI is presented.

4.2.4 Theoretical Results, ERA and SOBI

Theoretical results can be directly calculated from the original global stiffness and mass matrices. Mass proportional damping (Rayleigh damping) does not change the mode shapes from eigenvalue decomposition. The modal damping can be calculated using

$$\zeta_i = \frac{\alpha}{2\omega_i} \tag{4.12}$$

Since Juang and Papa [26] proposed ERA in 1985, ERA has been the most widely used output only modal analysis algorithm in civil engineering. ERA derives the mode shapes, natural frequencies and damping ratio from the eigenvectors and eigenvalues of Hankel matrix, which is constructed using cross-correlation functions of measured signals.

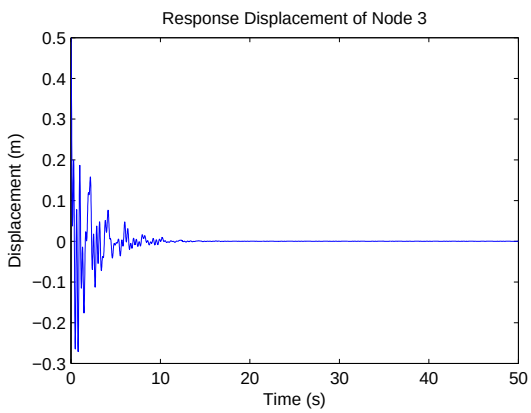

(a) Displacement Response of 3rd Node

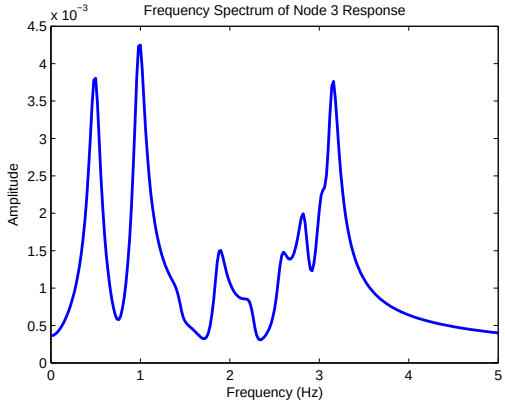

(b) Frequency Spectrum of 1st Node Response

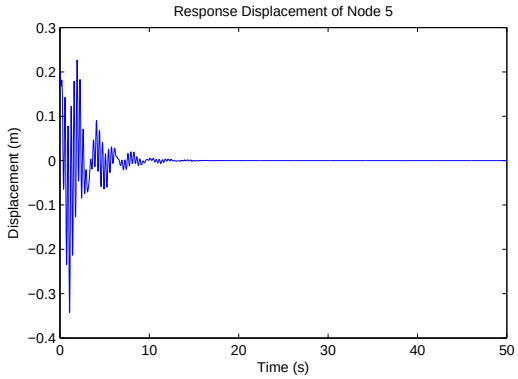

(c) Displacement Response of 5th Node

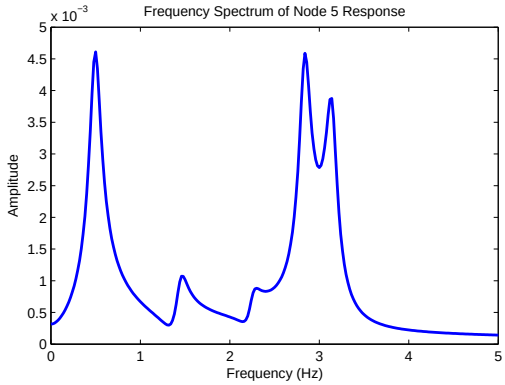

(d) Frequency Spectrum of 3rd Node Response

Figure 4.4 : Simulated Responses of Measured Nodes

4.2.4.1 Blind Identification using WMSOBI

To implement the proposed wavelet modified SOBI method, it is very important to know the structure one is dealing with. First, one should perform fast Fourier transform (FFT) of the measured responses to get the frequency range of primary structure. Then, according to the frequency range and sampling frequency of measurement, a suitable mother wavelet (such as 'Morlet') and a series of scales that correspond to the dominant frequencies are chosen. Then each scale of chosen wavelet coefficients

are processed using traditional SOBI. The sources de-mixed from SOBI process will be used to estimate the damped natural frequency (from the frequency domain of the obtained sourcees) and damping ratio (from the amplitude exponential decay curve of the sources).

Figure 4.4(b) indicates that the natural frequencies of the model bridge belong to range (0Hz, 3.5Hz). Morlet wavelet is chosen as the mother wavelet. The scale increment is chosen as 0.25. Maximum calculated scale is 3.62, which corresponding to 48.4Hz. The contour plot of the given scales' wavelet coefficients is shown in Figure 4.5. It is obvious that there are at least three peaks in the first few seconds. The dominant peak is around scale 1, which is corresponding to the 20th scale in the program. The second peak is around scale 2, which is corresponding to 16th scale. The third is around scale 0.38, the 27th scale. In addition, two other scales, 24th and 18th scale are also studied. The wavelet coefficients corresponding to above 5 scales are taken into processing using SOBI method.

The damped natural frequencies for SOBI and WMSOBI are identified by applying FFT to the separated sources. All the identified results are shown in Table 4.1. The table proves that even with only four-channel measurements, WMSOBI can identify all the modes. ERA can identify most of the modes. On the other hand, SOBI is limited by the number of sensors, four modes with the mixing matrix is assumed to be a square matrix. In addition, the recognized frequencies of WMSOBI are obviously more accurate than the results from SOBI compared to theoretical values. Comparing lower modes and unidentified modes from ERA, WMSOBI also shows better performance. Besides, the performance of ERA is strongly dependent on the choice of Hankel matrix size. Increasing or decreasing the size of Hankel matrix used in Table 4.1 may lead to different performance. On the other hand, multiple time steps

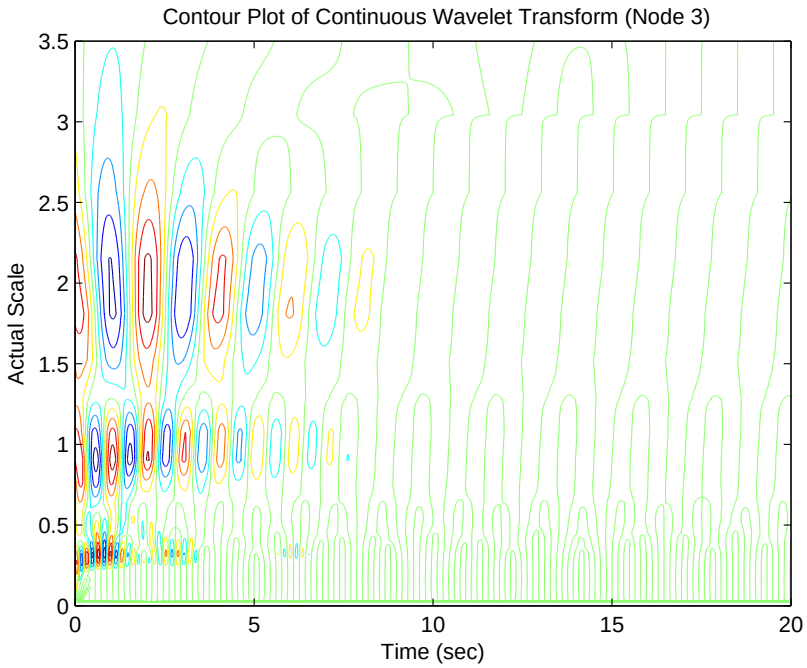

Figure 4.5 : Contour Plot of CWT Wavelet Coefficients from Node 3 with Chosen Scales

used in the JAD process of WMSOBI/SOBI makes the estimation more robust (as well as covariance matrix size smaller). Furthermore, the identified damping ratios from WMSOBI are more accurate than ERA and SOBI as well. Within the four shared modes, the maximum relative error to the theoretical value for ERA, SOBI and WMSOBI are 26.67%, 14.71% and 8.6%, respectively. Among all the nine modes, the maximum relative error for WMSOBI is 15.2% (Mode 5), much smaller than that of ERA,57.0% (Mode 9). The larger error from ERA is the result of higher damping because generally ERA is more accurate for lightly damped system. The fact that less number sensors as compared to the number of modes leads to the less accurate identification by SOBI than WMSOBI in both frequencies and damping ratios.

In addition, the CPU time for ERA always depends on the size of Hankel matrix as

Table 4.1 : Identified Results and Theoretical Values

	Theoretical		ERA		SOBI		WMSOBI	
Mode No.	Freq (Hz)	ζ (%)	Frequency (Hz)	ζ (%)	Freq (Hz)	ζ (%)	Freq (Hz)	ζ (%)
1	0.4979	12.7849	0.48/0.52	9.37	0.5000	10.90	0.5000	11.67
2	0.9836	6.4721	0.96/1.01	4.12	0.9799	6.50	0.9799	5.57
3	1.4451	4.4054	-	-	-	-	1.4599	5.89
4	1.8710	3.4026	1.8707	1.24	-	-	1.8698	3.12
5	2.2508	2.8284	-	-	-	-	2.2498	3.25
6	2.5752	2.4721	2.5716	0.95	2.5597	2.59	2.5797	2.38
7	2.8362	2.2447	2.8416	1.22	2.8297	2.56	2.8397	2.20
8	3.0273	2.1029	3.0268	1.05	-	-	3.0397	2.13
9	3.1439	2.0249	3.1488	0.87	-	-	3.1497	1.99
CPU Time (s)	-		1.64		0.15		0.33 per scale	

well as the length of the original signal. This dependency generally leads to more CPU time requirement as shown in Table 4.1. For WMSOBI, the CPU time corresponds to both the length of the original signal and how many scales of wavelet coefficients are selected for computation. In Table 4.1, each scale requires 0.33 sec computation CPU time; 5 of them lead to almost same CPU time as ERA in this study. However, if the length of the original signal and only the selected wavelet scales to be computed are fixed, the CPU time would be greatly reduced to as much as five times of the regular SOBI, which would be 0.75 sec in total.

Table 4.2 shows the identified results from WMSOBI in each selected scale. All the nine modal frequencies are identified by those five tests. The order number in

Table 4.2 : Identified Results from WMSOBI (5 scales)

Scale No.	16^{th}	18^{th}	20^{th}	24^{th}	27^{th}
Order No.	Test I	Test II	Test III	Test IV	Test V
1	0.5000	0.9799	1.8698	2.8397	3.1497
2	0.4500	0.5399	2.2498	3.1397	2.8397
3	0.5699	1.0199	1.4599	2.5697	3.0397
4	0.6799	0.8799	0.9899	3.0397	2.5797

column one of Table 4.2 represents the order of identified results. In general, the modes with larger participation factors in the wavelet coefficients of selected scale ranks higher. In other words, the first frequency of each test generally leads to the positive identification. In addition, if the theoretical or reference mode shapes and frequencies are known, the identified results can be verified using modal assurance criterion (MAC).

The MAC can be calculated using the equation below. ϕ_i, ψ_j represent the i^{th} mode shape from theoretical (reference) value and j^{th} mode shape from identified results. If the mode shapes are exactly the same, the MAC value is 1. On the other hand, if the mode shapes are independent to each other, the MAC value would be 0. This study takes the MAC values over 0.9 as a threshold criterion for identified mode shapes.

$$MAC_{ij} = \frac{\left(\phi_i^T \psi_j\right)^2}{\left(\phi_i^T \phi_i\right)\left(\psi_j^T \psi_j\right)} \tag{4.13}$$

The MAC values shown in Table 4.3 prove that WMSOBI can identify more accurate mode shapes as compared to ERA and SOBI methods. First, WMSOBI can identify more modes than SOBI and ERA, even the poorly excited modes like mode 3

and mode 5. Second, WMSOBI provides better mode shape estimation as compared to ERA for mode 8, 0.9897 v.s. 0.2777.

Table 4.3 : Comparison of Mode Assurance Criterion

Mode	Theoretical	ERA	SOBI	WMSOBI
1	1	1	0.9923	0.9992
2	1	0.9999	0.996	0.9906
3	1	-	-	0.7949
4	1	0.9997	-	0.9998
5	1	-	-	0.2671
6	1	0.9988	0.9185	0.9809
7	1	0.986	0.9933	0.9995
8	1	0.2777	-	0.9897
9	1	0.9998	-	0.9845

All the above comparisons confirm that WMSOBI can overcome the shortcomings of SOBI and obtain as good, if not better results, as compared to results from ERA and SOBI methods. In the next part, application of the proposed WMSOBI in bridge SHM is studied.

4.2.5 Experimental Study on a Bridges

To further study WMSOBI's capability, an experimental study is performed. This section will discuss different methods to obtain the static and dynamic properties of bridge structures, such as flexibility method, output only method using FFT, ERA, SOBI and WMSOBI. Since it is a scale model test, excitation signals can also be

measured. Hence, frequency response functions (FRF) can also be obtained. The identified results from flexibility method and FRF are treated as references. Similar to numerical study, the assumption of insufficient sensors for ERA, SOBI and WMSOBI (under-determined problem) is considered.

4.2.5.1 Experimental Setup

The arch bridge across US highway 59 and Mandell street in Houston, Texas, is chosen as the target bridge. The bridge is shown in Figure **??**(a). The arch bridge has a steel arch with nine pairs of steel hanger cables that support the deck. The deck is constructed with concrete supported by steel girders and simply supported at both abutments.

(a)Arch Bridge across US 59 and Mandell St

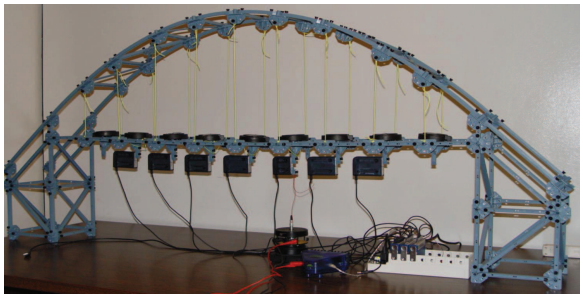

(b)Simplified Experimental Model

Figure 4.6 : Arch Bridge and Corresponding Experimental Model

Figure 4.6(b) shows the simplified arch bridge model assembled using PASCO model sets. Steel cables are replaced by nylon strings. There are nine pairs of strings supporting the deck. The deck is modeled using plastic truss. Additional nine weights are attached to the truss to simulate the mass. Vertical accelerations are measured at the deck level. The experimental model can be further simplified to a simply

supported beam with nine nodes by canceling out the remaining degrees of freedom. Each node has a lumped mass as shown in Figure 4.7.

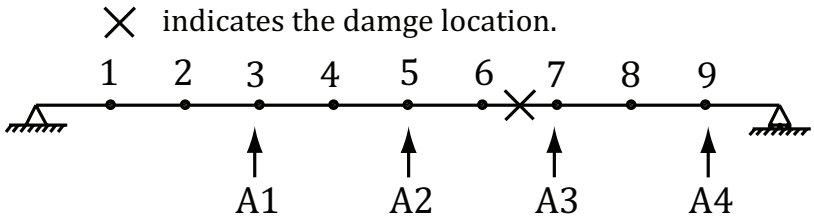

Figure 4.7 : Simply Supported Beam Model Arch Bridge

4.2.5.2 Modal Analysis using Statically Measured Flexibility

The global stiffness matrix is obtaiend by directly measuring the global flexibility matrix. The flexibility is defined as the displacement caused by unit load, as shown in Equation 4.14, provided that the bridge structure remains linear, which is satisfied by the model shown in Figure 4.7. In other words, the flexibility method provides approximate results for linear structure assumption.

$$\begin{aligned} f_{ij} &= \frac{\delta_{ij}}{p_i} \\ \mathbf{F_G} &= [f_{ij}], \quad i,j = 1,2,\cdots,N \\ \mathbf{K_G} &= \mathbf{F_G}^{-1} \end{aligned} \tag{4.14}$$

where $\mathbf{F_G}$ and $\mathbf{K_G}$ are global flexibility matrix and stiffness matrix, respectively; δ_{ij} is the deflection at node j caused by load p_i at node i.

A high resolution laser is used to measure the deflection of each node with and without a unit weight applied to one of the nodes. The stiffness matrix is obtained

using equation 4.14. Mass matrix is assumed to be uniformly distributed with 0.7 kg per node. Damping is assumed to be 5%. The natural frequencies are calculated by directly solving equation $\mathbf{K_G} - \omega_i^2 \mathbf{M} = 0$. The derived natural frequencies are shown in the second column of Table 4.4.

4.2.5.3 Modal Analysis using Measured Dynamic Responses

Dynamic tests have been performed for both impact and sine-sweep excitation. FRF functions from forced vibration are considered to be the references. Sampling time step for all the tests is 0.0005 sec.

Forced Vibration: A sine-sweep excitation analog signal ranging from 0 to 30Hz is generated using National Instrument Module 9263. The excitation actuator is connected to the node next to the center node to excite asymmetric modes. The excitation force applied on the bridge deck from the actuator is measured by a load cell. Accelerations of nine nodes are measured. FRFs are obtained using the frequency domain method.

$$|H(\omega)| = \frac{|X(\omega)\, U(\omega)|}{|U(\omega)|^2} \tag{4.15}$$

where $|H(\omega)|$ is the FRF (or frequency response function); $|U(\omega)|$ is the frequency spectrum for excitation signal and $|X(\omega)|$ is the frequency spectrum of one channel of response for given excitation. The results from peak picking method are shown in Figure 4.8. The identified peaks of all 9 channels provide estimates of the corresponding natural frequencies and mode shapes. The identified frequencies are included in the third column of Table 4.4.

Impact Test: Free vibration due to impact test is recorded. The center node of bridge model is node 5. The vertical impact is introduced by hammering at node 4, which is essentially an asymmetric impact. The key idea is to excite all the modes,

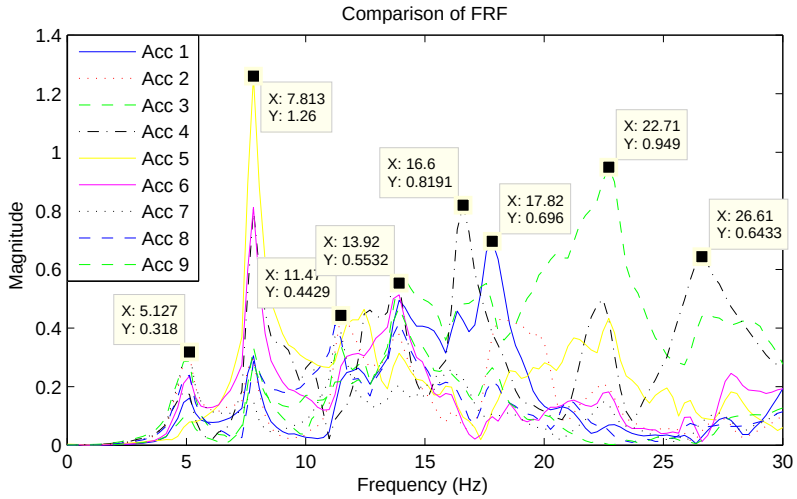

Figure 4.8 : FRFs for Arch Bridge Model

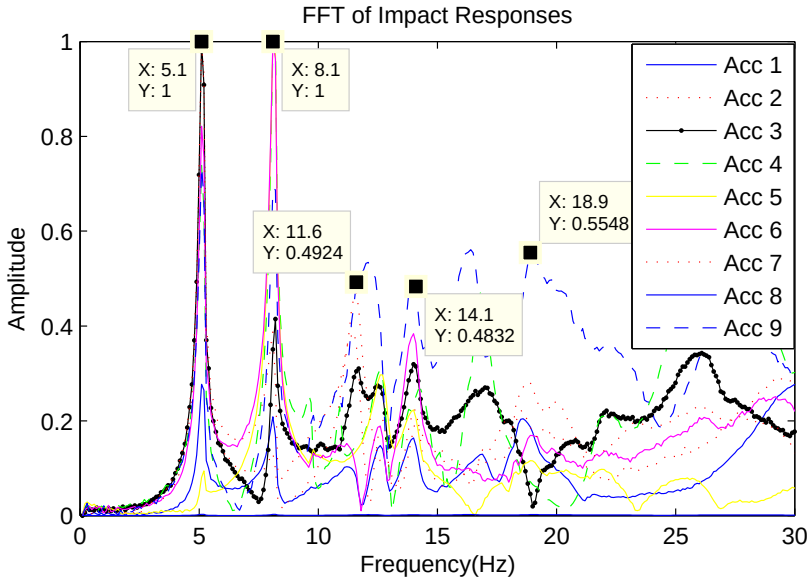

Figure 4.9 : FFT for Impact Reponse of Arch Bridge Model

including asymmetric modes. The acceleration signals of all nodes are measured. FFT is used to identify all the natural frequencies as shown in Figure 4.9.

Similar to the previous section on numerical study, only responses at nodes 3, 5, 7

and 9 are chosen as measured output signal. ERA, SOBI and WMSOBI are performed to identify as many modes as possible. The identified frequencies are shown in column 4 to 6 of Table 4.4.

Table 4.4 : Identified Natural Frequencies for Arch Bridge Model

	Analytical	FRF	FFT	ERA	SOBI	WMSOBI
Freq 1 (Hz)	5.427	5.127	5.100	4.984	5.000	5.000
Freq 2 (Hz)	7.936	7.813	8.100	8.075	8.088	8.088
Freq 3 (Hz)	11.62	11.42	11.60	11.69	–	11.47
Freq 4 (Hz)	14.64	13.92	14.10	13.74	13.97	13.97
Freq 5 (Hz)	18.50	16.60/17.82	16.48	15.59	–	16.32
Freq 6 (Hz)	22.56	22.20	–	–	–	22.94
Freq 7 (Hz)	24.85	–	25.41	–	–	25.88
Freq 8 (Hz)	26.58	26.60	26.80	26.67	–	27.35

In Table 4.4, the frequency results from FRF peak picking method using all node measurements are treated as references. All the impact test results are only based on response measured at 4 nodes and FFT. Large Hankel matrix is chosen in ERA to calculate more eigenvalues, which requires a lot of computing time. But it still misses some modes, such as mode 6 in Table 4.4. SOBI can only find as many modes as the number of sensors. The fourth mode found by SOBI is $\tilde{1}$55Hz, which is way above the frequency range of interest. On the other hand, since WMSOBI can utilize different scales of wavelet coefficients, all the modes in FRF are found using WMSOBI. In addition, the identified results from adjacent scales can mutually verify each other when they contain the same mode information.

4.3 Complex WMSOBI (CWMSOBI)

The above section proposed a wavelet modified SOBI method to identify the dynamic properties from responses of a structure. However, the key assumption that the structural vibration mode shapes are real (standing wave) prevents its application for complex mode shape estimation (traveling wave problem), which dominates large number of cases for deepwater risers. Hence, for deepwater risers, a complex blind identification method is needed, which is developed in the next section.

4.3.1 Wavelet Coefficients and Sources

Similar to WMSOBI method, wavelet transform is used to overcome the shortcoming of SOBI. The CWT is defined as

$$W(a,\tau) = \frac{1}{\sqrt{a}} \int_{-\infty}^{+\infty} x(t)\, \psi\left(\frac{t-\tau}{a}\right) dt \tag{4.16}$$

where $W(a,\tau)$ is the wavelet coefficients, a is the scale, $\psi\left(\frac{t-\tau}{a}\right)$ is the mother wavelet function, $x(t)$ is the original signal, τ is the current time step. From the 3D plot of the wavelet coefficients, we can easily find the scale range of interest by their amplitudes in the time-frequency domain.

In a discretized manner, the wavelet coefficients of measured signal from sensor i for scale j will be

$$\begin{aligned} g_{ki}^{j} &= g_i^j(k\Delta t) = \sum_m x_{mi}\psi^j((m-k)\Delta t) \quad i = 1, 2, \cdots, N \\ f_{ki}^{j} &= f_i^j(k\Delta t) = \sum_m s_{mi}\psi^j((m-k)\Delta t) \end{aligned} \tag{4.17}$$

For a chosen scale, j, the orthogonal continuous wavelet decomposition of measured signals can be discretized in terms of its decomposition coefficients like the

following equation:

$$x_i^j(t) = \sum_k g_{ki}^j \psi_k^j(t) \quad i = 1, 2, \cdots, N \tag{4.18}$$

where $\psi(t)$ is the chosen wavelet, and g_{ki}^j are the wavelet coefficients for scale j, sensor index i and the time shift index k. Similarly, the sources can also be processed using the same procedure, which results in the following equation:

$$s_i^j(t) = \sum_k f_{ki}^j \psi_k^j(t) \quad i = 1, 2, \cdots, N \tag{4.19}$$

where $s_i^j(t)$ is the ith source signal for scale j, and f_{ki}^j are the wavelet coefficients for scale j, source index i and the time shift index k.

The original BSS can be represented as following equation:

$$\mathbf{x} = \mathbf{A}\mathbf{s} \Leftrightarrow \begin{bmatrix} x_1 \\ x_2 \\ \vdots \\ x_N \end{bmatrix} = \mathbf{A} \begin{bmatrix} s_1 \\ s_2 \\ \vdots \\ s_N \end{bmatrix} \tag{4.20}$$

where $\mathbf{x}$ is measured signals with each i channel, represented by signal x_i, and similarly for sources $\mathbf{s}$ and each i channel, represented by signal s_i.

Performing wavelet transform using scale m on both sides of equation 4.19, the constant mixing matrix $\mathbf{A}$ will not change. And the equations can be re-written as:

$$WT^m(\mathbf{x}) = \mathbf{A} \cdot WT^m(\mathbf{s}) \Leftrightarrow \begin{bmatrix} WT^m(x_1) \\ WT^m(x_2) \\ \vdots \\ WT^m(x_N) \end{bmatrix} = \mathbf{A} \begin{bmatrix} WT^m(s_1) \\ WT^m(s_2) \\ \vdots \\ WT^m(s_N) \end{bmatrix} \tag{4.21}$$

$$\begin{bmatrix} g_{k1}^m \\ g_{k2}^m \\ \vdots \\ g_{kN}^m \end{bmatrix} = \mathbf{A} \begin{bmatrix} f_{k1}^m \\ f_{k2}^m \\ \vdots \\ f_{kN}^m \end{bmatrix} \Leftrightarrow \mathbf{g}_k^m = \mathbf{A}\mathbf{f}_k^m \tag{4.22}$$

where k is the time shift index; m is a given scale of the coefficients; $\mathbf{A} \in R^{N \times N}$ is the instantaneous mixing matrix for N sensors with assumption of N sources.

Equation 4.22 proves that transforming the time domain signal into time-frequency domain does not change the mixing matrix. The mixing matrix can be estimated using the wavelet coefficients instead of the noisy original measured signals. This replacement can greatly increase the signal noise ratio (SNR) as the widest application for wavelet is de-noising. Therefore, the first shortcoming for SOBI can be alleviated.

In addition, a certain scale of wavelet coefficients may only contain a few sources if not all of them. By choosing different scales for wavelet transformation, the identified sources can be different. This strategy can solve the dilemma of more sources then sensors as well as identification of poorly excited modes.

4.3.2 Complex Wavelet Coefficients for Morlet Wavelet

For Morlet wavelet, $\psi_0(t) = \pi^{-1/4} e^{i\omega_0 t} e^{-t^2/2}$, the discretized continuous wavelet transform will result in a series of complex wavelet coefficients. The imaginary part of the wavelet coefficients are the same as the 90 degree phase shifted of the real part.

If the structure was classical proportional damping (Rayleigh Damping), then the vibrations will be composed of real vibration mode shapes. Those real mode shapes can be treated as complex modes with a special condition. $\Phi = \Phi_{real} + i\Phi_{imag} =$

$\Phi_{real} + i\beta\Phi_{real}$, and β is a constant. In some cases, $\Phi = i\Phi_{real}$. In a matrix form,

$$\begin{array}{rcl} \mathbf{g}^m_{real} &=& \mathbf{A}_1\mathbf{f}^m_{real} \\ \mathbf{g}^m_{imag} &=& \mathbf{A}_2\mathbf{f}^m_{imag} \end{array} \Rightarrow \begin{array}{rcl} \mathbf{A}_1 &=& \beta\mathbf{A}_2 \\ or & & \\ \mathbf{A}_1 &=& -\mathbf{A}_2 \end{array} \tag{4.23}$$

If the damping is not classical damping, then the modes will be complex. For both sources and measured signals, wavelet coefficients are separated as real part, $\mathbf{g}^m_{real}$, and imaginary part, $\mathbf{g}^m_{imag}$. Taking consideration of equation 4.23 results in $\mathbf{A}_1 \neq \beta\mathbf{A}_2$.

To utilize the imaginary part of wavelet coefficients, the original measured signal is replaced with one composed wavelet coefficients signal of both real part and imaginary part. Similar procedure is applied to the sources. This replacement leads to the following equation:

$$\begin{bmatrix} \mathbf{g}^m_{real} \\ \mathbf{g}^m_{imag} \end{bmatrix} = \begin{bmatrix} \mathbf{A}_{11} & \mathbf{A}_{12} \\ \mathbf{A}_{21} & \mathbf{A}_{22} \end{bmatrix} \begin{bmatrix} \mathbf{f}^m_{real} \\ \mathbf{f}^m_{imag} \end{bmatrix} \tag{4.24}$$

As actual $\mathbf{g}^m = \mathbf{g}^m_{real} + i\mathbf{g}^m_{imag}$, equation 4.23 can be re-written as:

$$\begin{array}{rcl} \mathbf{g}^m_{real} + i\mathbf{g}^m_{imag} &=& \left(\mathbf{A}_{11}\mathbf{f}^m_{real} + \mathbf{A}_{12}\mathbf{f}^m_{imag}\right) + i\left(\mathbf{A}_{21}\mathbf{f}^m_{real} + \mathbf{A}_{22}\mathbf{f}^m_{imag}\right) \\ &=& (\mathbf{a} + i\mathbf{b})\left(\mathbf{f}^m_{real} + i\mathbf{f}^m_{imag}\right) \end{array} \tag{4.25}$$

where $\left(\mathbf{f}^m_{real} + i\mathbf{f}^m_{imag}\right)$ are the complex wavelet coefficients. Equation 4.25 matches equation 4.20, which shows that $(\mathbf{a} + i\mathbf{b})$ is the current complex mixing matrix.

To get the complex mixing matrix Φ, replacing $\left(\mathbf{f}^m_{real} + i\mathbf{f}^m_{imag}\right)$ with $(x + yi)$ in equation 4.25 will lead to

$$\begin{array}{rcl} (\mathbf{A}_{11}x + \mathbf{A}_{12}y) + i\,(\mathbf{A}_{21}x + \mathbf{A}_{22}y) &=& (\mathbf{a} + i\mathbf{b})\,(x + yi) \\ &=& (\mathbf{a}x - \mathbf{b}y) + i\,(\mathbf{b}x + \mathbf{a}y) \end{array} \tag{4.26}$$

As the above equation is valid, one can conclude that the coefficients for real part and imaginary part from the left side are equal to those from the right side, respectively.

$$\begin{aligned}(\mathbf{a}x - \mathbf{b}y) &= (\mathbf{A}_{11}x + \mathbf{A}_{12}y) \\ (\mathbf{b}x + \mathbf{a}y) &= (\mathbf{A}_{21}x + \mathbf{A}_{22}y)\end{aligned} \tag{4.27}$$

Furthermore, because both of the above equations are valid for measured time varying signals (x, y), the coefficients for x and y should match in both sides, respectively. As a result, equation 4.27 leads to two sets of solution.

$$\begin{cases} \mathbf{a} = \mathbf{A}_{11} \\ \mathbf{b} = -\mathbf{A}_{12} \end{cases} \& \begin{cases} \mathbf{a} = \mathbf{A}_{22} \\ \mathbf{b} = \mathbf{A}_{21} \end{cases} \tag{4.28}$$

According to McNeil and Zimmermann [87], averaging the equations in equation **??** will lead to a more accurate final estimated complex mode shapes,

$$\mathbf{\Phi} = (\mathbf{a} + i\mathbf{b}) = \frac{\mathbf{A}_{22} + \mathbf{A}_{11}}{2} + i\frac{\mathbf{A}_{21} - \mathbf{A}_{12}}{2} \tag{4.29}$$

The above conclusion is based on the assumption that the real part of source signals comes out earlier than imaginary part as shown in equation 4.24. However, the BMID method proposed by McNeil and Zimmermann [87] cannot guarantee the assumed order of sources.

In the proposed CWMSOBI method, the order of source signals is identified and processed for each mode shape, respectively. When imaginary part comes out earlier than the real part of source signals, $\begin{bmatrix} \mathbf{g}^m_{real} \\ \mathbf{g}^m_{imag} \end{bmatrix} = \begin{bmatrix} \mathbf{A}_{11} & \mathbf{A}_{12} \\ \mathbf{A}_{21} & \mathbf{A}_{22} \end{bmatrix} \begin{bmatrix} \mathbf{f}^m_{imag} \\ \mathbf{f}^m_{real} \end{bmatrix}$, the final mode shape equation will become

$$\mathbf{\Phi} = (\mathbf{a} + i\mathbf{b}) = \frac{\mathbf{A}_{12} + \mathbf{A}_{21}}{2} + i\frac{\mathbf{A}_{22} - \mathbf{A}_{11}}{2} \tag{4.30}$$

4.3.3 Theoretical Values for Complex Mode Shapes

Generally, the equations of motion for a N DOFs system can be written as $[\mathbf{M}]\{\ddot{x}\} + [\mathbf{C}]\{\dot{x}\} + [\mathbf{K}]\{x\} = 0$. By introducing an assistant equation $[\mathbf{M}]\{\dot{x}\} - [\mathbf{M}]\{\dot{x}\} = 0$, the EOMs become

$$\begin{bmatrix} [\mathbf{M}] & [\mathbf{0}] \\ [\mathbf{0}] & [\mathbf{M}] \end{bmatrix} \begin{Bmatrix} \dot{x} \\ \ddot{x} \end{Bmatrix} + \begin{bmatrix} [\mathbf{0}] & [-\mathbf{M}] \\ [\mathbf{K}] & [\mathbf{C}] \end{bmatrix} \begin{Bmatrix} x \\ \dot{x} \end{Bmatrix} = \begin{Bmatrix} 0 \\ \{f(t)\} \end{Bmatrix} \tag{4.31}$$

Introducing the state space variable $\{y(t)\} = [\{x(t)\}\, \dot{x}(t)]^T$, the above equation can be re-written in state space representation:

$$\{\dot{y}\} = [\mathbf{A}]\{y\} + [\mathbf{B}]\, f(t) \tag{4.32}$$

where $[\mathbf{A}] = \begin{bmatrix} [\mathbf{0}] & [\mathbf{I}] \\ [-\mathbf{M}^{-1}\mathbf{K}] & [-\mathbf{M}^{-1}\mathbf{C}] \end{bmatrix}$ and $[\mathbf{B}] = \begin{bmatrix} [\mathbf{0}] \\ [\mathbf{I}] \end{bmatrix}$.

Considering free vibration, then $f(t) = 0$, the above equation becomes $\dot{y} = Ay$. Using the traditional solution for this kind of differential equations, one can assume $\mathbf{y} = \mathbf{U}e^{\lambda t} = \begin{Bmatrix} \Psi \\ \lambda\Psi \end{Bmatrix} e^{\lambda t}$. In which, λ is the eigenvalue of matrix $\mathbf{A}$, $\mathbf{U}$ is its eigenvector.

As $\mathbf{A}$ has dimension 2*N and it is not symmetric, it should have N pairs of conjugate eigenvalues, $\Omega = [\Lambda, \Lambda^*]$ and accordingly eigenvectors, $U = [u, u^*]$. The eigenvector matrix $\mathbf{U}$ contains the complex mode shape matrix Φ for original system.

$$\mathbf{U} = \begin{bmatrix} [\mathbf{\Phi}] & [\mathbf{\Phi}^*] \\ [\mathbf{\Lambda\Phi}] & [\mathbf{\Lambda\Phi}^*] \end{bmatrix} \tag{4.33}$$

Obviously, it can be found that the complex mode shape will be the upper-left part of the whole eigenvector matrix of $\mathbf{A}$.

4.3.4 Numerical Study

To test the performance of the proposed method, a simple 3DOF system with non-classical damping is used in this paper.

4.3.4.1 Model Setup

As it is non-diagonal damping system, the system matrices are given as following:

$$[\mathbf{M}] = \begin{bmatrix} 2.5 & 0 & 0 \\ 0 & 2 & 0 \\ 0 & 0 & 1.5 \end{bmatrix}, [\mathbf{C}] = \begin{bmatrix} 0.40 & 0.5 & -0.60 \\ 0.50 & 0.06 & -0.06 \\ -0.60 & -0.06 & 0.30 \end{bmatrix}, [\mathbf{K}] = \begin{bmatrix} 6 & -3 & 0 \\ -3 & 6 & -3 \\ 0 & -3 & 10 \end{bmatrix}$$

With initial displacement $x = [0.5 \ -0.05 \ 0.6]^T$ and impact force $F = [0 \ 0 \ 100]^T$, the free vibration of the system was simulated.

4.3.4.2 Blind Identification without Noise

At first, no measurement noise is considered. The simulated response signals and their frequency spectra are shown in Fig. 4.10. Using equation 4.20 to 4.33, one can derive the theoretical modal information of the system. The frequency spectra shows that all three modes are fully excited. The blind identification methods should be able to pick up all vibration modes.

Theoretical results are shown in Table 4.5. A comprison of results from the second order blind identification (SOBI) method [86], blind modal identification (BMID) method [87], previously proposed wavelet modified SOBI (WMSOBI) and complex WMSOBI (CWMSOBI) proposed in this section is performed. The identified results from WMSOBI and CWMSOBI come from three different scales of wavelet coefficients. A full measurement of displacement is considered (no under-determinate problem). The identified natural frequencies and damping ratios are also shown in

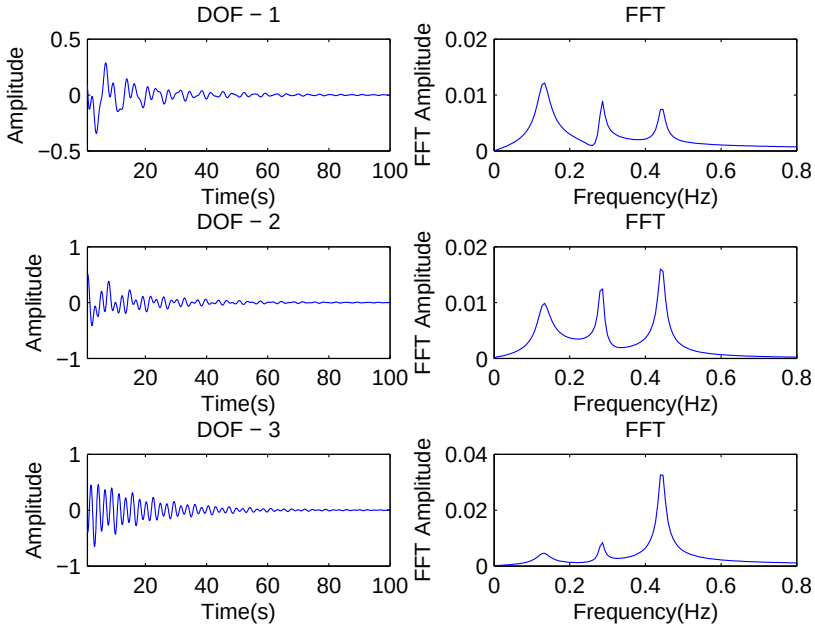

Figure 4.10 : Time History and Frequency Spectra for Impact Response

Table 4.5.

Table 4.5 : Theoretical and Identified Properties for 3DOF Model

Mode	Theoretical		SOBI		BMID		WMSOBI		CWMSOBI	
No.	Hz	%	Hz	%	Hz	%	Hz	%	Hz	%
1	0.1313	12.66	0.1333	10.64	0.1333	12.69	0.1266	11.00	0.1333	9.55
2	0.2841	2.09	0.2865	3.38	0.2865	2.42	0.2865	2.11	0.2865	2.36
3	0.4430	1.91	0.4398	1.79	0.4398	2.67	0.4398	1.73	0.4398	1.86

Comparing the identified frequency results, it is evident that all methods provide reasonable results. Except WMSOBI underestimates the first mode frequency when compared to the theoretical value. Comparing identified damping, WMSOBI and

CWMSOBI under estimate the first mode damping and overestimate the second mode damping when compared to theoretical damping.

To further compare the performance of the aforementioned methods, the identified source signals and their frequency spectra are presented in the Figs. 4.11 to 4.14.

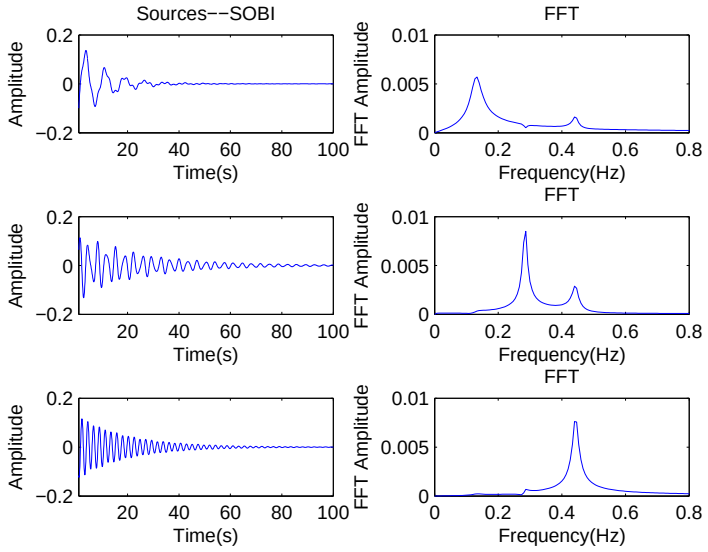

Figure 4.11 : Identified Source Signals and Frequency Spectra from SOBI

Comparing Figs. 4.11 to 4.14, the identified sources from CWMSOBI are better than the others because their frequency spectra are better, whereas the results from SOBI in Fig. 4.11 have multiple peaks that result in inaccurate second mode shape identification. The spectra of first mode source from BMID (Fig. 4.12) is not as good as that from CWMSOBI. Similar result occurs in the spectra of the first mode source from WMSOBI (Fig. 4.13).

Finally, the mode shapes identified from the above methods and their modal assurance criterion (MAC) value are compared in Table 4.6.

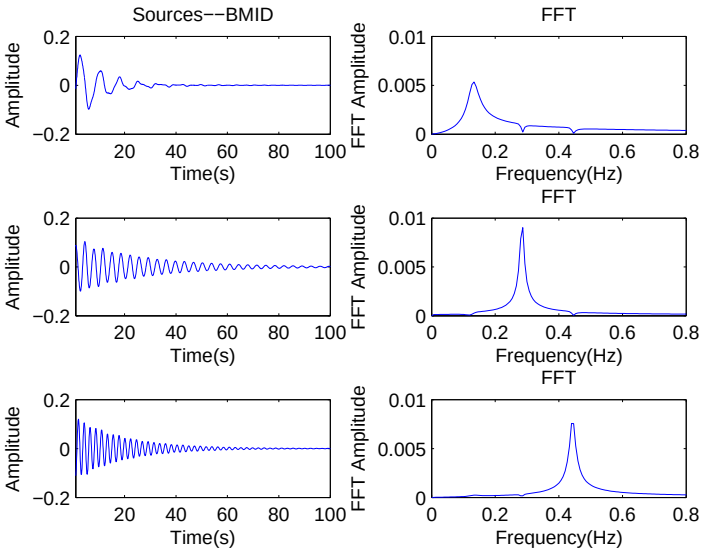

Figure 4.12 : Identified Source Signals and Frequency Spectra from BMID

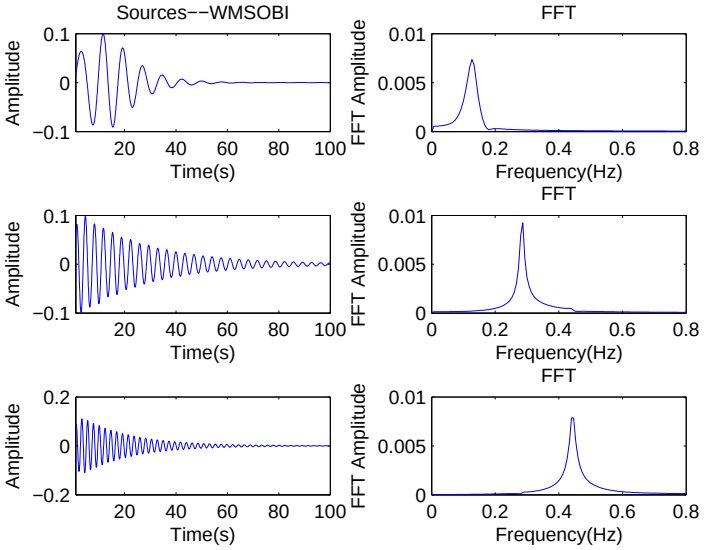

Figure 4.13 : Identified Source Signals and Frequency Spectra from WMSOBI

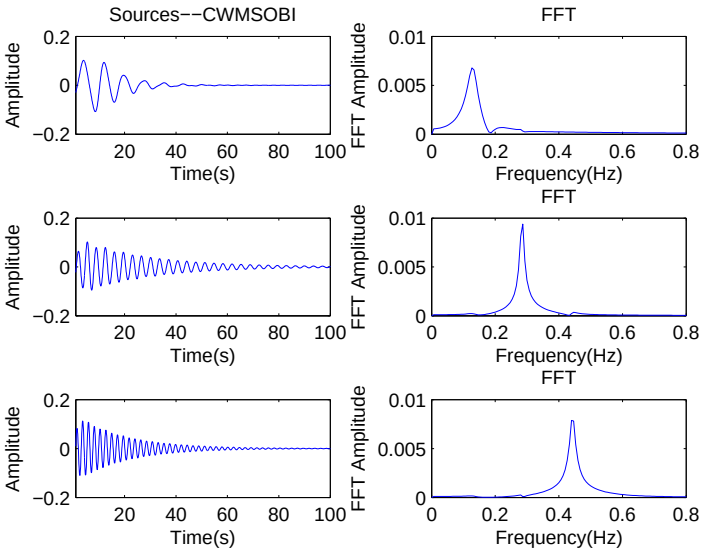

Figure 4.14 : Identified Source Signals and Frequency Spectra from CWMSOBI

- The identified real mode shapes of SOBI and WMSOBI have comparable MAC values for all modes when there are enough sensors (No under-determinate problem).

- The mode shape results from BMID provide two MAC values: one is calculated from the originally identified mode shapes; the other (The bold results in brackets) is calculated from the modified mode shapes after manually changing the sign of the imaginary part of identified mode shapes to match the theoretical values. The modified MAC values are clearly better. however, this manually modification is a drawback for the application of BMID in real-time SHM.

- Among all the MAC values in Table 4.6, the results from CWMSOBI have the largest and best MAC results.

Table 4.6 : Theoretical and Identified Mode Shapes

Theoretical	SOBI	BMID	WMSOBI	CWMSOBI
1.0000	1.0000	1.0000	1.0000	1.0000
0.7729+0.0181i	0.7545	0.7768+0.0484i	0.7917	0.8349+0.0050i
0.3365+0.0673i	0.3363	0.3881-0.0819i	0.3546	0.3545+0.0958i
MAC	0.9975	0.9866 (**0.9978**)	0.9974	0.9982
-0.8011-0.0609i	-0.7359	-0.6201-0.0992i	-0.7679	-0.7034+0.0485i
1.0000	1.0000	1.0000	1.0000	1.0000
0.7705-0.1934i	0.6351	0.3881-0.0819i	0.7791	0.6961-0.2947i
MAC	0.9774	0.9164 (**0.9769**)	0.9837	0.9916
0.0921-0.1644i	0.1198	0.1044+0.2017i	0.1094	0.0914-0.1894i
-0.4728+0.0777i	-0.4821	-0.4865-0.0632i	-0.4810	-0.4779+0.0768i
1.0000	1.0000	1.0000	1.0000	1.0000
MAC	0.9773	0.8896 (**0.9986**)	0.9755	0.9995

4.3.4.3 Blind Identification with Noise

Previous analysis considered no measurement noise, which is not the case in reality. A 10% white noise (amplitude 0.03) is added to the same signal studied in the previous analysis. The signal-to-noise ratio (SNR) is about 20 db. The noisy signal and its frequency spectra is shown in Fig. 4.15.

Same procedure is repeated to obtain the dynamic properties from the noisy response signals. Theoretical and identified results are shown in Table 4.7. The identified frequencies are the same, and CWMSOBI has better damping estimation when there is noise.

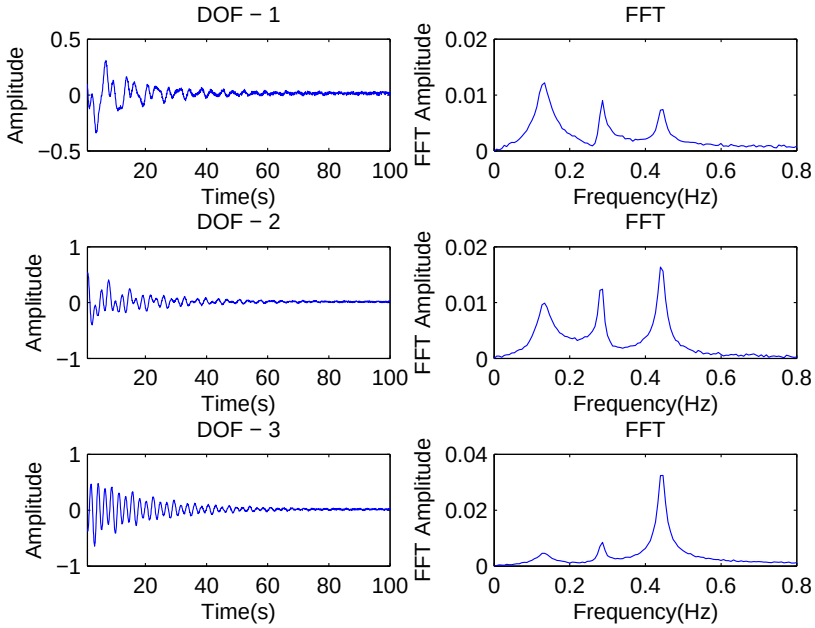

Figure 4.15 : Time History and Frequency Spectra for Noisy Response

Table 4.7 : Theoretical and Identified Properties for 3DOF Model

Mode	Theoretical		SOBI		BMID		WMSOBI		CWMSOBI	
No.	Hz	%	Hz	%	Hz	%	Hz	%	Hz	%
1	0.1313	12.66	0.1333	9.88	0.1333	9.04	0.1333	9.36	0.1333	10.16
2	0.2841	2.09	0.2865	1.22	0.2865	3.28	0.2865	2.30	0.2865	2.20
3	0.4430	1.91	0.4398	1.35	0.4398	2.89	0.4398	1.63	0.4398	1.53

To further compare the performance of aforementioned methods, the identified source signals and their frequency spectra are plotted in the following figures.

Similar trend can be found from Fig. 4.16 to 4.19, the identified sources from CWMSOBI are better than the others because their frequency spectra are much

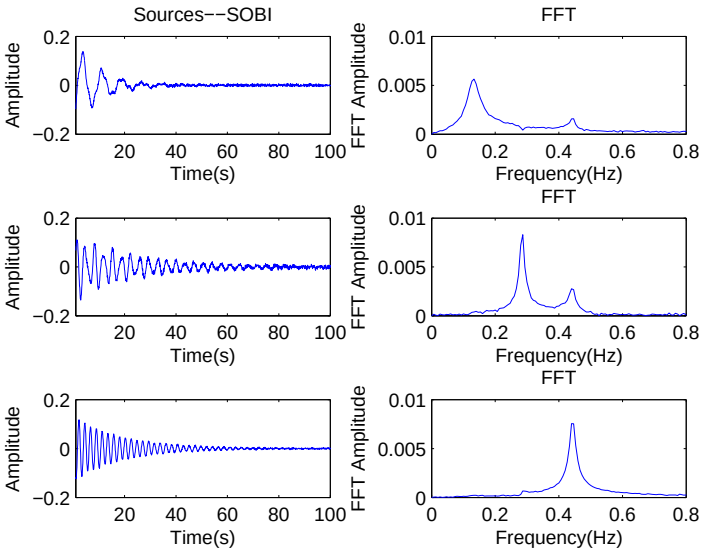

Figure 4.16 : Identified Source Signals and Frequency Spectra from SOBI

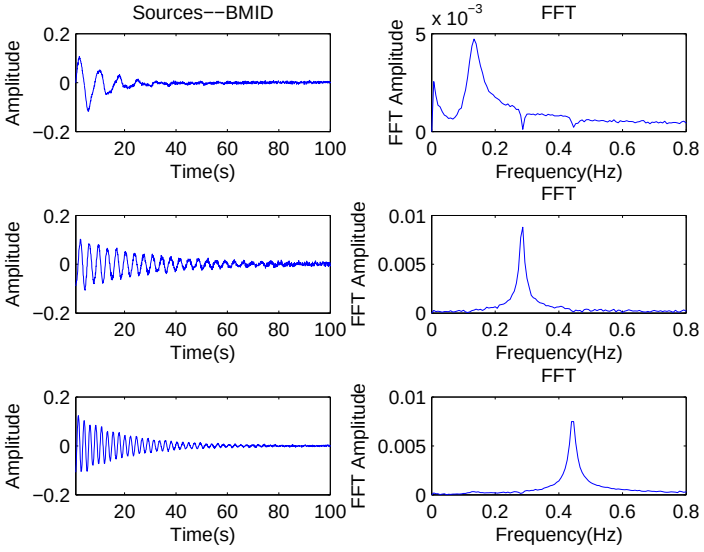

Figure 4.17 : Identified Source Signals and Frequency Spectra from BMID

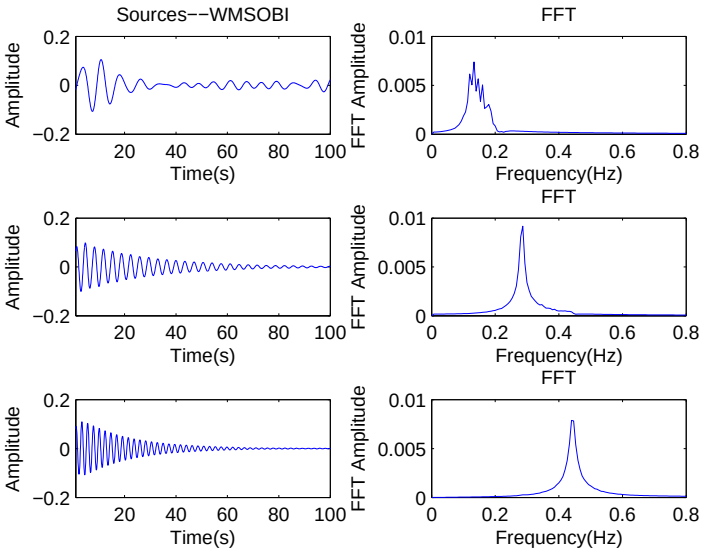

Figure 4.18 : Identified Source Signals and Frequency Spectra from WMSOBI

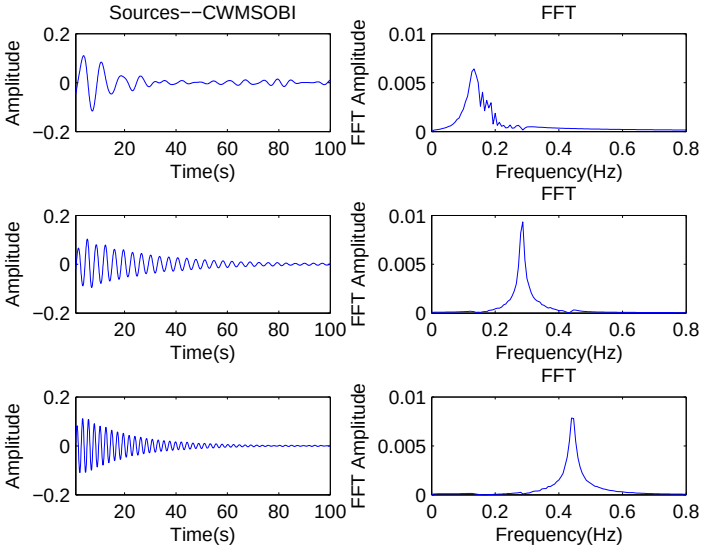

Figure 4.19 : Identified Source Signals and Frequency Spectra from CWMSOBI

cleaner than the others. So does the MAC values of mode shapes from CWMSOBI in Table 4.8.

Table 4.8 : Theoretical and Identified Mode Shapes

Theoretical	SOBI	BMID	WMSOBI	CWMSOBI
1.0000	1.0000	1.0000	1.0000	1.0000
0.7729+0.0181i	0.7571	0.7755+0.0247i	0.9191	0.8408+0.0115i
0.3365+0.0673i	0.3358	0.4116-0.0739i	0.3476	0.3557+0.1027i
MAC	0.9975	0.9864 (**0.9964**)	0.9969	0.9986
-0.8011-0.0609i	-0.7503	-0.6167-0.0757i	-0.7581	-0.7101+0.0324i
1.0000	1.0000	1.0000	1.0000	1.0000
0.7705-0.1934i	0.6401	0.6126+0.2404i	0.7591	0.7007-0.2918i
MAC	0.9780	0.9198 (**0.9801**)	0.9835	0.9926
0.0921-0.1644i	0.1237	0.1063+0.1998i	0.1129	0.0940-0.1875i
-0.4728+0.0777i	-0.4871	-0.4921-0.0676i	-0.4864	-0.4820+0.0837i
1.0000	1.0000	1.0000	1.0000	1.0000
MAC	0.9751	0.8902 (**0.9987**)	0.9754	0.9995

4.4 Summary

This chapter proposed two blind identification methods based on wavelet transform and second order blind identification method: (1) wavelet modified second order blind identification method (WMSOBI) and (2) complex wavelet modified second order blind identification method (CWMSOBI). Detailed strategy for each methods have been described.

Both numerical and experimental studies prove that WMSOBI is better than SOBI. The key achievements are as following:

- WMSOBI can identify as many modes as possible, while the number of modes that SOBI can identify is limited to the sensor numbers (under-determinate problem).
- WMSOBI can also be used to identify higher modes, which is hard for SOBI when there is noise.
- The wavelet transform's natural capability of de-noising enhances the accuracy by increasing signal-to-noise ratio (SNR).

For CWSOBI, its performance has been verified by numerical simulation with and without noise. Similar to WMSOBI, the key enhancements are

- CWMSOBI overcomes the under-determined problem which SOBI and BMID face.
- CWMSOBI can also be used to identify higher modes, which is hard for SOBI and BMID when there is noise.
- The wavelet transform's natural capability of de-noising enhances the accuracy by increasing signal-to-noise ratio (SNR).
- For system with complex vibration mode shapes, CWMSOBI provides more accurate identification results than SOBI, BMID and WMSOBI.
- In most of cases, the sign of imaginary part of identified mode shape from CWMSOBI does not need to be manually modified while BMID need it.

To summarize, CWMSOBI and WMSOBI are reliable blind identification methods for extracting dynamic properties. For real value vibration cases, WMSOBI works more efficiently (for smaller matrix computation size). For complex value vibration cases, CWMSOBI works better for more accurate identification.

Chapter 5

Vibration based Damage Detection for Deepwater Risers

Previous chapter presents the estimation of dynamic properties using the proposed blind identification algorithms. According to the SHM strategy in Fig. 1.3, the next step will be damage detection based on identified modal properties. This chapter concentrates on the damage detection based on obtained structural properties.

5.1 Current Algorithms for Risers Damage Detection

As mentioned in introduction chapter, most of the current applicable damage detection algorithms in offshore industry are not based on structural health monitoring, but on routine inspection methods or nondestructive techniques. Typically, these are visual inspections by divers or camera from remotely operated vehicles, ultrasonic techniques based ultrasonic waves,electro-magnetic method to detect the metal loss. Local monitoring in the proposed SHM system is based on a robotic crawler carrying magnetic flux leakage (MFL) sensors to check metal loss (thickness change) in risers.

However, inspection methods cannot detect damage in a timely manner as such inspections are performed only once every other year or several years. The timely detection of damage in deepwater risers is important to keep the consequence and economic loss due to damage to a minimum. Hence, a continuous monitoring is needed. Vibration based monitoring is the most widely used method used in onshore structures. A few researchers studied the possible applications of vibration based

damage detection methods in offshore structures.

Vandiver [20] proposed a natural frequency change index for damage detection. Sweetman et al. [21] proposed to use power spectra change as an indicator of damage. However, for TTR, the natural frequency is dominated by top tension. The variation in tension will cause variation in natural frequency, which makes it hard to detect damage using frequency based methods.

Riveros et al. [22] studied a statistical pattern recognition technique with a combined model of auto-regressive (AR) and auto-regressive with exogenous inputs (ARX). However, this requirement of measured excitation signals, which is not possible for deepwater risers, makes the technique unsuitable. The damage detection algorithm has to be based on output only or based on measured response only.

To address the aforementioned issues, damage detection algorithms purely based on the identified mode shapes can be one solution. Curvature mode change index [31] and modal assurance criterion (MAC) could be potential solutions. For MAC based methods, to locate the damage, a few different mode shapes are needed. However, in VIV, only few modes are excited, usually only one. Hence, MAC based methods cannot identify the presence of damage without enough modes. On the other hand, curvature mode shape change index only needs one mode shape to identify the damage location as long as the damage is located at non-node of the curvature mode shape. Hence, curvature mode shape change index is the only potential solution for deepwater risers.

5.1.1 Numerical Study of Curvature Mode Shape Change Index

To evaluate the performance of curvature mode shape change index in deepwater riser damage detection, numerical simulations using proposed 3D analytical model

are carried out. The parameters for Delta Flume (2003) [58] are used for the test of curvature mode shape change index. Case 6 with current speed $V = 0.60m/s$ is chosen with the assumption that the motion of all nodes are measured. For example, currently fiber optic sensors are used all along the riser.

5.1.1.1 Damage Simulation

As the most severe and frequent damage in deepwater risers is caused by corrosion, which will cause metal loss as wall thickness reduction. To simulate the effect of corrosion, a wall thickness or bending stiffness reduction is introduced to the damage location. Multiple damage locations are considered. A 50% bending stiffness (EI) reduction is introduced at the 25% and 75% of the riser depth. The curvature are calculated using central difference method from displacement.

$$\kappa_{y,z} = \frac{d^2y}{dz^2} = \frac{y_{i+1} + y_{i-1} - 2y_i}{2\Delta z^2} \tag{5.1}$$

where Δz is the element length, y_i is the displacement at node i and $\kappa_{y,z}$ is the curvature of deepwater riser in y direction respect to depth z.

In addition, in almost all the installed field health monitoring systems for deepwater risers, there are no synchronized measurement. Root mean square (RMS) values are widely used to estimate fatigue damage and vibration type. For the case 6 of Delta Flume (2003) [58], only one dominant mode is exited and the response of the riser is dominated by a standing wave. RMS values of curvature (strain) measurement can be directly used for curvature change index. On the other hand, the curvature vibration mode shapes are obtained using the proposed WMSOBI method (For standing wave, the CWMSOBI method will give the same results as WMSOBI method). Then the mode shapes are used for damage detection.

To summarize, the curvature change index can be applied in two different approaches depending on the synchronization condition: One is using the RMS values from independent signals; the other is using the identified curvature mode shapes from synchronized signals. The approaches are shown in Fig. 5.1.

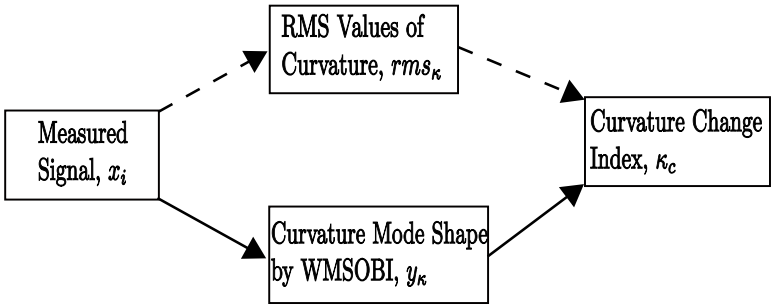

Figure 5.1 : Strategy for Curvature Change based Damage Detection Algorithm

In addition, since the cross-flow direction motion amplitude is much larger than that of the in-line direction (additionally, has no static component), the vibration based damage detection is performed mainly using the cross-flow vibration responses.

5.1.1.2 Results Analysis

As shown in Fig. 5.1, the curvature time histories are obtained using equation 5.1. Then the RMS values of each individual channel is calculated to get the RMS shapes in the first two profiles shown in Fig. 5.2. The first RMS profile is for the intact (undamaged) case, and the second is for the case with multiple damages. The difference between the intact and damaged case is plotted in the third plot of Fig. 5.2. There are peaks which indicate damages at locations $0.25\frac{z}{L}$ and $0.75\frac{z}{L}$. However, there are many false peaks at the other locations. Some of the false peaks have even larger absolute values. It is hard to differentiate between the true indicator and the false

indicator for RMS values. In other words, directly using RMS change of curvatures is not applicable for deepwater risers.

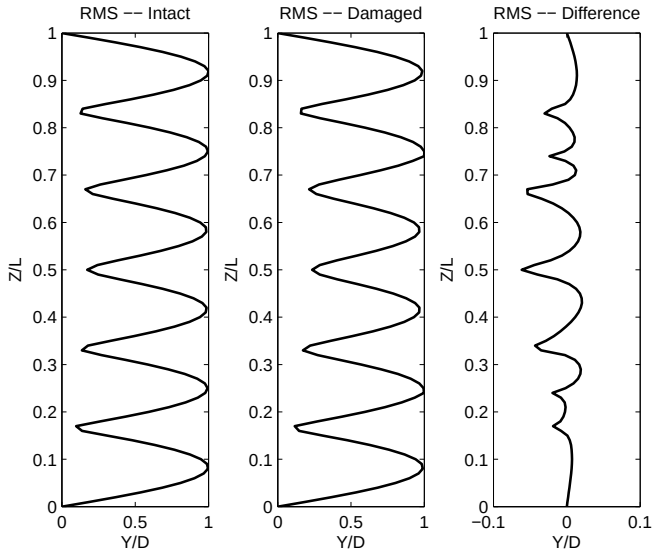

Figure 5.2 : Curvature RMS Change Profile: (a)Intact, (b)Damaged and (c) Difference

In Fig. 5.2, 5.3, 5.5, 5.6 and 5.9, y-axis denotes the normalized depth of the riser, where z represents the current depth of the riser, L represents the total depth or length of the riser; the x-axis denotes the normalized cross-flow (CF) response amplitude ($\frac{y}{D}$), the RMS values or identified mode shapes. In addition, the results utilize all motions from 100 nodes with assumption that all motions are measured.

The second approach using identified curvature mode shapes using the proposed WMSOBI/CWMSOBI methods is also carried out and presented in Fig. 5.3. Similar to Fig. 5.2, the first two profiles represent the curvature mode shapes from the undamaged and damaged simulation results. The difference, shown in the third profile of Fig. 5.3, indicates that at locations $0.25\frac{z}{L}$ and $0.75\frac{z}{L}$ there are sharp changes which indicate damages. Visually choosing the sharp changes of curvature should be ade-

quate. However, there are larger absolute changes in the center range (0.5 to 0.65$\frac{z}{L}$) and top range (0.85 to 0.95$\frac{z}{L}$). To make it easier to differentiate automatically, an improvement or modification from curvature change damage index is needed.

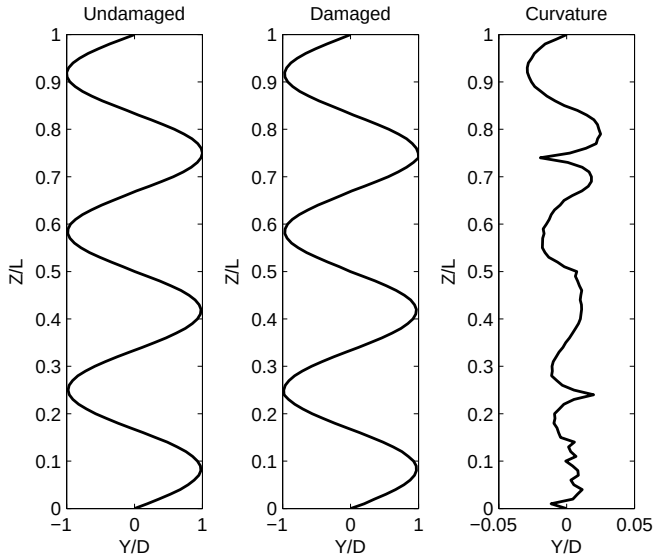

Figure 5.3 : Curvature Mode Shape Change Profile: (a)Intact, (b)Damaged and (c) Difference

5.2 Weighted Distributed Force Change (WDFC) Index

To overcome the limitation of curvature change index, a new damage index is proposed.

5.2.1 Concept of WDFC

A new damage index is proposed by choosing the fourth derivative of displacement mode shape, which is the second spatial derivative of the strain mode shape and proportional to the distributed force. Strain is proportional to curvature, which is

the second spatial derivatives of the displacement.

$$\kappa_{y,z} = \frac{d^2y}{dz^2} = \frac{M_{y,z}}{EI} \tag{5.2}$$

where y is the displacement in Y direction, z is the depth coordinate, $\kappa_{y,z}$is the curvature in Y direction at depth z. EI is bending stiffness, while $M(y,z)$ is the moment in Y direction at the section at riser depth z.

The fourth derivative of displacement over the depth, which is proportional to the distributed force term, is as follows

$$DF_{y,z} = \frac{d^4y}{dz^4} = -\frac{q_{y,z}}{EI} \tag{5.3}$$

where y is the displacement in Y direction, z is the depth coordinate. $DF_{y,z}$ is proportional to the distributed force (DF) term, represented by $q_{y,z}$. The actual DF index is obtained using central difference method to process the identified curvature mode shape, similar to equation 5.1.

The false indication can be removed from distributed force change by multiplying it by a weighting function, which results in the weighted distributed force (WDF) damage index for damage detection.

$$WDF_{y,z} = DF_{y,z} \times \kappa_{y,z}^2 \tag{5.4}$$

where $\kappa_{y,z}$ represents the curvature/strain mode shape obtained from responses of undamaged structure for both undamaged and damaged cases.

The difference (change) between the undamaged and damaged WDF (WDFC) index is treated as an indicator for damages in the test structure.

5.2.2 Numerical Evaluation of Damage in Standing Wave Case

The proposed WDFC index is applied to the previous simulation results-case 6 of Delta Flume (2003) [58]. For both curvature RMS value approach and curvature

mode shape approach, the motion of all 100 nodes are used. The process is shown in Fig. 5.4.

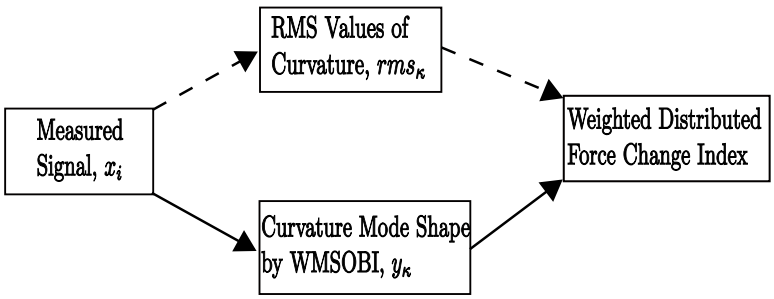

Figure 5.4 : Strategy for WDFC based Damage Detection Algorithm

The damage detection results are shown in Fig. 5.5 and 5.6. The fourth profile of Fig. 5.5 clearly shows only two distinct peaks where the damages are without any false peaks. All the previous false peaks are eradiated by WDFC. The program can automatically recognize the damage location by selecting the absolute values of WDFC over a threshold, such as 0.01 for the given case in Fig. 5.5.

Similar phenomenon is evident in Fig. 5.6 from WDFC using identified dominant mode shapes obtained from WMSOBI. The larger curvature change value ranges diminish in the WDFC plot, the fourth plot in Fig. 5.6. Damage detection system can be easily programmed to identify the damage locations by selecting the larger absolute values of WDFC over a threshold, such as 0.01 for the given case in Fig. 5.6.

5.2.3 Numerical Evaluation of Damage with Limited Measurement

The above numerical evaluations utilize all the output from simulated results at 100 nodes. In real applications, only a few sensors will be installed in the riser. In this

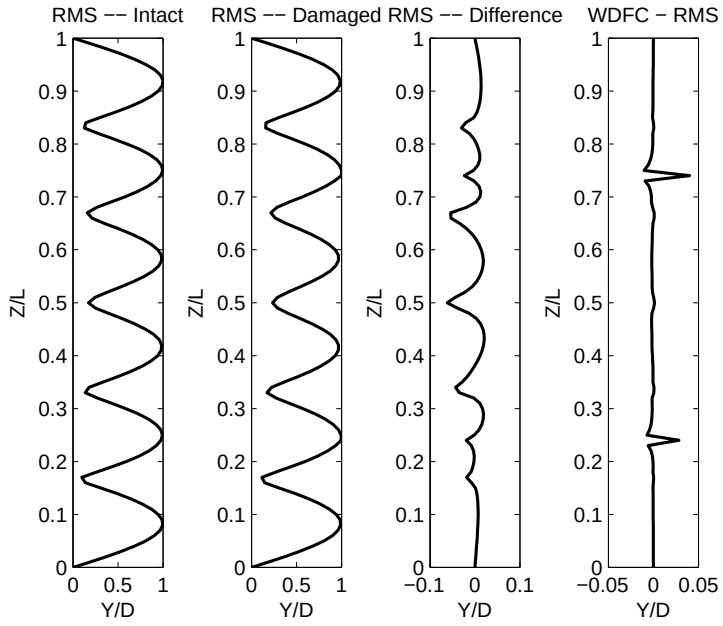

Figure 5.5 : RMS Profiles: (a)Intact,(b)Damaged,(c)Difference between(a)and(b) and (d)WDFC

case, 20 out of 100 nodes are uniformly selected as measured nodes. Then same procedure is carried out for both RMS approach and WMSOBI approach. Results shown in Fig. 5.7 and 5.8 for damage at 0.25 z/L and 0.75 z/L that further prove that for synchronized signals, identified dominant mode shape using WMSOBI method and WDFC is still able to identify the damage locations, while all curvature change methods and WDFC based on RMS profiles cannot.

5.2.4 Damage Severity Estimation in Standing Wave Case

To further study the properties of WDFC, another case in Delta Flume (2003) [58] is chosen with step current profile. The current speed of the lower part of the riser model is $0.31 m/s$. Respect to a single crack with different levels of damage at location 0.3 z/L are simulated. The comparison between curvature change and WDFC is presented in

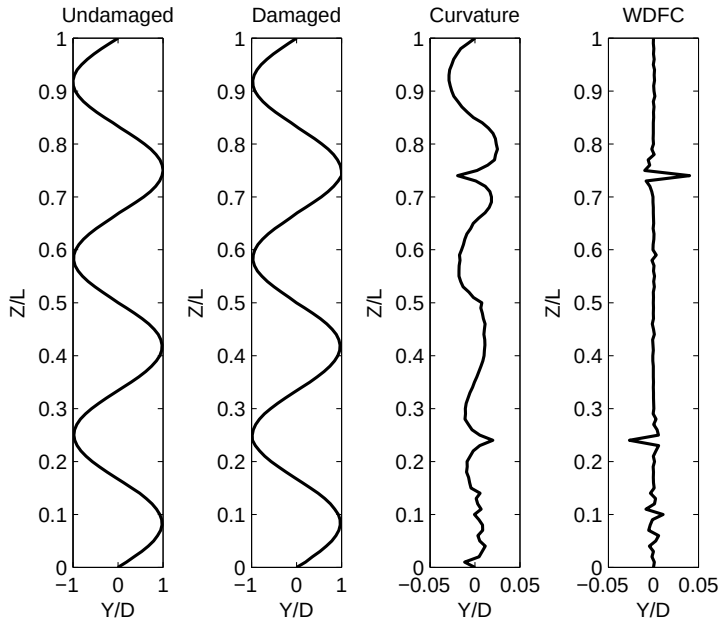

Figure 5.6 : WMSOBI Mode Shape Profiles: (a)Intact,(b)Damaged,(c)Difference between(a)and(b) and (d)WDFC

Fig. 5.9; it is evident that WDFC provides clearer indication than curvature change method.

The different damage levels range from 5% to 99% are presented in Fig. 5.10. In Fig. 5.10, x-axis represents the normalized depth (z/L) and is the relevant depth, and y-axis represents the WDFC values. The plot proves that larger damage will cause larger WDFC value with the same damage location and type.

To further study the relationship between the damage severity and values of WDFC, damage percentage (only bending stiffness reduction) v.s. WDFC values (blue circles) are plotted in Fig. 5.11 with y-axis in log scale. A second order curve (black solid line) is fitted to the given values. Though this fitted curve only suitable for location 0.3 z/L, it also shows that the relationship between damage severity and WDFC is in exponential and second order.

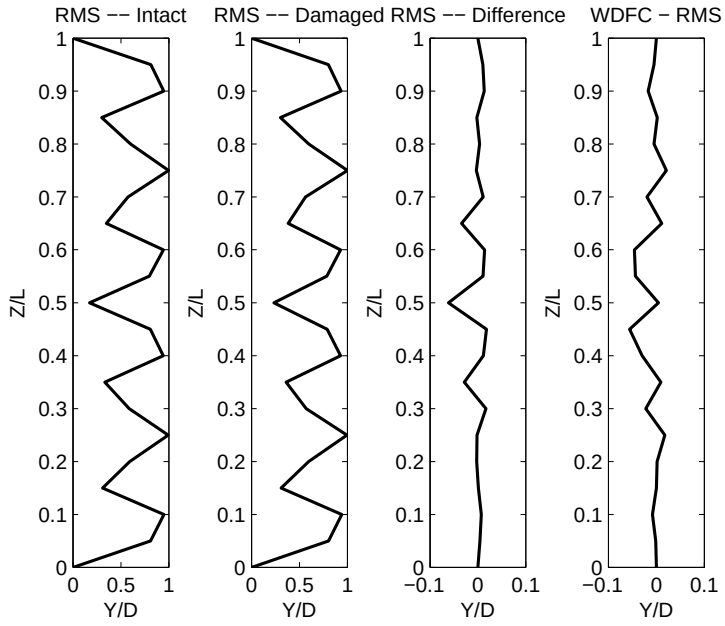

Figure 5.7 : RMS Profiles with 20 Sensors:(a)Intact,(b)Damaged,(c)Difference between(a)and(b) and (d)WDFC

5.2.5 Numerical Evaluation with Gulf Stream Riser Model

Previous two simulations are based on Delta Flume (2003) [58] experiments. The excitation current profile is a step function, which results in a standing wave response of the riser model. To further verify the effectiveness of the proposed WDFC index, Gulf stream (2006) field test with sheared current profile is simulated using proposed 3D analytical model by FEM approach.

5.2.5.1 Traveling Wave with Sheared Current Profile

The simulation parameters and settings are the same as mentioned in Chapter 3. The deepwater riser model is meshed into 70 elements (7 ft per element). Corrosion damages are considered as metal loss, which is simulated as wall thickness reduction. Hence, the section area reduction and bending stiffness reduction are considered at the

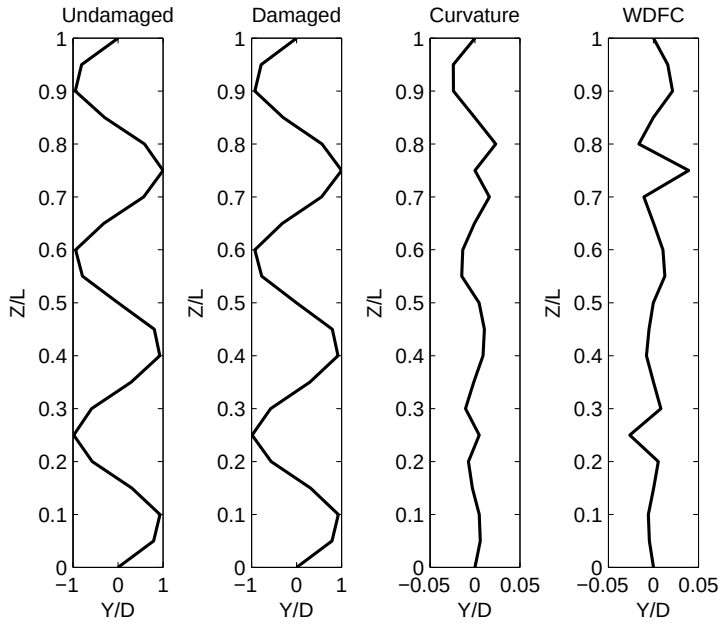

Figure 5.8 : Mode Shape Profiles from WMSOBI with 20 Sensors: (a)Intact,(b)Damaged,(c)Difference between(a)and(b) and (d)WDFC

same time. Both single damage and multiple damages are considered with deepwater riser models. As the fundamental natural frequency determined by tension is around 0.13 Hz, the frequency spectrum of the response of riser contains quite a few close modes, shown in Fig. 3.13. The dominant mode shape is obtained from simulated response using proposed complex wavelet modified second order blind identification method (CWMSOBI).

The real parts of the identified complex mode value for both intact and damaged case are shown in Fig. 5.12. The damage location is pointed by an arrow (at element 30, depth 210 ft). A 50% wall thickness reduction is assumed to simulate corrosion damage. For damaged riser, the dynamic properties will change. Among all the excited modes from damaged case, only one or two share the same natural frequency and mode shape with intact case. The thirtieth mode shape shown in Fig. 5.12 is

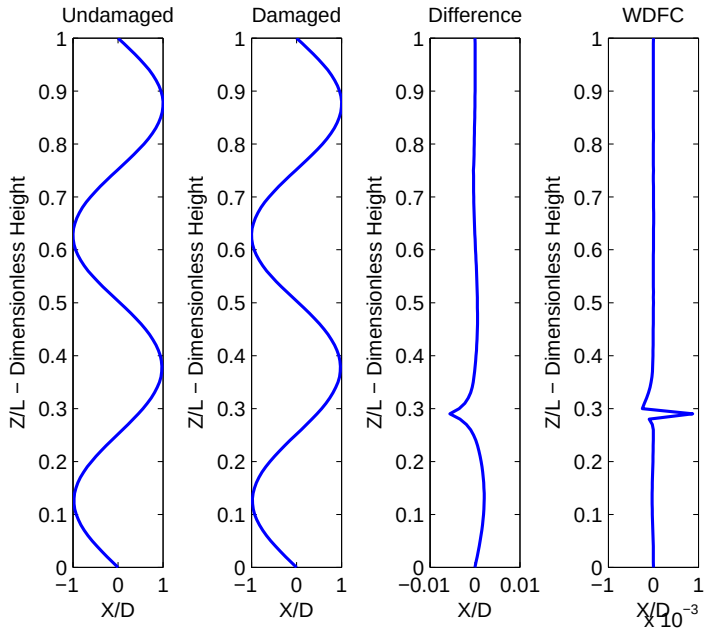

Figure 5.9 : WMSOBI Mode Shape Profiles for Case 3 in Delta Flume (2003): (a)Intact,(b)Damaged,(c)Difference between(a)and(b) and (d)WDFC

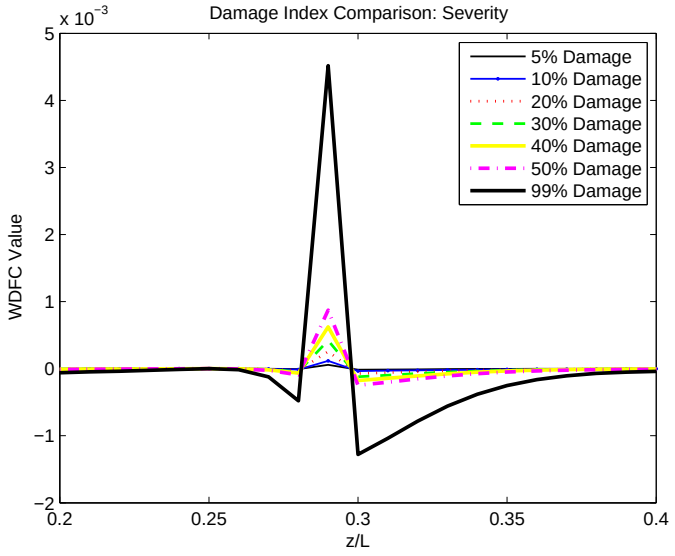

Figure 5.10 : Comparison among Different Damage Level at 0.3 z/L

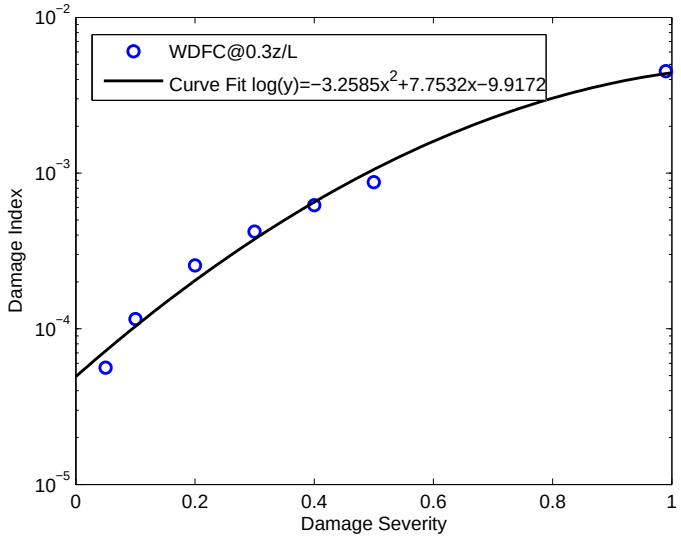

Figure 5.11 : Damage Severity - WDFC Relationship

excited with a natural frequency, 3.9266 Hz. Fig. 5.12(d) shows that in traveling wave case with sparse sensors, WDFC cannot point out where the damage is. The "sparse" is determined by the ratio between mode number and the number of sensors. The larger the ratio is, the sparser the sensors are comapared to the mode shape nodes, and hence less accurate. This simulation has a sparse ratio of nearly $\frac{3}{7}$.

5.2.5.2 Standing Wave with Uniform Current Profile

In order to reduce the sparseness and create a standing wave, a lower speed ($V = 0.5m/s$) uniform current profile is used to excite the Gulf Stream riser model. The fourteenth mode (2.1294 Hz) is excited in both intact and damaged case. The sparse ratio is $\frac{1}{5}$. The arrow is pointing where damage is located- 50th element at 350 ft depth with 50% wall thickness reduction. The final results are shown in Fig. 5.13. The fourth profile in Fig. 5.13 clearly shows a peak at the damaged location. However,

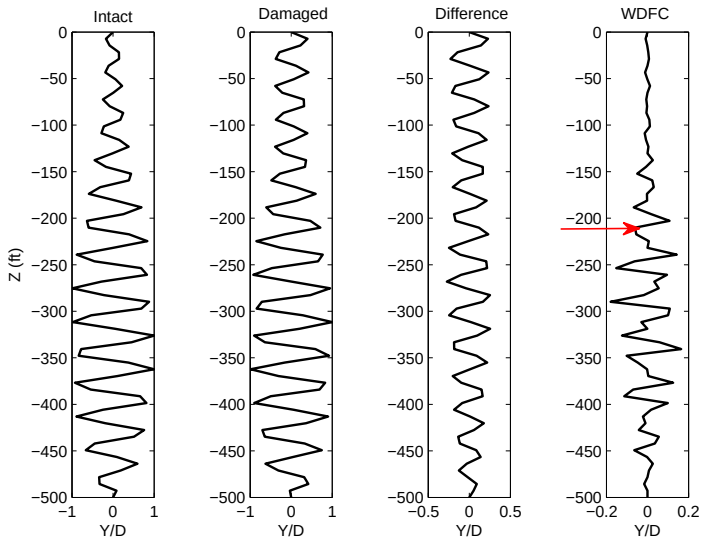

Figure 5.12 : Mode Shape Profiles with Gulf Stream Riser Model subject to Sheared Current: (a)Intact,(b)Damaged,(c)Difference between(a)and(b) and (d)WDFC

there is still a smaller false peak at depth 270 ft. A higher threshold can help the automation program to neglect the false peak.

5.2.6 Summary of WDFC

Comparing to curvature change damage index, the proposed WDFC damage index provides better damage location information. For standing wave cases, WDFC can even provide damage severity estimation if the database is established before and the second order curve (as Fig. 5.11) is known.

However, the WDFC methods gives poor damage detection results for traveling wave with sparse sensor distribution. A more robust method for sparse sensor distribution with traveling wave vibration is needed.

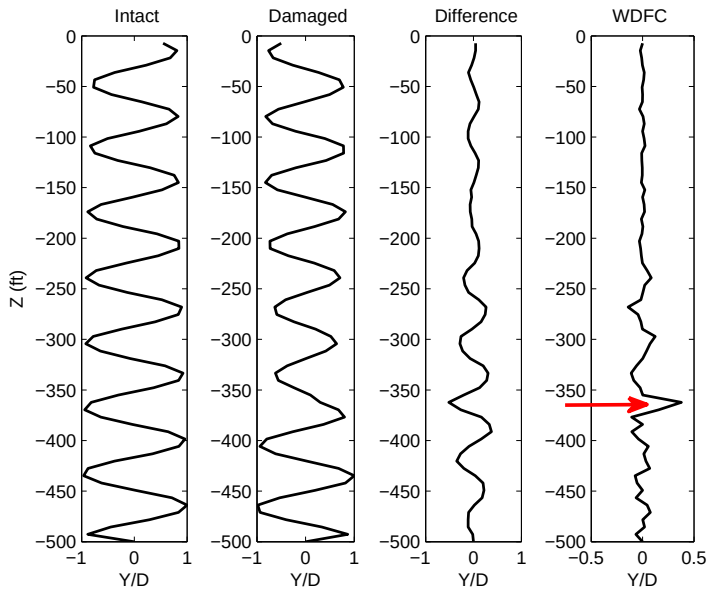

Figure 5.13 : Mode Shape Profiles for Damage Detection of Gulf Stream Riser Model subject to Uniform Current: (a)Intact,(b)Damaged,(c)Difference between(a)and(b) and (d)WDFC

5.3 Phase Angle Change Index for Damage Detection

To address the difficulties in damage detection for deepwater risers, such as traveling wave and sensor sparseness, a new damage index based on phase angle of the mode shape is proposed.

5.3.1 Definition of Phase Angle in Phase Angle Change (PAC) Index

The "phase" used in the proposed change index is the phase angle obtained from Hilbert transform of the real parts of the obtained complex mode shape. The phase angle is unwrapped, which means is not limited in $(-\pi, \pi)$ and is continuous. Previous numerical simulations on standing wave and traveling for Gulf Stream riser model are used for phase change index study.

Original Hilbert transform is defined as equation 5.5, where $u_{y,z}$ denotes the curvature in y-direction at depth z. dz means the transform is a spatial transform in vertical (z) direction.

$$H(u)_{y,z} = \frac{1}{\pi} \int_{-\infty}^{\infty} \left(\frac{u_{y,h}}{z-h} \right) dh \tag{5.5}$$

The final signal X combines the Hilbert transform from equation 5.5 as the imaginary part with the original signal as the real part to obtain an analytical signal [27], which is shown in equation 5.6.

$$X_{y,z} = u_{y,z} + iH(u)_{y,z} \tag{5.6}$$

Then the unwrapped phase angle of the final signal X is used for phase angle change damage index study.

5.3.2 Numerical Evaluation of Damage in a Standing Wave Case

A few single crack simulations and one two-crack simulation are carried out for uniform current excitation case. The common curvature mode shape excited among all the cases is the fourteenth mode with frequency 2.1294 Hz.

5.3.2.1 Single Crack Case

Phase change index plots with single damages at Element 30, 40 and 50 are shown in Fig. 5.14, 5.15 and 5.16, respectively.

The x-axis represents the sensor numbers (or the node numbers for 70 elements simulations); the y-axis shows the phase angle in radian. Figs. 5.14(a) to 5.17(a) show the absolute unwrapped spatial phase angle of the fourteenth curvature mode shapes identified from intact and damage cases. Figs. 5.14(b) to 5.17(b) show the

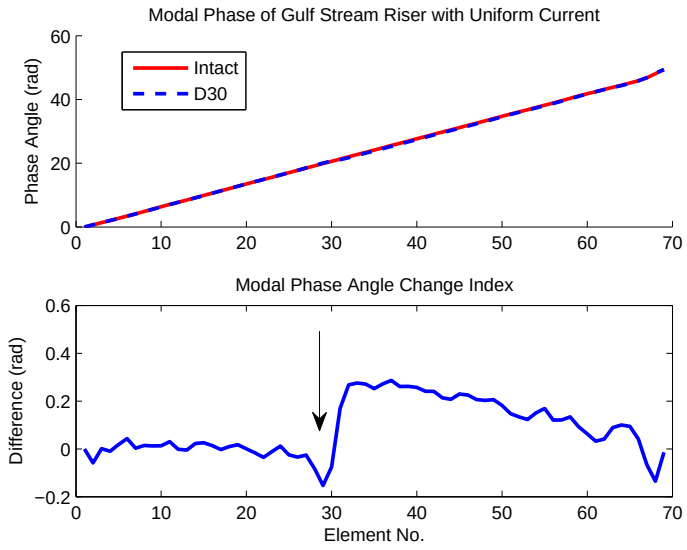

Figure 5.14 : Damage at Element 30-PAC Index with Uniform Current:(a)phase angle in intact and damaged (element 30) cases, (b)phase angle difference between intact and damaged case

phase angle differences between the intact and corresponding damaged cases. The peaks in Figs. 5.14(b) to 5.17(b) clearly indicate where the damage is located.

5.3.2.2 Multiple Crack Case

Furthermore, a two-crack case simulated and processed for phase angle change index is shown in Fig. 5.17. Similarly, the two distinct peaks locate the damages introduced as wall thickness reduction, at element 30 and element 50.

5.3.3 Numerical Evaluation of Damage in a Traveling Wave Case

The effectiveness of the proposed phase change index is evaluated next in the traveling wave vibration case. The actual sheared current profile from field test of Gulf Stream (2006) [28] is used as excitation. Both single crack and multiple crack cases are considered. Proposed procedure is used to get the unwrapped phase angle.

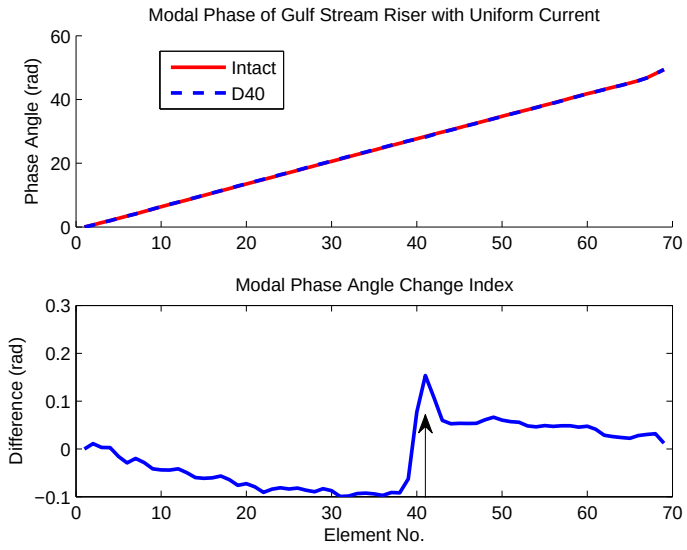

Figure 5.15 : Damages at Element 40-PAC Index with Uniform Current:(a)phase angle in intact and damaged (element 40) cases, (b)phase angle difference between intact and damaged case

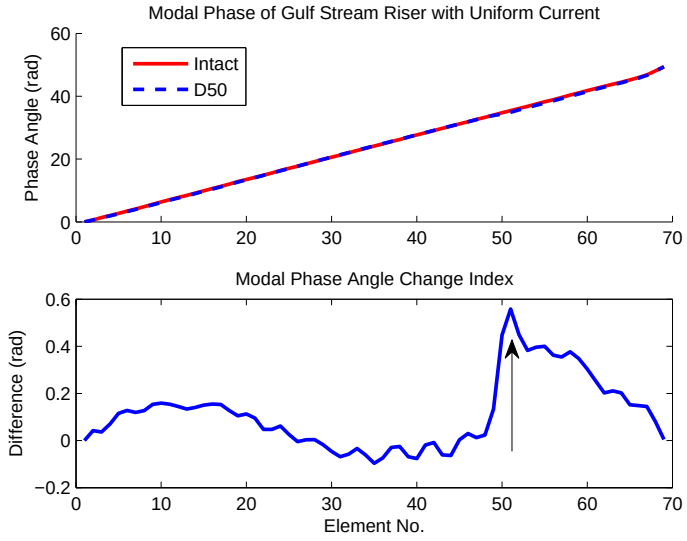

Figure 5.16 : Damages at Element 50-PAC Index with Uniform Current:(a)phase angle in intact and damaged (element 50) cases, (b)phase angle difference between intact and damaged case

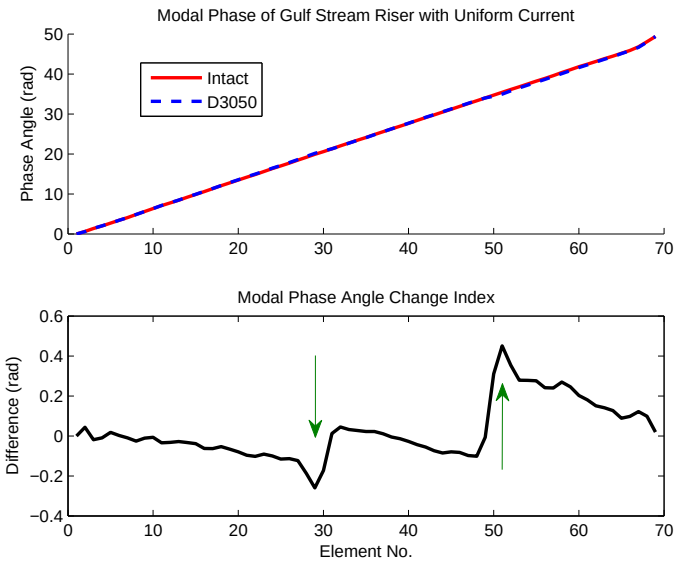

Figure 5.17 : Damages at Element 30 and 50-PAC Index with Uniform Current:(a)phase angle in intact and damaged (element 30 and 50) cases, (b)phase angle difference between intact and damaged case

5.3.3.1 Single Crack Case

Phase angle for single crack occurring at element 30 is presented in Fig. 5.18. Fig. 5.18(b) shows that there is no sharp peak in the phase angle difference between intact and damaged simulation results at element 30. However, there is a steep phase angle shift slope around the damaged location. The absolute slope is much larger than normal phase shift slope without cracks. In addition, at both ends there are usually some larger slopes or changes because ends are simulated as pin.

Single crack case at element 40 is presented in Fig. 5.19. Similar phenomenon can be observed at the location of damage. The phase angle difference shifts rapidly within 3 elements (the damaged element and its adjacent elements). As before and after the phase angle shift, the phase angle difference has a steep slope. This phase shift can be treated as the damage indicator.

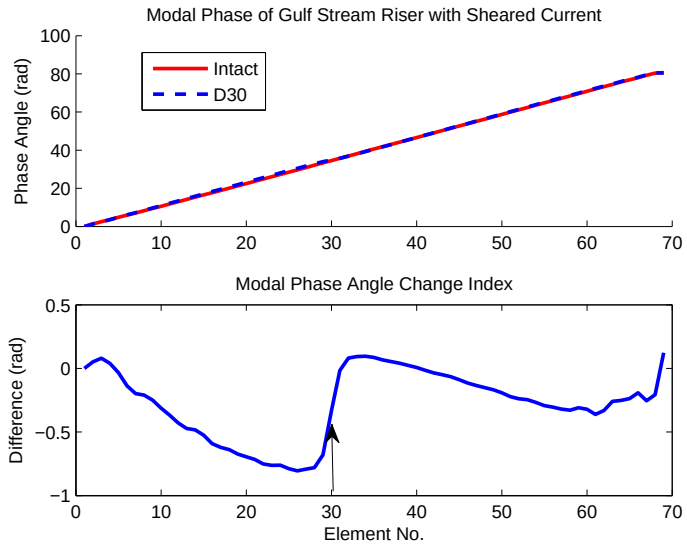

Figure 5.18 : Damage at Element 30-PAC Index with Sheared Current:(a)phase angle in intact and damaged (element 30) cases, (b)phase angle difference between intact and damaged case

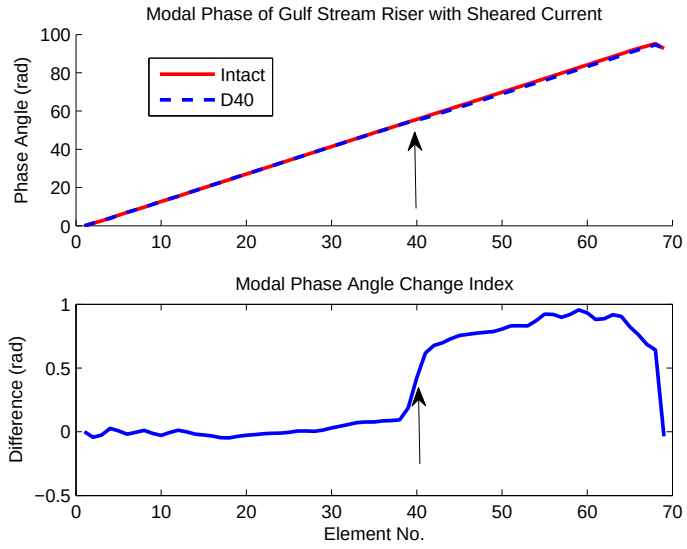

Figure 5.19 : Damage at Element 40 - PAC Index with Sheared Current:(a)phase angle in intact and damaged (element 40) cases, (b)phase angle difference between intact and damaged case

5.3.3.2 Multiple Crack Case

Next, a two-crack case is simulated. Damage is assumed to occur at element 30 and element 50. The PAC index from identified curvature mode shape is presented in Fig. 5.20. The rapid shifts of PAC index around element 30 and 50 are clear indicator of damage location.

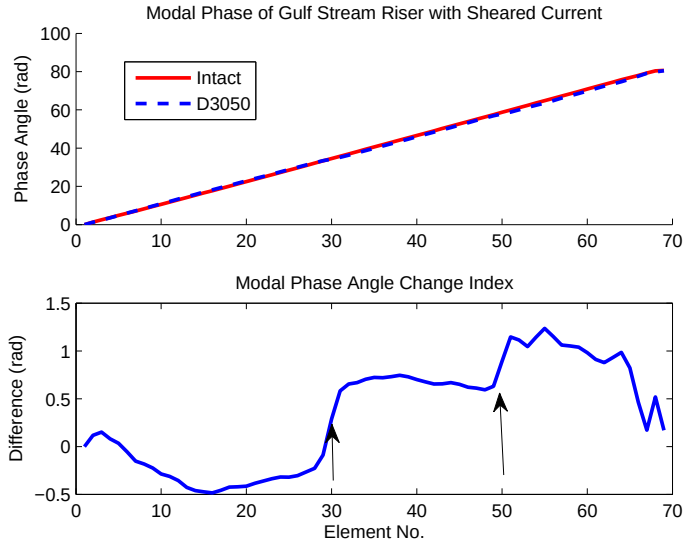

Figure 5.20 : Damages at Element 30 and 50 - PAC Index with Sheared Current:(a)phase angle in intact and damaged (element 30 and 50) cases, (b)phase angle difference between intact and damaged case

5.4 Summary

This chapter proposed two damage indices based on identified curvature mode shape: weighted distributed force change (WDFC) damage index and phase angle change (PAC) damage index.

For WDFC,

- WDFC provides better damage location information than curvature change damage index, for both limited sensor and full set sensor distribution.
- WDFC can give damage severity estimation as there is a second order exponential relationship between WDFC and the bending stiffness loss percentage.
- However, WDFC does not work when the vibration is a traveling wave type with sparse sensor distribution.

To overcome the issues with traveling wave and sparse sensors, PAC damage index is proposed.

- PAC can locate damages (metal loss) in deepwater riser for either standing wave or traveling wave vibration.
- PAC can indicate the range of damage location when the risers are sparsely instrumented. The indicator is the average phase angle difference shift around the damage location.
- However, PAC might not be able to capture the damage located close to either end, because both ends are close to the zero node in a mode shape.

Chapter 6

Fatigue Damage and Fatigue Life Estimation

"Fatigue" is defined as the gradual process of progressive and localized permanent structural damage occurring in a material subjected to cyclic loading (stress and strains) at certain nodes by American Society of Testing and Materials (ASTM); the damage is cumulative and eventually will lead to a sudden complete fracture (failure) after repeated loading cycles over a threshold number.

There are two types of fatigue damage: low-cycle fatigue and high-cycle fatigue. Low cycle fatigue occurs when the cyclic stress-strain amplitude are large enough to cause plastic strain residue in each loading cycle and only a few load cycles can lead to failure. Generally, the material behaviors for low-cycle fatigue are best modeled based on strains. On the other hand, high-cycle fatigue is a better known as stress dominant fatigue with stress-strain amplitude within elastic range. High-cycle fatigue is the one widely used in structural design codes. Safety factors are used in the design codes to ensure that plastic strain will not occur under regular loading.

Fatigue damage usually occurs at positions with sharp shape changes or large cyclic loadings, for example, the edges of square pipes or the connection joints of beams and columns. For offshore structures, tubular members are generally used to reduce the sharp edges, however, the interconnections between different section with welded joints are the most possible fatigue damage locations due to small welding defects.

Fatigue damage eventually will lead to a sudden fractural failure, which strongly

reduces the service life of the structure and gives little time before failure. Hence, fatigue failure is unwanted and should be avoided. To avoid or reduce the probability of fatigue failure, there are two ways:

1. to design the structures in a way that they can avoid the source of cyclic loading or they are strong enough to sustain a large number of cycles (a certain length of service life, usually in years, e.g., more than 25 years [10] for riser) of a certain stress amplitude of cyclic loading;

2. to detect/estimate the in-situ fatigue damage during the service life of the structure, which is even more important to prevent sudden failure as the actual loading may be larger than the designed loading.

The second way can be included in the proposed structural health monitoring system.

6.1 Fatigue Estimation Techniques in Offshore Structural Design

To avoid the sudden fractural failure caused by fatigue and to ensure required length of service life of offshore structures, fatigue estimation is one of the most important design criterion. Currently, there are mainly two types of fatigue estimation methods in design procedure: one is based on fracture mechanics; the other is based on S-N Curve (a constant stress range (S) and corresponding allowable number (N) of loading cycles).

6.1.1 Fatigue Estimation using Fracture Mechanics

In fracture mechanics, the fatigue damage is characterized into three stages: crack initiation (nucleation); crack propagation (growth) and failure (fracture, loss of stiff-

ness etc.) as shown in Fig. 6.1. When a certain number of cycles, N_I, of loading occurs, the initial cracks begin to grow and propagate. The cracks grow and cause sudden failure when the crack size reaches certain limit (or in other words, the cycle number reaches the the failure number, N_F). In high fatigue lives, the fatigue crack initiation period may exceed 95% of the fatigue life. Hence, in this case the structural component will cause the end of service life if repair is not possible once the crack reaches a certain size.

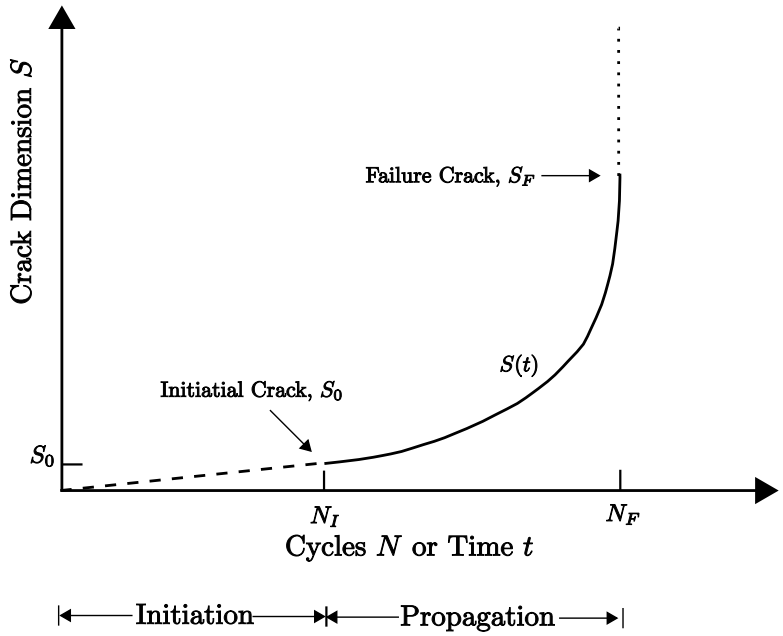

Figure 6.1 : Different Stages of Crack Growth

Fatigue estimation (crack propagation) can be simulated using fracture mechanics and finite element method (FEM). However, recognizing the complexity and time consumed for fracture mechanics approach with FEM, the simpler S-N approach is dominant as the fatigue design criterion. The fracture mechanics approach is often used to verify the S-N approach, to estimate the minimum detectable flaw size and

to predict crack propagation [90].

6.1.2 Fatigue Estimation using S-N Curve

General procedure for fatigue analysis based on S-N curve is divided into four steps:

1. Cyclic loading estimation based on recommended practice in codes such as DNV-OS-F201 considering the environmental loads such as wave, wind, current and floater motion etc.;

2. Initialization of fatigue assessment, including selection of S-N curve, fatigue design factor (FDF) and design fatigue life length etc.;

3. Fatigue estimation based on chosen fatigue damage estimation method with estimated cyclic loading and other parameters;

4. Fatigue safety check by comparing the design fatigue life and estimated fatigue life for a given design structure.

Since the loading estimation is not the main focus in this thesis, the latter three steps are detailed next.

6.1.2.1 S-N Curve

When the material of the structure is homogenous, the S-N curve is determined by the properties of the material. However, for offshore structures, there are welded materials as well as parental material (material of primary structure). Because the fatigue damage usually occurs at the welded joints due to higher stress as well as higher possibility of imperfection, the fatigue life is determined by the welded joints in the practical fatigue design. The welded joints are classified into different classes as shown in Fig. 6.2.

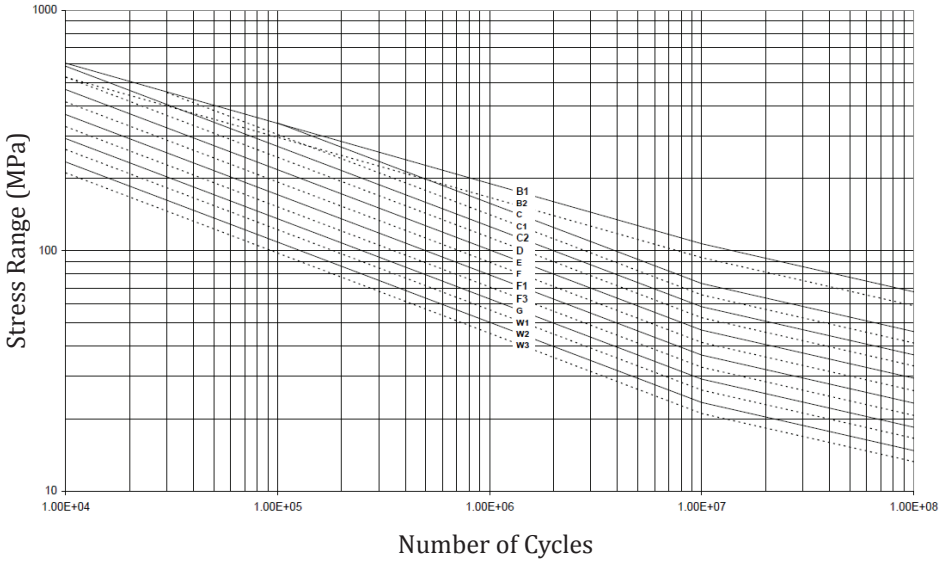

Figure 6.2 : Different Classes of S-N Curves in Seawater [10]

In the recommended practice of riser fatigue design from DNV [10], two-slope S-N curve, as shown Fig. 6.2, is chosen. The curves are obtained from fatigue testing. Generally, the cycle number between 1×10^6 and 1×10^7 are the point of slope change in the log-log plot. The allowable cycles for a given stress can be estimated using equation 6.1.

$$N = \begin{cases} a_1 \cdot S^{-m_1} \\ a_2 \cdot S^{-m_2} \end{cases} \tag{6.1}$$

where a_1, a_2, m_1 and m_2 are fatigue constants, the values of which are obtained from Fig. 6.2. m_i is the slope, while a_i is the strength constant.

6.1.2.2 Miner-Palmgren Rule

In the fatigue estimation step, the cumulative characteristics of fatigue damage is considered by using the Miner-Palmgren rule [37], given in equation 6.2.

$$D = \sum_i \frac{n(S_i)}{N(S_i)} \tag{6.2}$$

where $n(S_i)$ represents the actual cycles of loading stress S_i, and $N(S_i)$ denotes the allowable cycles (maximum numbers to failure) of loading stress S_i for the corresponding S-N curve [10].

6.1.2.3 Fatigue Safety Check

With the damage information obtained in equation 6.2, the acceptance criterion for fatigue damage can be written as

$$D \times FDF \leq 1.0 \tag{6.3}$$

where FDF is the abbreviation for fatigue design factor that is chosen.

In other words, the fatigue safety check has to make sure that the accumulated fatigue over the life time of riser multiplied with FDF is smaller than 1 when the riser is subjected to estimated cyclic loading.

6.2 In-Situ Fatigue Damage Estimation Methods

For offshore structures, there are not a lot of methods available to detect fatigue damage in a timely manner. Usually, the response time histories of strain (or acceleration) of particular nodes in the riser are measured, and then processed using rainflow count method to get the accumulated the fatigue damage. The details of

rainflow count method can be found in [41]. The strategy of Rychlik Rainflow count method is shown in Fig. 1.5.

However, the time history methods need lot of storage for the data and time for processing. In addition, the rainflow count method does not take advantage of synchronized data when available. To overcome these disadvantages, a frequency domain method is proposed for synchronized signals.

6.2.1 Proposed Frequency Domain Methods

The the frequency domain method for fatigue damage estimation is divided into four steps as shown in Fig. 6.3: blind identification, root mean square value computation, least square approximation and fatigue damage estimation.

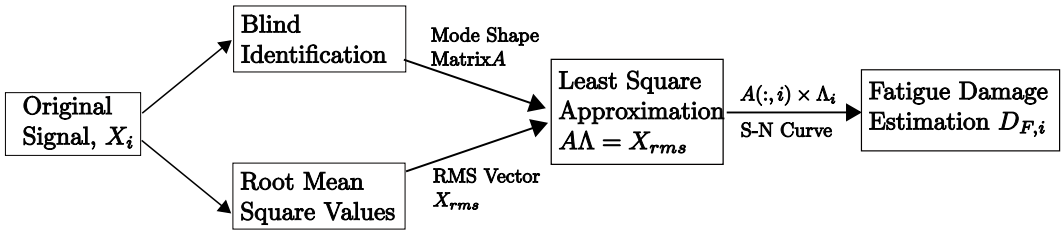

Figure 6.3 : Strategy of Proposed Frequency Domain Fatigue Estimation Method

6.2.1.1 Blind Identification

Using the same approach proposed in chapter 4, the dominant strain mode shapes are identified from the measured strain signals. The key equation is

$$X = AS \tag{6.4}$$

where A is the mode shape matrix, X is the vector of original signals and S is the vector of sources. Generally, the mode shapes are normalized to a maximum of one

in each column. In addition, not all the columns are needed when there are many channel signals. Only first few columns are enough for deepwater riser with vortex-induced vibration (VIV).

6.2.1.2 Root Mean Square Value

For each channel, the root mean square value is obtained for time period when VIV occurs using equation 6.5.

$$X_{rms,i} = \sqrt{\frac{\sum_{k=1}^{N} X_{i,k}^2}{N}} \tag{6.5}$$

where $X_{i,k}$ denotes the strain value of channel i at time step k and $X_{rms,i}$ represents the RMS value of channel i.

6.2.1.3 Least Square Approximation

In this step, identified mode shapes are combined with a vector of weights to match the RMS vector from actual measurement, such as shown in the equation 6.6. Since not all the mode shapes are chosen, the vector of weights will be approximate determined using least square method.

$$A_{chosen}\Lambda_{chosen} = X_{rms} \tag{6.6}$$

where A_{chosen} represents the chosen columns from the original matrix A obtained from blind identification, Λ_{chosen} represents the vector of weights.

6.2.1.4 Fatigue Damage Estimation

The fatigue damage estimation for each individual strain mode shape is carried out in the following steps:

1. Based on the results of equation 6.6, the component mode shape will have a strain amplitude, $\epsilon_i = \frac{A(:,i)}{\sqrt{2}}$, where $\sqrt{2}$ is the constant ratio between sine wave amplitude and its RMS value.

2. Based on equation $\sigma = E\epsilon$, stress can be easily calculated from strain ϵ.

3. Based on the corresponding stress amplitude in the S-N curve, the failure (allowable) cycles N_{F_i} is obtained, for the chosen i^{th} component mode.

4. The fatigue damage for the given time period, t, due to the chosen i^{th} component mode can be calculated according to Miner's rule using equation 6.7.

$$D_i = \frac{t * f_i}{N_{F_i}} \tag{6.7}$$

   where D_i is the fatigue damage due to i^{th} mode; f_i is the natural frequency of i^{th} mode with units in Hz.

In the given time t, the total fatigue damage is the sum of fatigue damage caused by different modes.

$$D = \sum_i D_i = \sum_i \frac{t * f_i}{N_{F_i}} \tag{6.8}$$

Furthermore, with the assumption that the loading conditions remain stationary for a long time, the fatigue life is estimated by combining Miner's rule and the total damage obtained in equation 6.8. The equation to estimate fatigue life is shown in equation 6.9.

$$L_f = \frac{t}{D} = \frac{t}{\sum_i D_i} = \frac{1}{\sum_i \frac{f_i}{N_{F_i}}} \tag{6.9}$$

The control center can delete the original data, but the mode shapes, corresponding frequencies and accumulated the fatigue damage from equation 6.8 can be re-

tained. Larger values in the fatigue damage vector, D, indicate the most likely location of fatigue damage.

6.3 Application on Gulf Stream Field Test Data

To evaluate the performance, of the proposed frequency domain method, it is applied to the field test data from Gulf Stream (2006) [28]; "EVENT20061020-174124" is chosen to be the test data. According to the spatial-frequency plot in Fig. 6.4, there are four dominant frequency components in the cross-flow direction. As a result, the four corresponding mode shapes are chosen to reconstruct the original signals.

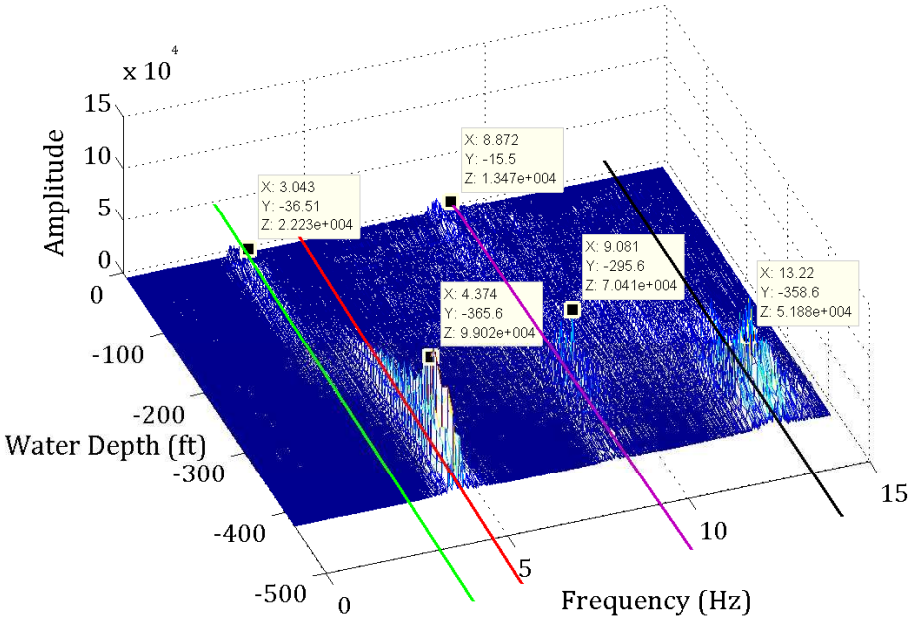

Figure 6.4 : Spatial-Frequency Plot for Event1020174124

6.3.1 Strain Mode from Blind Identification

After data calibration, the cross-flow direction data, Q2, is analyzed using wavelets/SOBI method. The peak normalized RMS value profile of extracted dominant frequency component (4.32 Hz) in Fig. 6.5(b) shows that it plays a dominant part in the riser vibration. The absolute value profile of the strain mode shape (in Fig. 6.5(c)), shown in Fig. 6.5(d), matches with the RMS value profile of extracted data shown in Fig. 6.5(b).

6.3.2 Least Square Approximation

To reconstruct the original RMS values of Q2 from Fig. 6.5(a) – the target vector, X_{rms}, four maximum normalized dominant strain modes are chosen to form the source matrix A_{chosen}. Least square method is used to get the vector of weights, Λ_{chosen}. Then each component strain mode is plotted in the following plot.

The dominant modes shown in Fig. 6.6 clearly show that for mode with frequency 3.03 Hz the power-in region is at the upper location, which matches with spatial-frequency plot in Fig. 6.4. So do the amplitudes for other three dominant modes. The amplitudes of the strain modes in Fig. 6.6 show that the dominant fatigue damage is caused by the mode with frequency 4.37 Hz. The strain modes also indicate that the high frequency low amplitude cyclic loading such as the third harmonic in the cross-flow direction cannot be neglected either.

The profile of RMS values from reconstructed signals are compared with the original profile of RMS values in Fig. 6.7. Though the absolute values vary a bit, the trend and average profile of RMS values from reconstructed signal matches with the original signal.

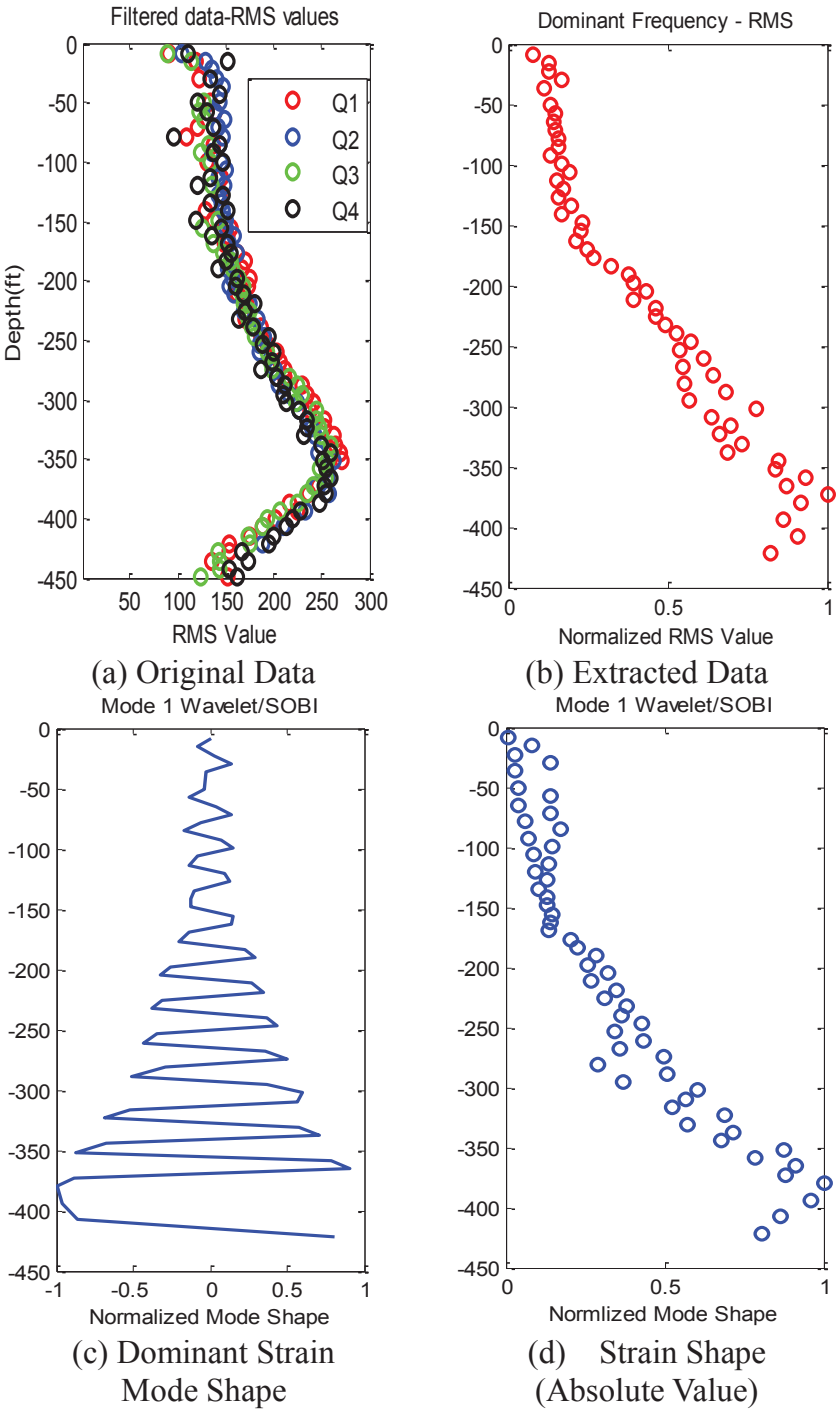

(a) Original Data

(b) Extracted Data

(c) Dominant Strain Mode Shape

(d) Strain Shape (Absolute Value)

Figure 6.5 : Blind Identification from Field Data

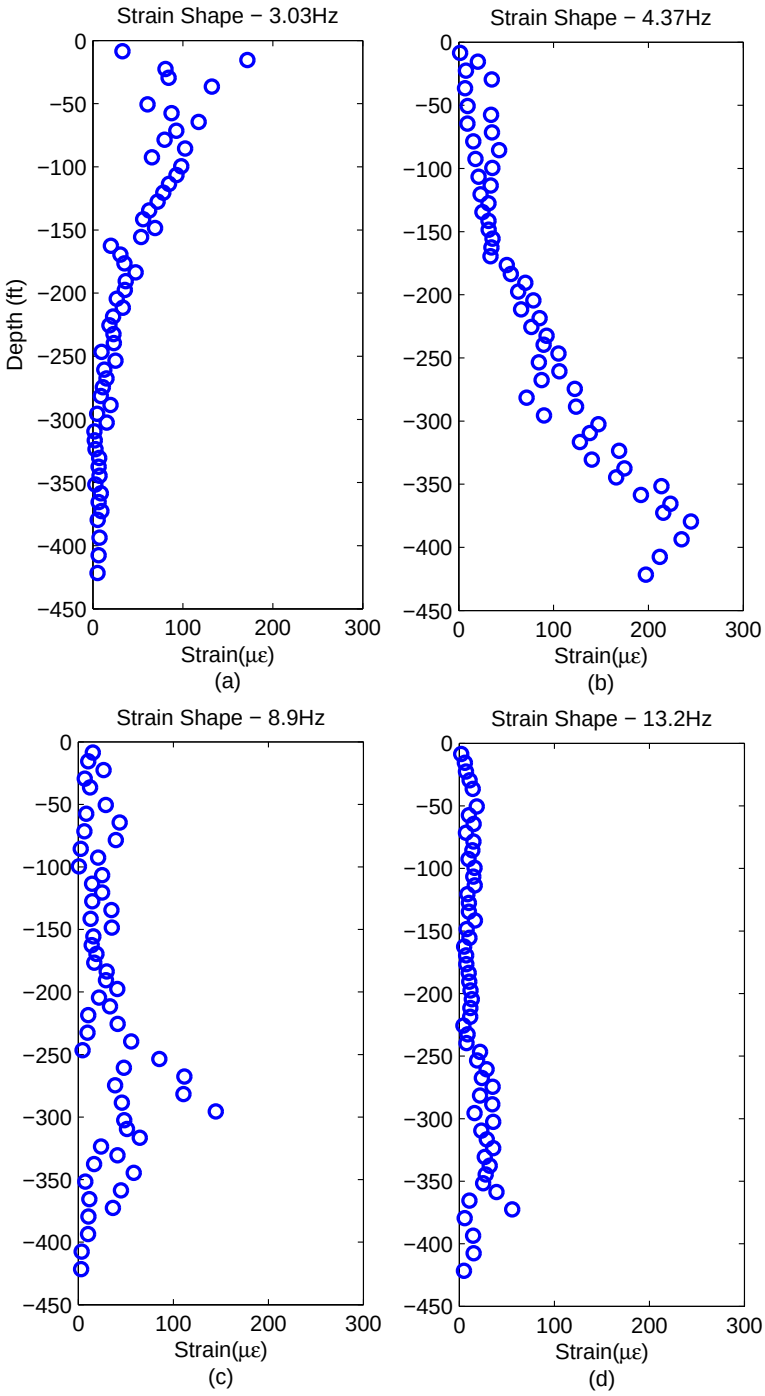

Figure 6.6 : Weighted Strain Mode Shapes

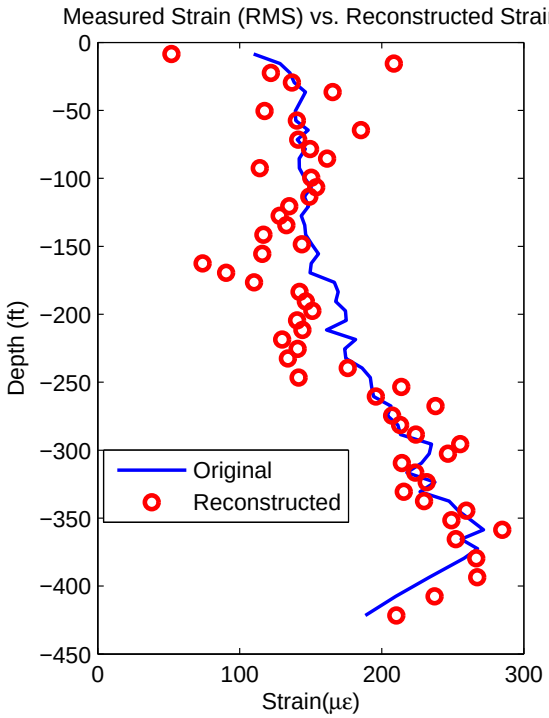

Figure 6.7 : Comparison of Profiles of RMS values from Reconstructed and Original Signals

6.3.3 Fatigue Estimation

With the chosen strain mode shapes and their corresponding vibration frequencies, the fatigue damage in given period and fatigue life under the same cyclic loading are estimated.

6.3.3.1 Fatigue Damage Estimation

For a given time period, the cumulative fatigue damage for each cyclic strain profile/mode is calculated based on to S-N curve widely used in steel fatigue analysis. Fatigue constant $a = 1.52 \times 10^{12}$, and $m = 3$ for steel with class D welds, is chosen for longer fatigue life [10].

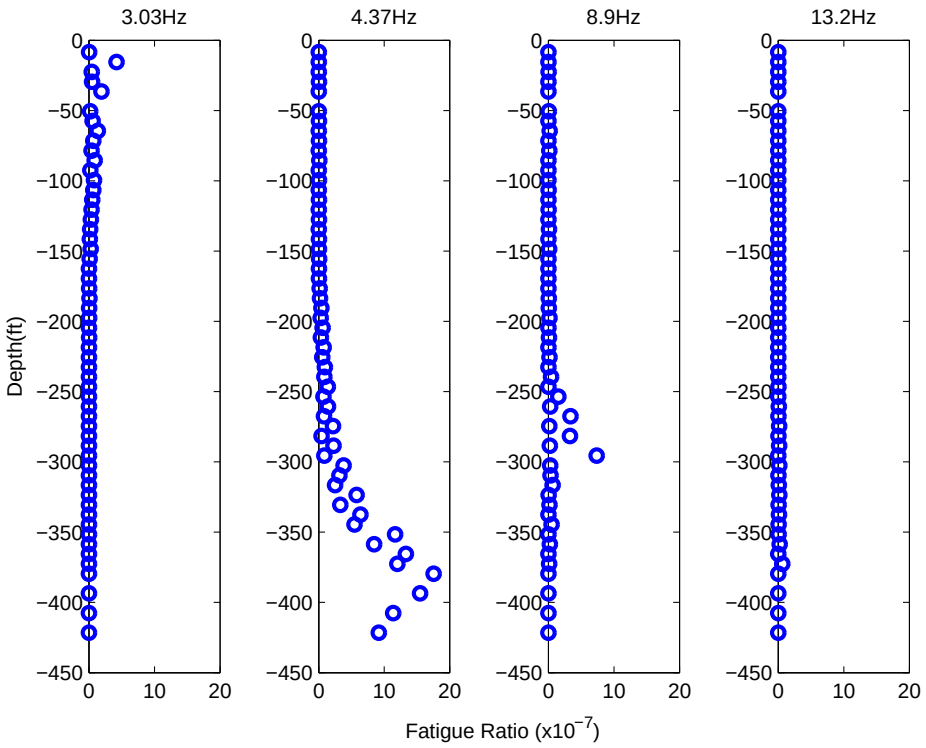

Figure 6.8 : Fatigue Damage by Each Mode in Unit Time

Fatigue damage is a cumulative process. The cumulative fatigue damages caused by each frequency component are carried out for a unit time, as shown in Fig. 6.8 . It is obvious that under the current loading, the fatigue damage is mainly caused by the dominant frequency component (4.37Hz).

6.3.3.2 Fatigue Life Estimation

Based on experimental researches and Miner's rule, fatigue damage is a cumulative process; any loading cycle will contribute to the process. Consequently, though the peak values in the top region of of 3.03 Hz fatigue ratio profile (Fig. 6.8(a)) and the middle range of 8.9 Hz fatigue ratio profile (Fig. 6.8(c)) are not high compared to

the peak values in 4.37 Hz profile, their contribution is very critical and cannot be neglected. Otherwise, the design is less conservative. As a result, the final fatigue damage estimation is combined with damages caused by all four dominant frequency components.

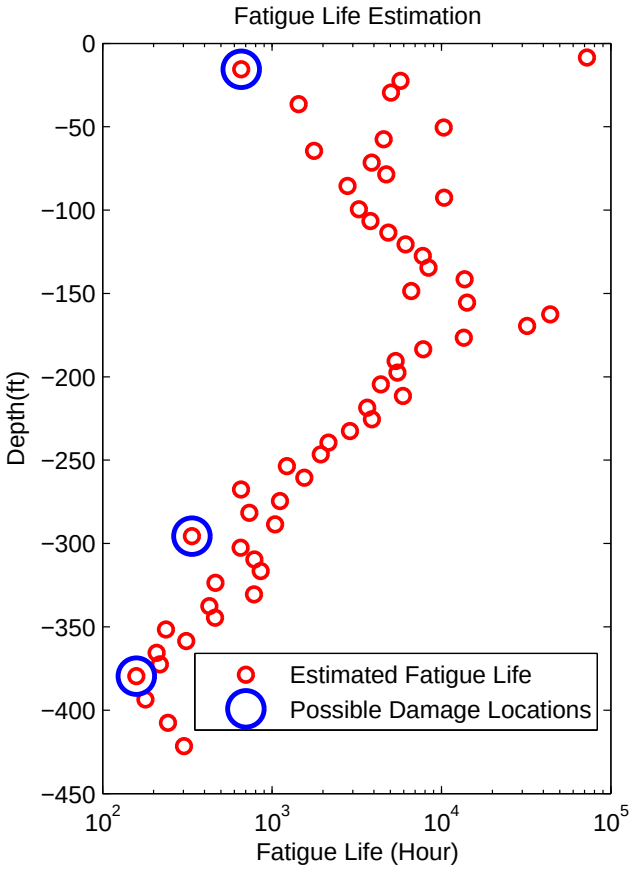

Figure 6.9 : Fatigue Life Estimation under Given Cyclic Loading

In Fig. 6.9, the circles represent the most likely fatigue damage locations. Under the given cyclic loading and chosen fatigue constants, the riser model cannot survive for a long time.

6.4 Conclusion

With the modal properties identified from the proposed blind identification method and chosen S-N curve, the actual fatigue damage (or corresponding fatigue life) can be estimated using proposed frequency based method.

1. The proposed method significantly reduces the data storage requirement by replacing the time domain data with identified strain mode shapes and corresponding frequencies.

2. The proposed method considers fatigue damages caused by multiple frequency components while some of the commercial software products only consider the dominant frequency (1X in the cross-flow direction).

3. Proposed blind identification method can provide good estimation of strain modes from response data.

4. The performance of proposed fatigue estimation relies on the accuracy of modal information extracted using blind identification.

Chapter 7

Experimental Study of Proposed Methods

7.1 Experimental Setup

In the previous chapters, the proposed finite element method, blind identification method and damage detection method are validated with both numerical simulations and experimental data obtained from other researchers. This chapter focuses on testing the proposed methods on a sealed pipe model.

7.1.1 Riser Model Setup

As shown in Fig. 7.1, a 186 inch long pipe with 2.5 inch inner diameter is placed horizontally and fixed at one end. Two shakers are attached to the pipe at 88.8 inch and 163.5 inch. The pipe is held using vertical cables and allowed to vibrate in the horizontal plane only.

The flowchart of test input (excitation signals), actual loading and output (vibration responses) with the data acquisition system is shown in Fig. 7.2. Excitation signal is commanded and measured response is recorded.

7.1.2 Actuator Setup

Because the current profiles in the field are generally non-uniform, two shakers are used to simulate the non-uniform excitation. Three different excitation signals are used in the experiments: chirp (sine sweep signal from 1 Hz up to 90 Hz for different

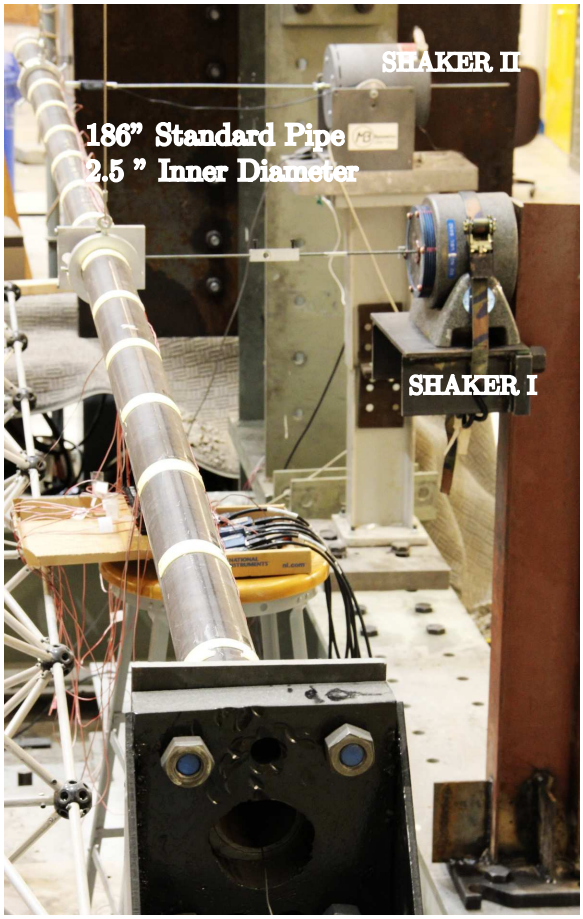

Figure 7.1 : Experimental Setup

time durations), white noise (random signal) and pure sine wave with different frequencies. Different combinations of these signals are commanded for both shakers.

Shaker I shown in Fig. 7.3, has a maximum output force, 500 lb. The stroke of Shaker I is 0.5 inch. Shaker II shown in Fig. 7.4 has a maximum output force, 50 lb. The stroke of Shaker II is 1 inch.

Excitation signals are generated using National Instruments c-DAQ 9178 chassis (8 module slots) with module NI-9263 (4 analog output channels). As the experiment

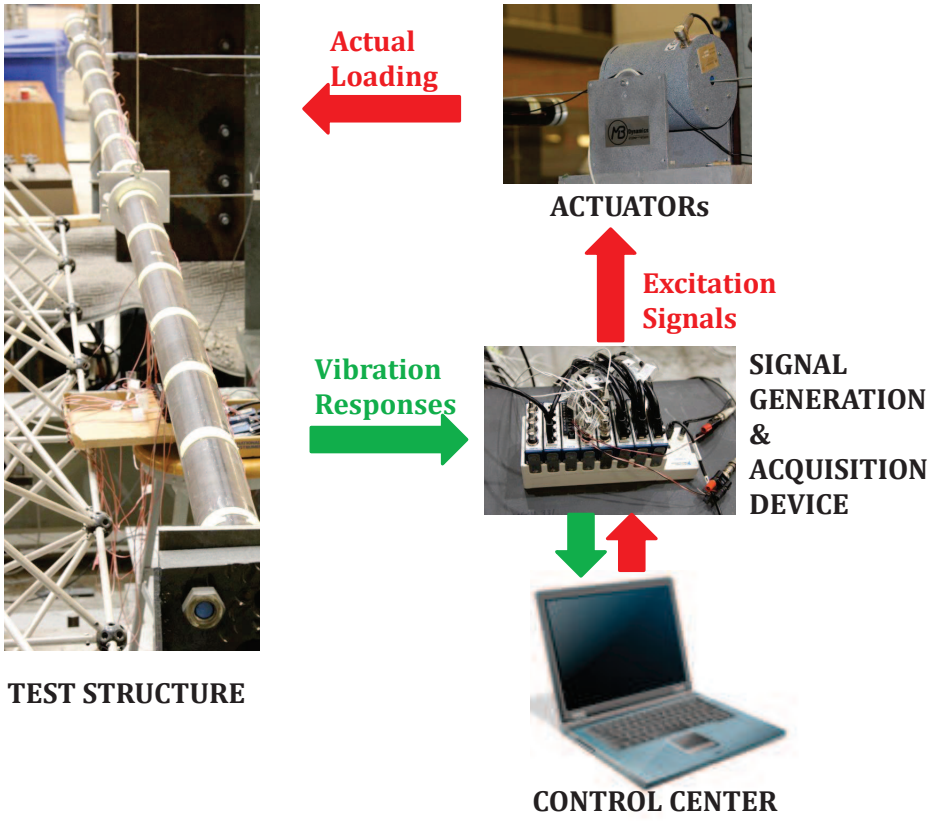

Figure 7.2 : Flowchart of Input/Output and Data Acquisition System

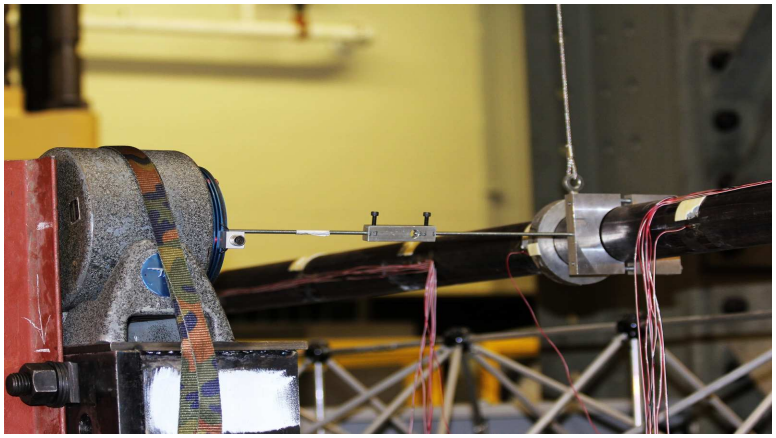

Figure 7.3 : Close Up of Shaker I

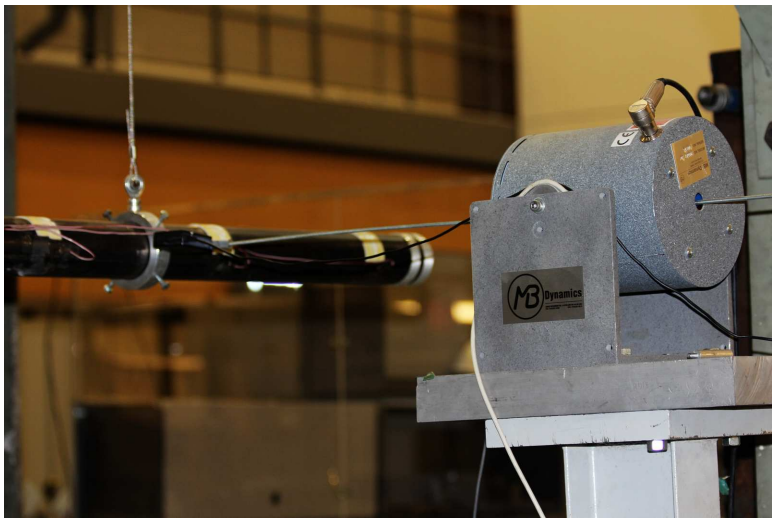

Figure 7.4 : Close Up of Shaker II

aims to solve output only problem with proposed blind identification methods, two control center computers are used: one for excitation signal generation and one for response signal acquisition. LabVIEW Signal Express is used to generate the excitation signals

7.1.3 Data Acquisition Setup

The devices used for the excitation and data acquisition system are shown in Fig. 7.5. 11 strain gages are installed on the test pipe from 3 ft to 13 ft at a spacing of 1 ft, as shown in Fig. 7.6. The data acquisition is obtained by National Instruments c-DAQ 9178 chassis with two NI-9234 analog input modules and four NI-9237 strain input modules. LabVIEW virtual instruments (VIs) are programmed to generate excitation signals like chirp and white noise and to acquire vibration responses from the test pipe structure at the same time. A high sampling rate (2,048 Hz) is used because the minimum allowable sampling frequency for the hardware is 1,600 Hz.

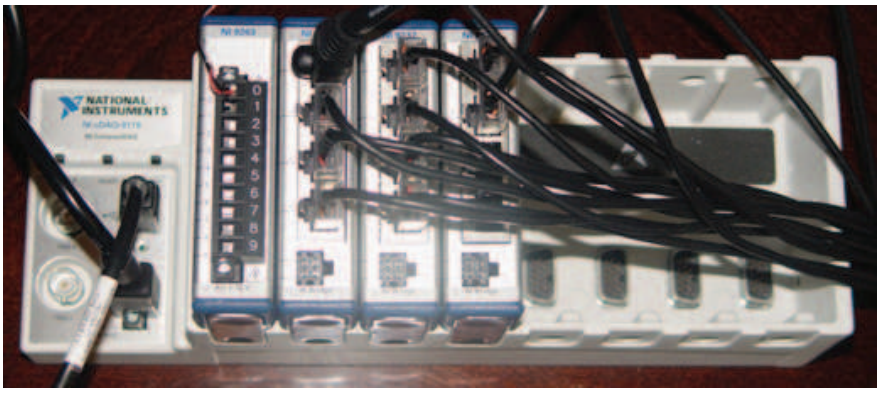

(a) cDAQ 9178 Chassis

(b)NI-9263 Output Module (c)NI-9237 Stain Input Module (d)NI-9234 Analog Input Module

Figure 7.5 : National Instruments DAQ Devices Used in the Experiment

7.2 Numerical Study with FEM Model

To study the behavior of the test model, a FEM model using previous FEM program is built without van der Pol oscillator and top tension. Hence, the system becomes linear without geometric nonlinearity. The parameters used in the simulation is included in Table 7.1. All units are in international standard. Since the test structure is a linear system, the mode shapes and natural frequencies can be directly obtained from the global stiffness matrix and mass matrix for the damage detection study.

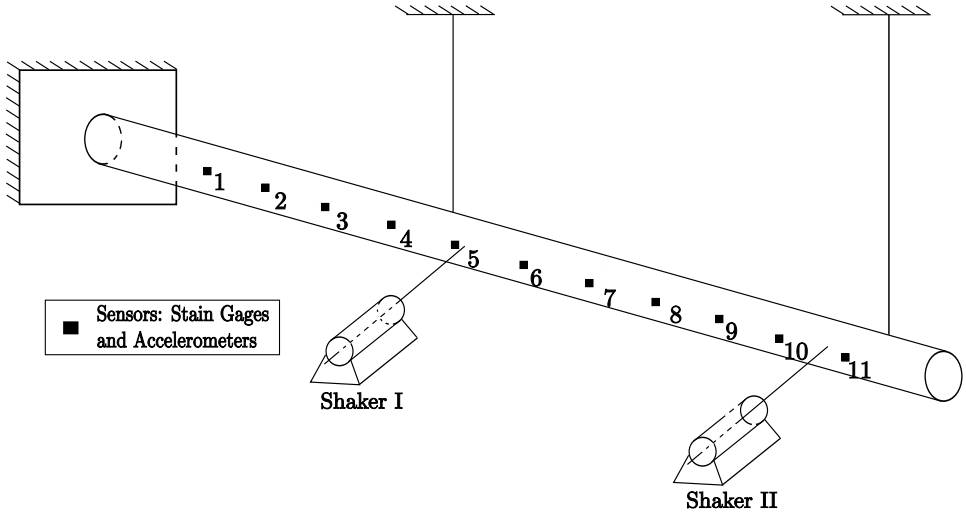

Figure 7.6 : Schematic of Experimental Setup and Sensor Locations

Table 7.1 : Parameters of Test Pipe

Inner Diameter	0.06375 m	Outer Diameter	0.07334 m
Density, ρ	$7.85 \times 10^3\ kg/m^3$	Modulus of Elasticity, E	$2 \times 10^{11}\ N/m^2$
Area	$0.01\ m^2$	Length, L	4.7244 m
Moment of Inertia, I	$6.094 \times 10^{-7} m^4$	Number of Elements, N_E	100

7.2.1 Damage Detection

Damage (property change) detection needs both the intact case and the damaged case to determine the change. To simulate the damage due to corrosion, metal loss is introduced in the test model by machining cracks.

7.2.1.1 Metal Loss

Corrosion is the most frequently occurring damage in deepwater risers. To simulate the metal loss caused by corrosion, the pipe wall thickness is reduced at element 50.

The modal properties are obtained and processed to detect damages using curvature change, DFC and PAC method.

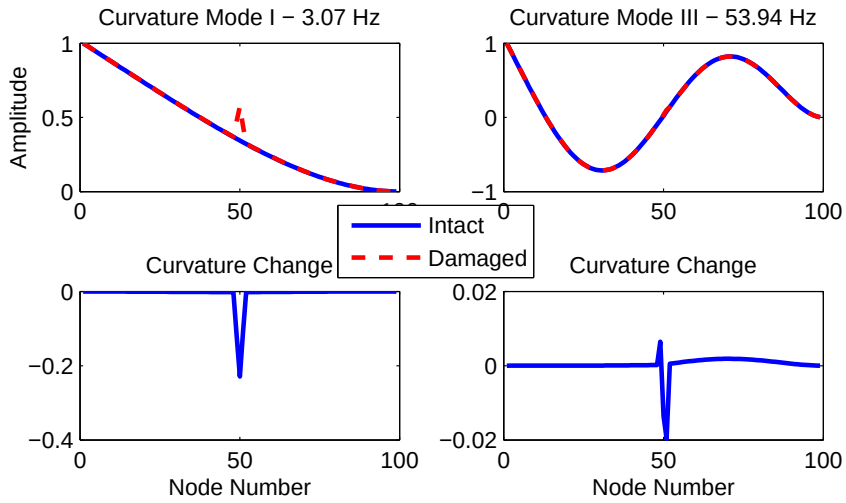

Figure 7.7 : Curvature Change Caused by Metal Loss at Element 50

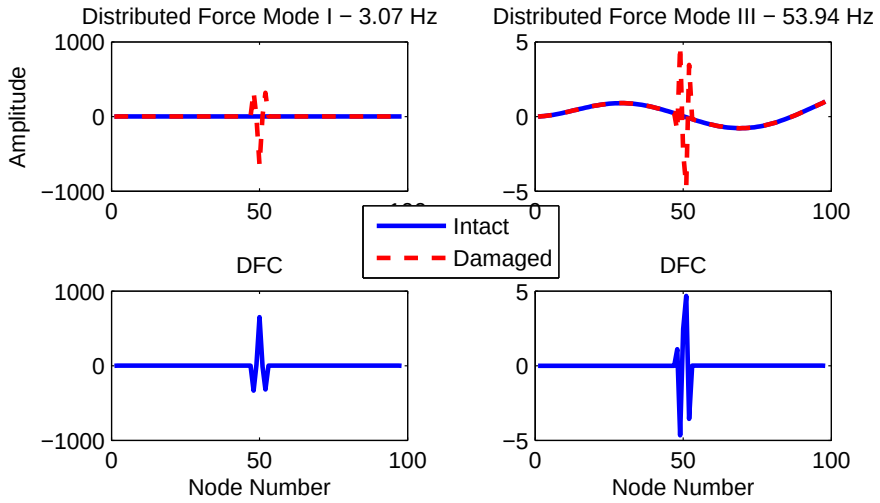

Figure 7.8 : Distributed Force Change Caused by Metal Loss Change at Element 50

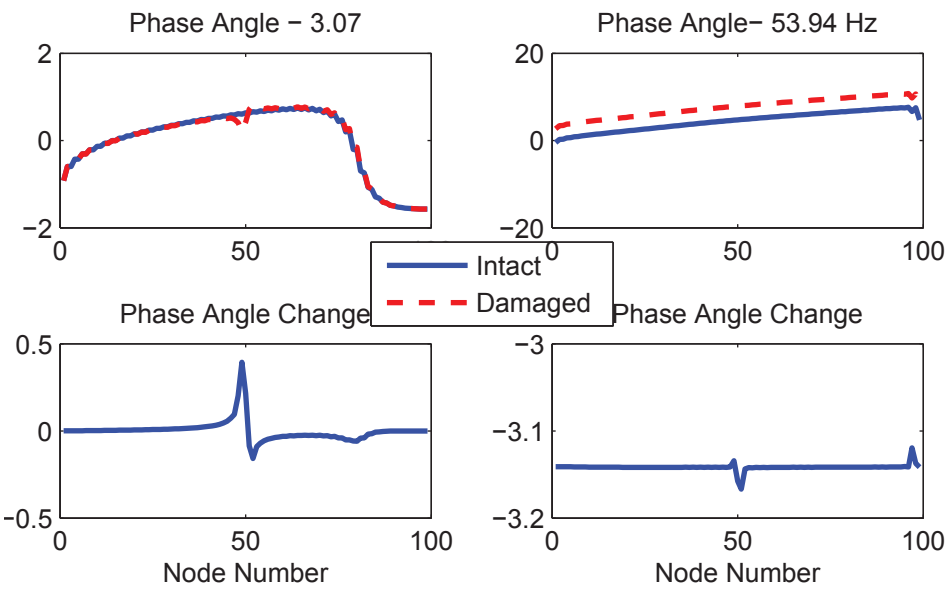

Figure 7.9 : Phase Angle Change Caused by Metal Loss Change at Element 50

From Fig. 7.7 to Fig. 7.9, for metal loss scenario all methods provide reasonable damage detection results based on the numerical model.

7.2.2 Summary of Numerical Study

In the numerical model, all the responses are assumed to be recorded and processed to get modal information. Based on the modal information, damage detection is carried out using curvature change, DFC and PAC methods. Among these three, DFC provides consistently reliable damage indication for metal scenarios.

However, in real experiments, not all the nodes can be measured, and the modal information obtained may not be accurate. Hence, the effectiveness of proposed method cannot be evaluated until being experimentally validation is performed.

7.3 Experimental Analysis

Multiple experiments are carried out with different structural health conditions and different excitation cases. There are four different structural health conditions: intact structure, structure with single level I Crack, structure with single level II crack and structure with multiple cracks. A physical crack is located at 40% of the pipe length from the fixed end. The crack location is chosen not to overlap with the zero nodes in the first three vibration mode shapes. To study the damage severity effect, level I crack and level II crack are chosen at the same location with increasing damage. The second crack is created at 0.63L from the fixed end. Detail information of the cracks is shown in Table 7.2.

Furthermore, three different excitation cases are tested for each structural health condition: Impact, White Noise and Chirp Signal.

Table 7.2 : Dimension Information about Cracks

Name	Location	Width	Length	Depth
Crack I Level I	$0.4L = 1.89$ m	2.32 mm	26.67 mm	2.54 mm
Crack I Level II	$0.4L = 1.89$ m	2.41 mm	35.50 mm	6.01 mm
Crack II	$0.63L = 3.01$ m	1.85 mm	31.99 mm	5.26 mm

The verification of the effectiveness of proposed methods is performed in two steps: blind identification and damage detection.

7.3.1 Blind Identification

To verify the performance of the proposed blind identification methods, modal parameters from both FEM models and frequency response functions (FRFs) of forced

excitation test are used as references. Since the FEM model may not reflect the actual structural properties of the test pipe, modal parameters from the FRFs are more appropriate references.

The modal properties from FRFs are obtained using the sine-sweep excitation test, and the modal properties from proposed WMSOBI method are obtained from white noise excitation test. For the FRFs approach, input-output based peak picking method is used to obtained the modal parameters from Fig. 7.10. For the blind identification approach, WMSOBI is a more proper choice than CWMSOBI since the vibration is a standing wave not a traveling wave. As the strain gages are powered by AC, there is a 60 Hz power line noise in all the strain measurements. Fortunately, the first three modal frequencies of the test structure are smaller than 60 Hz. The scales corresponding to 3 Hz, 16Hz and 50Hz are chosen for WMSOBI.

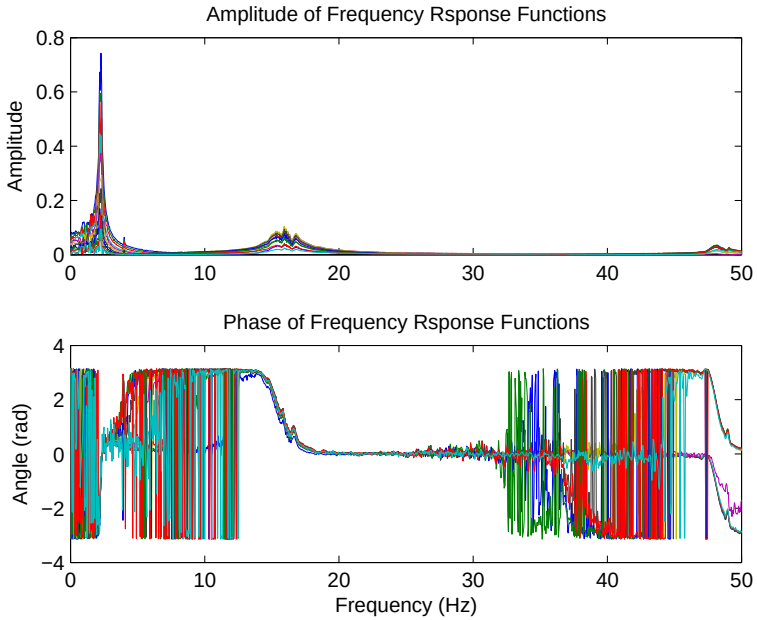

Figure 7.10 : Frequency Response Functions for Sine Sweep Excitation

7.3.1.1 WMSOBI Verification using Intact Case

The intact case test is used to validate the WMSOBI method. The identified modal frequencies from FRFs and WMSOBI are listed in Table 7.3. The results from FEM model are clearly different, while the results from WMSOBI and FRFs are compatible.

Table 7.3 : Identified Modal Properties and Corresponding Values from FEM

Name	FEM	FRFs	WMSOBI
Mode I	3.07 Hz	2.32 Hz	2.55 Hz
Mode II	19.26 Hz	16.07 Hz	16.59 Hz
Mode III	53.94 Hz	48.61 Hz	49.50 Hz

In addition, the mode shapes for all three modes are plotted in Fig. 7.11. The experimental values are scaled appropriately and the maximum normalized mode shapes from FEM. In Fig. 7.11, solid lines represent the modes from FEM model (labeled as theoretical); line with stars represents the modes from WMSOBI and the line with triangles represents the modes from FRFs. Mode shapes from FEM model contain the values all along the pipe (0 m to 4.74 m), while the modes from experiments only locate at those measured locations, from 3 ft to 13 ft (0.9 m to 3.9 m). In Fig. 7.11, it is evident that the mode shapes obtained from WMSOBI are compatible with those from FRFs.

The comparable frequencies and mode shapes identified from FRFs and WMSOBI demonstrate that the proposed WMSOBI method can identify reliable modal properties from output from measured response (output) only: the excitation signal is not considered in the WMSOBI.

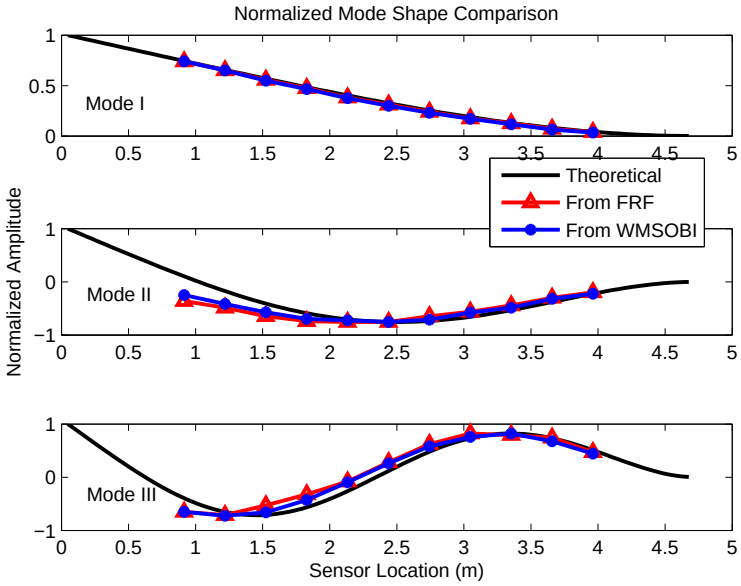

Figure 7.11 : Mode Shape Comparison

7.3.2 Single Crack with Damage Level I

The mode shapes obtained using FRFs are used to evaluate the proposed damage detection method-distributed force change index. The Phase Angle Change Index is not verified as it is more suitable for traveling wave test.

7.3.2.1 Damage Detection based on Curvature Change Index

The strain mode shapes obtained from experiments are proportional to curvature mode shape. According to Pandey [91], curvature mode shape change can be used as damage indicator. Hence, the curvature mode shape changes between intact case and damaged case with single crack level I are shown in Fig. 7.12.

The arrows in Fig. 7.12 indicate the actual damage location. The crack is located at 1.9 m between strain sensor 4 (1.829 m) and sensor 5 (2.134 m). Upper plots show

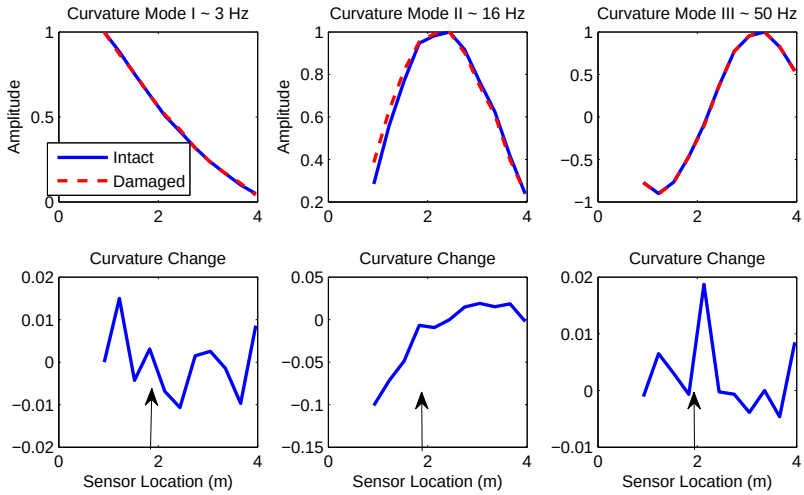

Figure 7.12 : Curvature Change for Mode I-III

the normalized experimental strain (curvature) mode shapes, and the lower plots show the curvature changes. Among all the three modes, only curvature change of mode III shows a clear peak around sensor 5 while the other modes do not provide a clear peak. In other words, curvature change based damage detection method cannot detect the damage location.

7.3.2.2 Damage Detection based on Distributed Force Change Index

The proposed damage detection method in Chapter 5 is based on Distributed Force Change (DFC) index. The DFCs for each mode is obtained using central difference method according to equation 5.2. Similar to curvature change index plots, the distributed force mode vectors and their corresponding differences are shown in Fig. 7.13.

For each individual mode comparison, DFC indices of mode II and mode III clearly indicate that there is a damage close to sensor 4 and sensor 5. The DFC index close

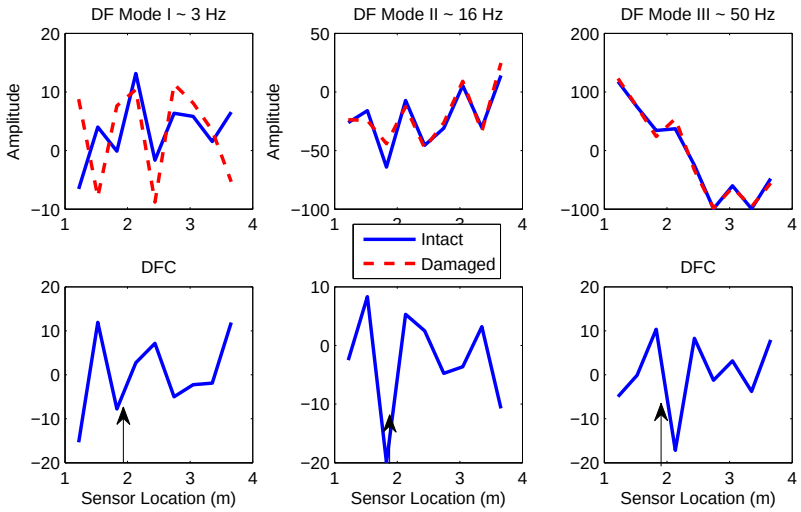

Figure 7.13 : Distributed Force Change for Mode I-III

to the damage location has a typical shape of two small positive peaks on each side of one large negative peak. This phenomenon is also shown in the numerical simulation in Fig. 7.8. DFC index in Mode I is as clear as the other modes.

7.3.2.3 Damage Detection based on Combined Distributed Force Change Index

To further take the advantage of multiple modal participation, a combined DFC (CDFC) index is proposed by summing the DFCs of three dominant modes with consideration of signs of strain mode shape. The CDFC is obtained using equation 7.1.

$$CDFC_z = \sum_{i=1}^{3} [sign\,(\mathbf{C_z}) * DFC_z] \tag{7.1}$$

where C_z represents normalized curvature (strain) mode shape values at location z; DFC_z represents the distributed force change values at location z.

The CDFC index for single crack with damage level I is shown in Fig. 7.14. The

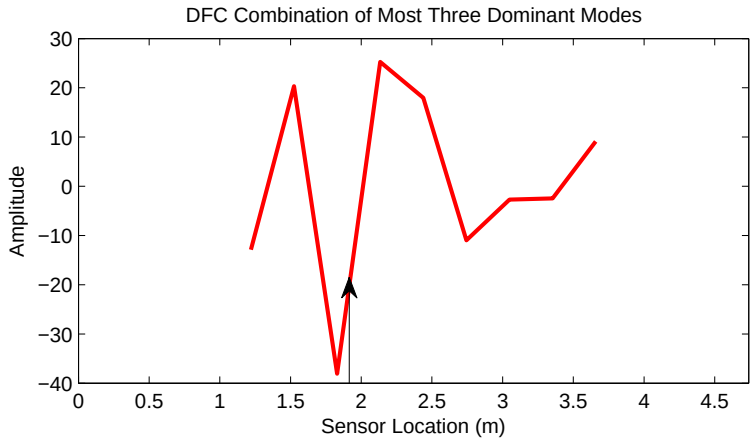

Figure 7.14 : Combined Distributed Force Change

typical damage shape of DFC clearly indicates that there is a damage close to sensor 5. While the other minor kinks in Fig. 7.14 do not have the same typical damage shape and have much smaller amplitudes, which means that there is no damage at those locations.

7.3.3 Single Crack with Damage Level II

Curvature change plots are shown in Fig. 7.15, where the dominant peaks in mode I to mode II clearly indicate the damage location. However, in the third mode, there are other high amplitude peaks which do not provide clear indication.

Similarly, Fig. 7.16 and 7.17 show the DFCs and CDFCs. The classic three-peak shapes in all the plots indicate damage is located close to sensor 4 (1.83 m).

Furthermore, noticing the amplitude difference of DFCs between level I and level II, one can clearly tell that level II damage with a peak amplitude of 60 is much larger than level I with a peak amplitude 20. Similarly, level II of CDFC has a peak amplitude of 150 while level I CDFC has a peak amplitude 37. This amplitude can

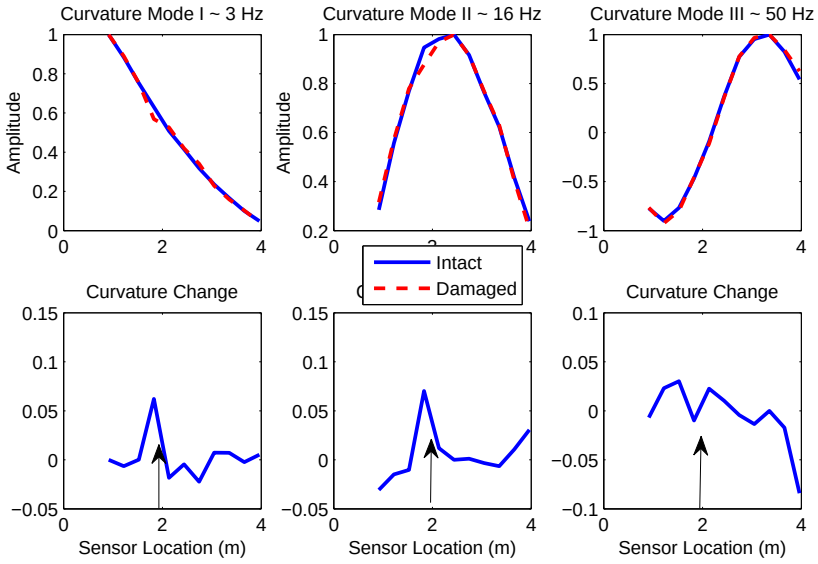

Figure 7.15 : Curvature Change Plot for Mode I-III

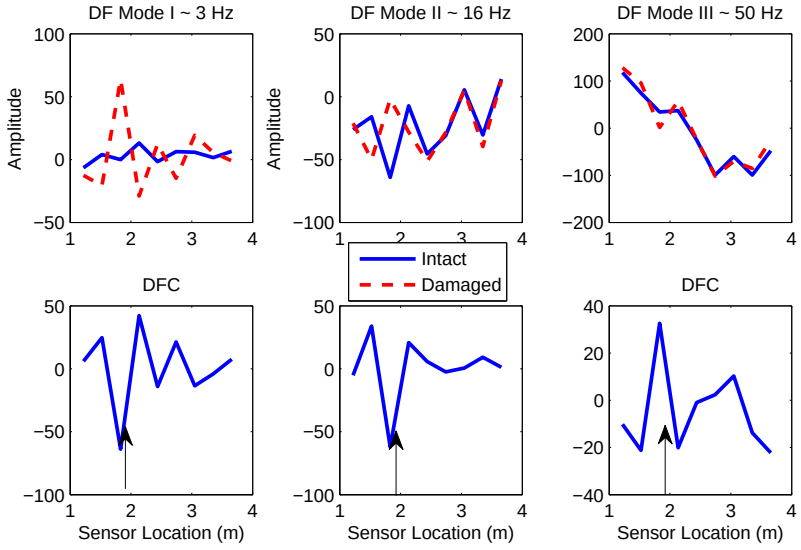

Figure 7.16 : Distributed Force Change Plot for Mode I-III

be used for estimating damage severity as discussed in Chapter 5. The larger the amplitude of DFC or CDFC is, the more severe the damage is.

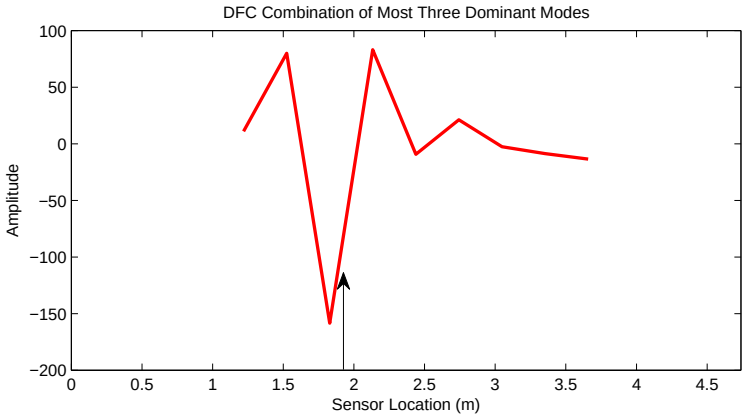

Figure 7.17 : Combined Distributed Force Change

7.3.4 Multiple Cracks

Finally, the performance of proposed damage detection method in multiple cracks case is evaluated. Damage detection based on curvature change index, DFC index and CDFC is performed.

7.3.4.1 Damage Detection based on Curvature Change Index

The curvature change index shown in Fig. 7.18, indicates that for mode I the damage location is evident, however, the curvature change index for mode II and mode III does not clearly indicate damage, as shown in Fig. 7.18. The maximum absolute curvature change values in mode I and II are not close to damage locations. Hence, it can be concluded that the curvature change index is not able to clearly detect damage.

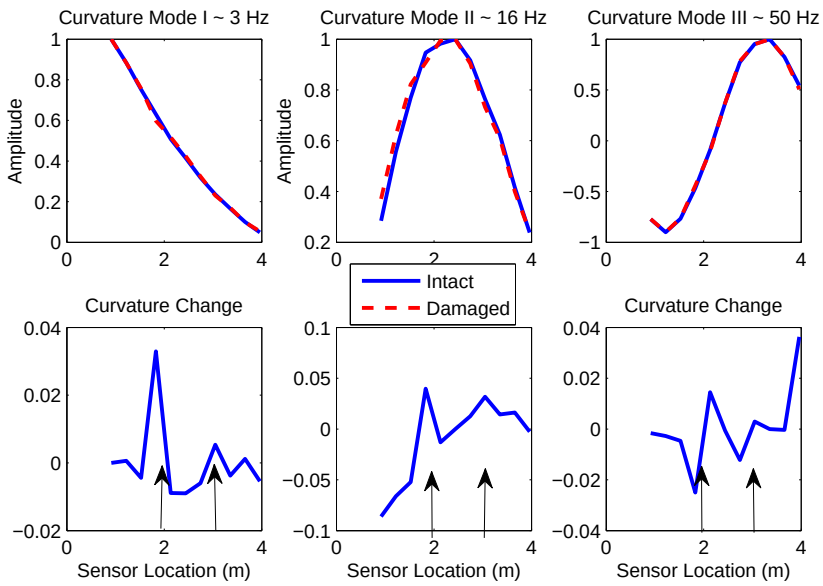

Figure 7.18 : Curvature Change for Mode I-III

7.3.4.2 Damage Detection based on Distributed Force Change Index

The classic DFC shapes for mode I and II shown in Fig. 7.19 clearly indicate that damages are located around sensor 4 (1.83 m) and sensor 8 (3.04 m). Though DFC shape in mode III might be a misleading, the peaks are actually located around crack I and crack II: two peaks around crack I (positive and negative) and one peak around crack II. The results confirms the effectiveness of DFC index for multiple crack damage detection.

7.3.4.3 Damage Detection based on Combined Distributed Force Change Index

The CDFC shown in Fig. 7.20 provides a clear and precise information about damage locations and severities. The negative peaks in the classic three-peak shapes locate

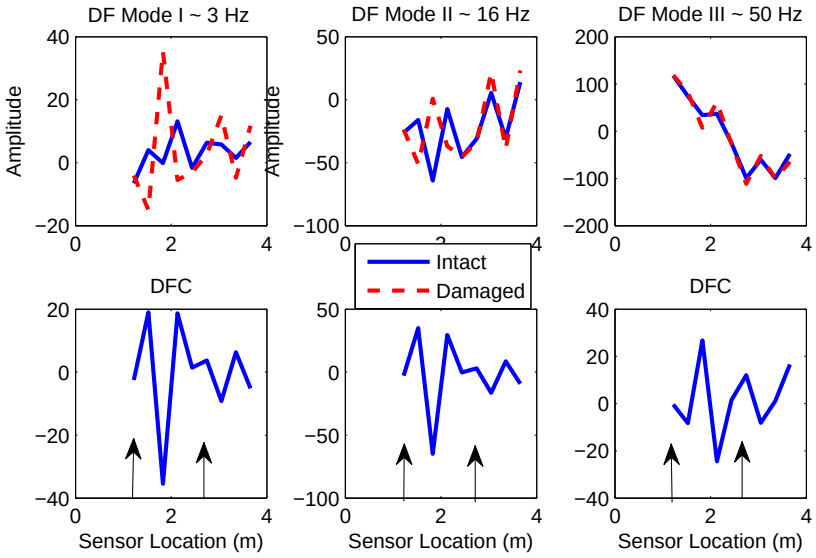

Figure 7.19 : Distributed Force Change for Mode I-III

the damages, while the amplitude of those negative peaks indicate the severity of the corresponding damages.

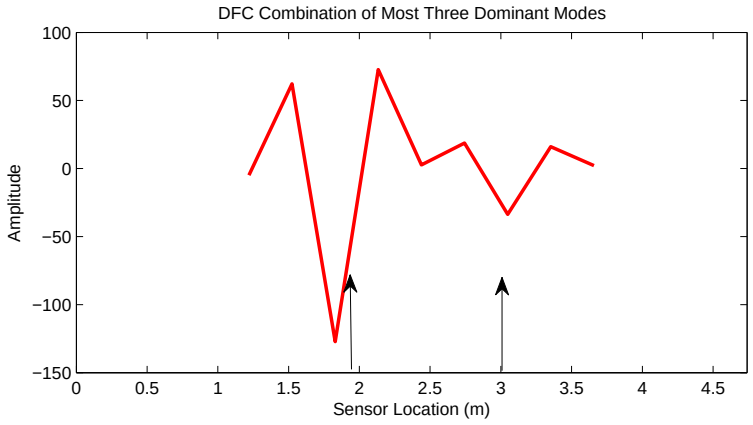

Figure 7.20 : Combined Distributed Force Change

7.4 Conclusion

This chapter evaluated the performance of proposed blind identification method and damage detection method in scaled test pipe model. The experiments verified the effectiveness of proposed WMSOBI method and DFC method as well as its derivative CDFC method.

1. Wavelet Modified Second Order Blind Identification (WMSOBI) method successfully estimates modal property and can provide as accurate results as modal analysis method using FRFs.

2. Even for a simple cantilever test pipe, curvature change index cannot guarantee the damage detection performance and may provide false indications. In addition, it has limitations in detecting minor damages such as single crack with damage level I in the experiments.

3. Distributed Force Change (DFC) index serves as a reasonably good indicator of damage locations and severities, even for minor damages such as single crack with damage level I in the experiments. The negative peaks in the classic three-peak shape indicates the damage locations and the amplitude of the corresponding peaks indicate the severity.

4. The combined DFC (CDFC) takes the advantage of multiple modes being excited at the same time and provides more reliable damage location and severity estimation.

Chapter 8

Local Monitoring based on Magnetic Flux Leakage

When an object made of ferromagnetic material is placed in a magnetic field (as shown in Fig. 8.1(a)) the magnetic flux lines prefer a path passing through the ferromagnetic material. The flux leaking through the air can be measured by magnetic flux leakage sensors. The amount of flux passing through a ferromagnetic object is directly proportional to the thickness of the object. When a ferromagnetic object with a small portion of reduced thickness is placed in a magnetic field as shown in Fig. 8.1(b) the flux leaking through the air in the region of reduced thickness is more in comparison to the magnetic flux in other regions surrounding the object. This leakage of magnetic flux lines into the air can be quantified via an increase in flux density. This phenomenon is called magnetic flux leakage (MFL) [92].

8.1 Review of Magnetic Flux Leakage (MFL)

MFL based damage detection technique is one of the most widely used non-destructive evaluation (NDE) techniques used for gas pipeline inspection as pipeline inspections gauges (PIGs) from 1960s [92] [93]. This technique is now very mature in gas pipeline inspection. Nestleroth and Bubenik [92] provides a detailed report about MFL inspection: from the basic concepts about magnetic field to MFL phenomenon; and from MFL based damage detection techniques to detailed factors that influence the final measured MFL results. Recent advances in the field include the development of MFL

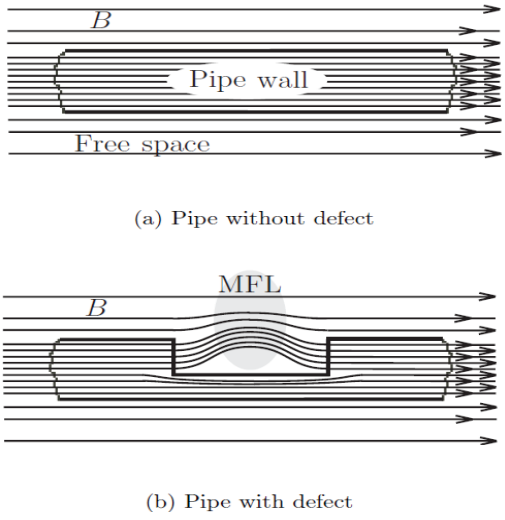

Figure 8.1 : Phenomenon of Magnetic Flux Leakage (Dutta[121])

based damage detection using residual magnetic field [94] and using MFL to detect fatigue damage [95]. In this chapter, a technique proposed by Dr. Dutta [93] using MFL to estimate wall thickness is adapted and tested for its potential application in local monitoring.

8.1.1 Internal Robotic Crawler verses External Remote Operated Vehicle

Generally, there are two types of measurement technique for pipeline inspection:

- Internal Measurement using a smart pig type of device, which is widely used, such as internal robotic crawlers with MFL sensors [96].
- External Measurement using external devices such as a remote operated vehicle (ROV), which can sustain high pressure due to deepwater conditions.

However, as the external device has to go all around the riser, the variation of riser diameter and the different connector sizes make it almost impossible to ensure a good

MFL measurement from outside. In addition, the latest risers are designed to be covered with composite materials to prevent corrosion, such as pipe-in-pie, which makes it even harder for external devices to obtain reliable measurements.

As a result, an internal device such as tetherless robotic crawler with MFL sensors is a better choice. Not only can it automatically adjust the crawling legs to the diameter variation, but also inspection/monitoring can be performed with minimal production disruption. Furthermore, permanent magnets are used to generate the magnetic field, which greatly reduces the power consumption requirement compared to other techniques such as eddy current method and ultrasonic technique.

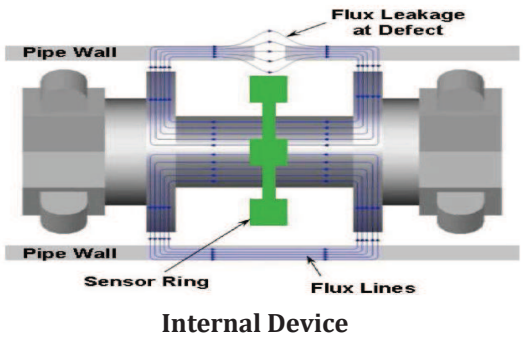

Figure 8.2 : Internal Devices (Dutta[121])

8.1.2 Induction Coil Sensor verses Hall-Effect Sensor

For MFL measurements, there are two commonly used types of sensors: induction coil sensors and hall-effect sensors.

8.1.2.1 Induction Coils

The most commonly used sensor for MFL measurement is an induction coil. Induction coils are made of fine wires with a few turns. Changing magnetic field induces a

voltage across these fine wires, the measured signal reflects the changes in magnetic flux [92], as shown in Fig. 8.3.

8.1.2.2 Hall-Effects Sensors

More recently, MFL systems [92] prefer to directly measure magnetic field, such as hall-effects sensors. The hall-effect sensors directly convert the magnetic field to a voltage output. As magnetic flux density and magnetic field are proportional to each other with a constant ratio in air, the voltage output can reflect the magnetic flux density.

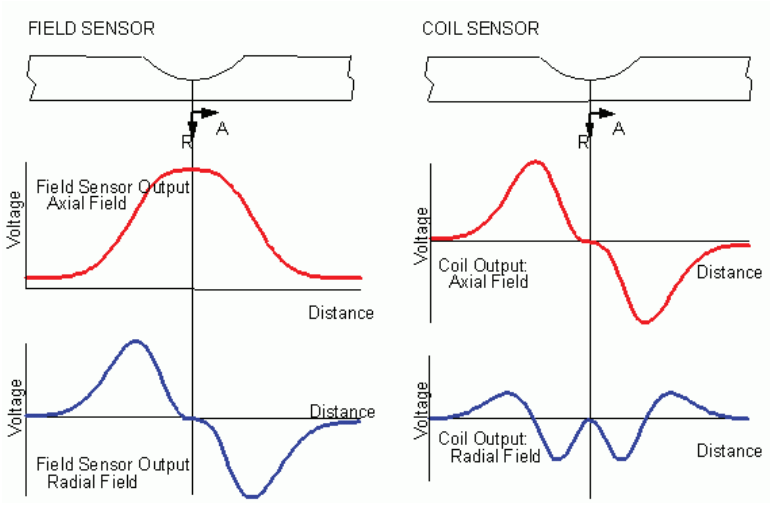

Figure 8.3 : Signals from Hall-Effect and Induction Coil Sensors (Nestleroth et al.)

Fig. 8.3 shows that hall-effect sensors directly measures the magnetic flux density, which can later be directly used to estimate wall thickness. Hence, hall-effect sensors are chosen for experimental verification prosecuted next. And the measured MFL signals are generally converted to values in radial and axial directions, shown in Fig. 8.3.

8.2 Experimental Verification

8.2.1 Experimental Setup

An experiment was carried out by Lynch [96] and the author to verify the capability of measuring the wall thickness reduction, caused by corrosion. The test specimen is made from three two-foot steel pipe sections connected using two PVC pipe sleeves as shown in Fig. 8.4. A photograph of the test setup and a schematic showing wall thinnings are shown in Fig. 8.4 and wall thinning is shown as concave area. Six different wall thickness reductions are machined to simulate the corrosion damage. The thickness reduction ranges from 5% (0.2 mm) to 60% (2.4 mm) of intact pipe thickness, which is 4 mm.

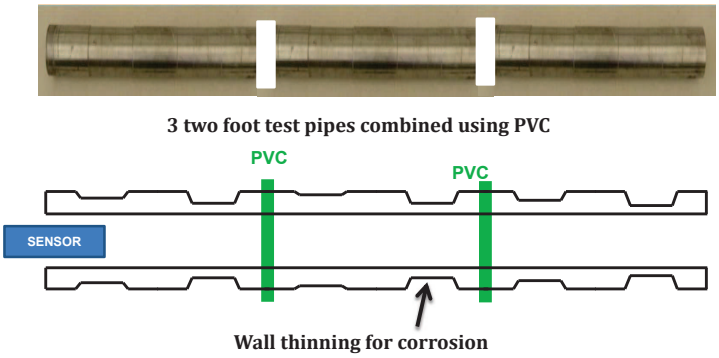

Figure 8.4 : Experimental Setup for MFL Test

8.2.2 Wall Thickness Constant Curve

Because the measured MFL is influenced by quite a few parameters [92], among which wall thickness is the one that is the most imporatnt and we are interested in,

individual experiments are carried out for pipe sections with different wall thickness to study the relationship between the wall thickness and MFL measurement.

8.2.2.1 Measured Data and Data Analysis

The measured MFL signals around the reduced thickness areas are plotted in both axial direction and radial direction in Fig. 8.5. The dashed lines represent the axial MFL measurement with their corresponding y-axis values shown on the right side of each plot. On the other hand, the solid lines represents the radial MFL measurement with their corresponding y-axis values shown on the left side of each plot with blue color.

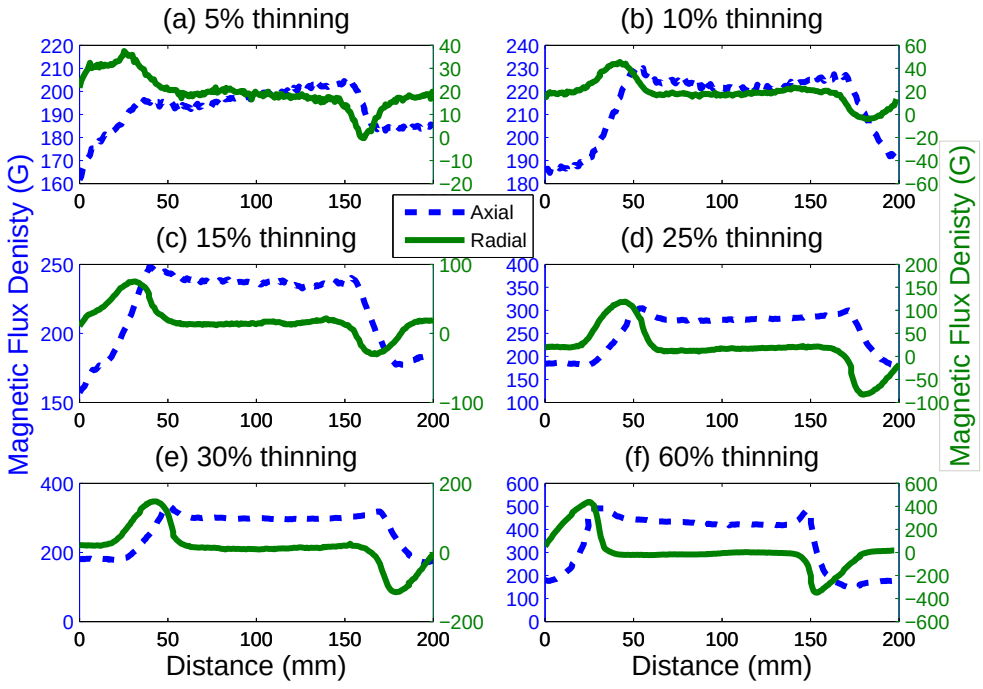

Figure 8.5 : Measured Data for Different Wall Thicknesses

To study the relationship between the MFL measurement and defects due to

reduced thickness, the actual locations of those defects are compared to the radial MFL measurements. The comparison confirms that the positive and negative peaks in radial MFL measurements indicate the start and end of the defects, as shown in Fig. 8.6(a). Furthermore, according to Nestleroth and Bubenik [92], the axial MFL can be used to estimate the wall thickness. In the box range shown in Fig. 8.6(b), the average axial MFL value of the center 50% length is taken as the axial value for the corresponding wall thickness with 25% thinning, which leads to the fourth circle in Fig. 8.7. Similar procedures are carried out for all the other wall thinning shown in Fig. 8.5 (see Fig. 8.7 for other circles representing different wall thinning).

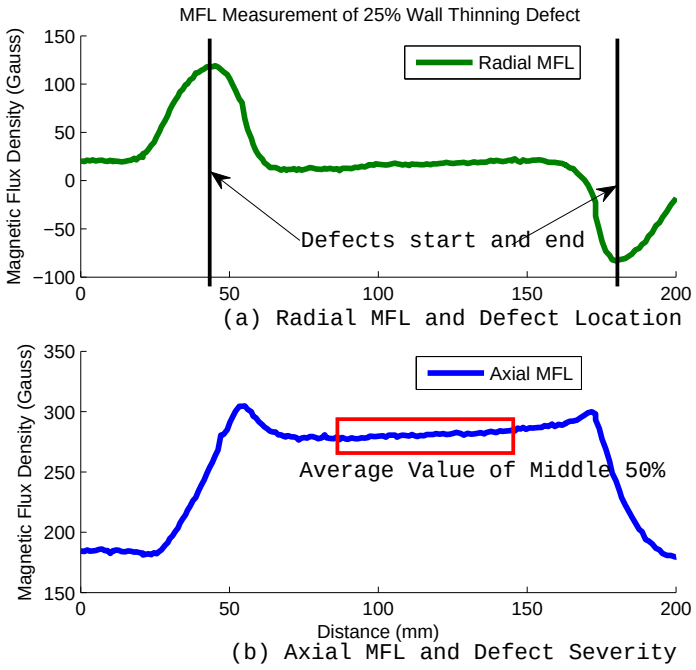

Figure 8.6 : Detailed Analysis of 25% Wall Thinning

8.2.2.2 Wall Thickness Constant

The averaged axial MFL values and corresponding to different wall thinning are shown in Fig. 8.7. A linear relationship between average axial MFL value and wall thinning obtained by least square estimation is shown in Fig. 8.7. The slope and the y-intercept are defined as wall thinning constants-damage severity constant and the intercept for 0% wall thinning, respectively.

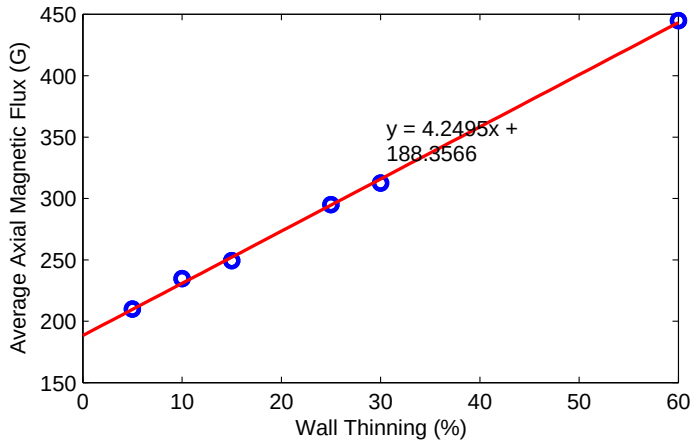

Figure 8.7 : Wall Thinning Constant Curve

The intercept value $B_I = 188.3566G$ represents the constant for pipeline section with full wall thickness, $T_I = 0\%$; the slope of fitted line, K_E, can be then used to estimate the pipe wall thinning (severity of the defects). Combining both wall thinning constants and the axial MFL measurement, B_M, the predicted wall thinning can be estimated using

$$T_p = T_I + \frac{B_M - B_I}{K_E} = \tag{8.1}$$

where T_p is the predicted wall thinning. Consequently, the actual remaining wall thickness $WT_a = WT_{original}(1 - T_p)$.

8.2.3 Comparison between Actual and Predicted Results

A robotic crawler equipped with internal hall effect MFL sensors was deployed in the pipe. The setup is shown in Fig. 8.4. Measurement was carried out with the crawler moving from one end to the other. Fig. 8.8 shows the average axial magnetic flux density along the length of the pipe. The axial magnetic flux's fluctuations match the thickness change locations.

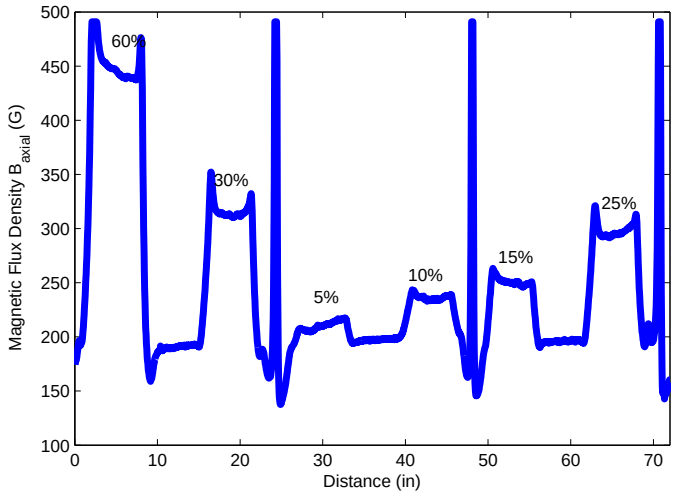

Figure 8.8 : Average Axial Flux from Experiment

The estimated wall thickness using equation 8.1 and actual wall thickness, shown in Fig. 8.9 match very well. Due to the linear estimation and noisy measurement, the low signal-to-noise ratio MFL measurements at the complete cut-off locations cause the incorrect thickness estimations. The experimental validation indicates that local monitoring with MFL sensors is an effective non-contact technique and provides high resolution thickness estimations (0.2 mm resolution).

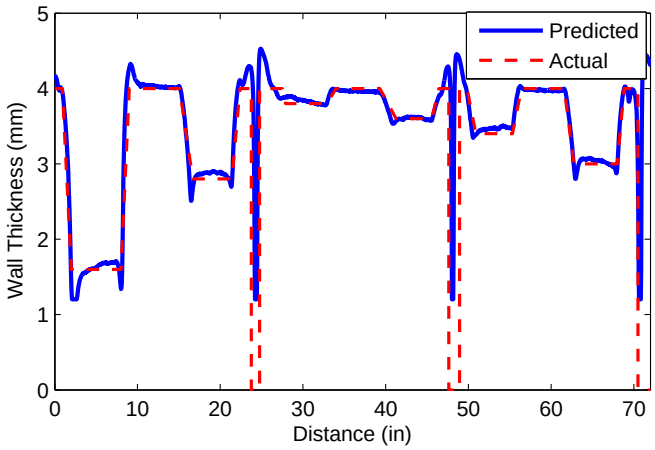

Figure 8.9 : Comparison between Actual and Predict Wall Thickness

8.3 Summary

This chapter described the most important step within local monitoring: damage estimation using MFL data. An experiment was designed to verify the effectiveness of MFL based defect detection algorithm. This chapter confirms that

1. MFL based defect detection technique utilizes a non-contact measurement to detect changes in wall thickness with high resolution (as low as 0.2 mm thickness change, 5% of base 4 mm).

2. Internal robotic crawler can be power efficient with permanent magnets, which means only the measuring sensor and the motor of the crawler consumes the power.

3. The limitation of MFL is that it is applicable only for ferromagnetic materials, which makes it unsuitable for composite flexible risers.

In summary, local monitoring using MFL is a reliable method for deepwater risers made of ferromagnetic materials.

Chapter 9

Conclusion

9.1 Concluding Remarks

A comprehensive study on health monitoring system for deepwater risers has been accomplished in the dissertation. A novel heath monitoring strategy combining the global monitoring, based on vortex-induced vibration and the local monitoring (inspection) based on magnetic flux leakage (MFL) phenomenon provides a plausible solution for deepwater risers.

Local monitoring is validated by experiments, which prove that MFL is a power efficient and non-contact damage detection technique. MFL gives high resolution estimation for wall thicknesses changes in deepwater risers. However, it is only applicable to risers made up of ferromagnetic materials.

For global monitoring, an intensive study of damage detection based on vortex induced vibration (VIV) is accomplished. The key contributions of the proposed global monitoring strategy are divided into four parts: Nonlinear Modeling, Blind Identification and Damage Detection.

9.1.1 Nonlinear Modeling

A novel 3D analytical model with coupled cross-flow and in-line VIV is proposed to overcome the difficulty that no response data is available for deepwater risers both before and after damage. The analytical model is described, evaluated and validated

in two different approaches: Finite Difference Method (FDM) and Finite Element Method (FEM).

In FDM, Lagrangian coordinates and Green-Lagrangian strains are used in the model. Van der Pol oscilltors are used to simulate the hydrodynamic fluid structure interaction force coefficients. Based on extended Hamilton's equation, the proposed model is verified by both computational fluid dynamics (CFD) using direct numerical simulation (DNS) and Delta Flume (2003) experiments. The comparison between proposed model and commercial software products such as SHEAR7 indicates that the proposed model is a more appropriate solution for VIV response prediction of deepwater risers.

In FEM, Jaumann strain with modified von Karman nonlinearity is used to overcome the limitation of large rigid body motion (especially, rotation). Newmark-β method is used to solve the FEM model. Both DNS simulation and Gulf Stream 2006 field tests validate the effectiveness and performance of FEM.

9.1.2 Blind Identification

A novel wavelet modified second order blind identification (WMSOBI) method is proposed to identify the modal properties from vibration responses. The output only WMSOBI method overcomes the limitations in second order blind identification method (SOBI): under-determined problem (more sources than sensors), noise issue and issues of not fully excited modes. Comparisons between WMSOBI and other known output modal analysis methods for both numerical simulations and bridge model experiments show that WMSOBI has higher computing efficiency and provides good identified results.

A further study on complex WMSOBI (CWMSOBI) method is carried out since

the vibrations of deepwater risers are more often traveling waves than standing waves. CWMSOBI using Morlet wavelet provides more accurate identification results and has higher efficiency than WMSOBI and other methods (such as eigensytem realization algorithm (ERA)) for systems with complex vibration mode shapes.

9.1.3 Damage Detection

To detect damage caused by corrosion, a new weighted distributed force change index (WDFC) is proposed. Unlike the curvature change index, the WDFC can clearly indicate the damage location as well as damage severity for corrosion caused bending stiffness reduction. Numerical simulations of Delta Flume (2003) experiment with both full measurement and limited sensor case proves the effectiveness of WDFC method. However, the WDFC method did not work for Gulf Stream Field Test Data because of traveling waves. Further in-lab experiments on cantilever pipe also show the high efficiency and accuracy of WDFC on detecting the occurrence and locations for crack damage.

The phase angle change (PAC) index is proposed based on the phase angle change of analytic signal from Hilbert transform of strain mode shapes. Simulations of Gulf Stream field test responses validate the proposed PAC method to detect bending stiffness reduction caused by corrosion when the vibration of riser is generally traveling wave.

A novel fatigue damage estimations based on identified strain mode shapes, S-N curve and Miner's rule is proposed. There are two key contributions for the fatigue method: one is to estimate the fatigue damage locations and severity; the other is to reduce the data storage by replacing the time history data with the identified dominant strain modes (mode shapes and frequencies) and their corresponding time

of occurrence.

9.2 Future Research

The presented research in this study can be further improved and extended on several areas. The recommended areas for future research are as follows:

1. An experimental study with riser model in towing tank can be carried out considering both the intact and damaged scenarios. This experiment can be used to further validate and study the properties of proposed analytical model and monitoring system (blind identification and damage detection).

2. A further study on applications of WMSOBI and CWMSOBI methods on health monitoring system for regular structures such as bridge or high riser building is needed.

3. The effectiveness of WDFC and PAC methods for damage detection on regular civil structures can be further explored.

4. Optimal sensor localization for deepwater riser monitoring system can be further explored for different real-time damage detection strategies.

5. Expanding the current 3D analytical model from top-tensioned riser (TTR) to other types of deepwater risers is a very important step before commercializing the proposed system.

6. Combining the available technologies and above research achievements in a cost-effective way can lead to possible commercial products: either a design software product like SHEAR7 or a whole structural health monitoring system.

Appendix A

List of Symbols

X	in-line direction
Y	cross-flow direction
Z	vertical direction along riser axis
u	in-line dynamic displacement
x, x_0	in-line equivalent static displacement (mean drift)
v	cross-flow (dynamic) displacement
s	Lagrangian coordinate
ϵ	strain
ϵ_0	initial strain
ϵ_I	dynamic strain
ε	nonlinear parameter for van der Pol oscillator
η	curvature
η_0	initial curvature
∂	partial differentiation
$'$	spatial differentiation
$\dot{}$	time differentiation/derivative
$\mathbf{H}$	Hamilton equation
$\mathbf{K_v}$	kinetic energy
$\mathbf{\Pi_v}$	potential energy
$\mathbf{W_v}$	work done by non-conservative forces

$\mathbf{\Phi}$	strain energy
C_M	added mass coefficient
C_D	drag coefficient
C_{D_0}	drag coefficient from fixed rigid riser experiments
$C_{D,S}$	mean drag coefficient
C_L	lift coefficient
C_{L_0}	lift coefficient from fixed rigid riser experiments
γ	hydrodynamic damping paramter
D	outer diameter of riser
Λ	aspect ratio of riser $\frac{L}{D}$
U	current velocity
U_{ref}	reference current velocity
f_v	vortex shedding frequency (in Hz)
$\Omega_{z,IL}$, $\Omega_{z,CF}$	in-line and cross-flow vortex shedding frequency (in rad)
Ω_{ref}	reference vortex shedding frequency (in rad)
$\omega_{z,IL}$, $\omega_{z,CF}$	scaled in-line and cross-flow vortex shedding frequency
ρ	fluid density
EA	axial rigidity
EI	bending density
T, T_{top}	tension at top of TTR
δ	variation
w	self weight of riser per unit length in fluid
p, q	in-line and cross-flow van der Pol variables
m	mass of riser per unit length
m_a	added mass per unit length

m_f	mass of displaced fluid per unit length
m_w	mass constant defined as ρD^2
μ	mass ratio between $m_a + m$ and m_w
R_e	Reynolds number
S_t	Strouhal number
A_{CF}, B_{IL}	hydrodynamic force parameters for van der Pol oscillators
$[\mathbf{M}]$	system mass matrix
$[\mathbf{C}]$	system damping matrix
$[\mathbf{K}]_\mathbf{t}$	tangent system stiffness matrix
$[\mathbf{B}]$	Jaumann strain tensor
$[\mathbf{U}]$	right stretch tensor

Appendix B

List of Acronyms

ALP	adaptive length pendulum
AMD	active mass damper
AR	auto-regressive
ARX	auto-regressive with exogenous inputs
ASTM	American Society of Testing and Materials
BSS	blind source separation
CDFC	combined distributed force change
CF	cross-flow
CPU	central processing unit
CWMSOBI	complex wavelet modified second order blind identification
CWT	continuous wavelet tranform
DFC	distributed force change
DNS	direct numerical simulation
DOE	Department of Energy
EEG	electroencephalograph/y
EMD	empirical mode decomposition
EOM	equation of motion
EPS	earthquake protection system
ERA	eigensystem realization algorithm
EXP	experiment(al)

FDD	frequency domain decomposition
FDM	finite difference method
FEM	finite element method
FFT	fast Fourier transform
FLI	frequency lock-in
FPSO	floating production, storage and off-loading
FRF	frequency response function
FSI	fluid-structure interaction
GBS	gravity based structure
ICA	independent component analysis
IIV	ice-induced vibration
IL	in-line
ITD	Ibrahim time domain
LCD	liquid column damper
MAC	modal assurance criterion
MEG	magnetoencephalograph/y
MFL	magnetic flux leakage
MMS	Mineral Management Service
MR	Magneto-rheological
NDE	non-destructive evaluation
NDT	non-destructive technique
PAC	phase angle change
PCA	principle component analysis
PIG	pipe inspection gauge
PVC	Polyvinyl Chloride

RFC	rain-flow count
RMS	root mean square
RPSEA	research partnership to secure energy for America
SAIVS	semi-active independently variable stiffness device
SDOF	single degree of freedom
SHM	structural health monitoring
SOBI	second order blind identification
STD	standard deviation
STFT	short time Fourier transform
STLCD	semi-active tuned liquid column damper
STMD	semi-active tuned mass damper
TLCD	tuned liquid column damper
TLP	tensioned leg platform
TMD	tuned mass damper
TTR	top-tensioned riser
UT	ultrasonic technique
VIV	vortex-induced vibration
WDFC	weighted distributed force change
WMSOBI	wavelet modified second order blind indentification

Bibliography

[1] U. S. Energy Information Administration, "Total energy supply, deposition, and price summary, aeo2011 reference case," *Annual Report*, 2011.

[2] C. Townsend, "Charles Townsend's Rig Work Web," *http://acrigs.com/.*, 2007.

[3] D. Howard, "Investigation of the Exxon Company U.S.A. Pipeline Leak Eugene Island Block 314, May 6, 1990," *U.S. Department of Interior, Mineral Management Services, Gulf of Mexico Regional Office: New Orleans*, 1991.

[4] A. Alvarado and W. Bertges, "Investigation of Shell Offshore Inc, Hobbit Pipeline Leak, Ship Shoal Block 281, November 16, 1994," *U.S. Department of Interior, Mineral Management Services, Gulf of Mexico Regional Office: New Orleans*, 1994.

[5] A. Gobert, F. Patton, and J. Williams, "Investigation of Pipeline Leak Pipeline Segment No. 4582 Main Pass Area Block 288, 23 June 2007.," *U.S. Department of Interior, Mineral Management Services, Gulf of Mexico Regional Office: New Orleans*, 2008.

[6] T. Zeller, "Estimates Suggest Spill Is Biggest in U.S. History," *http://www.nytimes.com/2010/05/28/us/28flow.html?-r=1.*, May 2010.

[7] C. Krauss, "Gulf Spill Is the Largest of Its Kind, Scientists Say," *http://www.nytimes.com/2010/08/03/us/03spill.html*, August 2010.

[8] M. Lozev, R. Smith, and B. Grimmett, "Evaluation of Methods for Detecting and Monitoring of Corrosion Damage in Risers," *ASME Conference Proceedings*, pp. 363–374, 2003.

[9] M. U.S. Department of the Interior, "Data Base for Pipeline Failure Statistics in the Gulf of Mexico 2002," *Annual Report*, 2002.

[10] D. N. Veritas, *Recommended Practice Det Norske Veritas DNV-RP-F204 Riser Fatigue*. Det Norske Veritas, October 2010.

[11] M. G. Lozev, R. W. Smith, and B. B. Grimmett, "Evaluation of methods for detecting and monitoring of corrosion damage in risers," *Journal of Pressure Vessel Technology*, vol. 127, no. 3, pp. 244–254, 2005.

[12] A. Birring, "Overview of Factors Affecting Ultrasonic Inspection of Tension Leg Platforms," in *Proceedings of the Sixth ASME Symposium on Offshore Mechanics and Arctic Engineering*, (Houston,TX), 1987.

[13] R. Thomas, L. Favro, X. Han, and Z. Ouyang, "Infrared imaging of ultrasonically excited subsurface defects in materials," *U.S. Patent-6236049 B1*, May 2001.

[14] A. Yuyama, "Fundamental Aspects of Acoustic Emission Applications to the Problems Caused by Corrosion, in Corrosion Monitoring in Industrial Plants Using Nondestructive Testing and Electrochemical Methods," in *ASTM STP 908 American Society of Testing and Materials*, (Philadelphia.), pp. 43–74, 1986.

[15] A. Raine and M. Lugg, "A review of the alternating current field measurement inspection technique," *Sensor Review*, vol. 19, no. 3, pp. 207–213, 1999.

[16] Y. Sun, S. Udpa, and W. Lord, "A remote field eddy current NDT probe for the inspection of metallic plates," *Materials Evalauation*, vol. 54, pp. 510–512, April 1996.

[17] G. P. Mhatre and R. A. Brooks, "Pulse eddy current testing apparatus for magnetic materials, particularly tubes," *U.S. Patent-4188577*, Feb 1980.

[18] D. Atherton and S. Sullivan, "The remote-field through-wall electromagnetic inspection technique for pressure tubes," in *ETATS-UNIS: American Society for Nondestructive Testing*, vol. 44, (Columbus, OH), 1986.

[19] T. Bubenik, J. Nestlroth, R. Eiber, and B. Saffell, "Magnetic flux leakage (mfl) technology for natural gas pipeline inspection," *NDT and E International*, vol. 30, no. 1, pp. 36–36, 1997.

[20] J. K. Vandiver, "Detection of structural failure on fixed platforms by measurement of dynamic response," in *Offshore Technology Conference*, (Houston, TX), 1975.

[21] B. Sweetman and M. Choi, "The modal distribution method: a new statistical algorithm for analyzing measured acceleration data," in *Smart Structures and Materials 2006: Sensors and Smart Structures Technologies for Civil, Mechanical, and Aerospace Systems* (M. Tomizuka, C.-B. Yun, and V. Giurgiutiu, eds.), vol. 6174, SPIE, 2006.

[22] C. Riveros, T. Utsunomiya, K. Maeda, and K. Itoh, "Vibration-based damage detection in flexible risers using time series analysis," *Doboku Gakkai Ronbunshuu A*, vol. 63, no. 3, pp. 423–433, 2007.

[23] T. Sarpkaya, "A critical review of the intrinsic nature of vortex-induced vibrations," *Journal of Fluids and Structures*, vol. 19, no. 4, pp. 389–447, 2004.

[24] R. Brincker, L. Zhang, and P. Andersen, "Modal identification of output-only systems using frequency domain decomposition," *Smart Materials and Structures*, vol. 10, no. 3, p. 441, 2001.

[25] R. S. Pappa and S. R. Ibrahim, "A parametric study of the ibrahim time domain modal identification algorithm," *Report from NASA*, 1981.

[26] J. N. Juang and R. S. Pappa, "An eigensystem realization algorithm for modal parameter identification and model reduction," *Journal of Guidance Control and Dynamics*, vol. 8, no. 5, pp. 620–627, 1985.

[27] N. E. Huang, Z. Shen, S. R. Long, M. C. Wu, H. H. Shih, Q. Zheng, N.-C. Yen, C. C. Tung, and H. H. Liu, "The empirical mode decomposition and the hilbert spectrum for nonlinear and non-stationary time series analysis," *Proceedings of the Royal Society of London. Series A: Mathematical, Physical and Engineering Sciences*, vol. 454, no. 1971, pp. 903–995, 1998.

[28] MIT, "Vortex induced vibration data repository." http://oe.mit.edu/VIV/index.html.

[29] A. Zak, M. Krawczuk, and W. Ostachowicz, "Vibration of a laminated composite plate with closing delamination," *Journal of Intelligent Material Systems and Structures*, vol. 12, no. 8, pp. 545–551, 2001.

[30] W. M. West, "Illustration of the use of modal assurance criterion to detect structural changes in an orbiter test specimen," *Proceedings of the Air Force Conference on Aircraft Structural Integrity*, pp. 1–6, 1986.

[31] A. Pandey, M. Biswas, and M. Samman, "Damage detection from changes in curvature mode shapes," *Journal of Sound and Vibration*, vol. 145, no. 2, pp. 321 – 332, 1991.

[32] L. Zhang, W. Quiong, and M. Link, *A structural damage identification approach based on element modal strain energy*, pp. 223–230. Katholieke Universiteit Leuven, 1999.

[33] D. Bernal and B. Gunes, "Flexibility based approach for damage characterization: Benchmark application," *Journal of Engineering Mechanics*, vol. 130, no. 1, pp. 61–70, 2004.

[34] J. L. Humar, *Dynamics of structures*. Prentice Hall, 1990.

[35] IMPRESS Education, "Mechanical properties, creep." http://www.spaceflight.esa.int /impress/text/education/Mechanical

[36] A. M. Horn, M. R. Andersen, M. Biot, B. Bohlmann, S. Mahrault-Mougin, J. Kozak, N. Osawa, Y. S. J. H. Remes, J. Ringsberg, and J. van der Cammen, "Fatigue and fracture," in *International Ship and Offshore Structures Congress, Committee III.2*, vol. 1, (Seoul, Korea), pp. 475–585, August 2009.

[37] M. Miner, "Cumulative damage in fatigue," *Journal of applied mechanics*, vol. 3, p. 159, December 1945.

[38] D. N. Veritas, *DNV-RP-F204 Riser Fatigue*, October 2010.

[39] M. Matsuishi and T. Endo, "Fatigue of metals subjected to varying stress," *Proceedings of Japan Society of Mechanical Engineers*, 1968.

[40] S. Downing and D. Socie, "Simple rainflow counting algorithms," *International Journal of Fatigue*, vol. 4, no. 1, pp. 31 – 40, 1982.

[41] I. Rychlik, "A new definition of the rainflow cycle counting method," *International Journal of Fatigue*, vol. 9, no. 2, pp. 119 – 121, 1987.

[42] H. Le, P. Moin, and J. Kim, "Direct numerical simulation of turbulent flow over a backward-facing step," *Journal of Fluid Mechanics*, vol. 330, pp. 349–374, 1997.

[43] R. Basu and B. Vickery, "Across-wind vibrations of structure of circular cross-section. part ii. development of a mathematical model for full-scale application," *Journal of Wind Engineering and Industrial Aerodynamics*, vol. 12, no. 1, pp. 75–97, 1983.

[44] R. E. D. Bishop and A. Y. Hassan, "The lift and drag forces on a circular cylinder oscillating in a flowing fluid," *Proceedings of the Royal Society of London. Series A. Mathematical and Physical Sciences*, vol. 277, no. 1368, pp. 51–75, 1964.

[45] R. Skop and O. Griffin, "On a theory for the vortex-excited oscillations of flexible cylindrical structures," *Journal of Sound and Vibration*, vol. 41, no. 3, pp. 263 – 274, 1975.

[46] O. Griffin, R. Skop, and G. Koopmann, "The vortex-excited resonant vibrations of circular cylinders," *Journal of Sound and Vibration*, vol. 31, no. 2, pp. 235 – IN3, 1973.

[47] C. Feng, "The measurement of vortex-induced effects in flow past a stationary and oscillating circular and d-section cylinders," diploma thesis, University of British Columbia., 1968.

[48] M. Facchinetti, E. de Langre, and F. Biolley, "Coupling of structure and wake oscillators in vortex-induced vibrations," *Journal of Fluids and Structures*, vol. 19, no. 2, pp. 123 – 140, 2004.

[49] R. Violette, E. de Langre, and J. Szydlowski, "A linear stability approach to vortex-induced vibrations and waves," *Journal of Fluids and Structures*, vol. 26, no. 3, pp. 442 – 466, 2010.

[50] R. Violette, E. de Langre, and J. Szydlowski, "Computation of vortex-induced vibrations of long structures using a wake oscillator model: Comparison with dns and experiments," *Comput. Struct.*, vol. 85, pp. 1134–1141, June 2007.

[51] J. K. Vandiver, "Shear7 v4.4 program theoretical manual." Massachusetts Institute of Technology, 2005.

[52] R. Gabbai and H. Benaroya, "An overview of modeling and experiments of vortex-induced vibration of circular cylinders," *Journal of Sound and Vibration*, vol. 282, no. 35, pp. 575 – 616, 2005.

[53] H. Benaroya, T. Wei, S. Kuchnicki, and P. Dong, "Extended hamilton's principle for fluid-structure interaction," *Proceedings of the Institution of Mechanical Engineers, Part K: Journal of Multi-body Dynamics*, vol. 217, no. 2, pp. 153–170, 2003.

[54] K. Wendel, "Hydrodynamic masses and. hydrodynamic moments of inertia," , *Translation 260: David Taylor Naval Sip Research and Development*, 1956.

[55] R. Blevins, *Flow induced vibration.* Van Nostrand Reinhold Co., Inc., 115 Fifth Ave., New York, NY 10003 (USA): New York, NY (USA); Van Nostrand Reinhold Co., Inc., Jan 1990.

[56] R. T. Hartlen and I. G. Currie, "Lift-oscillator model of vortex-induced vibration," *Journal of the Engineering Mechanics Division*, vol. 96, no. 5, pp. 577–591, 1970.

[57] S. Krenk and S. R. K. Nielsen, "Energy balanced double oscillator model for vortex-induced vibrations," *Journal of Engineering Mechanics*, vol. 125, no. 3, pp. 263–271, 1999.

[58] J. R. Chaplin and P. W. Bearman, "Vortex-induced vibrations of deep water tension risers." http://www.energy.soton.ac.uk/civEng2/www.civil.soton.ac.uk/hydraulics/riser/index.html, 2005.

[59] M. S. Pantazopoulos, "Vortex-induced vibration parameters: critical review," in *Proceedings of the OMAE*, vol. I, 1994.

[60] Larsen, C.M.,, "Vivana-theory manual (version 3.4).." Norwegian Marine Technology Research Institute: SINTEF, 2005.

[61] D. J. Newman and G. E. Karniadakis, "A direct numerical simulation study of flow past a freely vibrating cable," *Journal of Fluid Mechanics*, vol. 344, pp. 95–136, 1997.

[62] J. Crank, *The Mathematics of Diffusion*. Oxford Science Publications, Clarendon Press, 1979.

[63] J. Chaplin, P. Bearman, F. H. Huarte, and R. Pattenden, "Laboratory measurements of vortex-induced vibrations of a vertical tension riser in a stepped current," *Journal of Fluids and Structures*, vol. 21, no. 1, pp. 3 – 24, 2005. ¡ce:title¿Fluid-Structure and Flow-Acoustic Interactions involving Bluff Bodies¡/ce:title¿.

[64] OrcaFlex, "Vortex tracking models." http://www.orcina.com/SoftwareProducts/OrcaFlex/Documentation/Help/Content/html/VortexTrackingModels.htm., 2005.

[65] P. F. Pai, *Highly flexible structures: modeling, computation, and experimentation.* American Institute of Aeronautics and Astronautics, November 2007.

[66] P. F. Pai, "Personal communications." Emails, April 2011.

[67] A. Nayfeh and P. Pai, *Linear and Nonlinear Structural Mechanics.* Wiley Series in Nonlinear Science, Wiley-Interscience, 2004.

[68] R. Courant, K. Friedrichs, and H. Lewy, "On the partial difference equations of mathematical physics," *IBM J. Res. Dev.*, vol. 11, pp. 215–234, Mar. 1967.

[69] D. LUCOR, L. IMAS, and G. KARNIADAKIS, "Vortex dislocations and force distribution of long flexible cylinders subjected to sheared flows," *Journal of Fluids and Structures*, vol. 15, no. 3, pp. 641 – 650, 2001.

[70] T. Srivilairit, "A study of current velocity profiles and vortex-induced vibration for deepwater drilling risers," diploma thesis, University of Texas at Austin, Austin, TX, 2006.

[71] C. Shi, L. Manuel, M. A. Tognarelli, and T. Botros, "On the vortex-induced vibration response of a model riser and location of sensors for fatigue damage prediction," *ASME Conference Proceedings*, vol. 2010, no. 49149, pp. 901–910, 2010.

[72] A. A. Mufti, G. Tadros, and P. R. Jones, "Field assessment of fibre-optic bragg grating strain sensors in the confederation bridge," *Canadian Journal of Civil*

Engineering, vol. 24, no. 6, pp. 963–966, 1997.

[73] B. F. Spencer, M. E. Ruiz-Sandoval, and N. Kurata, "Smart sensing technology: opportunities and challenges," *Structural Control and Health Monitoring*, vol. 11, no. 4, pp. 349–368, 2004.

[74] J. P. Lynch, K. H. Law, A. S. Kiremidjian, and E. Carryer, "Design and performance validation of a wireless sensing unit for structural monitoring applications," *Structural Engineering and Mechanics*, 2004.

[75] E. C. Cherry, "Some experiments on the recognition of speech, with one and with two ears," *The Journal of the Acoustical Society of America*, vol. 25, no. 5, pp. 975–979, 1953.

[76] C. Jutten and J. Herault, "Blind separation of sources, part i: An adaptive algorithm based on neuromimetic architecture," *Signal Processing*, vol. 24, no. 1, pp. 1 – 10, 1991.

[77] T. ping Jung, S. Makeig, and A. J. Bell, "Independent component analysis of electroencephalographic data," *Adv. Neural Inform. Process. Syst*, pp. 145–151, 1996.

[78] J. Tugnait, "Blind equalization and estimation of digital communication fir channels using cumulant matching," *Communications, IEEE Transactions on*, vol. 43, pp. 1240 – 1245, feb/mar/apr 1995.

[79] A. D. Back, A. D. Back, A. S. Weigend, and A. S. Weigend, "A first application of independent component analysis to extracting structure from stock returns," *International Journal of Neural Systems*, 1997.

[80] A. T. Walden, "Non-gaussian reflectivity, entropy, and deconvolution," *Geophysics*, vol. 50, no. 12, pp. 2862–2888, 1985.

[81] M. S. Lewicki, "Bayesian modeling and classification of neural signals," *Neural Comput.*, vol. 6, pp. 1005–1030, Sept. 1994.

[82] J.-F. Cardoso, "Source separation using higher order moments," in *Acoustics, Speech, and Signal Processing, 1989. ICASSP-89., 1989 International Conference on*, pp. 2109 –2112 vol.4, may 1989.

[83] P. Comon, "Independent component analysis, a new concept?," *Signal Process.*, vol. 36, pp. 287–314, Apr. 1994.

[84] A. Hyvärinen and E. Oja, "Independent component analysis: algorithms and applications.," *Neural Netw*, vol. 13, no. 4-5, pp. 411–430, 2000.

[85] F. Poncelet, G. Kerschen, J.-C. Golinval, and D. Verhelst, "Output-only modal analysis using blind source separation techniques," *Mechanical Systems and Signal Processing*, vol. 21, no. 6, pp. 2335 – 2358, 2007.

[86] G. Kerschen, F. Poncelet, and J.-C. Golinval, "Physical interpretation of independent component analysis in structural dynamics," *Mechanical Systems and Signal Processing*, vol. 21, no. 4, pp. 1561 – 1575, 2007.

[87] S. McNeill and D. Zimmerman, "A framework for blind modal identification using joint approximate diagonalization," *Mechanical Systems and Signal Processing*, vol. 22, no. 7, pp. 1526 – 1548, 2008.

[88] S. Nagarajaiah and B. Basu, "Output only modal identification and structural damage detection using time frequency & wavelet techniques," *Earthquake En-*

gineering and Engineering Vibration, vol. 8, pp. 583–605, 2009. 10.1007/s11803-009-9120-6.

[89] B. Hazra, A. J. Roffel, S. Narasimhan, and M. D. Pandey, "Modified cross-correlation method for the blind identification of structures," *Journal of Engineering Mechanics*, vol. 136, no. 7, pp. 889–897, 2010.

[90] A. B. of Shipping, *Guide for the fatigue assessment of offshore strctures*. American Bureau of Shipping, November 2010.

[91] A. Pandey and M. Biswas, "Damage detection in structures using changes in flexibility," *Journal of Sound and Vibration*, vol. 169, no. 1, pp. 3 – 17, 1994.

[92] J. B. Nestleroth and T. A. Bubenik, "Magnetic flux leakage (mfl) technology for natural gas pipeline inspection," *The Gas Research Institute*, 1999.

[93] S. Dutta, *Magnetic flux leakage sensing: The forward and inverse problems*. diploma thesis, Rice University, Houston, TX, 2008.

[94] Y. Li, J. Wilson, and G. Y. Tian, "Experiment and simulation study of 3d magnetic field sensing for magnetic flux leakage defect characterisation," *NDT E International*, vol. 40, no. 2, pp. 179 – 184, 2007.

[95] M. Oka, Y. Tsuchida, S. Nagato, T. Yakushiji, and M. Enokizono, "Estimation of fatigue damage for an austenitic stainless steel (sus304) using a pancake type coil," *AIP Conference Proceedings*, vol. 975, no. 1, pp. 1244–1251, 2008.

[96] A. Lynch, "Magnetic flux leakage robotic pipe inspection: Internal and external methods," diploma thesis, Rice University, Houston, TX, 2010.